10 November 2006 | $10

Science

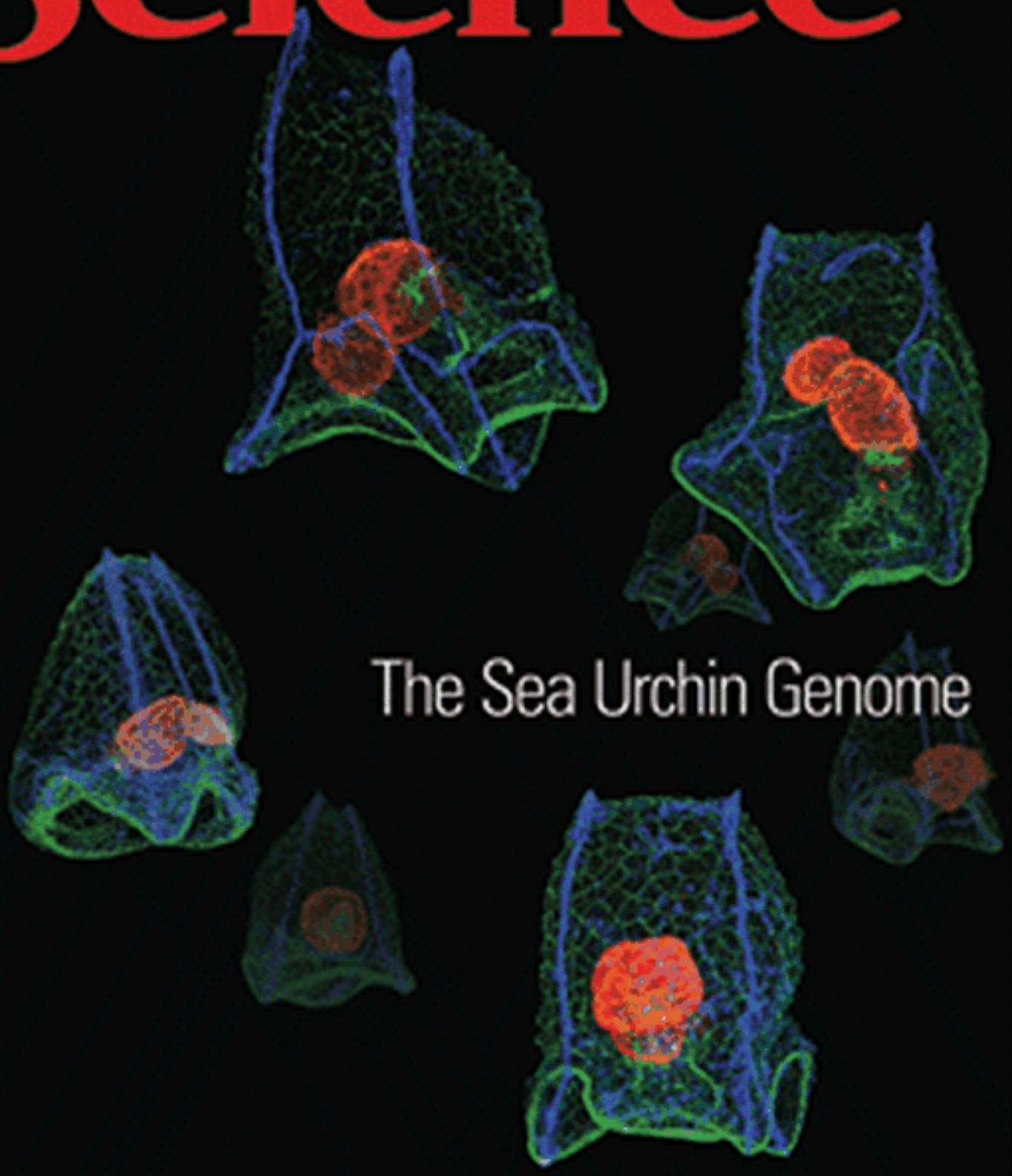

The Sea Urchin Genome

AAAS

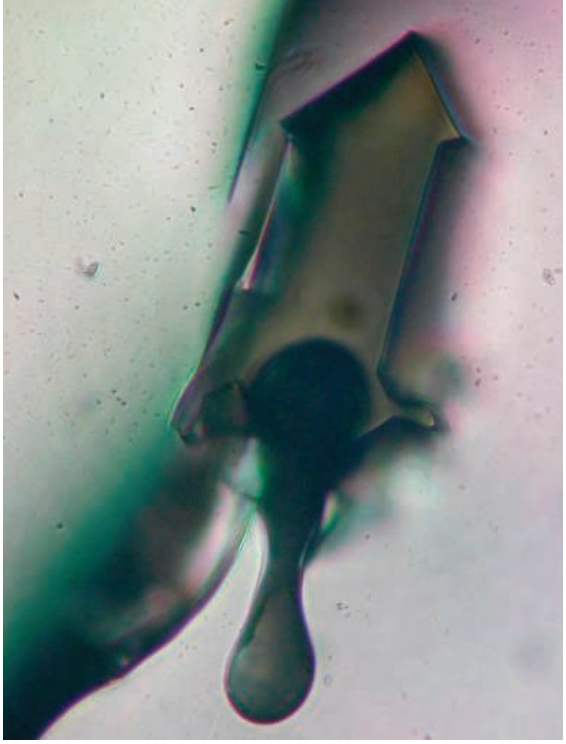

<< Silicate Slide Show

How molten magma and other geophysical fluids move through rocks is a basic question in geology. **Schiano *et al.*** (p. 970; see the Perspective by **Holness**) show that when driven by a temperature gradient, a silicate melt can move through the lattice structure of olivine but gas-rich fluid inclusions do not. The melt migrates within the mineral matrix instead of along crystal edges in a series of progressive dissolution and recrystallization steps. This process is controlled by interface kinetics and not chemical diffusion. In contrast, bubbles of gas-rich fluids remain stuck and do not migrate. Thus, transcrystalline migration is faster than intergranular porous flow at all melt fractions less than 0.1% and allows for grain-scale percolation and segregation of early mantle melts that have a low degree of melting.

Core Conundrum

The Earth's inner core grows slowly from the solidification of the outer core, and the heat released helps drive convection in the outer core and fuels the magnetic dynamo. **Wen** (p. 967, published online 28 September) measured the inner core's growth directly in one spot using seismic compression waves reflected off the inner core boundary. Similar waves received at seismic stations in Russia and Kyrgyzstan after a pair of earthquakes in 1993 and 2003 were tens of milliseconds earlier in the later earthquake, which indicates that this part of the inner-core boundary had grown by about 1 kilometer in a decade. This speed is much greater than predicted by the thermal history model of the core. Such a rapid change may indicate either differential rotation of an irregular inner core boundary or nonuniform growth of the inner core.

Well-Rounded Diet

The diets of early human ancestors have been difficult to determine. Our closest common ancestor, the chimpanzee, forages primarily on fruits and nuts that come from plants that use the C_3 photosynthetic pathway. Later hominins, of the genus *Homo* clearly had a diverse diet that included animals feeding on grasses (which use the C_4 pathway). It has been thought that the development of tools by *Homo* allowed this diversification in diet. **Sponheimer *et al.*** (p. 980; see the Perspective by **Ambrose**) studied the carbon isotope signature of enamel layers from teeth of *Paranthropus robustus*. This early hominin switched from a diet rich in C_3 plants to one with a C_4 source seasonally. Thus, the extinction of *P. robustus*, who apparently did not use tools, cannot be explained by a restricted diet.

CREDITS (TOP TO BOTTOM): LABORATOIRE PIERRE SÜE; YAVUZ *ET AL.*

Etching a Route to Nanotube Electronics

Carbon nanotube preparation processes generally produce mixtures of semiconducting and metallic nanotubes, which has hindered their development for large-scale electronics. **Zhang *et al.*** (p. 974) describe how a methane plasma and annealing treatment can selectively remove the metallic nanotubes. Combined with controlling the diameter of nanotubes during growth, pure semiconducting devices can be reliably obtained, as demonstrated by fabrication of high-current transistors.

Microwave Cloaking Realized

The ability to tune the electromagnetic response of materials recently provided theorists with the cue to propose the construction of a "cloak," a space that not only excludes electromagnetic radiation but also steers that radiation around itself as if it was not there. **Schurig *et al.*** (p. 977, published online 19 October; see the 20 October news story by **Cho**) present experimental results demonstrating that such a cloak can be constructed in the microwave regime from a metamaterial consisting of split-ring resonators. Although this system suffers from losses and only works in two dimensions, the results demonstrate the principle of cloaking.

Magnetic Separation with Single Domains

Mesoporous materials such as zeolites have high sorption capacities for separations, but mass transport through these materials can be a limiting factor. Nanoparticles offer potentially high surface areas and rapid contact with the sample, but as their size decreases, their separation from solution becomes more difficult. Magnetic separation routes, either batchwise or continuously from solution, that are useful with larger particles would appear to need prohibitively large-field gradients for submicrometer-sized particles. **Yavuz *et al.*** (p. 964) now show that this supposed limitation does not apply to single-domain magnetite particles about 10 nanometers in diameter; at relatively modest fields, these particles aggregated, apparently because of their much higher surface field strength compared to multidomain particles. Particles of different sizes could be

Continued on page 891

Published by AAAS

Continued from page 889

separated, and sorption onto the magnetite surfaces was used to capture and remove arsenic impurities from water.

The Bald Truth About Lipids

Hair loss can be traumatic, whether it is linked to illness or simply part of the natural aging process, and there is considerable interest in dissecting its underlying mechanisms. **Kazantseva *et al.*** (p. 982) identify a culprit gene in a group of Russian families who show an inherited deficiency in hair growth but are otherwise healthy. The mutant gene, *LIPH*, encodes lipase H, a phospholipase thought to regulate the production of lipid-signaling molecules. This discovery will likely stimulate investigations aimed at understanding the precise role of lipase H in hair follicle biology and whether the *LIPH* gene also contributes to the more common forms of baldness in the general population.

I'm a Pathogen, Let Me Out of Here

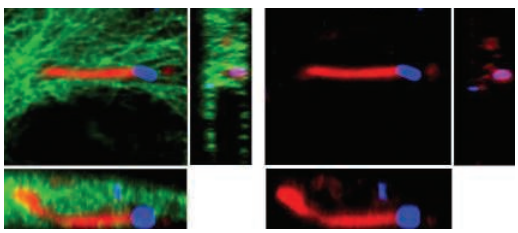

Certain microbial pathogens replicate within host cells, and virulence requires the dissemination of bacteria from cell to cell within the host. **Yoshida *et al.*** (p. 985; see the Perspective by **Gorvel**) now show that intracellular *Shigella* secretes VirA, a cysteine protease–like effector, into the host cell, which destroys microtubules and promotes its own intracellular motility. This process helps *Shigella* spread intracellularly and subsequently disseminate into adjacent epithelial cells.

Toward Defeating Blindness in the Elderly

Age-related macular degeneration (AMD) is a common cause of blindness in the elderly and is characterized by a breakdown of light-sensitive cells in the retina that results in progressive loss of central vision. The neovascular, or "wet," form of AMD is especially devastating for patients because vision loss is rapid. Studying a Chinese population, **DeWan *et al.*** (p. 989, published online 19 October) identified a single nucleotide polymorphism (SNP) in the *HTRA1* gene that confers a greatly increased risk of developing wet AMD. The *HTRA1* gene, located on chromosome 10q26, encodes a heat shock serine protease, and the SNP resides within the gene's promoter region. **Yang *et al.*** (p. 992, published online 19 October) find that the same SNP also increases AMD risk in a Caucasian population and is associated with higher expression levels of *HTRA1* messenger RNA and protein. Identification of this gene may ultimately lead to improved diagnosis and treatment of AMD (see the 20 October news story by **Marx**).

Spotting Invaders

The cell's ability to distinguish invading RNA or DNA from the plethora of its own nucleic acid sequences plays a critical role in protecting the genome from potentially harmful damage, and a number of systems have evolved to sniff out unwanted alien genes and trigger cellular responses (see the Perspective by **Fujita**). Retinoic acid–inducible protein I (RIG-I), part of the cellular alarm system in the cytoplasm, specifically recognizes a number of RNA viruses, but what is RIG-I actually sensing? **Hornung *et al.*** (p. 994, published online 12 October) and **Pichlmair *et al.*** (p. 997, published online 12 October) show that RIG-I detects and binds to an unusual feature of the 5′ end of the viral RNA, specifically, a 5′-phosphate group.

Choosing Channel Selectivity

Ion channel proteins form pores in the membranes of cells and are regulated by voltage or small messenger molecules to control information flow to and from cells. The K^+ channel, important for the excitability of nerve cells, conducts only K^+ ions, while completely excluding a smaller ion, Na^+. **Valiyaveetil *et al.*** (p. 1004) show that this selectivity is accomplished in two ways: In the presence of K^+, the pore remains open and conductive, but collapses when K^+ concentrations are low, excluding Na^+. In addition, in the conductive state, the pore is lined with multiple binding sites that are specific for K^+.

CREDIT: YOSHIDA *ET AL.*

Published by AAAS

Maxine Singer, a biochemist, is president emerita of the Carnegie Institution of Washington. She was chair of the National Academies' Committee on Science, Engineering, and Public Policy when it decided to sponsor the report described here.
E-mail: msinger@ciw.edu

Beyond Bias and Barriers

EARLIER THIS YEAR, THE U.S. NATIONAL ACADEMIES PUBLISHED *THE GATHERING STORM*,* a compelling statement describing the dependence of future national prosperity on increasing the numbers of scientists, engineers, and mathematicians. Now, a new Academies' study, *Beyond Bias and Barriers*,† argues that in spite of that need, our universities are wasting the skills and talents of many individuals by discouraging and inhibiting women from fulfilling their potential in academic science and engineering.

The new report avoids the uncritical hype and extreme positions that have accompanied recent public discussion of these issues. Instead, it is an exhaustive and critical review of relevant published research and analyses, as might be expected given the distinguished authoring panel of scientists and engineers. In spite of this, media response to the report has already included uninformed repetition of stereotypical views about women's talents. These data clearly demonstrate the flaws in several frequently offered explanations for why so few women hold science and engineering professorships. For example, the "pipeline" can no longer be blamed for the dearth of women.

Societal assumptions and their cultural consequences can account for most of the actually minor cognitive differences measured between the sexes. Boys and girls now come to college equally well prepared for coursework in science and mathematics. Even controlling for mathematics test scores among gifted youth, less than half as many women as men pursue scientific careers. Starting at the high school–to–college transition, a greater percent of women than men opt out of science and engineering at almost every step of the academic ladder. The one exception: Women who make it far enough through the minefields to be considered for tenure are as likely as men to succeed.

The report concludes that the current situation stems largely from unintentional bias harbored by both men and women and outmoded institutional structures. In one telling study, the same curricula vitae received lower evaluations when attached to a woman's name than to a man's. Gender stereotypes also produce anxiety that can decrease performance. Even seemingly minor, inadvertent exclusions from the encouragement that is routine for boys and men can eventually add up to serious discouragement from pursuing academic careers.

Most university policies reflect outmoded male expectations for a scientific career and lifestyle, including a wife at home. However, today many married male faculty have working wives. Many young men are unhappy with 80-hour work weeks, but they are a real hardship for women, especially because the early years of their careers coincide with childbearing years. Women should, if they wish, be able to have and raise children without suffering a reevaluation of their commitment and ability to do research. University policies and faculty attitudes must change to recognize these realities if they are to attract the gifted women postdocs who will otherwise opt out of academia. Even the financial sector is considering "reshaping the very architecture of Wall Street work in order to keep women involved" because 80-hour work weeks are a problem and diversity is important to success.‡

Beyond Bias and Barriers makes specific recommendations for action by universities, professional societies, funding agents, and federal enforcement agents. Recognizing that federal law requires an equal playing field for science as well as sports, it recommends the formation of an interuniversity oversight body analogous to that of the National Collegiate Athletic Association to gather data and monitor progress toward compliance with federal antidiscrimination rules.

National needs, equity, and common sense speak with one voice. Schools and universities must find ways to encourage and ease the path for women who are inspired by the great scientific adventure. As Donna Shalala, chair of the authoring panel, says in her preface, "It is time—our time—for a peaceful, thoughtful revolution."

– Maxine Singer

10.1126/science.1135744

**Rising Above The Gathering Storm: Energizing and Employing America for a Brighter Economic Future* (National Academies Press, Washington, DC, 2006), www.nap.edu/catalog/11463.html. †*Beyond Bias and Barriers: Fulfilling the Potential of Women in Academic Science and Engineering* (National Academies Press, Washington, DC, 2006), www.nap.edu/catalog/11741.html. ‡*New York Times*, 6 August 2006, Sunday Business section, p. 1.

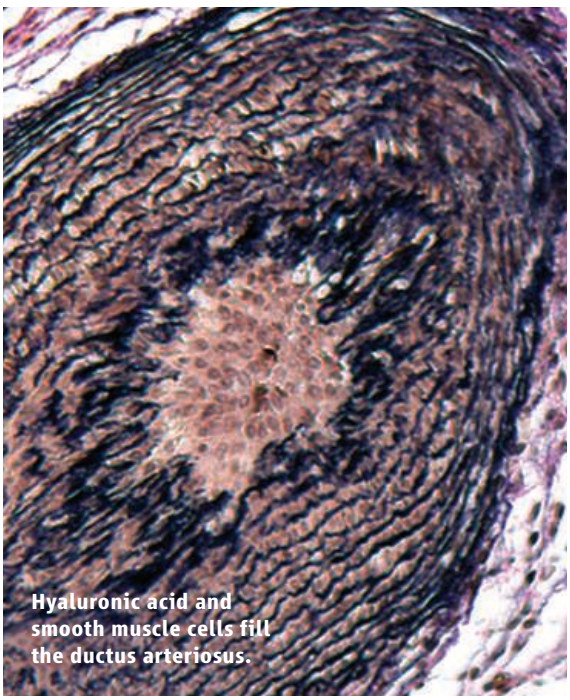

Hyaluronic acid and smooth muscle cells fill the ductus arteriosus.

BIOMEDICINE

Cushioning the Flow

The ductus arteriosus (DA) is a vessel that connects the pulmonary artery and aorta in a developing fetus; blood bypasses the immature fetal lungs and flows to the placenta, where the carbon dioxide is exchanged for oxygen. Shortly after birth, when the neonatal lungs take over responsibility for oxygenation of the blood, there is no longer any need for the DA, and, normally, it closes. However, in about 1 in 2000 infants, and more frequently in those born prematurely, the DA fails to close. This condition, called patent DA (PDA), can strain the lungs and lead to various forms of vascular disease.

The DA remains open in the fetus in part through the vasodilatory effects of circulating prostaglandins such as PGE, and for this reason drugs (such as indomethicin) that inhibit the production of PGE by cyclooxygenase (COX) are commonly used to treat PDA. Working in a rat model system, Yokoyama *et al*. discover that the role of PGE in this setting may be more complex than previously thought. They find that PGE prepares the fetal DA for closure by promoting the formation of the "intimal cushion," a buildup of smooth muscle cells and extracellular matrix that anatomically occludes the vessel. If PGE is found to have the same opposing effects on DA patency in humans, then this discovery could lead to better treatments for PDA. — PAK

J. Clin. Invest. **116**, 3026 (2006).

DEVELOPMENT

Timing Out

In response to adverse conditions, some animals enter into reproductive or developmental arrest (for example, mammalian hibernation, insect diapause, and worm dauer-stage formation). Williams *et al.* examine the molecular contributors to *Drosophila* diapause, an overwintering strategy. By evaluating natural diapause variants representing different climates (one from Canada and one from the southern United States), genetic variation was mapped to the *Dp110* locus, coding for phosphatidylinositol 3-kinase (PI 3-kinase). They found that a reduction in dosage of *Dp110* increased the proportion of flies in diapause, but neuronal expression of *Dp110*, reduced it. Hence, effects on *Drosophila* diapause are seen upon altering signaling from the insulin-regulated PI 3-kinase pathway. The conservation of this pathway in the fly and *Caenorhabditis elegans* as revealed by the involvement of PI 3-kinase in diapause and dauer formation, respectively, provides a link between reproductive and developmental arrest. — BAP

Proc. Natl. Acad. Sci. U.S.A. **103**, 15911 (2006).

GENETICS

Live Fast, Die Early

How an organism repairs damage to its DNA has important implications for disease and, potentially, for aging, as the latter is correlated with increasing DNA damage. Double-stranded breaks (DSBs) in DNA are particularly noxious, and cells have evolved several ways to cope: Homologous recombination (HR) uses the sequences of a homologous chromosome to patch the damaged site, which minimizes the chance of mutation, whereas nonhomologous end joining (NHEJ) is faster but may introduce small additions or deletions.

Preston *et al.* have looked at the way germ cells in male *Drosophila* deal with DSB damage over the lifetime of the individual. They find that the importance of the various pathways changes substantially, with young (1-week-old) males showing a low level (~15%) of repair via HR, which increases to 60% in 6-week-old flies. On the other hand, flies that died or became infertile after only 4 weeks had a tendency to show increasing NHEJ-based repair of the DSB with age. The authors speculate that young flies might benefit from rapid gamete development and production (and thus being first to mate), and therefore evolution favors the rapidity of NHEJ repairs, which outweighs the mutational burden. Older flies, having outlived most of the competition, might find themselves in an environment where the frequency of mating is low and speed is no longer a critical factor. — GR

Screening for DSB repair by fluorescence.

Curr. Biol. **16**, 2009 (2006).

CHEMISTRY

Roaming Around the Saddle

Transition state theory has proven to be a powerful framework for understanding and predicting chemical reaction kinetics. A central tenet of the theory is passage of each productive reaction trajectory through a specific configuration, or transition state, corresponding to a potential energy saddle point. Rate models therefore tend to focus on determination of this configuration. Recently, however, experimental and theoretical analyses of formaldehyde (CH_2O) dissociation implicated a pathway that skirted the transition state and instead relied on the roaming or wandering motion of one H atom about the HCO core.

Houston and Kable have observed evidence of a similar roaming mechanism in the photo-induced dissociation of an acetaldehyde (CH_3CHO) sample to CO and CH_4. By resolving the rotational states of the CO product using laser-induced fluorescence, they found that ~15% of the dissociation events distributed an unexpectedly large proportion of the excitation

Continued on page 897

CREDITS (TOP TO BOTTOM): YOKOYAMA *ET AL., J. CLIN. INVEST.* **116**, 3026 (2006); PRESTON ET AL., GENETICS 172, 1060 (2006).

Continued from page 895

energy to the methane co-product. To explain this outcome, the authors favor a mechanism involving a roaming methyl group, though they note that theoretical simulations will be necessary to rule out an alternative higher-energy H-atom roaming mechanism. — JSY

Proc. Natl. Acad. Sci. USA **103**, 16079 (2006).

APPLIED MATHEMATICS

Unraveling Cellular Motion

The mechanisms whereby living cells propel themselves across various media involve a remarkably complicated set of factors. Experiments 25 years ago sought to track the wrinkle patterns induced by cell motion on an elastic film, and thus to determine the forces underlying cellular motion, but the problem proved highly nonlinear. A later proposal was to monitor the movement of fluorescent marker beads in a soft gel that remained in the linear elastic regime, but these results were highly sensitive to input data. Most recently, cells were observed on a bed of microneedles, with the degree of needle bending used to extract the force exerted by the cells as they traveled. However, in this case spatial resolution was limited and the environment somewhat unrealistic.

Calculations in such a context, which rely on incomplete data to create a model, are called inverse problems and crop up in many fields, including geophysics, medical imaging, and astronomy. Unfortunately, solving this class of ill-posed problems is often difficult on account of their high sensitivity to changes in the data. Ambrosi presents a fresh strategy for solving the inverse problem of cell traction on an elastic substrate, employing marker data to reveal the forces that cells exert on a gel. The method uses minimization followed by numerical solution of coupled partial differential equations and may also be applicable to other similar inverse problems. — DV

SIAM J. Appl. Math. **66**, 2049 (2006).

GEOPHYSICS

Rumbles After Rain

Water buried in the earth has appeared to cause earthquakes beneath certain reservoirs and in other areas with fluctuating groundwater levels. The fluid is thought to lubricate faults and alter pressure, thus making it easier for rocks to slip. Hainzl *et al.* have monitored seismic signals from the landscape surrounding Mount Hochstaufen in southeastern Germany, and they find that minor earthquake swarms tend to follow periods of high precipitation there. Seismic activity has been observed in this range of limestone and dolomite mountains for some 600 years, although such behavior is unusual in the wider region. The earthquakes tend to be small but numerous: approximately 1100 small shallow earthquakes (with moment magnitudes less than 2.4) were detected by a seismic array in 2002. Most earthquakes occurred in the summer months, particularly after wet periods in March and August. The resulting seismic events correlate in space and time with the calculated distribution of pore pressure changes due to diffusing rainwater and the frictional behavior of faults. The seismicity data indicate the sensitivity of the Earth's crust to local disturbances and offer a potential means of predicting earthquakes on the basis of weather patterns in such regions. — JB

Geophys. Res. Lett. **33**, L19303 (2006).

CHEMISTRY

Expansive Accommodations

The interaction of porous metal-organic framework (MOF) materials with adsorbed guest molecules can result in reversible structural transformations. Kondo *et al*. have observed such a transition induced by carbon dioxide adsorption in a $[Cu(BF_4)_2(bpy)_2]$ lattice, where bpy is 4,4′-bipyridine. The authors prepared this MOF, which adopts a two-dimensional (2D) quasi-square grid

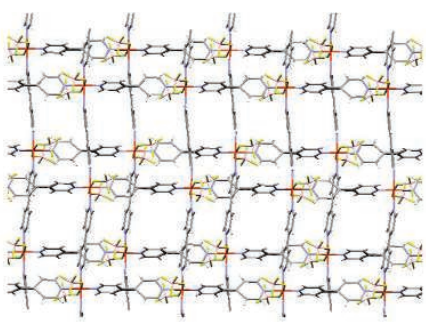

MOF structure.

structure, by crystal-to-crystal transformation of a hydrated 3-D interpenetrating network precursor, which they heated under vacuum for several hours to remove the incorporated water.

Exposure of the MOF to CO_2 at 273 K resulted in an abrupt jump in adsorption as the incoming gas pressure approached 35 kPa. To explain this observation, the authors carried out structural modeling of the material, with and without adsorbed CO_2, on the basis of extended x-ray absorption fine structure and powder x-ray diffraction data. The results indicated that CO_2 adsorption and subsequent clathrate formation increased the interlayer distance in the host lattice by ~50% to 0.68 nm. This process, which though reversible exhibited significant hysteresis, led to a macroscopic volume change of 6.6% at a final pressure of 101 kPa. — PDS

Nano Lett. **6**, 10.1021/nl062032b (2006).

CREDIT: KONDO *ET AL.*, *NANO LETT.* **6**, 10.1021/NL062032B (2006)

Published by AAAS

Tongues on the Brain

"Speaking in tongues," or glossolalia—an intense, trancelike state where the speaker is ostensibly in direct connection with God—has been around for thousands of years.

Now psychiatrist Andrew Newberg and colleagues at the University of Pennsylvania in Philadelphia say they have captured glossolalia on brain scans. They recruited 5 black women from a local Pentecostal congregation, where speaking in tongues is common, and asked them to sing gospel songs and to speak in tongues. During each activity, the women were injected with a radioactive tracer that provided brain-scanning equipment with a snapshot, in effect, of which areas were most active as indicated by blood flow.

The scientists report in the November issue of *Psychiatry Research: Neuroimaging* that compared to when the women were singing, frontal lobe function decreased during glossolalia. "The part of the brain that normally makes them feel in control has been essentially shut down," explains Newberg. And there was increased activity in the brain's parietal region, which he says "takes sensory information and tries to create a sense of self and how you relate to the rest of the world." Both of these shifts are the opposite of what happens to the brain in a meditative state, he says.

Psychologist Michael Persinger of Laurentian University in Ontario, who has done brainwave research with glossolalia, agrees that increased parietal activity "would be associated with … an enhancement of 'touching' sensations over the entire body—i.e., being touched by the 'spirit.' "

GETTING AFRICA BACK TO ITS ROOTS

The enset of Ethiopia (below), which resembles a banana tree and has a thick trunk filled with pithy starch, was called "the tree against hunger" in a 1997 report by the AAAS (publisher of *Science*), which said it was "very likely the most unstudied domesticated crop in Africa."

Nine years later, little has changed. The enset is listed among 18 indigenous African vegetables that have been largely ignored by scientists and agriculture planners, in a report released last week by the National Research Council. "[L]ack of research attention to them is a disgrace of our time," says the report* on Africa's "lost crops," written by a group chaired by Norman Borlaug, the father of agriculture's Green Revolution who now is at CIMMYT, the international maize center in Mexico City. With countries throwing their research funding into commercial non-native crops, little work has gone into improving the cultivation of many resilient and nutritious vegetables, including beans, nuts, melons, roots, and tubers, that traditionally formed the backbone of African diets. Nowadays, Africa's most widely consumed vegetables are largely of foreign extraction, says the report. The only exceptions are cowpea, yam, and okra.

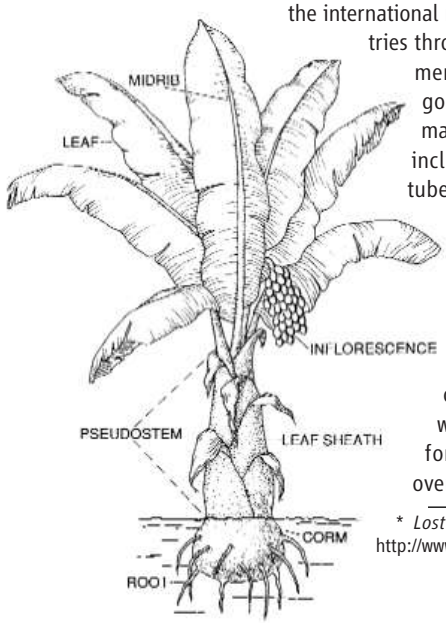

The 378-page volume is the second in a series. The first, in 1996, dealt with the ignored grains of Africa. Soon forthcoming is one on the continent's overlooked fruits.

* *Lost Crops of Africa, Volume II: Vegetables* at http://www.nap.edu

Alpha Paper Producers

Despite all of its political turmoil, Harvard is still on top of the charts, according to the research trend-tracking *Science Watch* in Philadelphia, Pennsylvania. The ranking of the top 100 federally funded U.S. universities is based on numbers of high-impact (heavily cited) papers published in 21 fields of science and social science over the past 5 years. Harvard and Stanford are the usual leaders in *Science Watch*'s quadrennial roundup; this year, the University of California (UC), San Francisco, and the University of Pennsylvania make their first appearances on the highest impact list.

In separate rankings of universities in nine fields in biology, Harvard and Stanford emerge as the most prolific high-impact paper producers in clinical medicine and immunology, respectively.

Tops in the Sciences, 2001–2005

University	Number of Fields in which ranked in Top 10
1. Harvard University	15
2. Stanford University	13
3. UC, Berkeley	10
4. University of Washington	8
5. Massachusetts Institute of Technology	7
6. Yale University	6
7. UC, San Diego	6
8. Princeton University	5
9. University of Pennsylvania	5
10. California Institute of Technology	5
11. UC, San Francisco	5
12. Columbia University	5

NETWATCH >>

Free Journals For the Third World

Researchers in the poorest nations can nab a free pass to environmental science literature, thanks to a collaboration between the United Nations Environment Programme, Yale University, and more than 200 journal publishers. Announced on 30 October, Online Access to Research in the Environment (OARE) takes after similar projects to eliminate barriers to medical and agricultural publications. Educational organizations in 70 "low-income" countries can apply for access to full-text content from 1000 databases and journals, including *Science*, *Nature*, and *Ecology*. In 2 years, organizations from slightly wealthier countries can join for a small fee. >> www.oaresciences.org

A spiky kinship
908

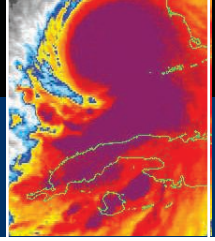

Blowing hot and cold
910

ASTRONOMY

Panel Prunes NSF Orchard to Make Room for Growth

Two major U.S. radio astronomy facilities funded by the National Science Foundation may need to close by 2011 to make room for new NSF astronomy projects. Last week, an expert panel put the two facilities—including the massive Arecibo radio telescope that fills a sinkhole in Puerto Rico—on a hit list ordered by NSF to save $30 million a year in its $191 million astronomy budget. Although researchers generally applaud the panel for its ability to make tough choices, some say the proposed cuts are unrealistic and may not achieve the desired savings.

"I think they made as reasonable recommendations as possible," says Virginia Trimble, an astronomer at the University of California, Irvine. But Jeremy Mould, director of the National Optical Astronomy Observatory in Tucson, Arizona, says the committee underestimated the observatory's needs in part because it did not visit NOAO's facilities at nearby Kitt Peak and in Chile.

NSF requested the review a year ago to help accommodate new projects—in particular, the Atacama Large Millimeter Array, an array of 50 radio telescopes under construction in Chile—in an anticipated flat astronomy budget. "We were headed for a train wreck between the aspirations of the community and the reasonable budget prospects," says Wayne Van Citters, director of NSF's division of astronomical sciences. Only $50 million devoted to research grants was off-limits.

Help wanted. The Arecibo radio telescope may need new benefactors to stay in business.

The committee, chaired by astrophysicist Roger Blandford of Stanford University in Palo Alto, California, held seven town meetings and met with the groups that run NSF's five observatories. "We were faced with the choice of closing facilities that are doing tremendous science or having no future program," Blandford says.

In the end, the panel said NSF should cut Arecibo's annual $12 million operating budget by one-third starting in 2009 and look for partners to split the remaining $8 million tab. If no partners can be found by 2011, the panel said, the facility should be dismantled. Similarly, the panel recommended finding partners to assume half of the $6 million operating budget of the Very Long Baseline Array (VLBA), a network of 10 radio dishes stretching from Hawaii to the Virgin Islands. If no partners appear, the committee concluded, then the dishes should come down.

Officials in charge of Arecibo fear the worst. "We're not very optimistic about being able to find $4 million from foreign partners," ▶

MALARIA

Chloroquine Makes a Comeback

Chloroquine, a malaria drug rendered useless in most of the world by drug-resistant parasites, is once again effective in Malawi. In a study in the 9 November *New England Journal of Medicine*, researchers report that chloroquine cured 99% of 80 malaria cases in Blantyre, the country's commercial capital.

Cheap, easy to administer, and with few side effects, chloroquine was once considered a miracle drug. But by the 1980s, resistance had spread, and in 1993, Malawi became the first African country to officially discourage its use. Few suspected that natural susceptibility would return. But in 2001, molecular studies in Malawi suggested that the resistance mutation had nearly disappeared, and studies of adults hinted that the drug could again clear the parasite.

The new study shows that chloroquine can also work in children with acute infections. Miriam Laufer and Christopher Plowe of the University of Maryland, Baltimore, and their colleagues treated children suffering from uncomplicated malaria with either chloroquine or sulfadoxine-pyrimethamine (SP), the standard first-line drug in Malawi. Chloroquine was effective in 79 of 80 children who received it. In contrast, SP failed in 71 of 87 children. (Those children received backup treatment, and all made full recoveries.)

The result does not mean that Malawi should go back to using chloroquine, Plowe stresses. "Malawi is a little island of sensitivity surrounded by a sea of resistance," he says. "Resistance would come washing back in" if the drug were widely used.

But knowing that the drug can regain its usefulness after a prolonged absence gives researchers hope that the same might be true for other resistance-plagued drug regimes. The result "is another argument for getting chloroquine out of Africa," says malaria expert Thomas Wellems of the U.S. National Institute of Allergy and Infectious Diseases in Bethesda, Maryland. **–GRETCHEN VOGEL**

CREDIT: NAIC/ARECIBO OBSERVATORY

says Joseph Burns, vice provost for physical sciences and engineering at Cornell University, which manages Arecibo. The 305-meter-wide dish discovered the first binary pulsar, has probed the planets, and is the best instrument for spotting near-Earth asteroids, says Burns, who hopes NSF will reconsider the proposal.

In contrast, Fred K. Y. Lo, director of the National Radio Astronomy Observatory (NRAO) in Charlottesville, Virginia, says he's cautiously optimistic that other countries will come forward to help save VLBA, which can pinpoint radio sources to an unrivaled precision. "The VLBA has a lot of unique capabilities that people would miss," Lo says. "So we are certainly talking to our partners to see if we can keep it going."

The committee also recommended a 50% cut in the $13 million a year spent on administrative and scientific staff, instrument development, and data products by NOAO, which supports 4-meter telescopes at Kitt Peak and at the Cerro Tololo Inter-American Observatory in Chile. NRAO's $5 million staffing budget faces similar cuts.

Blandford admits that cost cutting is an inexact science. "By economic shenanigans, I can find you anywhere between $16 million and $60 million in our recommendations," he says. NSF will conduct detailed cost analyses to determine precisely how much money the proposed cuts will save, Van Citters says.

Staff members are also preparing specific recommendations for NSF Director Arden Bement to take to the National Science Board, NSF's oversight body, which must sign off on any decision. "We take the report very seriously," says Bement. "I intend to act on it." **–ADRIAN CHO**

AVIAN INFLUENZA

Is China Coming Clean on Bird Flu?

World Health Organization (WHO) officials last week renewed calls for China to share information and data on avian influenza after a group of Hong Kong and U.S. researchers reported that a new H5N1 strain is circulating in southern China. But China's Ministry of Foreign Affairs denies reports of the new strain and insists that the country is cooperating.

The row was set off last week by a report from a group led by Yi Guan of the State Key Laboratory of Emerging Infectious Diseases at the University of Hong Kong that a new strain of the H5N1 influenza virus had become predominant in southern China. Based on surveillance of live poultry markets in six provinces, the authors speculated in the online *Proceedings of the National Academy of Sciences* (*PNAS*) that the new Fujian-like strain emerged in response to poultry vaccination and might be resistant to current vaccines. Other experts said further work was needed to confirm those conclusions (*Science*, 3 November, p. 742).

After the paper appeared, Beijing-based WHO officials publicly urged China to share samples of viruses circulating among the nation's poultry, which they say are needed to update diagnostic tests and develop prototype vaccines for humans. Responding to a question at a 2 November press conference, Foreign Ministry spokesperson Liu Jianchao said that China's own monitoring showed there to be "no distinct changes in [the virus's] biological characteristics." Liu insisted that government departments are sharing all relevant epidemic and viral information, noting that Chinese authorities recently informed the United Nations Food and Agriculture Organization in Rome and the Paris-based World Organization for Animal Health of a new viral strain circulating in northern China.

Julie Hall, the WHO coordinator for communicable disease surveillance and response in Beijing, says China's Ministry of Health has shared six virus samples from human cases over the past year, but the Ministry of Agriculture hasn't shared any since 2004. Over the past year, the Health Ministry has reported human cases in provinces where there are no reported poultry outbreaks. Now the *PNAS* paper suggests that the virus is circulating in poultry in six provinces even more widely than it has in the past, yet information from the Ministry of Agriculture's surveillance efforts is not showing the same results. "What we need is a clear and comprehensive picture" of which substrains are increasing and which are disappearing—and in what regions—as well as sharing of samples, Hall says.

A better understanding would enable China to evaluate and fine-tune its control measures. And sharing samples could help in the development of vaccines and diagnostics tailored to the strains in circulation. As an example, Hall notes that early this year a human case in northeast Liaoning Province tested negative using then-current diagnostic tests. But once viral strains circulating among poultry in the region were used to tweak the diagnostic test, it produced accurate positive results. "Even a minor change [in the virus] can affect the sensitivity of diagnostic tests," Hall says.

Last year, China's Ministry of Agriculture agreed to share 20 viral samples from strains circulating within China in 2004 and 2005. But Hall says that the samples have yet to be shipped to international reference labs. Ministry of Agriculture officials did not return e-mails seeking comment.

–DENNIS NORMILE

With reporting by Hao Xin in Beijing.

CREDIT: COLOR CHINA PHOTO/AP PHOTO

True or false? Chinese authorities have denied a report from Hong Kong and U.S. researchers that a new H5N1 strain is circulating widely in southern China.

CONSERVATION BIOLOGY

Indian Wildlife Researchers Show Their Fangs Over Permit Hassles

NEW DELHI—Little is known about the Malabar civet (*Viverra civettina*), an endangered mammal the size of a small dog that lives in the wet forests of southern India. It has never even been photographed in the wild. To get a better understanding of this vanishing beast, N. V. K. Ashraf, a veterinarian with the Wildlife Trust of India in New Delhi, sought a research permit last January from the Kerala Forest Department, which manages the civet's last-known habitat. Permission was granted—but to work only between 6 a.m. and 6 p.m. The Malabar civet, however, is a nocturnal animal. Not surprisingly, Ashraf has found no trace of the civet during his daylight-hours research.

Ashraf's frustrations are far from unique—and now India's wildlife researchers have had enough. Writing in the 25 October issue of the journal *Current Science*, 14 of the country's leading experts bemoan "a disturbing trend across India where scientists are increasingly denied access to wildlife reserves for scientific research or are seriously impeded, without scope for redress." They blame the antiquated Wildlife Protection Act of 1972, which puts research and hunting permits in the same general category. They also claim that unnamed officials "arbitrarily" deny access to reserves and "demand co-authorship on publications as a precondition" for a research permit.

In a report last year, the Tiger Task Force, set up by India's prime minister to determine the causes for the sudden decline in tiger numbers, noted that "almost every wildlife researcher has a grouse against the wildlife bureaucracy: either for its failure to aid in their research or for ignoring the findings of their research."

One tiger researcher, Raghunandan Chundawat, says that last year he was abruptly asked to quit his research area in Panna National Park in central India. Chundawat, formerly of the Wildlife Conservation Society in New York City and now based in India for the International Snow Leopard Trust in Seattle, Washington, says his research permit was revoked soon after he filed a complaint about the unnatural death of one of his radio-collared tigers. Rajesh Gopal, director of Project Tiger for the Ministry of Environment and Forests in New Delhi, claims that Chundawat "appeared to have a hidden agenda" in that he set up a nongovernmental organization near the Panna National Park with "an antisystem posture." Chundawat dismisses the allegations as baseless. Prodipto Ghosh, secretary of the Ministry of Environment and Forests in New Delhi, accepts that wildlife researchers have "genuine complaints" and acknowledges that "the approach in the past [for awarding research permits] has been too conservative." Ghosh says that the ministry plans to amend the Wildlife Protection Act to make procuring research permits easier. But he says strict controls must continue.

Beauty and the bureaucrats. Tiger and civet experts are among those who accuse officials of capricious rulings on reserve access.

CREDIT: P. BAGLA/*SCIENCE*

Amending the wildlife act is one change that the *Current Science* authors seek. They also recommend a sweeping overhaul of wildlife research regulations. The Tiger Task Force has also recommended that parks "streamline existing procedures for clearances and co-ordination of research" for those who receive research permits. "We need to change the attitude of our managers from a guard protecting jewels to a librarian who is managing a library of unexplored knowledge and inviting people for learning," says Chundawat. For now, however, India's wildlife researchers will have to continue working under the accustomed constraints. **–PALLAVA BAGLA**

Animal Eggsploitation

Two British research groups have asked the government for permission to use animal eggs in attempts to develop populations of human embryonic stem cells for studies of human diseases. A team headed by Lyle Armstrong of the International Centre for Life in Newcastle upon Tyne wants to generate stem cell lines for studying muscle neuron disease (amyotrophic lateral sclerosis) by inserting the nucleus from a patient's skin cell into a cow oocyte. At the same time, Stephen Minger of King's College London has applied for permission to use cow, sheep, goat, and rabbit eggs to create embryos to study Parkinson's and Alzheimer's diseases. A third group, headed by Ian Wilmut of the University of Edinburgh, is also planning to apply for permission to use animal eggs.

Such research is forbidden now in the United Kingdom because it would require growing hybrid embryos to the blastocyst stage. That's about 4 days beyond the legal limit for mixing human and animal gametes, set for a technique that uses guinea pig eggs to test human sperm. The U.K.'s Human Fertilisation and Embryology Authority says some oppose such proposals—the Scottish Council on Human Bioethics said they threaten "the very concept of being entirely human"—but Minger and others say that using plentiful animal eggs makes more sense than using hard-to-obtain human eggs for this unproven technique.

–CONSTANCE HOLDEN

Missing: Climate Data

Although the African continent is likely to be hit hardest by climate change, its monitoring facilities are the least prepared to track the shifts, says a report issued this week by the United Nations Framework Convention on Climate Change. Some 1165 stations in the Global Climate Observing System span more than 50 nations worldwide to provide coordinated climate data. But roughly 21 of the 84 surface posts in eastern and southern Africa, which collect temperature and precipitation data, are damaged. Also, two of the upper-air stations in the region, which record wind and temperature data, are silent. That leaves data gaps and a weakened "ability to predict the global climate system," the report laments.

David Goodrich, director of the worldwide sensor network, says he's "optimistic" that he'll get the roughly $60 million in commitments he'll need to fix things during this month's United Nations Climate Change Conference in Nairobi, Kenya. **–ROBERT KOENIG**

Well protected. The purple sea urchin's unusually complex immune system may explain how this echinoderm can survive for decades.

GENETICS

Sea Urchin Genome Confirms Kinship To Humans and Other Vertebrates

Looking like old-fashioned pincushions and lacking legs, eyes, and even an obvious brain, sea urchins seem nothing like humans. But looks can be deceptive.

On page 941, George Weinstock of Baylor College of Medicine in Houston, Texas, and his colleagues describe the 814 million DNA bases that make up the genome of the purple sea urchin, *Strongylocentrotus purpuratus*. Its 23,500 genes suggest that these algae-eating invertebrates have more complex immune and sensory systems than researchers had appreciated. The genome also includes many genes essential to humans and other vertebrates, although notably missing are numerous genes typical of flies and worms. The genome "casts in concrete the reality" that sea urchins and other echinoderms really are closer kin to humans and other chordates than to beetles, flies, crabs, and clams, says Eric Davidson, a developmental geneticist at the California Institute of Technology in Pasadena.

Even if the sea urchin didn't share an ancestor with the chordates, its genome warranted deciphering. The animal has been a boon to biologists and biomedical researchers for more than a century. In the late 1870s, researchers observed for the first time the fusion of the egg's and sperm's nuclei by studying sea urchin eggs. Twenty-five years later, in 1902, Theodor Boveri used urchins to show that development was impossible unless each embryonic cell had the full complement of chromosomes.

Female sea urchins spew out millions of eggs at a time, which are easy to modify genetically, making them a perennial favorite of developmental and cell biologists. More recently, researchers have begun piecing together gene networks by tracing gene interactions during the sea urchin's development.

Now this organism's contributions to genetics, developmental biology, immunology, and other fields should explode even further, and not just because of the genome sequence. For the first time, a new genome sequence is accompanied by a comprehensive analysis (p. 960) of when and where genes are expressed—the so-called transcriptome. Other reports on pages 939, 940, and 956, and in the 1 December issue of *Developmental Biology*, help define the sets of sea urchin genes associated with specific functions such as biomineralization, as well as unravel the evolution of the genome.

Researchers have found unexpected sophistication in the urchin genome—particularly among its immune system genes—and in how the genes are employed for

Forty-eight hours. The sea urchin requires half its genes just to get to this simple gastrula stage.

reproduction, development, and sensing the outside world. This complexity shows that "evolution was pretty successful in developing most of the major [genetic] building blocks of a very complex organism quite a long time ago," says Francis Collins, director of the National Human Genome Research Institute in Bethesda, Maryland. The sea urchin "provides a global view of the genes necessary for evolution to a human," adds Gary Wessel, a developmental biologist at Brown University.

Complex simplicity

With about 1500 cells and just a dozen cell types, the sea urchin embryo doesn't begin to approach the complexity of a human fetus. Yet the new analyses are showing that "it takes a lot of genetic information to make a really simple embryo," says Davidson. For the transcriptome study, biochemist Viktor Stolc of NASA's Ames Genome Research Facility in Moffett Field, California, and his colleagues used NASA supercomputers to design microarrays covering all the urchin genes. The devices tracked which genes turned on and off during the first 2 days of development. About 11,500 protein-coding genes were involved, but the microarrays also revealed another 51,000 RNAs of as-yet-unidentified function.

Meanwhile, Meredith Howard-Ashby in Davidson's lab and her colleagues looked in depth at most of the urchin's known transcription factors during the same 2 days, using a sensitive technique for measuring messenger RNA in cells. Over this 48-hour period, about 80% of the 283 transcription factors helped set up the embryo, they report in *Developmental Biology*. They calculate that by the time the larva was fully formed, 95% of these factors would be employed. "This tells us that most regulatory genes have to be used over and over again," says Davidson, likely in different places during different times over the organism's life.

Another genome analysis reported in *Developmental Biology* by Wessel, Jia Song, and Julian Wong at Brown shows that a different set of the urchin's transcription factors, many of which are not expressed in the embryo, are responsible for the maturation of the egg inside the adult. That work also illuminated the genes activated just after fertilization to prevent penetration by other sperm. Such detail "means we will have a better global perspective on the process of reproduction in general," says Charles Walker, an

invertebrate zoologist at the University of New Hampshire in Durham.

Sensory puzzles

Other details about the urchin genome have left researchers scratching their heads. The urchin has about 979 genes for proteins expressly designed to sense light or odors—a number on par with what vertebrates have and more than in the invertebrates studied to date, Florian Raible of the European Molecular Biology Laboratory in Heidelberg, Germany, Maria Ina Arnone of the Anton Dohrn Zoological Station in Naples, Italy, and their colleagues report in *Developmental Biology*. Yet the sea urchin lacks eyes, nose, antennae, and a centralized brain for coordinating and responding to incoming signals.

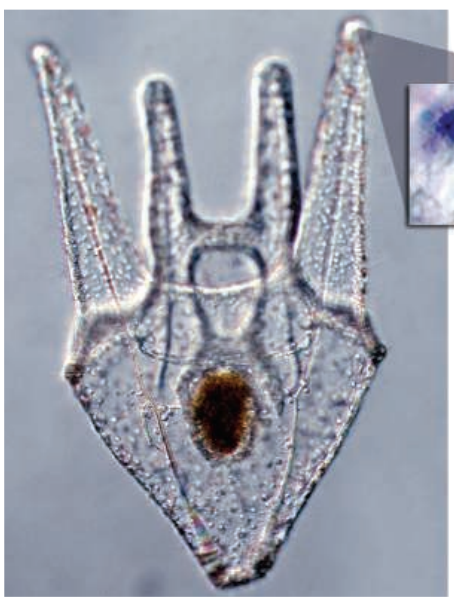

Look and see? A larval sea urchin lacks eyes—as do adults—but its "arms" do have light-sensing proteins (*inset*, blue).

Moreover, the urchin has six genes for opsins, molecules that are key to sensing light. Some of the urchin's opsin genes had previously been found only in the "eyes" of scallops. Raible and Arnone have found that tiny pincers tucked in below the spines, as well as the tips of the tube feet, express opsin and some of the other newfound genes. These appendages may not be "eyes" and "noses" per se, but "it is really interesting that the same [genes] are used in different ways, presumably to perceive the environment," says Weinstock.

Pathogen protection

The sea urchin's immune system genes are also giving researchers pause. Invertebrates depend primarily on innate immunity, with pathogen-sensitive receptors encoded in their genomes sparking an immune attack. Vertebrates have this innate immune defense, but they also have an adaptive system, whose customized immune cells and proteins are capable of a more targeted response. Yet the sea urchin has genes for supposedly vertebrate-specific immune proteins, Jonathan Rast, a comparative immunologist at the University of Toronto, Canada, and his colleagues report on page 952.

The sea urchin's innate immune repertoire is also more complex than the vertebrate one. The urchin has 10 times as many *SRCR* genes, which encode proteins that home in on microbial lipids, as vertebrates have. And it has 222 cell surface proteins called toll-like receptors; humans have just 10. "There is almost an embarrassment of riches of ways to generate diversified [immune responses]," says Eric Loker, a comparative immunologist at the University of New Mexico, Albuquerque.

Some of the urchin's immune system genes pose evolutionary puzzles. The urchin can make both interleukins and tumor necrosis factors, even though it seems to lack the specialized immune cells that these chemicals control in vertebrates. The sea urchin also has *Rag* genes, which mix up DNA to generate an infinite set of antibodies in vertebrates—yet the echinoderm makes no antibodies. "Most elements of our immune system were already there [in the urchin]," says Louis Du Pasquier of the University of Basel, Switzerland.

Other urchin genes not related to immunity also seem out of place. When Richard Hynes and Charles Whittaker of the Massachusetts Institute of Technology in Cambridge and their colleagues tallied the sea urchin's "adhesome"—the genes whose proteins help hold cells together and link a cell with the local environs—they found among the 1000-plus genes one important for mammalian brain development and several others implicated in human diseases. The urchin versions must serve different functions, says Hynes.

The newly unveiled sea urchin genome shows that vertebrates evolved by elaborating on and adapting a sophisticated, preexisting set of genes, some of which have changed roles over the course of evolution. "It's mind-boggling to think of all the many inferences one can make with the genome sequence [of the sea urchin] in hand," says Chris Amemiya, a comparative immunologist at Benaroya Research Institute at Virginia Mason in Seattle, Washington.

–ELIZABETH PENNISI

CREDITS: ENRIQUE ARBOLEDA AND MARIA INA ARNONE

Share and Share Alike

China will set up 20 data-sharing centers and networks by 2010, according to a new national plan on technical development. The centers will store data in areas including agriculture and health. The move expands a well-received 2001 pilot program to share data in 12 disciplines such as meteorology and hydrology, including a widely used online forestry database. Chinese Academy of Forestry researcher Yi Haoruo says the expansion will "enhance the competitiveness of Chinese science and technology" by helping scientists share resources and eliminate redundant efforts. But he says some "are concerned" that sharing could harm their competitive advantage.

–GONG YIDONG

Dem Union Blues

Leaders of an abortive attempt to form a postdoctoral union at the University of California (UC) plan to try again. In July, the United Automobile, Aerospace, and Agricultural Implement Workers Union (UAW) filed a petition with California's Public Employment Relations Board (PERB) to represent 6000 UC postdocs based on having collected signatures from a majority of them. Some UC postdocs have alleged that UAW representatives didn't fully explain the implications of forming a union while collecting signatures. But last week, before PERB had ruled on the validity of the organizing drive, UAW withdrew the petition. Between 500 and 600 signatures "were from individuals who are no longer postdocs," explains UAW's Maureen Boyd, which left them short 100 signatures. Pro-union postdocs say organizing will increase negotiating leverage and hope to eventually resubmit the petition. But Jerome Breslin, head of the postdoc association at UC Davis, says unionizing is "combative" and less effective than friendly dialogue.

–YUDHIJIT BHATTACHARJEE

New Top Quarks at Fermilab

The U.S.'s premier particle physics lab is hoping a partnership with the University of Chicago will help it effectively compete with European particle physics. Managers at Fermilab in Batavia, Illinois, say the deal, which was finalized in a new federal contract last week, will strengthen data sharing between the two institutions and bolster long-standing research ties.

–ELI KINTISCH

ATMOSPHERIC SCIENCE

Global Warming May Be Homing In on Atlantic Hurricanes

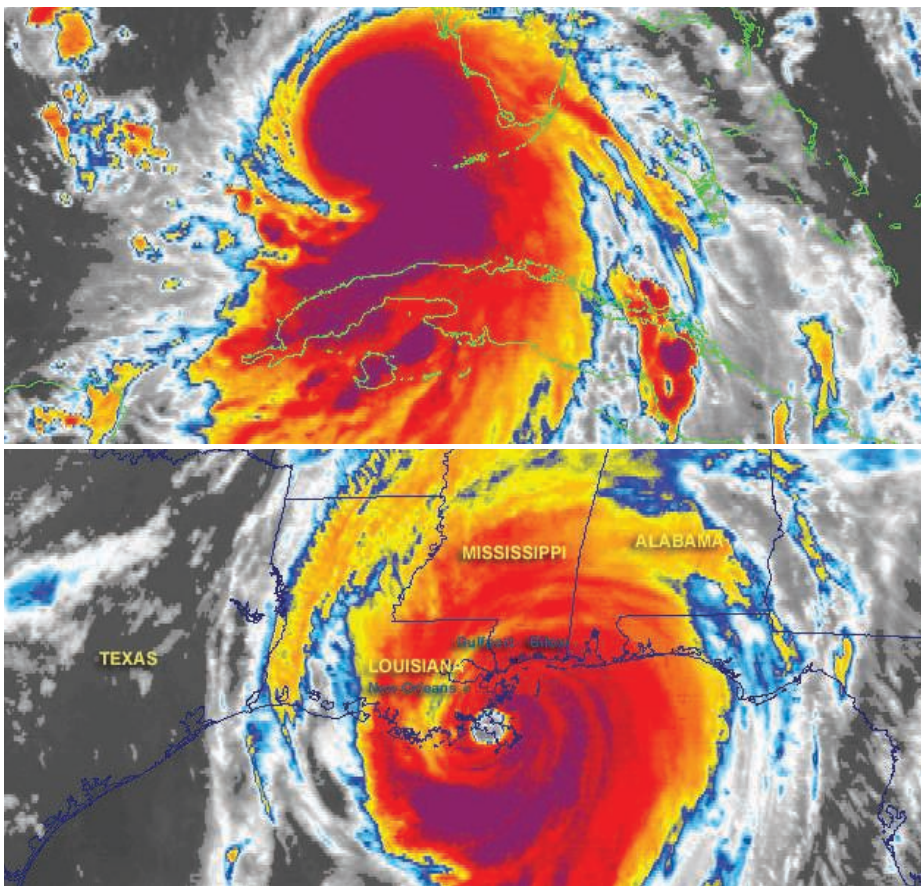

CREDIT: NCDC/NOAA

Killer. An analysis of satellite infrared images shows Katrina strengthening from maximum wind speeds of 157 km/h (*top*) to 232 km/h (*bottom*).

WASHINGTON, D.C.—The idea that increased hurricane activity might be connected to global warming first blew in with Katrina and her cohorts of the horrendous 2005 Atlantic hurricane season. Then two studies reported a striking increase in the number of intense storms around the world. And that increase was suspiciously in step with the warming of tropical waters whose heat fuels tropical cyclones (also called hurricanes or typhoons). But skeptics wondered: Should anyone trust the patchwork records of tropical cyclones compiled over the past century? And couldn't the surge in storms be part of a natural cycle?

New analyses have something to offer both skeptics and proponents. For most of the world's tropical cyclones, existing records should *not* be trusted, according to a new study presented here at a 20 October seminar on Capitol Hill sponsored by the American Meteorological Society (www.ametsoc.org/atmospolicy/environmentalsssarchives.html). The study showed that records of the intensity of most storms around the world have been skewed, producing the impression that tropical cyclones have been getting stronger globally. Records for the Atlantic Ocean, however, do seem to be reliable, and reanalyzed records from the Atlantic going back to 1983 still show a sharp increase in hurricane intensity as tropical Atlantic waters warmed. Other work presented at the seminar suggests that the Atlantic jump was a combination of a long-term increase in the number of storms—possibly under the influence of global warming—and a natural oscillation in storm intensity.

Last year's provocative findings "woke people up," says meteorologist Greg Holland of the National Center for Atmospheric Research (NCAR) in Boulder, Colorado, who co-authored a global intensification paper. Now "you're starting to see us make our minds up."

The trouble with tropical cyclone records is that techniques of observation and analysis have changed over the decades. And although observations are now more direct and analyses more objective than before, they still differ from place to place. To create a single, consistent record, tropical meteorologist James Kossin of the University of Wisconsin, Madison, and colleagues altered the satellite records of storm intensity so that they would be uniform from end to end; any trends would reflect trends in the data, not trends induced by changing techniques.

Satellites provide infrared images of storms. Meteorologists can calculate the intensities of those storms from their temperatures: The warmer the eye of a storm and the colder (that is, the higher in altitude) its cloud tops, the stronger the storm. So Kossin and his colleagues altered records to a single spatial resolution of 8 kilometers and a uniform time resolution of 3 hours. They then applied a single algorithm to calculate an objective intensity, as calibrated against Atlantic storms reconnoitered by instrumented aircraft.

Kossin first gave the good news about record reliability. In two regions, the reanalysis was in excellent agreement with previous records. In the Atlantic, the storm energy released in a hurricane season did in fact more than double between the first and second halves of the 1983-to-2005 record. That pattern supports a record that meteorologist and hurricane specialist Kerry Emanuel of the Massachusetts Institute of Technology published in 2005 (*Science*, 16 September 2005, p. 1807). Agreement was also very good in the eastern North Pacific, where energy release declined 60%. These two trends are well-supported, said Kossin.

Then again, there was "not so good news everywhere else," Kossin noted. Where the standard records from the northern Indian Ocean, the southern Indian Ocean, the western North Pacific, and the South Pacific showed rising trends of intensity, the reanalysis showed modest declines or no trend at all. And 85% of the world's tropical cyclones occur in these ocean basins. Outside the Atlantic, Kossin concluded, storms show no signs of intensifying as the underlying waters warm, at least in the past 23 years.

Meteorologist Philip Klotzbach of Colorado State University in Fort Collins says he generally agrees with Kossin's findings. The work "indicates that increases in [tropical cyclone] activity are likely much smaller than some recent papers have claimed,"

Klotzbach says. Holland, an author of one of those papers, says the work "moves in the direction of what might be the truth. We need to look into this a little bit more."

Holland and tropical meteorologist Peter Webster of the Georgia Institute of Technology in Atlanta have been focusing lately on what many experts consider the most reliable tropical cyclone observations: the number of named tropical cyclones in the North Atlantic and the broad classification of hurricanes as minor or major. At the seminar, Holland reported that the overall number of named Atlantic storms jumped up twice since 1900: in the late 1920s and again in the mid-1990s. That rise was roughly in step with lasting increases in the temperature of waters in the eastern tropical Atlantic, where most storms form. The proportion of those hurricanes classified as "major," however, shows no long-term trend but has oscillated up and down every few decades.

Together, Holland said, the two patterns explain both the lull in hurricane activity in the 1950s and '60s and the surge in the 1990s. The latter was a "double whammy": High storm numbers due to unprecedented tropical warmth coincided with a periodic—and presumably temporary—upswing in the proportion of major hurricanes. Klotzbach isn't so sure. He thinks that the more thorough and precise monitoring of recent decades could well have increased the number of storms rating a name and the number promoted to major status.

Researchers may be edging toward some agreement about how storms respond to warming tropical waters, but they still don't understand why they respond. Modeling studies suggest that greenhouse warming played a substantial role in the recent warming of tropical waters, as climate researcher Thomas Wigley of NCAR and modeler Thomas Delworth of the Geophysical Fluid Dynamics Laboratory (GFDL) in Princeton, New Jersey, separately reiterated at the seminar. But the best theory and modeling still indicate that ocean temperature has only a minimal direct effect on storms.

As for indirect effects, researchers are just starting to sort them out. One promising step, Delworth said, comes from new work by Thomas Knutson of GFDL and his colleagues, who ran a highly detailed model of the Atlantic region. The model formed realistic tropical cyclones when the modelers fed in the actual ocean and global atmospheric conditions of the past 25 years. The results matched much of the year-to-year variability in actual hurricane numbers, as well as the surge in numbers after the mid-1990s. Now researchers will have to dissect the model's behavior to understand what factors combined to make that happen.

–RICHARD A. KERR

ACADEMIC CAREERS

Spain Reconsiders Its University Reform Law

BARCELONA—Eight years ago, astrophysicist Antonio Ferriz sued the University of Salamanca, charging that it violated hiring rules by passing him over for a local candidate. The case, and several similar ones, drew widespread publicity to complaints that Spain's system for appointing professors was flawed and inbred. The government paid heed: It reformed the law in 2001 to open up academic hiring, imposing a national system for vetting candidates. But now a bill being debated in Spain's Parliament would give more leeway to universities in hiring, and the academic community is deeply divided. Some academic leaders are pleased, but critics such as Ferriz say it could be a step backward.

Spanish universities rarely seek talent from afar when they hire professors. "Some people say that the Spanish system is particularly inward-looking," says Ferriz, a professor at the University of Vigo who is currently a visiting scientist at the Max Planck Institute for Solar System Research in Göttingen, Germany. "I think this is a very soft description of reality." Spain's university system "operates like a mafia," he fumes. Under the old system, Ferriz says, advertised positions were sometimes so narrowly defined that "only the preselected candidate fit."

The 2001 law sought to break this grip on academic posts by creating a centralized *habilitation* system to pass judgment on the quality of job applicants. However, the change proved unpopular among professors and administrators. Former education and culture minister Maria Jesús San Segundo and others proposed a model reform plan, which was approved early in September by the Ministerial Council and is now being debated in Parliament.

The proposed law would still require candidates to submit their curriculum vitae for evaluation by "commissions made up of professors with a renowned teaching and research prestige." But universities would be free to pick and choose candidates. The law would also create new posts for assistant professors and postdocs; permit mixed research institutes involving universities, the Higher Research Council, and private companies; and mandate gender equality in university decision-making bodies. It could also lead to academic evaluations like the U.K.'s "research assessment exercise."

CREDITS: ANTONIO FERRIZ

Seeking reform. Astrophysicist Antonio Ferriz has campaigned to open up a system that he says promotes favorites "like a mafia."

Critics such as José Vicente, a professor of inorganic chemistry at the University of Murcia, say the new plan is no reform. It "simply consists of proposing the worst system for contracting with professors," he says, adding that universities will be able to hire accredited researchers "after a pantomime competition before an ad hoc panel." Less than 10% of successful professorial applicants in Spanish universities are outsiders, he says, predicting that "inbreeding will now increase up to 100%."

Others are more optimistic. Eugenio Degroote, a professor of mathematics at the Polytechnic University of Madrid, says that the first accreditation stage will be selective. Unlike in the past, "bad or mediocre researchers will be eliminated," he argues. The parliamentary debate on the new law is expected to conclude with a vote before the end of the year.

–XAVIER BOSCH

Xavier Bosch is a science writer in Barcelona, Spain.

U.S. ACADEMIC RESEARCH

MIT Report Finds 'Breakdown' In Neuroscience Programs

What began this spring as a private squabble over a faculty appointment led last week to a finding that the Massachusetts Institute of Technology's (MIT's) extensive neuroscience program has deep-seated flaws. A report from an internal panel warns that turf battles among numerous institutes, labs, and departments have created a "breakdown of this system." MIT officials responded immediately with a new advisory board to examine the neuroscience effort, a reaction that critics of the report say is inadequate.

The fracas began when a young neuroscientist named Alla Karpova declined a position at MIT's McGovern Institute for Brain Research. She cited resistance to her appointment by Nobel laureate Susumu Tonegawa, who heads the rival Picower Institute for Learning and Memory at MIT. Karpova's supporters say that e-mails sent to her by Tonegawa were inappropriate and intimidating—and that senior MIT officials refused to intervene. Some accused Tonegawa of actively seeking to keep women off the faculty. After the matter went public in July (*Science*, 21 July, p. 285), Provost Rafael Reif set up a panel to investigate.

That committee found numerous flaws in how neuroscience is conducted at MIT, a complicated structure consisting of the McGovern and Picower institutes—both handsomely funded by wealthy donors—as well as the biology department and the department of brain and cognitive sciences. Although all but the biology department are based in a single building, the report concludes that the two institutes "have not worked cooperatively to serve the entire neuroscience community."

The panel criticizes the McGovern—which has been under fire since its inception for a lack of direction (*Science*, 24 August 2001, p. 1418)—as having no clearly defined mission. "The mission of the Picower," on the other hand, "is too broad." The independence of both, in addition, "makes it difficult if not impossible for the dean to resolve disagreements between the units." Without changes, the panel predicts more trouble.

Young and restless. MIT Provost Rafael Reif sees neuroscience problems as "growing pains."

As for Karpova, the report says that MIT's effort to recruit her was "unusual and flawed" because of faculty infighting over whether to make her an offer and attempts to dissuade her from taking the job once that offer was made. In particular, it faults McGovern Director Robert Desimone for "inappropriately attempt[ing] to influence the decisions of the biology faculty and department head." And although the committee said Tonegawa had a legitimate right to inform Karpova that his lab would not work with hers, it also found that it was inappropriate for him to send her discouraging e-mails once she was offered a job.

On the job. MIT grad student Aaron Andalman assembles devices to record the brain activity of songbirds.

CREDITS (TOP TO BOTTOM): LEN RUBENSTEIN; GAYLE LUTCHEN/MCGOVERN INSTITUTE

The panel found plenty of blame to go around. It concluded that "to some extent, Tonegawa was provoked," because his concerns about research overlap were dismissed by members of the biology department. It also found no evidence that gender played a role in Tonegawa's attempt to keep Karpova off the faculty. Yet the panel fretted that "the negative publicity [from the ill-fated attempt to recruit Karpova] may be particularly damaging to MIT's efforts to increase the number of women on its faculty."

Senior MIT officials accepted the conclusions of the panel, chaired by MIT astrophysicist Jacqueline Hewitt. "We're talking about growing pains here," says Reif. "This is a new model in a young research area." In a prepared statement, MIT President Susan Hockfield, herself a neuroscientist, emphasized that "we cannot allow internal competitiveness to undercut the integrity, values, and mission of the Institute as a whole." Reif added that he is talking privately with the relevant parties but does not plan to take disciplinary action against anyone. Desimone agrees that more cooperation is necessary, although he complained about numerous "factual errors, misstatements, and omissions" in the report.

Materials scientist Lorna Gibson will lead the neuroscience advisory panel, which Reif said would address the broader issues troubling the field at MIT. But MIT biologist Nancy Hopkins, who led the effort to put the issue of women faculty on the university's agenda, criticized "this indecisive response by the administration" and said that it "perpetuates destructive behavior by senior faculty and administrators against young scientists, particularly women."

Ben Barres, an MIT alumnus and Stanford University neuroscientist, shares Hopkins's concerns that the incident will scare off potential recruits and that an advisory panel could prove toothless. "I am dismayed that MIT has essentially done nothing in response to the McGovern-Picower situation," he says.

Tonegawa issued a statement welcoming the advisory panel as a good step and maintains that he never acted inappropriately. Meanwhile, Karpova plans to finish a postdoc at Cold Spring Harbor Laboratory in New York next spring and become a group leader at the new Janelia Farm research campus of Howard Hughes Medical Institute outside Washington, D.C.

–ANDREW LAWLER

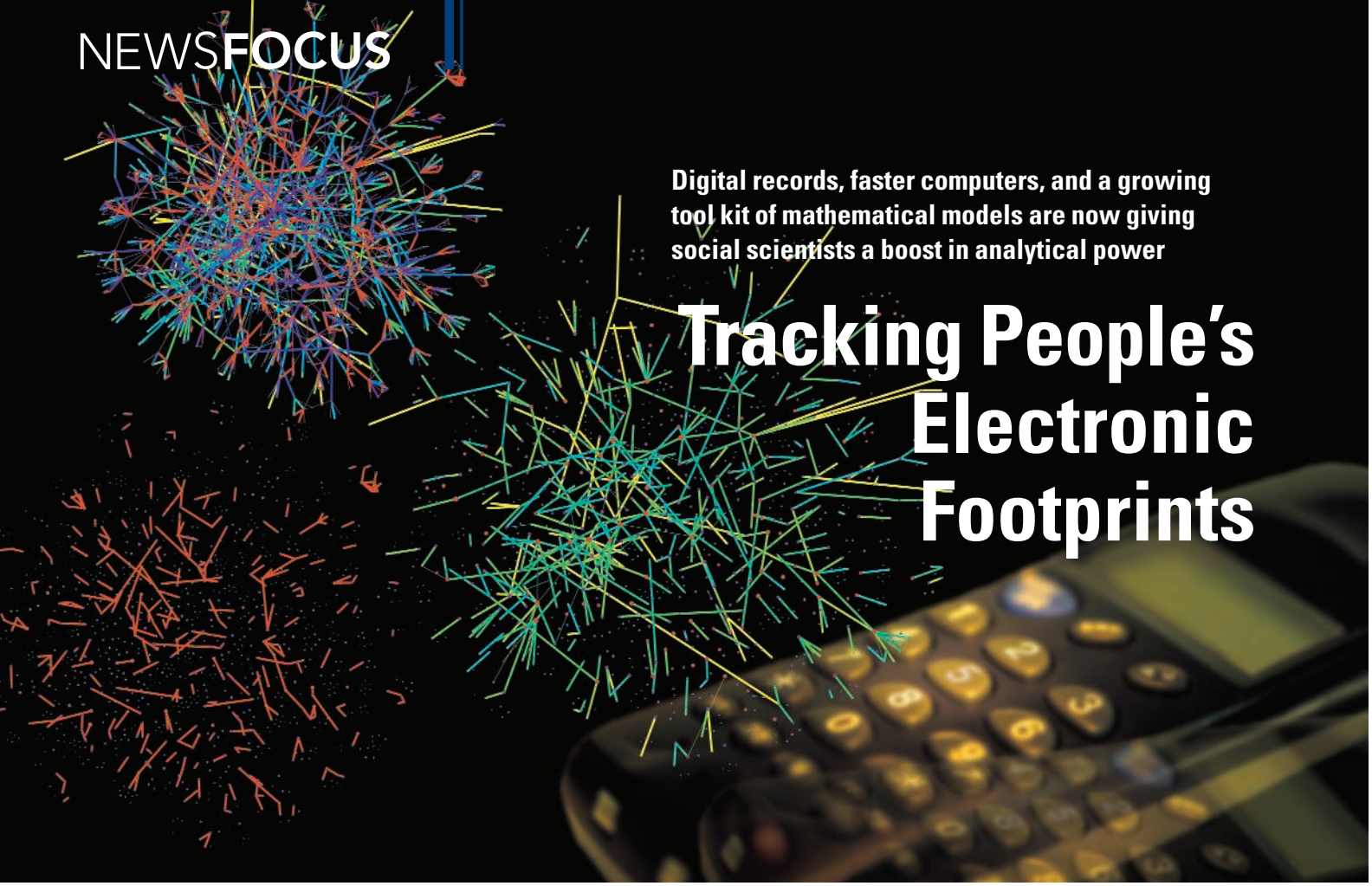

Digital records, faster computers, and a growing tool kit of mathematical models are now giving social scientists a boost in analytical power

Tracking People's Electronic Footprints

OXFORD, UNITED KINGDOM—The audience perked up noticeably when physicist Jukka-Pekka Onnela clicked to the slide showing his results—something like a big, colorful hairball. The average viewer might not be impressed. But it caused a buzz among the scientists meeting here recently to talk about complex networks.* The vast flurry of points and lines represents relationships between people in a communication network. What makes it remarkable is that it is no simulation: The data are from actual telephone calls among 7 million real people over an 18-month period.

The data set was given to Onnela and his team at Helsinki University of Technology and the University of Oxford by a mobile telephone company, after replacing phone numbers with codes. "I felt a little surge of jealousy," admitted Marco van der Leij, an economist at Erasmus University in Rotterdam, the Netherlands. Social scientists have dreamed for decades of getting their hands on such a global lode of data.

The mobile phone data set was one of a variety of new collections on display at the meeting—many of them based on the captured digital signatures of human interactions such as communication, travel, voting, and shopping. These interactions have long been the bread and butter of the social sciences. But researchers have been frustrated by the size and complexity of the phenomena they study. Electronic footprints, faster computers, and a growing tool kit of mathematical models are now giving researchers a boost in analytical power.

* European Conference on Complex Systems, Saïd Business School, University of Oxford, U.K., 25–29 September 2006.

Up close and personal

Some of the new data sets are downright intimate. Take for example a study by Oxford sociologist Peter Hedström of the records of the 3 million people above the age of 16 who lived in Stockholm from 1990 to 2003. After an ethics panel granted approval, the Swedish government gave Hedström data covering everything from workplace absenteeism and divorces to taxes, school grades, and criminal records. (Names and addresses were replaced by codes.)

Hedström's goal is to see how the decisions of individuals add up to large-scale patterns such as unemployment, crime, and gender bias. "We often resort to hand waving" in trying to make the connection between individual behavior and social phenomena, he says. Having data for individuals in an entire society allows questions to be asked that "traditional social scientists simply could not address."

For example: Are suicides contagious? The traditional method of studying the social causes of suicide "has been either to do small case studies or try to include some questions in larger surveys about the very local networks individuals are embedded in," says Hedström. But he notes that this approach will never capture a complete web of social interactions. Hedström's team is trying to track the ripple effect caused by each of the 2621 recorded suicides in Stockholm over a decade by looking for the social connections that link them. Although the results are "preliminary," he says, they indicate that the chance that exposure to a suicide will tip an already unstable person into taking his or her own life is related to the strength of the social ties. "Not surprisingly," he says, "the suicide of a family member has the strongest effect on an individual's suicide risk." But a suicide in a school or workplace exposes far more people, so although the individual effect may be smaller, "the public health effect is large."

Others, such as Onnela, are studying the architecture of social webs. His team is interested in how information flows through soci-

ADAPTED FROM NETWORK DATA: WWW.ARXIV.ORG/ABS/PHYSICS/0610104; (PHOTO) PHOTOS.COM

Intimate links. Researchers are probing a data set of real calls made by 7 million telephone users in an unnamed European country.

ety, and how the network imposes "constraints," he says. His data set of 7 million people represents 20% of the population of a European country where 90% have mobile phones. (The team agreed to keep the country's identity secret.) Aside from the very young and old, says Onnela, "this is a good representation of the entire society." Because the phone records contain no personal information, the researchers characterized relationships by weighing the "intimacy" of the links based on the number and duration of phone conversations. Because the data only include calls between mobile phones, most business calls are excluded, says Onnela, because most businesses use landline phones. "We think this is a reasonable proxy" for intimacy, says Onnela.

To examine patterns of diffusion, Onnela's team "infected" a single individual in a simulated version of the real network with a piece of information and watched it spread, with the chance of it passing between two people determined by the intimacy of their relationship. The result suggests that a classic idea in network theory—that large, complex networks tend to maximize flow efficiency—does not apply. The information tended to become trapped within tightly knit communities rather than spreading freely across the society.

Probing the network further, Onnela's team blocked the phone connections between people in different categories, starting with the most intimate relationships. In another case, they started from the opposite end, severing the least intimate relationships. The difference is dramatic. Although losing 20% of the most intimate connections causes individual communities to break down, society's interconnections hold together, and information still flows from one end to the other. But after the same fraction of the weakest links are cut, the system shatters into islands (see figure on p. 914). Van der Leij calls this the first large-scale, empirical confirmation of a theory, first proposed in 1973 by Mark Granovetter, a sociologist at Stanford University in California, that "for keeping society connected, acquaintances are more important than close friends."

The big picture

On the macro end of the scale, the search is on for fundamental rules that may undergird collective behavior. This work is aided by recent progress on the mathematics of networks (*Science*, 4 August, p. 604). But "getting our

Google's Hidden Wealth

Type the word "science" into the Google search engine, and a list of one-and-a-half million Web pages appears in a fraction of a second. Behind this service lies an enormous reservoir of data that researchers would like to harness for science of their own, in fields from social psychology to global economics. But although some computer-based companies such as Microsoft have eagerly embraced scientific collaboration, Google so far has not. "Google has a reputation … for being very negative to letting researchers in," says Richard Swedberg, a sociologist at Cornell University. This could soon change, a Google spokesperson has told *Science*.

Google's data are a potential social science gold mine, "both for observing social interactions in real time and also for measuring their consequences for individual and collective behavior," says Duncan Watts, a sociologist at Columbia University. The key is the electronic "cookie." As you browse the Internet, many Web sites such as Google's record a string of text—the cookie—representing the identity of your computer. And when you use Google, its servers keep track not only of what you search for but also where you go next. People add new entries to this record at the rate of 200 million Web searches per day. This electronic record is key to Google's business model: Most of its $1 billion annual revenue comes from Internet advertising targeted to individuals.

Google expanded its reach in 2001 when it acquired the largest group of Internet-based communities, or "chat groups," known as Usenet and rechristened as Google Groups, including Usenet's records of topic-specific conversations between 25 million people going back to 1981, all of it searchable. And Google is amassing other treasures, such as its regularly updated satellite-based map of Earth. Users can instantly retrieve many kinds of sociological data such as local crime rates from that map. Thousands of people are voluntarily developing new (but not peer-reviewed or verified) layers of data with so-called mash-ups that are freely available on the Internet.

Google has been cautious about scientific collaboration because "we don't want to give users the impression that we're free and easy with their data," says Rachel Whetstone, a London-based Google spokesperson, "especially in light of what happened with AOL." In August, the Internet company American Online (AOL) released a record of Internet searches done by 650,000 people. A furor erupted when it was discovered that people's identities were easily reconstructed from the data. AOL removed the data from the Internet 3 days later, but the file had already been downloaded and replicated worldwide. In what may be Google's first invitation, the company's public relations department said in an e-mail to *Science* that "Google wants to support scientific endeavors" and would consider providing data for "legitimate scientific research … so long as we could ensure that it included no personally-identifiable information."

Some academics are urging caution. There is "significant potential for abuse, given the ease of transporting computerized data," says Frank Miller, a bioethicist at the National Institutes of Health in Bethesda, Maryland. "Ethics review committees will need to scrutinize research using such data very carefully to ensure that adequate protections are in place." Requiring people's consent will be difficult, he says, and "investigators might resist this move, as it could narrow the pool of subjects." **–J.B.**

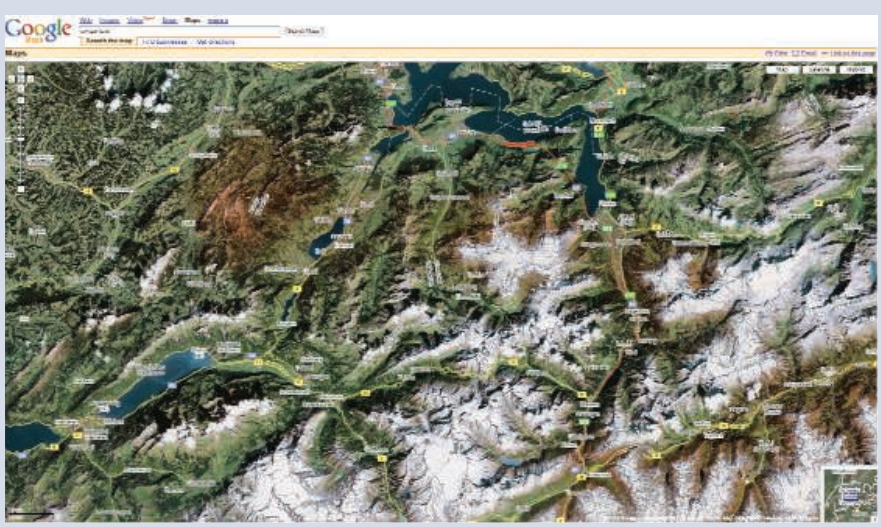

Added value. Users are adding their own data overlays, or "mash-ups," to Google Earth.

CREDIT: GOOGLE EARTH

hands on real and sufficiently detailed empirical data is what is truly exciting and new," says Felix Reed-Tsochas, a theoretical physicist who now does network research at Oxford's Saïd Business School.

In an effort to understand how social networks survive stress, Reed-Tsochas, Serguei Saavedra, an engineer at Oxford, and Brian Uzzi, a sociologist at Northwestern University in Evanston, Illinois, are studying the New York City garment industry. In a complex web of collaborations, clothing is designed, manufactured from raw materials, distributed, and finally sold in retail stores. New York's industry shrank over 2 decades as garment production shifted to Asia, declining from 300,000 workers in 3000 firms during the 1980s to 190 firms today.

In spite of this big shrink, the network has held together and continued to function throughout. That robustness is a mystery, says Uzzi, because "there is no master planner," and "the individual actors are not even aware of the system beyond their local part of the network." When the team modeled the same contraction based on what is known about network dynamics, the garment industry quickly fell apart, he says.

Luckily for science, a New York garment workers union has kept a digital record since 1985 of 700,000 financial transactions among the firms and gave Uzzi access. Nearly all of the research on network dynamics has been based on periods of expansion, says Reed-Tsochas, but "this is the first well-characterized example of a network undergoing sustained contraction."

The researchers have created an evolving map of the flow of money. As companies went bankrupt, relocated, and cut budgets, the remaining ones were forced to decide which relations to sever and which to keep. The study is at an early stage, but some ingredients of the network's robustness are becoming clear, says Uzzi. The contraction looks like a movie of the expansion "played backwards in time," says Reed-Tsochas. The team has devised a model that, they say, can explain how robustness is an unintended consequence of individuals following their own self-interest based on local information. It will debut in a journal soon.

Reed-Tsochas and his colleagues built their model from a wealth of data. Social scientists studying the collective behavior of terrorist groups don't have that luxury: Members of such groups don't keep detailed records. But their deadly attacks are chronicled. To see what can be gleaned from such data, a pair of Oxford physicists, Neil Johnson and Sean Gourley, have teamed up with social scientists at the Conflict Analysis Resource Center (CERAC), based in Bogotá, Columbia. Researchers at CERAC have so far amassed a record of more than 55,000 attacks going back to the 1960s, compiled from other studies; they have also sifted information on events around the world from media and government reports, ranging in size from a single death to the 3000 killed at the World Trade Center.

Shrinkable. A study in New York City's garment district found that social networks remained strong during a period of attrition.

A striking pattern has emerged. When the researchers graphed all the attacks within a given conflict, with the number of attacks plotted against the number killed in each, it produces a fat-tailed exponential curve. And the exponent of the function, which determines the curve's shape, is nearly always the same. "Terrorism and guerrilla warfare everywhere in the world has a signature of about 2.5," says Gourley. Plotting the distribution of these events over time produces another, distinctive signature.

Johnson and Gourley have been building computer models of terrorism to see what kind of social networks can fit the patterns. Only one does the job, says Gourley, and it's a surprisingly simple model of human gregariousness. "All you need is to have people forming cohesive groups that share information, technology, and supplies," he says. Using this simplified social network model, they are drawing conclusions about the Iraq insurgency that are extremely difficult to assess from the ground. For example, "the bursty distribution of attacks over time shows that terrorists don't rely on a hierarchical organization to pass along orders, nor do they attack at random," says Gourley. Instead, "they must be coordinating by proxy," such as by reading the very same media reports of each other's attacks.

Johnson and Gourley also believe they can infer how many different factions are involved throughout Iraq. "In the first 180 days of the war, there were 15 to 35 groups," he says, and "after day 540, our model estimates there to be 100 to 130 different groups." The model assumes that each group is capable of no more than one attack per day, he adds, so that number could be lower if some groups are capable of multiple daily attacks.

The fact that all the conflicts around the world they have analyzed share these patterns "is extraordinary," says Gourley, "when you consider how different they are, involving actors with very different motives and goals, operating in very different environments." They must be following rules without being aware of them, he says: "There seem to be only a limited number of ways for people to form networks and coordinate activities."

Whether laws governing social groups can be found is an open question. But many social scientists are optimistic that such sets of real-world data will lead the way, and they are hungrily eyeing new sources (see sidebar on p. 915). "Great science can potentially come out of these efforts," says James Moody, a sociologist at Duke University in Durham, North Carolina. But he and others agree that it will take more than "just mining the data" to learn what drives social phenomena. What's needed is an exponential boost in the power of social science theory and analysis. And this, says Granovetter, "is a very tall order."

–JOHN BOHANNON

CREDIT: GAIL MOONEY/CORBIS

RUSSIAN SCIENCE

Kremlin Brings Russian Academy Of Sciences to Heel

New oversight measures, insists the president of the venerable academy, will spur evolutionary change. Others contend that the Kremlin is mounting a hostile takeover

MOSCOW—Thanks to lavish support and autonomy even during the darkest Stalin years, the Russian Academy of Sciences (RAS) became a national refuge for intellectuals, nurturing a parade of Nobel Prize winners and training a formidable scientific diaspora. In the last decade or so, however, the 282-year-old academy has come under attack. A rising chorus of critics has caricatured it as a bastion of privilege, bloated with mediocre scientists who draw salaries year after year and resist every attempt at reform. During his 4 years as science minister, Andrey Fursenko has vowed repeatedly to modernize RAS and its 400 institutes. For the first time, he has won a small victory: In September, the Kremlin unveiled amendments to the science law that would give Russian President Vladimir Putin's cabinet the right to approve the selection of future RAS presidents and the academy's charter. RAS has postponed its upcoming presidential election, scheduled for next month, until after parliament signs off on the amendments.

RAS and ministry leaders insist that the academy will continue to manage its affairs without meddling from the state. RAS President Yuri Osipov, for one, is putting on a brave face. "Some people say [the new procedure according to the amendments] is wrong. I think it is right. It would even strengthen the academy's position," he says. Because the next RAS president will have the explicit endorsement of Putin, says Osipov, "that will highlight the responsibility of this person for the immense financial and material resources of the academy."

Privately, however, sources say the latest developments are the first shots in a battle over RAS's substantial land assets, including prime real estate in central Moscow and on the Neva River in St. Petersburg. Many contend that the Kremlin's ultimate aim is to acquire these assets and transform RAS into a club or honor society akin to the U.S. National Academy of Sciences. "We are being castrated," complains nuclear physicist Nikolay Ponomarev-Stepnoy, an academician at the Kurchatov Institute in Moscow. "They are demolishing the academy."

Soon after the Soviet breakup in 1991, then–science minister Boris Saltykov argued that RAS needed to shrink and focus spending on quality research teams. The reforms he prescribed included peer review of labs and competitions for funding rather than block grants. Osipov beat back the challenge. But the mathematician, completing a third term as RAS president this year, has been less effective at thwarting Fursenko, a young reform-minded physicist who has survived a couple of cabinet shakeups. Fursenko did not respond to an interview request. But his deputy, Dmitry Livanov, says the ministry's intention is to make the academy more "cost-effective." It's necessary, he says, "to focus support on world-class researchers" and to favor areas, such as physics and life sciences, "in which Russia already shows world-class results or can achieve such results in the shortest time."

Taking one for the team? RAS president Yuri Osipov receives an honor from President Vladimir Putin. The Kremlin may covet juicier prizes, such as the RAS leadership's Moscow mansion.

CREDITS (TOP TO BOTTOM): ANDREY ALLAKHVERDOV; VLADIMIR RODIONOV/AFP/GETTY IMAGES

Osipov, who has assented to the changes, insists they are evolutionary. Livanov agrees, noting that there are no plans at present to strip RAS of its institutes—even if some don't merit support. "It cannot be that all the institutes are world-class," Osipov says. "As in chess, you cannot have only grand masters." RAS will continue to receive about 35% of the Russian government's R&D spending, which in 2006 amounted to $1.27 billion. The big change is that the next RAS president will be held accountable for spending it wisely. And if RAS fails to modernize on its own, Livanov says, "it may happen that more radical measures will become urgent."

Saltykov argues that the ministry's reforms do not go far enough. He says that a new system is needed to manage Russian R&D. "It is not a secret that the academy is dying," he says. At many institutes, he continues, "scientific life has stopped. There are dusty passages instead of working laboratories. And something has to be done. A serious audit is needed to define where there is life and where there is simulation of life." After that, he says, steps must be taken to salvage the good science. To reform the academy, Saltykov says, "one must do it seriously. And I do not see any seriousness."

Some observers contend that the Kremlin has a darker motive for bringing the academy under its wing. In 2004, RAS institutes lost a vital perk: sharply discounted property taxes. Now they are obliged to pay in full. As most institutes cannot afford the tax, which can run more than an institute's annual budget, the cabinet for the past 2 years has covered the payments. Osipov says he does not know how long the cabinet will continue bestowing this favor. "At the moment, the property remains at RAS's disposal," says Osipov, who adds that it has not been easy safeguarding academy assets.

Rank-and-file scientists hope that something good will come out of the battle over the academy's future. Certainly, RAS needs to change, says Ponomarev-Stepnoy. But the way the ministry and the Kremlin are going about it could well sound a death knell for the venerable institution established by Peter the Great in 1724, he says: "We'll have to wait for another Peter to reconstruct it."

–ANDREY ALLAKHVERDOV AND VLADIMIR POKROVSKY

Andrey Allakhverdov and Vladimir Pokrovsky are science writers in Moscow.

Rolling up her sleeves. In Italy, Capua pioneered a vaccination strategy called DIVA to battle outbreaks of bird flu.

PROFILE: ILARIA CAPUA

Italy's Influenza Diva

She set in motion a worldwide movement to share information on avian influenza. Italian bird flu scientist Ilaria Capua says what she thinks—and often gets what she wants

LEGNARO, ITALY—When she traveled from Italy to Paris in mid-March, Ilaria Capua had a plan. She was going to attend a meeting of the scientific committee of OFFLU, an international network of bird flu experts, and she wanted participants to commit to getting more genetic data about the H5N1 bird flu strain in the public domain—a cause she had championed since January of this year. With scientists sitting on their samples, Capua believes, it's impossible to track the virus' movements and understand the tricks it may play on humankind.

But persuading her 13 colleagues, gathered in the graceful Parisian mansion of the World Animal Health Organization (OIE), wasn't easy, and the debate dragged on. Some were opposed, whereas others were sympathetic to Capua's cause but saw clear drawbacks as well. For instance, if every sequence became public information, how could they prevent others from scooping them with a scientific paper? But Capua insisted, and in the end, the group committed to sharing. As a first step, all participants identified at least 20 bird flu strains in their collections to be fully sequenced by the U.S. National Institutes of Health, which has a flu genome sequencing project, and then released.

It was quintessential Capua, says Christianne Bruschke, an OIE officer charged with bird flu who was at the meeting. "She's somebody with strong opinions," says Bruschke. "She's very dominant; she knows how to convince people." Adds Juan Lubroth of the Food and Agriculture Organization (FAO) of the United Nations: "She is very charismatic, and she has a big persona. When Ilaria says something, it carries weight."

Capua's in-your-face opinions do occasionally rub people the wrong way. "There are people who don't like her because of that," says virologist Albert Osterhaus of Erasmus University Medical Center in Rotterdam, the Netherlands. Still, her campaign for openness around H5N1 data has been unexpectedly successful and has won her wide admiration. Colleagues, newspaper editorialists, and even Web loggers have heaped praise on her.

Within the world of avian influenza, however, Capua already had a "very good reputation," says Michael Perdue, an avian influenza expert at the World Health Organization (WHO) headquarters in Geneva, Switzerland. In 8 years, she has put the Istituto Zooprofilattico Sperimentale delle Venezie (IZSVe) in Legnaro—a lab with regional as well as national responsibilities located in a small town outside Padua—firmly on the global flu map. And within Italy, she has pioneered a controversial vaccination strategy for bird flu, dubbed Differentiating Infected and Vaccinated Animals (DIVA), that has helped deal with two devastating outbreaks.

Modesty is not her strong suit, Capua readily admits. "I'm very brave," she said matter-of-factly on a recent Wednesday morning, while driving her black mini-Mercedes to a restaurant close to her lab for a pasta lunch. "I'm often ahead of others in thinking about important issues." Later, back at her lab, she asserted: "My colleagues at the lab respect me very much because of what I have achieved."

Tall and invariably stylishly dressed with trademark rectangular glasses, Capua, 40, also adds an unmistakable element of glamour to often-staid meetings of the international veterinary circuit, a heavily male-dominated world. In Italy, she has become something of a media darling, especially after reporters discovered that she's a cousin of Roberta Capua, a former Miss Italy. She has turned down requests for a joint interview with the beauty queen.

Not so crazy

Born in Rome, Capua obtained a degree in veterinary science at the University of Perugia in 1989, then worked at a few other labs before she became head of the virology department at the institute here in 1998, in a calm period when bird flu wasn't considered much of a problem. That changed, at least in Italy, in 2000, when a major outbreak of a highly pathogenic (HP) influenza strain named H7N1—which, unlike H5N1, is not dangerous to humans—struck poultry farms in a belt stretching roughly from Milan to Venice.

Although the Italian government managed to quash the outbreak by culling more than 13 million poultry, a so-called low-pathogenic (LP) version of H7N1 kept circulating, and researchers feared it might revert without warning to the HP version and kick off a new disaster. A massive poultry vaccination campaign in the area might help root out the LP strain. But widespread use of an H7N1 vaccine would pose an economic problem: Like any vaccine, this one would trigger the same antibodies as the disease, so that a standard test wouldn't be able to tell vaccinated from infected chickens. That, in turn, would prevent the country from showing that it was disease-free, endangering its trading status.

Capua's team argued that the so-called DIVA strategy might circumvent that classic problem. Instead of basing a vaccine on the H7N1 strain already infecting poultry, they

CREDIT: ISTITUTO ZOOPROFILATTICO SPERIMENTALE DELLE VENEZIE

suggested using a closely related strain, H7N3, which differs in a viral coat protein called neuraminidase. Vaccinated animals could be distinguished from infected ones because they would carry antibodies against the N3 variety of the neuraminidase protein instead of N1, the team argued.

Convincing European Union authorities that this approach would wipe out the disease was tough. "Some people thought I was crazy, that we would make the disease endemic," says Capua. But the team persisted, developing a new, fast test for antibodies against N1 and showing that it was reliable. And 4 months after the vaccination campaign went live in November 2000, the LP strain of H7N1 was eliminated. A year later, when an H7N3 outbreak swept the area, the same trick was put in reverse, using an H7N1 vaccine.

"Many people were talking and thinking about DIVA strategies, but she was the first to actually take it to the field and implement it," says Perdue. In theory, the same tactic, called heterologous vaccination, could also be used against H5N1, but it hasn't so far. Many at-risk countries don't have a good network of veterinary labs to screen poultry for infection.

After the Italian outbreaks died down, bird flu surfaced in other locations: There was an outbreak of H7N2 in Virginia in 2002, a massive H7N7 outbreak in the Netherlands in 2003, and the worldwide spread of H5N1, now in its third year. The increasing prominence of the disease helped Capua build up her lab. Staff tripled to almost 50 in 6 years. More than 70% of them are women—not necessarily because Capua wanted it that way, but because most graduates in veterinary science these days are women. It does have an advantage, however, she observes: "Men are incapable of multitasking, as I'm sure you're aware."

After Capua took over, IZSVe became Italy's reference lab for bird flu, testing samples from all over the country. In 2002, OIE asked Capua if IZSVe could serve as one of its global reference labs as well; FAO asked in 2004. As a result, the institute has received a steady stream of samples from H5N1-affected countries, primarily in the Middle East and Africa.

It was because she was at the hub of this research that Capua became aware of the lapse in data sharing. Her discomfort began in February, when WHO asked her to deposit the sequence of a sample from Nigeria, the first African country affected, in a closed-off compartment of a flu database at Los Alamos National Laboratory in New Mexico, to which fewer than 20 labs have access. If she shared her sequence, WHO scientists said, she would have access to the rest of the hidden Los Alamos data.

> **"I'm very brave.** I'm often ahead of others in thinking about important issues."
>
> —Ilaria Capua

Capua refused and instead deposited her sequences in GenBank for the entire world to see. At the same time, in a message on ProMED, an e-mail list for emerging infectious diseases, she asked her colleagues to follow suit (her posting won ProMED's annual award in August); she also asked *Science* to investigate (3 March, p. 1224).

WHO defended the closed database on the grounds that H5N1-affected countries often don't want reference labs in the developed world to publish information about the strains circulating within their borders. But Giovanni Cattoli, the director of research and development in Capua's lab, says that "is simply not our experience," noting that of the 15 countries the Capua team has dealt with, 14 said sharing data was "fine." As to scientists' worries that they might be scooped if they post their sequences in real time, Capua says: "What is more important? Another paper for Ilaria Capua's team or addressing a major health threat? Let's get our priorities straight."

CREDIT: M. ENSERINK/*SCIENCE*

Help wanted. Capua, here with colleagues Giovanni Cattoli and Paola De Benedictis, says she'd like to lure Italian talent working abroad back home.

Sexist world

Eventually, Capua's call resulted in a new organization uniting dozens of researchers, called the Global Initiative on Sharing Avian Influenza Data (GISAID), that plans to set up a system for sharing (*Science*, 25 August, p. 1026). GISAID's charter is still being hashed out with specialists in intellectual property and bioinformatics, and it's unclear exactly how it will work.

But no matter what comes of the deal, says Capua, momentum for sharing is clearly building. Although some at WHO were irked by the sudden announcement of GISAID—most people weren't aware of what was going on, Perdue says—WHO does support the idea. The Indonesian government and the U.S. Centers for Disease Control and Prevention in Atlanta, Georgia, both recently released a series of sequences. And on a visit to the United States this week, Capua was set to discuss the sequencing of a large number of strains from OFFLU labs at The Institute for Genomic Research in Rockville, Maryland.

Meanwhile, Capua's lab seems set to grow. She'd like to lure back Italian talent now working overseas. "Italians are very creative," she says. "Look at the food, the fashion." It pains her that Italian science has such a bad image; in a recent issue of *Nature*, for instance, one editorial praised Capua's sharing initiative whereas another one on the same page slammed the Italian government for its research management.

Capua says she's driven in part by the desire to show that it's possible to do outstanding research in Italy. Doing so, however, requires a hefty dose of determination—especially if you're a woman, she says. "My husband tells me I come off as a dragon, like Condoleezza Rice," she says, slamming her hand on her desk as if to illustrate what she's talking about. "But I have to defend my ideas and make sure I get heard. We live in a sexist world, especially here in Italy."

Then she adds: "But I'm not very concerned about how other people perceive me. I just tend to do my thing and get on with it."

–MARTIN ENSERINK

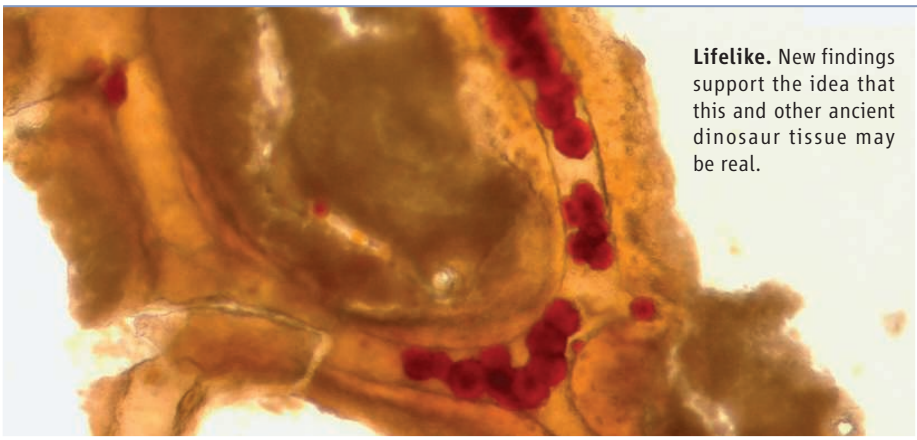

Lifelike. New findings support the idea that this and other ancient dinosaur tissue may be real.

Soft Tissue in Dinosaur Fossils? The Evidence Hardens

Two of the hottest discoveries in dinosaurs last year—the first definitive sexing of a dinosaur, from egg-laying tissue, and the amazing preservation of what looks like original cells and still-stretchy blood vessels—came from the lab of Mary Schweitzer of North Carolina State University in Raleigh. At the meeting, another group reported further evidence of egg-laying tissue, suggesting that it evolved early in dinosaur history. And Schweitzer discussed additional evidence that the tissue may be original, although doubters remain.

The egg-laying tissue, called medullary bone, was previously known only in living birds. Ovulating females rapidly create this mineral-rich tissue inside their legs and other bones as a storehouse for calcium for making eggshell. In a paper in *Science* (3 June 2005, p. 1456), Schweitzer and her colleagues compared the fossilized leg bone of a roughly 70-million-year-old *Tyrannosaurus rex* with modern ostrich bone, showing many similarities.

Now Sarah Werning and Andrew Lee, graduate students at the University of California, Berkeley, and paleontologist Paul Bybee of Utah Valley State College in Orem have found medullary bone in two other kinds of dinosaurs. Looking at a nearly 150-million-year-old tibia of the large predator *Allosaurus fragilis* from Utah, the trio found a layer of bone in which the tissue was disorganized and replete with traces of blood vessels, suggesting it had grown quickly. "It was really convincing," says paleontologist Martin Sander of the University of Bonn, Germany.

The same pattern turned up in a femur and tibia of an approximately 110-million-year-old *Tenontosaurus tilletti* from Montana. What's striking is that *Tenontosaurus* belongs to a major division of dinosaurs called the Ornithischia. This group split more than 230 million years ago from the other major group of dinosaurs, the Saurischia. Because members of both groups had medullary bone, the tissue likely evolved in a common ancestor, after it split from the crocodilians (see figure, below). "This really pushes [the origin] back," Werning told the audience.

Meanwhile, Schweitzer has been testing whether the medullary bone and other soft tissue she discovered are original. Her first report of the preserved tissue (*Science*, 25 March 2005, p. 1952) was based on preliminary tests. At the meeting, Schweitzer reported that she had looked at the transparent vessels and cell-like structures using a transmission electron microscope. Elemental analyses revealed the presence of the mineral hydroxyapatite of a type created by living organisms. "There is a small fragment of mineral that the dinosaur laid down originally," Schweitzer said.

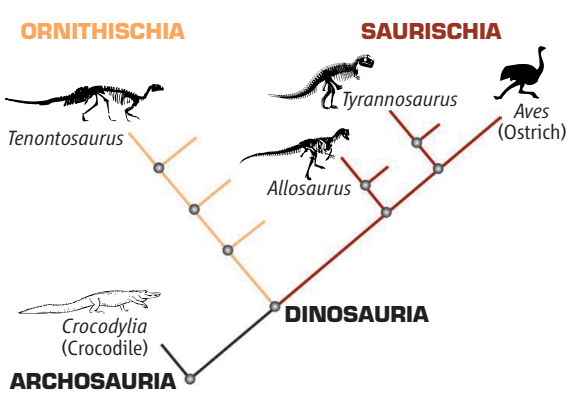

Family trait. Medullary bone occurs in both branches of dinosaurs, so it likely evolved soon after the split from crocodilians.

She has also found what appears to be collagen, which could be authentic dinosaur protein. Atomic force microscopy of fibers showed 67-nanometer-wide bands like those of emu collagen. Schweitzer even managed to get short sequences of peptides that matched collagen. "Looks like collagen, behaves like collagen, and it's 68 million years old. How cool is that?" says David Martill of the University of Portsmouth, U.K., who was not at the meeting but is familiar with the findings.

Gel electrophoresis revealed signals consistent with osteocalcin, a protein thought to help in bone mineralization. Antibodies to osteocalcin reacted to extracts of the bone matrix, but much less strongly than they do to extant bird tissue. The tests suggest that any remaining original material is quite scarce—on the order of parts per trillion. "It's very frustrating," Schweitzer said, explaining that the tiny amounts make confirmation difficult.

But skeptics have another, less sexy, explanation for the tissue: the replacement of original tissue by microbes. Thomas Kaye, a full-time amateur paleontologist in Prospect Heights, Illinois, examined well-preserved bone from four kinds of late-Cretaceous dinosaurs using a scanning electron microscope and sees signs that microbes have replaced the original tissue. During 200 hours of observations, Kaye found hollow vascular canals like those of Schweitzer's specimen. But he also discovered evidence that microbes had moved through a thick film. In some samples, this film had dried out and had a carbon-14 date of 1960–1970. As for the structures resembling cells called osteocytes, Kaye and colleagues think they could be microbes that filled in a void in the bone.

Hans Larsson, a paleontologist at McGill University in Montreal, Canada, says the theory of microbial replacement is "totally logical" and that carbon-14 dating should be done to rule out modern biofilms. The debate is expected to continue. "The proof is going to be tricky," Larsson says. "It's going to take years."

CREDIT (TOP): M. H. SCHWEITZER

Crestfallen: Sexually Dimorphic No More

Paleontologists had long thought that the skulls of certain duck-billed dinosaurs might provide a clue about the largely mysterious sex lives of dinosaurs. The animals sported crests that seemed to become more prominent as the creatures matured. Some were more ornate than others—presumably a display that males used to impress females. But research presented at the meeting shows that the crests differ not by gender but by species. "A very nice story of sexual selection just doesn't hold up," says Zhexi Luo of the Carnegie Museum of Natural History in Pittsburgh, Pennsylvania, about the new evidence.

The story began in 1975, when Peter Dodson of the University of Pennsylvania (UPenn) proposed that several species of hadrosaur described from Dinosaur Provincial Park in Alberta, Canada, over the previous decades were actually just two genera—*Lambeosaurus* and *Corythosaurus*—that changed their crest shape as they matured. The variation among adults, he argued, was due to differences between male and female animals, known as sexual dimorphism. A few years ago, David Evans, then a graduate student at the University of Toronto in Mississauga, Canada, decided to test Dodson's idea.

Evans worked with paleontologist Philip Currie of the University of Alberta in Edmonton and others to pinpoint the locations of the several dozen specimens of *Lambeosaurus* and *Corythosaurus* within the 120-meter-thick formation of sedimentary rock in the Dinosaur Provincial Park. They searched for markers left at each field site by earlier paleontologists, then used centimeter-resolution GPS to pinpoint what rock layer the bones had come from.

It turned out that all of the presumably female forms of *Corythosaurus* came from the uppermost portion of the formation, ranging in age from 75.3 million to 74.8 million years. The males were exclusively from lower rocks, stretching back 500,000 years earlier. "These guys would have had to wait a long time for a date," Evans quips. *Lambeosaurus* had a similar pattern. Instead of sexual dimorphism, Evan concluded, the forms probably represent separate lineages.

The different clusters likely represent changes in form within the groups, called anagenic evolution, says Kevin Padian of the University of California, Berkeley. He believes the head crests may have helped dinosaurs recognize members of the same species. "It's a beautiful study," adds Dodson, who is still at UPenn. "I embrace the findings wholeheartedly." An example of sexual dimorphism that Dodson identified in the horned dinosaur *Protoceratops* is still generally accepted.

–ERIK STOKSTAD

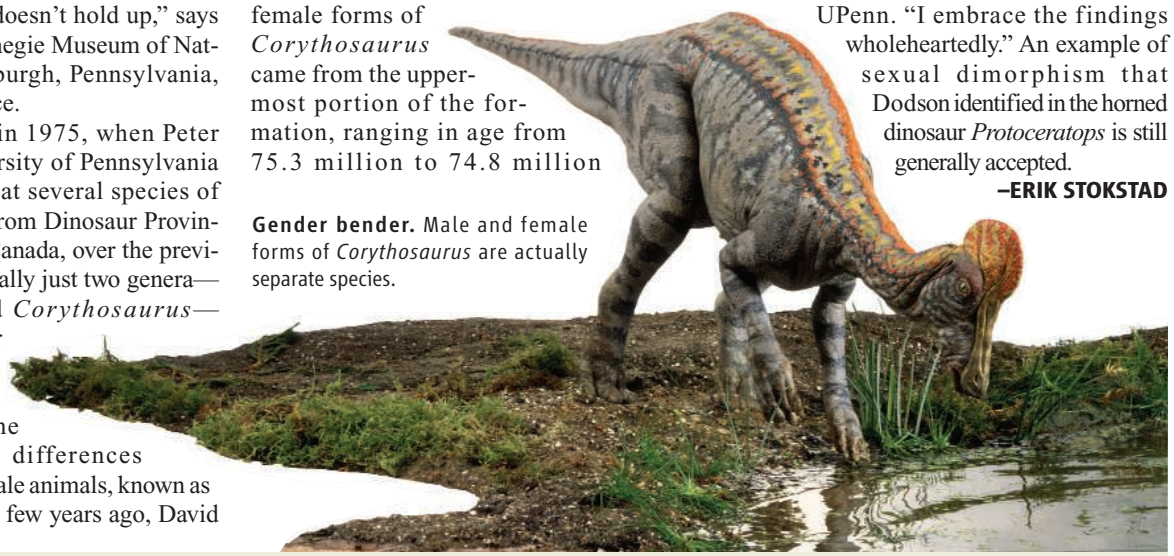

Gender bender. Male and female forms of *Corythosaurus* are actually separate species.

CREDIT: DK LIMITED/CORBIS

Snapshots From The Meeting >>

Amphibian development. The origin and evolutionary relationships of amphibians—frogs, salamanders, and the limbless caecilians—have long been murky. Some paleontologists think all three groups evolved from a single, long-extinct ancestor, whereas others suspect that each had separate evolutionary roots. A new study provides the first developmental evidence from the fossil record, but it doesn't settle the question.

One fact that has long puzzled paleontologists is the order in which salamanders develop their digits. In frogs and every other terrestrial tetrapod, the fourth finger and toe develop first, followed by the third, fifth, second, and first digits. Salamanders buck this trend, starting with the thumb, a process called postaxial dominance.

So, too, it turns out, did extinct amphibians called branchiosaurids, graduate student Nadia Fröbisch of McGill University in Montreal, Canada, concluded after examining more than 600 well-preserved specimens of a branchiosaurid called *Apateon*. That means that postaxial dominance developed more than 300 million years ago. To Robert Carroll of McGill University, a co-author on Fröbisch's paper in press at *Evolution & Development*, the evolutionary kinship between salamanders and branchiosaurids helps demonstrate that salamanders evolved from a different fossil ancestor than did frogs or caecilians.

Andrew Milner of the Natural History Museum in London and others aren't so sure. They point to another possibility: What if a single ancestor of all modern amphibians developed like salamanders, and then frogs reverted to standard tetrapod pattern? More fossils are needed to resolve the issue.

Baleen and teeth. Blue whales and other mysticetes feed like no other mammal, sucking in great volumes of seawater and straining out plankton with great racks of keratinous fibers called baleen. How toothed whales developed baleen is a mystery, because the tissue hardly ever fossilizes. Now, paleontologists have taken a step toward solving the issue by reporting the first transitional fossil with both teeth and evidence of baleen. "That's pretty cool," says Mark Uhen, a whale paleontologist until recently at the Cranbrook Institute of Science in Bloomfield Hills, Michigan.

Thomas Deméré of the San Diego Natural History Museum in California described how he and colleagues studied an ancient toothed whale from Oregon called *Aetiocetus weltoni*. After removing rock from the skull to expose the palate, they spotted tiny grooves and holes that match those in the palate of baleen whales, where the grooves contain nerves and blood vessels that connect to the baleen. Lawrence Barnes of the Natural History Museum of Los Angeles County isn't convinced. Barnes, who first described *A. weltoni*, notes that some living toothed whales have similar palatal grooves.

Aetiocetus lived between 24 million and 28 million years ago and coexisted with baleen whales, so it's not their direct ancestor. But it provides a glimpse of the stepwise transition toward baleen feeding. Deméré says he has no idea about the role of incipient baleen. **–E.S.**

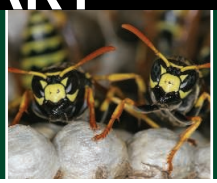

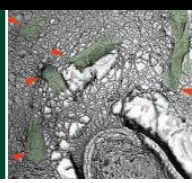

LETTERS

edited by Etta Kavanagh

Animal Activism and Intimidation of Scientists

SCIENCE EDITOR-IN-CHIEF DONALD KENNEDY IS ON THE MARK WITH HIS CALL FOR INSTITUtions to support their scientists and researchers under siege by animal rights terrorists ("Animal activism: out of control," 15 Sept., p. 1541). As directors of Americans for Medical Progress, we feel that it is equally important to urge the entire scientific community and their supporters to rally publicly for those targeted by extremists.

Animal rights activists march in Miami 20 November 2003.

Our scientific brethren in the United Kingdom have been unified and proactive in their successful efforts to moderate the public debate over the humane use of animals in research. Initiatives expressing popular support for animal research, such as Pro-Test and The People's Petition, have demonstrated that science will not be cowed and have helped scientists to speak out in public.

The assault on University of California, Los Angeles (UCLA) primate researcher Dario Ringach is an attack on responsible research being conducted everywhere. It is not enough for UCLA administrators, faculty members, and researchers to support him. All scientists and advocates of biomedical research should abandon their silence, speak out, and show public solidarity with our colleagues who are under threat.

JOHN D. YOUNG,* RICHARD W. BIANCO, JOHN J. FUNG, ANDREW A. LACKNER

Americans for Medical Progress, 908 King Street, Suite 301, Alexandria, VA 22314, USA.

*Chairman

IN RESPONSE TO DONALD KENNEDY'S Editorial "Animal activism: out of control" (15 Sept., p. 1541), we say a pox on both sides. Although we criticize illegal and harassing conduct, we also criticize the persistent opposition to animal welfare measures and strident antiregulation posture of the research community.

Millions of Americans care about animal welfare and also hold that harassment and violence are wholly unacceptable and inconsistent with a core ethic of promoting compassion and respect. The Humane Society of the United States, which represents nearly 10 million members and constituents, has repeatedly criticized individuals who break the law in the name of supposedly protecting animals.

However, reasonable animal welfare proposals have been ignored by biomedical research institutions or dismissed with claims that they would lead to the end of all animal research. The biomedical community has opposed providing basic protections to mice, rats, and birds; eliminating the Class B dealers who continue to mistreat and sell pets into research; and stopping the use of chimpanzees in harmful research. But even more damning for a community that professes to encourage open and vigorous debate, organized academe dismisses legitimate animal welfare critics as dangerous zealots and engages in blatant political control of the terms and the content of the animal welfare debate.

The biomedical research community plays into the hands of the radicals when it resists reasonable reforms. Their obduracy also hurts the efforts of groups like the Humane Society of the United States when we counsel young people to work through the system.

ANDREW N. ROWAN

Executive Vice President, Operations, The Humane Society of the United States, Washington, DC 20037, USA. E-mail: arowan@hsus.org

DONALD KENNEDY'S EDITORIAL "ANIMAL activism: out of control" (15 Sept., p. 1541) addresses an issue rarely raised in scientific journals despite an onslaught of activist and public agitation. Intimidation of scientists, whose studies are dependent on laboratory animals, has a long extremist-based history in both the United States and Europe. Congressional action on H.R.4239 (the Animal Enterprise Terrorism Act) to defend against direct and indirect attacks on those involved in research and their families is encouraging and should be supported by all in the scientific community.

The failure of the scientific organization hosting the research to publicly defend the use of animals by one of its scientists is not uncommon. Such reluctance seems irrational in light of the fact that institutions review such research before it is conducted, assure granting agencies such as the NIH that appropriate care and use of animals will occur, and accept the funding, including indirect costs, to conduct the studies in question. Likewise, corporate and privately funded institutes dedicated to the advancement of biomedical research are often less-than-inspired defenders of their employees and the need to utilize animals in the advancement of knowledge.

Admittedly, there have been some rare cases where scientists have failed to comply with the common-sense and legal requirements that enable us to have the privilege to work with animals. However, the future of

CREDIT: MARC SEROTA/REUTERS

life sciences and those interested in pursuing science as a career depends on our scientific institutions publicly expressing support for the type of work needed to advance mankind, including the use of research animals.

DENNIS M. STARK

Bristol Myers Squibb, Princeton, NJ 08543, USA.

A Plea for Justice for Jailed Medical Workers

IN 2000–01, REPORTS BEGAN TO SURFACE of an HIV-1 outbreak in approximately 400 children who were hospitalized or treated as outpatients in the Al-Fateh Hospital, Benghazi, Libya. The Libyan government accused six medical workers (five Bulgarian nurses and a Palestinian doctor) of intentionally infecting these children with HIV-1. The Libyan Head of State, Moammar Kadafi, speaking at the HIV/AIDS summit in Abuja, Nigeria, in April 2001, stated that these children had been deliberately infected as part of a vast international conspiracy to destabilize his country. The six health care workers were imprisoned, tortured with electric shocks to extract "confessions," tried in a Libyan court, convicted, and sentenced to death by firing squad. The resulting publicity caused the Benghazi pediatric HIV-1 outbreak to become the focus of international scientific efforts to understand how it occurred.

The Benghazi Children's Hospital was visited by international experts, and the records of infected children were compiled. Many of these children were treated in European hospitals, making it possible to obtain clinical specimens for virology studies. The examination of hospital records showed that without question, HIV-infected children were admitted to several wards of the Al Fateh Benghazi Children's Hospital in 1997 and early 1998 (with some possibility that HIV-infected children were present in the hospital as early as 1994), before the arrival in Libya of the six accused. The results of serology studies (*1*) and viral genome sequencing (*1*, *2*) established that the HIV-1 infections in all the children arose from a single source with very low intrastrain variation and the virus was of the CRF02 A/G subtype that is common in sub-Saharan Africa. A high percentage of the HIV-1–infected children were also infected with hepatitis C virus, of several different genotypes, and many also had hepatitis B virus infection despite an active pediatric immunization program (*1*). All three viruses were present in the children at rates far above those in the local population. Documentation of HIV-infected children admitted to the hospital in 1997 and the prevalence of multiple blood-borne viruses within the children, proves that HIV was present in the Al-Fateh Hospital by 1997, and the most reasonable explanation is that poor infection control practices, including the lack of sterile, disposable injecting equipment, led to the spread of HIV-1, hepatitis B, and hepatitis C. A change in medical practices at the hospital, including the introduction of disposable injection materials, stopped the further spread of HIV-1 infection (*1*).

Convicting a small group of individuals of such an appalling crime as the deliberate infection of 400 innocent children requires a very high degree of proof. Yet the Libyan court chose to exclude expert testimony from independent scientists and to prevent access to crucial pieces of evidence to test for HIV contamination, while relying instead on "confessions" extracted under torture and making threats of execution for any noncooperation by the accused. At the same time, the Libyan government made demands for ever-increasing financial compensation from Bulgaria for the parents of the infected children. These six innocent health care workers have been incarcerated in a Libyan prison for nearly 8 years, for what we believe was performing their jobs with inadequate equipment, after receiving inadequate training and having been exposed to the same risk of HIV infection as the Libyan children and hospital staff. What has happened to the accused sends a chilling message to all heath care workers who choose to work in difficult circumstances to deliver life-saving care to HIV-1–infected or at-risk people worldwide.

Libya is now seeking closer ties with the Western world. We therefore request that our governments reach out to the Libyan people and their political leadership to find a way to release the imprisoned health care workers, provide means to look after the HIV-1–infected children, and help with all efforts to detect, treat, and prevent HIV-1 infection within Libya. If Libya is truly willing to enter into meaningful dialogues with Western nations, it should take the opportunity to benefit from the knowledge Western scientists have gained about HIV-1 and AIDS over the past 25 years and not instead create yet more victims of the AIDS epidemic—in this case, the five Bulgarian nurses and Palestinian doctor.

SUNIL K. AHUJA,[1] FERNANDO AIUTI,[2] BEN BERKHOUT,[3] PETER BIBERFELD,[4] DENNIS R. BURTON,[5] VITTORIO COLIZZI,[6] STEVEN G. DEEKS,[7] RONALD C. DESROSIERS,[8] MANFRED P. DIERICH,[9] ROBERT W. DOMS,[10] MICHAEL EMERMAN,[11] ROBERT C. GALLO,[12]* MARC GIRARD,[13] WARNER C. GREENE,[14] JAMES A. HOXIE,[15] ERIC HUNTER,[16] GEORGE KLEIN,[4] BETTE KORBER,[17] DANIEL R. KURITZKES,[18] MICHAEL M. LEDERMAN,[19] MICHAEL H. MALIM,[20] PRESTON A. MARX,[21] JOSEPH M. MCCUNE,[7] ANDREW MCMICHAEL,[22] CHRISTOPHER MILLER,[23] VERONICA MILLER,[24] LUC MONTAGNIER,[25] DAVID C. MONTEFIORI,[26] JOHN P. MOORE,[27] DOUGLAS F. NIXON,[7] JULIE OVERBAUGH,[11] C. DAVID PAUZA,[12] DOUGLAS D. RICHMAN,[28] MICHAEL S. SAAG,[29] QUENTIN SATTENTAU,[30] ROBERT T. SCHOOLEY,[28] ROBIN SHATTOCK,[31] GEORGE M. SHAW,[32] MARIO STEVENSON,[33] ALEXANDRA TRKOLA,[34] MARK A. WAINBERG,[35] ROBIN A. WEISS,[36] STEVEN WOLINSKY,[37] JEROME A. ZACK[38]

[1]University of Texas Health Science Center, San Antonio, TX, USA. [2]University of Rome "La Sapienza," Rome, Italy. [3]University of Amsterdam, Amsterdam, The Netherlands. [4]Karolinska Hospital/Institute, Stockholm, Sweden. [5]The Scripps Research Institute, La Jolla, CA, USA. [6]University of Rome "Tor Vergata," Rome, Italy. [7]University of California, San Francisco, San Francisco, CA, USA. [8]Harvard Medical School, New England Primate Research Center, Southboro, MA, USA. [9]Innsbruck Medical University, Innsbruck, Austria. [10]University of Pennsylvania, Philadelphia, PA, USA. [11]Fred Hutchinson Cancer Research Center, Seattle, WA, USA. [12]Institute of Human Virology, University of Maryland at Baltimore, Baltimore, MD, USA. [13]Lyon, France. [14]Gladstone Institute of Virology and Immunology, University of California, San Francisco, San Francisco, CA, USA. [15]Penn Center for AIDS Research, University of Pennsylvania, Philadelphia, PA, USA. [16]Emory University, Atlanta, GA, USA. [17]Santa Fe Institute, Santa Fe, NM, USA. [18]Harvard Medical School, Cambridge, MA, USA. [19]Center for AIDS Research, Case Western Reserve University/University Hospitals of Cleveland, Cleveland, OH, USA. [20]King's College London School of Medicine, London, UK. [21]Tulane National Primate Research Center, Covington, LA, USA. [22]Weatherall Institute of Molecular Medicine, John Radcliffe Hospital, Headington, Oxford, UK. [23]California National Primate Research Center, University of California-Davis, Davis, CA, USA [24]The George Washington University, Washington, DC, USA. [25]World Foundation for AIDS Research and Prevention, Paris, France. [26]Duke University Medical Center, Durham, NC, USA. [27]Weill Medical College of Cornell University, New York, NY, USA. [28]University of California, San Diego, San Diego, CA, USA. [29]UAB Center for AIDS Research, Birmingham, AL, USA. [30]University of Oxford, Oxford, UK. [31]University of London, London, UK. [32]University of Alabama at Birmingham, Birmingham, AL, USA. [33]University of Massachusetts Medical School, Worcester, MA, USA. [34]University Hospital Zurich, Zurich, Switzerland. [35]McGill University AIDS Centre, Montreal, Canada. [36]University College London, London, UK.

Letters to the Editor

Letters (~300 words) discuss material published in *Science* in the previous 6 months or issues of general interest. They can be submitted through the Web (www.submit2science.org) or by regular mail (1200 New York Ave., NW, Washington, DC 20005, USA). Letters are not acknowledged upon receipt, nor are authors generally consulted before publication. Whether published in full or in part, letters are subject to editing for clarity and space.

[37]Northwestern University, Chicago, IL, USA. [38]David Geffen School of Medicine at UCLA, Los Angeles, CA, USA.

*To whom correspondence should be addressed. E-mail: gallo@umbi.umd.edu

References

1. S. Yerly *et al.*, *J. Infect. Dis.* **184**, 369 (2001).
2. U. Visco-Comandini *et al.*, *AIDS Res. Hum. Retroviruses* **18**, 727 (2002).

Published online 24 October 2006;
10.1126/science.1136578
Include this information when citing this paper.

Throwing the Dice

THE COVER OF THE 30 JUNE ISSUE SHOWS A board game called "Life Cycles." Also shown are two dice. For those not familiar with dice, there are "proper" and "not proper" die. A proper die must have the sum of the numbers on opposite sides equal to seven. It is clear that the die on the left is not proper, because it shows on one face a 2, which is not opposite the 5 that is showing on another face.

The die on the right could be proper; it is impossible to tell. If it were proper, it could be either "left-handed" or "right-handed." To be right-handed, the faces marked with a 1, 2, and 3 must be normal (at right angles) to a right-handed set of *x*-*y*-*z* coordinate axes. To be right-handed, it must have the number 3 on the face on the left. If instead it has the number 4, then it is left-handed.

I make the above comments because it is unlike *Science* to promote improper information, and it is an advantage for all young researchers to be able to put the correct "spin" on their dice when they play the game of life.

RONALD GREEN

Fitzroy, Adelaide, Australia.

The Dangers of Pyramid-Mania

IN HIS ARTICLE "MAD ABOUT PYRAMIDS" (News Focus, 22 Sept., p. 1718), J. Bohannon discusses the current Bosnian pyramid-mania and its ramifications, but there is one aspect he did not mention: the loss of important paleontological resources. At the invitation of Semir Osmanagic (also spelled Osmanagich), chairman of the Bosnian Pyramid of the Sun Foundation, I visited Visoko in late July and early August to study the "pyramids" and surrounding geology. The "pyramid" hills are composed of Late Miocene lacustrine and fluvial deposits; certain strata are highly fossiliferous, containing a variety of thus-far undocumented angiosperm leaves and other plant remains as well as animal trace fossils. I believe this area merits serious paleontological study. On the basis of the sedimentology, the hills could well yield scientifically valuable terrestrial vertebrate specimens. Presently, the fossils are being ignored and destroyed during the "excavations," as crews work to shape the natural hills into crude semblances of the Mayan-style step pyramids with which Osmanagic is so enamored (*1*–*3*).

ROBERT M. SCHOCH

Associate Professor of Natural Science, College of General Studies, Boston University, Boston, MA 02215, USA.

References

1. S. Osmanagich, *The World of the Maya* (Gorgias, Piscataway, NJ, 2005).
2. S. Osmanagic, *Bosanska Piramida Sunca* (Klepsidra, Sarajevo, 2005).
3. S. Osmanagic, *Bosanska Dolina Piramida* (Maunagic, Sarajevo, 2006).

CORRECTIONS AND CLARIFICATIONS

Reports: "Large punctuational contribution of speciation to evolutionary divergence at the molecular level" by M. Pagel *et al.* (6 Oct., p. 119). In conducting further work to identify punctuational episodes of evolution such as reported in the paper, the authors have discovered a previously undescribed bias that affects Bayesian posterior distributions of phylogenetic trees derived from Markov chain Monte Carlo methods. The bias arises when species are closely related and thus the phylogenetic signal is difficult to detect. The bias manifests itself as a tendency in the posterior sample toward asymmetrically branching trees with short but variable branch lengths. Under these circumstances, the posterior distribution of trees can support the inference of punctuational evolution even when no such effect is present. The bias is distinct from the node-density artifact [e.g., C. Venditti, A. Meade, M. Pagel, *Syst. Biol*. **55**, 637 (2006)], and the authors will describe it in detail elsewhere. Having reanalyzed in light of this discovery the 122 phylogenetic data sets that comprise the data, the authors think that 11 may suffer from this bias, in addition to the 22 trees previously identified and removed for having node-density effects. Removing these 11 trees from the sample does not alter the conclusions. The authors find that 27 ± 4.7% of the remaining trees show the punctuational effect compared to the 35 ± 4.8% that was previously reported. They still find that the frequency of punctuational effects among plants (43.5 ± 10.0%) and fungi (60.0 ± 22%) is at least double that in animals (18.0 ± 4.9%; $\chi^2 = 7.97$, $P < 0.02$), and the asymptotic estimate of the percentage of genetic changes that can be attributed to the punctuational episodes as the tree size approaches infinity is 16 ± 5.4% as compared with 22 ± 3.6% in the original sample. The size of the punctuational effect predicts departures from a molecular clock-like mode of evolution: The correlation of $r = 0.79$ reported in Fig. 4 of the Report that measures this effect has increased to $r = 0.87$, $P < 0.0001$. The Supplementary Online Material has been modified to reflect these changes.

Reports: "Oxygen-mediated diffusion of oxygen vacancies on the TiO_2(110) surface" by R. Schaub *et al.* (17 Jan. 2003, p. 377). Since the publication of this Report, the authors have realized that the background water pressure in the UHV chamber used was sufficient to replace all oxygen vacancies by bridging hydroxyls (OH_{br}), as reported in S. Wendt *et al.*, *Surf. Sci.* **598**, 226 (2005). Furthermore, new experiments performed under improved vacuum conditions have revealed that the diffusing species observed in the Report are indeed adsorbed water molecules and not O_2 [S. Wendt *et al.*, *Phys. Rev. Lett.* **96**, 066107 (2006)]. All observations in the Report are fully reproducible under a deliberate residual water pressure. However, the interpretation proposed in the Report must be revised. The STM movies and images presented actually show water molecules diffusing in Ti troughs and jumping across OH_{br} defects. The reinterpretation of the data reported is revealed from additional STM movies together with DFT calculations presented elsewhere [S. Wendt *et al.*, *Phys. Rev. Lett.* **96**, 066107 (2006)].

TECHNICAL COMMENT ABSTRACTS

COMMENT ON "Statistical Independence of Escalatory Ecological Trends in Phanerozoic Marine Invertebrates"

Peter D. Roopnarine, Kenneth D. Angielczyk, Rachel Hertog

The analysis of Madin *et al*. (Reports, 12 May 2006, p. 897) of Phanerozoic diversity failed to support expected correlations between carnivores and noncarnivores, leading the authors to reject escalation as an important macroevolutionary process. The test, however, is based on a flawed model of causality, and the ecological groups are improperly delineated with regard to the hypothesis.

Full text at www.sciencemag.org/cgi/content/full/314/5801/925d

COMMENT ON "Statistical Independence of Escalatory Ecological Trends in Phanerozoic Marine Invertebrates"

Gregory P. Dietl and Geerat J. Vermeij

Madin *et al*. (Reports, 12 May 2006, p. 897) reported that escalation has not been an important cause of biological change throughout the history of life. However, they evaluated the escalation hypothesis with inappropriate data. First, global-scale data integrate heterogeneous signals that obscure the economic context of life. Second, diversity data cannot yield information about selection and adaptation.

Full text at www.sciencemag.org/cgi/content/full/314/5801/925e

RESPONSE TO COMMENTS ON "Statistical Independence of Escalatory Ecological Trends in Phanerozoic Marine Invertebrates"

Joshua S. Madin, John Alroy, Martin Aberhan, Franz T. Fürsich, Wolfgang Kiessling, Matthew A. Kosnik, Peter J. Wagner

Roopnarine *et al*. and Dietl and Vermeij do not challenge our results but argue that escalation can be seen only at fine scales. This claim diminishes the theory and needs to be tested, not asserted. Roopnarine *et al*. incorrectly presume that our data are dominated by carnivores. Dietl and Vermeij overlook the fact that in addition to having no effect on global diversity, escalation has no effect on occurrence frequency.

Full text at www.sciencemag.org/cgi/content/full/314/5801/925f

Comment on "Statistical Independence of Escalatory Ecological Trends in Phanerozoic Marine Invertebrates"

Peter D. Roopnarine,[1]* Kenneth D. Angielczyk,[2] Rachel Hertog[1]

The analysis of Madin *et al*. (Reports, 12 May 2006, p. 897) of Phanerozoic diversity failed to support expected correlations between carnivores and noncarnivores, leading the authors to reject escalation as an important macroevolutionary process. The test, however, is based on a flawed model of causality, and the ecological groups are improperly delineated with regard to the hypothesis.

Madin *et al*. (*1*) present a hypothesis predicting that because of escalating interactions, changes in the diversity of an ecologically defined set of carnivores will cause changes of composition in noncarnivore sets, substantiating the claim that predators act as important agents of selection. Their examination of such trophically delineated groups in the Phanerozoic fossil record yielded significant rank correlations between an ecological set comprising carnivores and other sets comprising the proportions of noncarnivores of various habits, such as infaunal and mobile. Subsequent first-order differencing of diversity time series, presumably to correct for taphonomic bias and other factors such as clade-specific rates of origination and extinction (assuming that clades do not span more than one of the ecological sets), reduced most of the correlations to insignificance, leading the authors to reject escalation as a causative explanation. The absence of correlation, however, is insufficient confirmation of independence because the model of causality is inadequate.

[1]Department of Invertebrate Zoology and Geology, California Academy of Sciences, 875 Howard Street, San Francisco, CA 94103, USA. [2]Department of Earth Sciences, University of Bristol, Wills Memorial Building, Queens Road, Bristol BS8 1RJ, UK.

*To whom correspondence should be addressed. E-mail: proopnarine@calacademy.org

Division of the Phanerozoic fauna into carnivores and noncarnivores is inappropriate because if animals indeed evolve in response to their enemies, then the set of carnivores comprises relevant disjointed subsets of carnivores of various trophic levels, making the variance of the set itself a function of carnivore diversity. Consider the set of carnivores, for example, to comprise the exclusive subsets of top carnivores and intermediate carnivores. The true correlation between noncarnivores and carnivores therefore depends on the relative proportions of top and intermediate carnivores. These data were not presented by Madin *et al*. Several other factors that are expected to show temporal and geographic variation also influence the correlation, including (i) the strengths of the interactions between top and intermediate carnivores, because the latter may respond in escalatory fashion to predation; (ii) the intensity of escalation of intermediate carnivores in response to their predators and the phenotypic diversity of those responses; (iii) the strengths of interactions between top carnivores and their noncarnivore prey, as well as between intermediate carnivores and their noncarnivore prey; and (iv) the relative intensities of escalation of true noncarnivores to their top and intermediate predators. If the expression of variations in the intensities of the interactions is itself a nonstationary feature (e.g., escalated defenses of intermediate carnivores do not always result in enhanced predatory capabilities), then disparities in the relative ranks within carnivore and noncarnivore sets will increase, resulting in lower rank correlations between those sets. In other words, noncarnivore diversity may not reflect escalatory increases within the set of carnivores.

Three brief examples serve to highlight these issues. First, ammonites were important intermediate predators in Paleozoic and Mesozoic oceans, yet conflicting demands on the shell for both buoyancy and defense resulted in fluctuations in the degree of ammonite shell armor during the Mesozoic, even as the frequency of shell repair increased (*2*). Such variation in escalation is unmeasured in the Madin *et al*. analysis, and one wonders how this variation would drive escalation in noncarnivores. Second, examination of the trophic habits of carnivores in the eight middle Permian to middle Triassic terrestrial fossil assemblages from the Karoo Basin of South Africa (*3*) reveals significant fluctuations in the relative proportions of the number of genera of top and intermediate carnivores. Third, compilations of ancient and modern food webs reveal complex networks of trophic relationships among carnivores (including omnivores) (*4*–*6*), where the total evolutionary impact of predation on noncarnivores must be filtered through numerous intermediate species. These data suggest that the expectation of simple relationships between patterns of global Phanerozoic diversity and processes of biological interaction is an insufficient framework for testing macroevolutionary hypotheses. Instead, hypotheses of adaptation must be tested at relevant organismal scales.

References and Notes

1. J. S. Madin *et al.*, *Science* **312**, 897 (2006).
2. G. J. Vermeij, *Evolution and Escalation: An Ecological History of Life* (Princeton Univ. Press, Princeton, NJ, 1987).
3. B. S. Rubidge, Ed., *S. Afr. Comm. Stratigr. Biostratigr. Ser.* **1**, 1 (1995).
4. K. D. Angielczyk *et al.*, *N. M. Mus. Nat. Hist. Sci. Bull.* **30**, 16 (2005).
5. J. M. Montoya *et al.*, *Nature* **442**, 259 (2006).
6. P. D. Roopnarine, *Paleobiology* **32**, 1 (2006).

16 May 2006; accepted 17 October 2006
10.1126/science.1130073

Comment on "Statistical Independence of Escalatory Ecological Trends in Phanerozoic Marine Invertebrates"

Gregory P. Dietl[1]*† and Geerat J. Vermeij[2]

Madin *et al.* (Reports, 12 May 2006, p. 897) reported that escalation has not been an important cause of biological change throughout the history of life. However, they evaluated the escalation hypothesis with inappropriate data. First, global-scale data integrate heterogeneous signals that obscure the economic context of life. Second, diversity data cannot yield information about selection and adaptation.

Madin *et al.* (*1*) presented evidence from a global analysis of diversity and abundance of fossil invertebrates that escalation, or enemy-directed evolution, has not been an important causal driver of biological change throughout the history of life. The authors set up their paper by stating that escalation—fundamentally a hypothesis of adaptation of organisms to their enemies (*2*)—needs "to be tested by examining trends in relative diversity and counts of occurrences … among marine metazoans as a whole (p. 897)." However, this philosophical approach, which has dominated the field of paleobiology over the past 30 years, comes up short of testing the escalation hypothesis because it combines information from an immense array of clades, ecosystems, selection regimes, and geographic regions.

First, the global scale is too large to be relevant to the lives of organisms. The hypothesis of escalation has to be tested at a spatial scale equivalent to the scale of interaction among the units in which selection operates (*2*). The context—environment, interaction, functional role, adaptive syndrome, and geographic origin—in which organisms live and evolve varies dramatically from place to place and over time, making any global analysis an amalgam that integrates heterogeneous signals. Tests of the escalation hypothesis therefore must be conducted at local to regional scales so that emergent heterogeneity at the global scale does not mask the economic interactions of relevant evolutionary individuals. By ignoring the context of life, global analyses inevitably obscure the economic processes that account for the historical patterns we are trying to explain.

Second, when we consider the character of selection as a causal economic process, it becomes evident that analyses of diversity patterns through time cannot yield biologically meaningful information about adaptation. Diversity reflects adaptation (the ecological and evolutionary effects of competition, cooperation, and predation, among other ways of acquiring or retaining the same locally limiting resources), but it cannot serve as a surrogate for it. Evolutionary units do not live or evolve as independent entities (*2*). At all scales of economic life, from the cell to ecosystems, entities create, and are affected by, an economic system of responsive, interacting entities. Diversity is not a measure of any biological interaction; it is an abstract number that incorporates a multitude of processes in addition to economic interactions among individuals. Results based exclusively on diversity patterns—abstract epiphenomena devoid of the context of life—are therefore incomplete tests of the escalation hypothesis and prone to be misleading.

An understanding of the role of competition in the history of life can come only from studies of the interacting economic units themselves and the local and regional environments in which they are embedded.

[1]Department of Geology and Geophysics, Yale University, New Haven, CT 06520, USA. [2]Department of Geology, University of California, Davis, CA 95616, USA.

*Present address: Paleontological Research Institution, 1259 Trumansburg Road, Ithaca, NY 14850, USA.
†To whom correspondence should be addressed. E-mail: gpd3@cornell.edu

References and Notes

1. J. S. Madin *et al.*, *Science* **312**, 897 (2006).
2. G. J. Vermeij, *Evolution and Escalation: An Ecological History of Life* (Princeton Univ. Press, Princeton, NJ, 1987).

23 May 2006; accepted 17 October 2006
10.1126/science.1130419

Response to Comments on "Statistical Independence of Escalatory Ecological Trends in Phanerozoic Marine Invertebrates"

Joshua S. Madin,[1]* John Alroy,[1] Martin Aberhan,[2] Franz T. Fürsich,[3] Wolfgang Kiessling,[2] Matthew A. Kosnik,[4] Peter J. Wagner[5]

Roopnarine *et al*. and Dietl and Vermeij do not challenge our results but argue that escalation can be seen only at fine scales. This claim diminishes the theory and needs to be tested, not asserted. Roopnarine *et al*. incorrectly presume that our data are dominated by carnivores. Dietl and Vermeij overlook the fact that in addition to having no effect on global diversity, escalation has no effect on occurrence frequency.

We thank Roopnarine *et al*. (*1*) and Dietl and Vermeij (*2*) for their comments on our time series analysis of ecological trends through the Phanerozoic eon (*3*), and although we agree that some scenarios may explain our results, we do not agree that large-scale analyses are irrelevant because we can assume that the world is too complex to demonstrate causal relations at the largest scales. The central argument of both comments is that escalation in one place or in one trophic or taxonomic group is always canceled out at larger scales by de-escalation in others, and therefore cannot be tested at these scales. This claim is an empirical induction, not a philosophical deduction, so it needs to be tested instead of asserted. Shielding escalation by redefining it as partially untestable may be tempting, but the use of such a strategy is the hallmark of a paradigm in retreat.

Not only does the escalation hypothesis make a clear and crucial prediction of a global-scale tradeoff between different ecological groups, but a longer time series may well have evidenced a weak statistical interdependency. We have conducted a power analysis showing that nontrivial but still unimpressive r^2 values of up to 0.24 could exist. Our point is not that there is no relationship whatsoever but that it is not important at the global scale that is of the greatest interest to biologists.

Roopnarine *et al*. (*1*) misrepresent the motivation and implications of our time series analysis, which was intended to isolate correlations with possible causal significance from correlations with no such significance and only secondarily was meant to correct for taphonomic bias. Cross-correlations of autocorrelated time series are expected in the absence of even indirect causal connections; any two generally upward- or downward-trending time series will cross-correlate. Therefore, differencing is necessary to provide even the most basic evidence of a relationship.

Roopnarine *et al*. (*1*) state that a model of causality relating carnivore to noncarnivore frequency is flawed because of its simplicity, but escalation is just such a model, and its predictions are straightforward. More substantively, they argue that in marine ecosystems that are strongly dominated by carnivores, escalation may only be visible within carnivore guilds at different trophic levels. This seems plausible but not apropos of our data.

First, Roopnarine *et al*.'s evidence that long trophic chains exist in our data consists of citations to papers on terrestrial vertebrates, terrestrial plants and insects, predominantly nonbenthic marine organisms like fish, morphology, and theoretical models. The paleontological literature on escalation, however, almost entirely concerns benthic invertebrates such as gastropods, bivalves, and brachiopods. Second, our data show that the relative frequency and diversity of carnivorous invertebrates was rarely more than 10% throughout most of the Phanerozoic, and never more than 27%. Most of the few carnivores were likely to be primary consumers, and populations of high trophic-level predators were likely to have been too small to have had much of an effect. Third, the major groups comprising our noncarnivore categories are mostly immobile or infaunal, so it is unlikely that we have scored them incorrectly. Fourth, we specifically excluded vertebrates from our analysis because their fossil record is poor relative to shelly invertebrates. Finally, the range of body masses within our major carnivore groups, like gastropods and ammonites, is rather narrow, so it is unlikely that many trophic levels were represented.

Roopnarine *et al*. present several scenarios that might explain why correlations might not emerge. None of these scenarios is testable in the absence of clear criteria for separating top and intermediate predators within benthic shelly invertebrates; an explanation for our results is not a criticism of them.

Dietl and Vermeij (*2*) object first to our having analyzed global data and second to our use of diversity data. They state that global data are not relevant to the trends they are trying to explain. However, they are the trends we are trying to explain, and global biodiversity is a topic of much discussion. Much of the literature on escalation is premised on the idea that it is a global phenomenon, and if it is not, then perhaps it is not such a key evolutionary process.

More specifically, they, like Roopnarine *et al*., suggest that escalation might be more visible at local scales. We agree that it might be and hope that our results will encourage analyses at multiple scales that will explore the scale dependence of evolutionary processes instead of holding them back. Furthermore, as we stated, data on local areas and data spanning short time intervals are typically not open to the kind of rigorous time series analysis we performed. Although we strongly believe that local and global studies are complementary, we also hold that time series analysis is a good way to test for evolutionary processes, not just patterns.

Dietl and Vermeij (*2*) also state that diversity patterns are abstract epiphenomena that cannot yield information about selection or adaptation. The suggestion is that one should assume that all evolutionary processes operate at the population level. Again, the large amount of research on global diversity shows that researchers in such areas as systematics, macroevolution, macroecology, community ecology, and conservation biology hold other, less reductionistic views.

Dietl and Vermeij overlook the fact that our data did not just address diversity but also occurrence frequency, which we showed to capture the same temporal signals. Occurrence frequency is a product of ecological factors such as geographic range size, breadth of environmental distribution, and local abundance that are the focus of much research and presumably have some connection to evolution.

Dietl and Vermeij's main point is to assert that organisms do evolve through interactions, instead

[1]National Center for Ecological Analysis and Synthesis, University of California, Santa Barbara, CA 93101, USA. [2]Museum für Naturkunde, Humboldt-Universität, 10115 Berlin, Germany. [3]Institut für Paläontologie, Universität Würzburg, 97070 Würzburg, Germany. [4]School of Marine Biology and Aquaculture, James Cook University, Townsville 4811, Australia. [5]Department of Geology, Field Museum of Natural History, Chicago, IL 60605, USA.

*To whom correspondence should be addressed. E-mail: madin@nceas.ucsb.edu

of addressing our data, methods, or argumentation. This hypothesis is exactly what we tested and found not to be demonstrable at the scale that is amenable to proper time series analysis. Arguing that a hypothesis is untestable when it is contradicted does not provide evidence for it, and actually showing that the causal emergence it predicts is not very strong does provide evidence against it.

References and Notes

1. P. D. Roopnarine, K. D. Angielczyk, R. Hertog, *Science* **314**, 925 (2006); www.sciencemag.org/cgi/content/full/314/5801/925d.
2. G. P. Dietl, G. J. Vermeij, *Science* **314**, 925 (2006); www.sciencemag.org/cgi/content/full/314/5801/925e.
3. J. S. Madin *et al.*, *Science* **312**, 897 (2006).

14 June 2006; accepted 19 October 2006
10.1126/science.1131363

LANGUAGE

Are We Dancing Apes?

Joseph T. Devlin

Language is a universal skill in humans that develops even when children are raised in impoverished linguistic environments. In contrast, nonhuman primates—even when reared in the most supportive surroundings—appear unable to learn language beyond the level of a two- or three-year-old child. Identifying the evolutionary changes that underlie human language, however, has proved to be an extremely difficult problem. The anatomical changes to the supralaryngeal vocal tract that support language co-occurred with changes in brain structure, and language itself evolved over time, leading to a dynamic interplay between biology, function, and environment (*1*). To complicate matters, language apparently evolved only once and has left no fossil records.

Toward an Evolutionary Biology of Language

by Philip Lieberman

Harvard University Press, Cambridge, MA, 2006. 441 pp. $49.95, £32.95, €46.10. ISBN 0-674-02184-3.

In his *Toward an Evolutionary Biology of Language*, Philip Lieberman tackles this problem and explains how traces of protolinguistic ability present in a wide range of animals can guide an evolutionary account of language development. Lieberman (a cognitive scientist at Brown University) argues that the three crucial differences between humans and other species are a large vocabulary, a rapid (and robust) transmission system, and the ability to combine a finite set of words into a potentially infinite set of sentences. Critically, each of these is based on existing nonlinguistic abilities present in other species.

Although words are the basic building blocks of language, the ability to use words is not specific to humans. Vervet monkeys in the wild produce different alarm calls for specific predators. Like human words, these are not innate but learned, with young monkeys initially overgeneralizing before converging on the correct referent. In controlled environments, chimps have been taught much larger vocabularies. Two of the most successful, Washoe and Kanzi, have each learned to use roughly 150 to 200 words, which they can apply in novel ways. In contrast, typical adult speakers of English know 30,000 to 60,000 words, far more than the most precocious animals are able to learn. Even so, the mere fact that monkeys and apes can learn to associate abstract symbols with real-world referents suggests the existence of a basic vocabulary mechanism and provides evidence for a protolinguistic ability that was adapted in humans to enable the enormous expanse in our vocabularies.

Our ability to verbally communicate information rapidly and accurately offers a second difference between human languages and animal vocalizations. Humans are able to understand speech delivered at a rate of 20 to 30 basic speech sounds (or phonemes) per second, whereas we find even 10 to 15 nonspeech sounds per second produce a buzzing noise. This speed is made possible by adaptations in both production and comprehension mechanisms. We largely share with other species the basic vocal anatomy used to generate speech, and almost all phonetic distinctions that humans produce can be found elsewhere in the animal kingdom. Changes to the position and shape of our tongue, however, have enhanced our vocal communication by enabling us to generate more distinct vowel sounds that reduce ambiguity in the acoustic signal. Because these changes also increase the risk of choking on our food, the communicative advantages must outweigh the potential costs. Even so, the basic acoustic signal in speech retains considerable ambiguity, and Lieberman argues that this ambiguity forces listeners to use a mental model of the articulatory system to help understand speech. This internal model appears to be shared by other species, who use the information to determine the size of (and therefore their social relation to) animals they hear. Humans put this model to a novel use in decoding the acoustic transitions that define phonemes, thereby producing a faster data transmission rate than would otherwise be attainable. One obvious benefit is that rapid communication reduces the demands on working memory—preventing us from forgetting the beginning of a sentence before hearing its end.

CREDIT: JOE SUTLIFF

Lastly, language is only possible because a finite number of words can be combined into a potentially infinite number of sentences. According to the linguistic theories developed by Noam Chomsky, Steven Pinker, and others, this combinatorial power arises because people have a species-specific, innate knowledge of universal grammar, a mechanism for specifying the possible human linguistic structures (*2*). Lieberman, however, rejects this influential hypothesis, arguing instead for a "reiterative" mechanism that underlies the production of both linguistic and nonlinguistic sequences. By the author's account, the evolutionary antecedent to grammar was the ability to sequence complex actions and thoughts by means of a subcortical brain region, the basal ganglia. Dancing, Lieberman argues, uses a limited repertoire of movements to produce a variety of performances in much the same manner as words are combined into different sentences. In both cases, the basal ganglia play an important role in the sequencing. Indeed, the book's motto "I walk, run, and talk—therefore I am" captures the interplay between movement, thought, and speech that he stresses.

In my mind, Lieberman's reiterative hypothesis raises two difficult issues. First, not all sequences are created equal. Motor actions such as walking and dancing tend to have linear structure, whereas even simple sentences are based on a hierarchical structure. Consequently, sequencing in dance and language is likely to require fundamentally different mechanisms, and equating the two will be misleading. In other words, it is not sequencing, per se, that is important for language but the ability to produce and comprehend hierarchically structured sequences (*3*). It seems that European starlings (*Sturnus vulgaris*, a songbird) can learn to recognize hierarchical organized sequences (*4*), whereas cotton-top tamarins (*Saguinus oedipus*, a neotropical primate) cannot (*5*). Thus, the critical evolutionary antecedents to grammar

The reviewer is at the Oxford Centre for Functional Magnetic Resonance Imaging of the Brain, Department of Clinical Neurology, University of Oxford, Headley Way, Oxford OX3 9DU, UK. E-mail: devlin@fmrib.ox.ac.uk

may exist in the animal kingdom, but it is not clear that sequencing alone is sufficient.

The second difficult issue is that Lieberman's account places too strong an emphasis on the basal ganglia, to the exclusion of the cortex. In part, this may be due to his criticism of universal grammar. He claims that proponents of universal grammar equate dedicated language "modules" with localized cortical structures such as Broca's and Wernicke's areas, but I do not believe that either Chomsky or Pinker has actually made that claim. Although Lieberman demonstrates that neither region is dedicated to language, in the process he appears to go too far and discounts a substantial body of evidence for cortical involvement in language. Even if no cortical region is actually dedicated to language, many clearly contribute to it and, by most accounts, play more important roles than subcortical structures. Consequently, some discussion of these contributions would have helped to balance the focus on the basal ganglia. Nonetheless, Lieberman's emphasis on the basal ganglia highlights the fact that subcortical structures are undoubtedly an important, if underappreciated, component of neural language circuits and may provide an evolutionary link to our prelinguistic past.

Discussions of language tend to start from the assumption that it is a uniquely human trait without antecedent in the animal kingdom. *Toward an Evolutionary Biology of Language* forcefully challenges this assumption. Lieberman brings together a wide range of evidence from comparative anatomy, physiology, neurobiology, genetics, neuropsychology, and linguistics to illuminate the protolinguistic abilities in other species. Specific aspects of his arguments are certainly contentious, but his basic premise is compelling: Although the individual traits necessary for language can be found in other animals, it is the unique combination of these abilities in humans that yields language.

References

1. M. H. Christiansen, S. Kirby, *Trends Cogn. Sci.* **7**, 300 (2003).
2. N. Chomsky, *Aspects of the Theory of Syntax* (MIT Press, Cambridge, MA, 1965).
3. M. D. Hauser, N. Chomsky, W. T. Fitch, *Science* **298**, 1569 (2002).
4. T. Q. Gentner, K. M. Fenn, D. Margoliash, H. C. Nusbaum, *Nature* **440**, 1204 (2006).
5. W. T. Fitch, M. D. Hauser, *Science* **303**, 377 (2004).

10.1126/science.1132135

BEHAVIORAL ECOLOGY

An Honest and Deceitful Review

Katherine E. LeVan and Noah Wilson-Rich

These words are signals. Their sole purpose is to convey information to you, the receiver. But should you trust these words or view them skeptically?

With *The Evolution of Animal Communication: Reliability and Deception in Signaling Systems*, William Searcy and Stephen Nowicki provide a fascinating perspective on the honesty of signals in animal communication systems. Their contribution to the Princeton series Monographs in Behavior and Ecology is a timely addition to research on the evolution of animal signaling systems. Searcy (the University of Miami) and Nowicki (Duke University) offer a comprehensive yet concise review of what we currently know concerning signal reliability in animals, enriched with many in-depth examples.

The Evolution of Animal Communication
Reliability and Deception in Signaling Systems
by William A. Searcy and Stephen Nowicki
Princeton University Press, Princeton, NJ, 2005. 286 pp. $85, £55. ISBN 0-691-07094-6. Paper, $39.50, £26.95. ISBN 0-691-07095-4. Monographs in Behavior and Ecology.

Signaling at a nest. Studies of social communication in animals often use social insects such as the European paper wasp (*Polistes dominulus*).

The book starts strongly by explicitly setting forth necessary definitions (e.g., signal, reliable, deception) and by providing a detailed yet accessible explanation of biological signaling models. The useful introduction also presents a succinct historical overview of ideas concerning reliability and deceit in animal communication, which should prove valuable for students seeking to gain perspective on this sometimes highly contentious field.

In an innovative organizational scheme, three subsequent chapters consider signaling systems located at three positions along a continuum that ranges from overlapping to opposing evolutionary interests: "Signaling When Interests Overlap" focuses on communications between related individuals, "Signaling When Interests Diverge" considers signaling between the sexes, and "Signaling When Interests Oppose" concentrates on interchanges between competitors. The authors' account is strengthened by their use of a uniform framework across these chapters, each of which begins by reviewing theoretical models and then explores a few relevant signaling systems in detail. The reviews of the illustrative signaling systems are organized to consider several important questions: Do receivers respond to these signals? How reliably do these signals convey information? What costs do these signals incur? What evidence exists for deceptive use of signals? Each example is carefully reviewed and thoughtfully discussed. Searcy and Nowicki do an outstanding job of presenting evidence concisely yet accurately; they often include data figures reproduced from the original research papers. We especially appreciated the recurrent reminders of how difficult it can be to gauge what specific aspect of signaler quality is (or is not) reflected in a signal. Also, the authors give thorough consideration to the many potential categories of signal costs (including development, energy, and perform-

The reviewers are at the Department of Biology, Tufts University, Medford, MA 02155, USA. E-mail: noah.wilson_rich@tufts.edu

ance costs as well as costs imposed by third-party receivers).

At the outset, the authors defend their focus on communication within rather than between species, yet the chapter "Honesty and Deception in Communication Networks" convincingly demonstrates the importance of considering the broader social environment in which signaling occurs. The study of communication networks expands the scope of dyadic animal relations (i.e., parenting, mating, and aggression) in a way that includes eavesdroppers who act upon the signals meant for the primary receiver (*1*). These third-party receivers may exert additional selective pressures on signals and thus affect signal reliability at evolutionary equilibrium.

Arguably, the book's principal weakness lies in the limited range of examples the authors provide to illustrate in these four chapters, which are heavily biased toward birds. Contrary to the (possibly deceitful) cover illustrations, the book includes relatively few examples of signaling drawn from invertebrates, amphibians, and mammals. This emphasis is somewhat understandable because the authors' own research interests provide them with considerable expertise on avian signals, and it also reflects the fact that much research has been devoted to understanding the reliability of bird signals. However, the absence of insect signaling examples seems particularly unfortunate. For example, the exclusion of social insects (the epitome of signalers and receivers with overlapping interests) is puzzling. Furthermore, although Searcy and Nowicki discuss a wide variety of signaling modalities, they give little consideration to and no examples of chemical signals.

The Evolution of Animal Communication will serve as a wonderful reference for any researcher looking to understand what is currently known about the reliability of animal signals. In addition, it provides an accessible entry into a large and wide-ranging body of literature, usefully highlights the many gaps in our knowledge, and points out fruitful directions for future research. The book also provides an excellent basis for a seminar course at an advanced undergraduate or graduate level (*2*). Trust us.

References and Notes

1. P. McGregor, *Animal Communication Networks* (Cambridge Univ. Press, Cambridge, 2005).
2. The book formed the basis of a seminar course at Tufts University, and we thank the organizers, P. Starks and S. Lewis, and our fellow students for many insightful discussions.

10.1126/science.1135747

NOTA BENE: FILM

Some Noble Causes from Nobelists

Actor and filmmaker Turk Pipkin's independent film *Nobelity* opens with a question: How can we secure the future for the next generations? Beginning with images of his own children, Pipkin expands the picture to view children around the globe. The film presents nine recent Nobel laureates who discuss what they consider the major problems currently confronting humanity and the solutions that they propose. These contemporary geniuses obviously enjoyed the opportunity to present their opinions on a personal level, and proceeds from the film will help support particular projects (many of which were started by the laureates themselves) that work toward possible solutions. In some ways, the goals of the film are reminiscent of the Grand Challenges in Global Health enumerated by Harold Varmus (Medicine, 1989) and his colleagues [*Science* **302**, 398 (2003)]. But the film goes further: it challenges us to vocalize a need for change and take positive steps toward solutions.

Nobelity
by Turk Pipkin
Monterey Media, Thousand Oaks, CA, 2006. 84 minutes. DVD, $24.95. www.nobelitythemovie.com

Nine Nobelists. Sen, Maathai, Smalley, Rotblat, Tutu, Varmus, Zewail, Weinberg, and Williams.

While the film serves as a call to action, it also offers a personal glimpse of scientists as real people who want to solve problems facing us all. The laureates' opinions and concerns fall under various themes of decisions, challenges, disparities, change, knowledge, persistence, and peace. Steven Weinberg (Physics, 1979) starts off with a strong statement on climate change and global warming, noting that "the burden of proof should be not to prove that it is happening but that it isn't." Pipkin then takes the viewer to exotic locales and hometowns of the featured laureates. The physicist Ahmed Zewail (Chemistry, 1999) talks about topics ranging from his femtosecond research to using education to build understanding between cultures. Environmentalist Wangari Maathai (Peace, 2004) considers persistence, deforestation, and erosion. Varmus addresses disease and health disparities. Two of the laureates are no longer with us: Joseph Rotblat (Peace, 1995) discusses the need for clean water, and Richard Smalley (Chemistry, 1996) argues for nuclear disarmament. In light of current events—the technological boom in India side by side with a growing water deficit and the issue of the nuclear capabilities of North Korea and Iran—their statements remind us of the valuable wealth of knowledge they left.

Amartya Sen (Economics, 1998) highlights the need to eliminate hunger, concerns over population, and the advantages of offering experiential education. Jody Williams (Peace, 1997) calls for a ban on land mines. Their statements are thought provoking, but tend to reinforce the film's mood as more of an ethnographic documentary of scientists' views of the state of the planet than an exhortation to social or political change. The movie ends with a moving summation on our approach to life by Desmond Tutu (Peace, 1984): "The sea is actually made up of drops of water. What you do, where you are, is of significance."

Documentaries have become a fashionable venue for individuals and groups to advocate favored agendas. At first, it may seem that *Nobelity* is following the same popular formula. But the sincerity of the Nobel laureates makes this film a uniquely intimate though sobering effort by these individuals to express themselves outside of research labs or scientific journals. **–ANITA C. WYNN**

10.1126/science.1136769

CREDIT: MONTEREY VIDEO

PUBLIC HEALTH

Next Flu Pandemic: What to Do Until the Vaccine Arrives?

Most scientists consider another influenza pandemic inevitable, but there is little information on how best to protect the public before a vaccine can be made available.

Stephen S. Morse,[1]* Richard L. Garwin,[2] Paula J. Olsiewski[3]

Experience indicates we are overdue for another influenza pandemic (*1*, *2*). Unless effective action is taken now, we will be in dire straits. Immunization remains the cornerstone of our strategy, with antiviral agents as a backup (*3*, *4*), but producing and distributing a vaccine will take at least 4 to 6 months currently (*5*). In the meantime, our main defenses will be nonpharmacological interventions, such as hand washing, "respiratory etiquette," face masks, school closure, and social distancing or isolation (*6*, *7*). These are ironically similar to the measures used in 1918 to combat the greatest of all known influenza pandemics (*8*, *9*).

Recent attempts to identify the most effective nonpharmacological interventions have revealed that these measures have a thin science base (*6*, *7*, *10*–*13*). For example, it is uncertain whether influenza transmission from person to person is primarily by large droplets or by fine particles. Although this may seem a specialist issue, it has a direct bearing on how far apart people should position themselves to prevent infection and on whether relatively inexpensive face masks might be useful. Recent results in the guinea pig (*14*) indicated that transmission of influenza could occur even when cages were kept ~3 feet apart, which contradicts conventional wisdom. The results should be confirmed in other models.

Another aspect of transmission that we don't understand is why, when the number of secondary infections arising from each infected individual (R_0) is relatively low (*15*), breaking the transmission chain by nonpharmacological measures has proved so challenging. $R_0 < 1$ would imply that transmission is no longer self-sustaining.

Many of our assumptions are based on analogies with other respiratory infections, such as rhinoviruses, which are generally more stable than influenza viruses and differ in other physical properties. These analogies are useful, but should be interpreted with caution. Many rhinovirus infections can be transmitted via contamination on hands, but there is no evidence to indicate that this transmission mechanism is important for influenza. Although there are excellent literature reviews (*6*, *7*), there are no readily accessible compendia of best practices or even comprehensive databases of community epidemiologic data, which might help to design the most effective interventions.

Community studies and clinical trials in humans are needed. Seasonal influenza provides regular real-world opportunities to fill some of the enormous gaps in our knowledge. Availability of attenuated live influenza vaccines (e.g., FluMist) may allow transmission and intervention studies to be done safely under more carefully controlled conditions than have previously been possible.

Also often neglected are protective measures that fall between individual protection and the whole population—the "excluded middle," such as buildings, facilities, and smaller areas, including work places and homes. Examples might include improved air-handling systems, room-size fans, portable air-filtration units, or physical barriers such as room dividers and doors. Industrial hygienists and engineers have considerable accumulated expertise that could be more regularly applied to protecting the built environment from pandemics. Lessons learned from protecting buildings or large spaces from bioterrorist agents (*17*) are also relevant. Protection should be included in new construction and retrofitted in older spaces (*17*), from work spaces to buildings to indoor public areas.

Individuals must have good information on which to base choices. Guidelines remain a menu of general options with little specific advice. Some modeling results (*18*) suggest that simple measures could be quite effective. Although many of these suggestions seem just common sense (such as keeping a sick family member in a separate room with a closed door), there is no systematic evaluation of best practices for "home infection control." A starting point might be modifying experience from health-care settings for the home.

On the positive side, there has been increasing interest in nonpharmacological strategies and in filling the data gaps in epidemiology and transmission (*6*, *7*, *10*–*13*). The Centers for Disease Control and Prevention (CDC) recently awarded grants to study nonpharmacological interventions in community settings. Although a commendable start, the CDC program so far represents $5.2 million in a total proposed pandemic influenza budget of $7.1 billion. The National Institute of Allergy and Infectious Diseases (NIAID) may also include related areas in their funding. We should systematically address knowledge gaps now during upcoming flu seasons, rather than wait to empirically test measures ad hoc when the next pandemic is upon us.

[1]Department of Epidemiology and Center for Public Health Preparedness (CPHP) of the National Center for Disaster Preparedness (NCDP), Mailman School of Public Health, Columbia University, New York, NY 10032, USA. [2]IBM Research Laboratories, Yorktown Heights, NY 10598, USA. [3]Alfred P. Sloan Foundation, New York, NY 10111, USA.

*Author for correspondence. E-mail: ssm20@columbia.edu

References and Notes

1. W. P. Glezen, *Epidemiol. Rev*. **18**, 64 (2003).
2. E. D. Kilbourne, *Emerg. Infect. Dis.* **12**, 9 (2006).
3. *National Strategy for Pandemic Influenza* (Homeland Security Council and Department of Health and Human Services, November 2005; available at: www.pandemicflu.gov/).
4. A. S. Monto, *Emerg. Infect. Dis.* **12**, 55 (2006).
5. Institute of Medicine, *Emerging Infections. Microbial Threats to Health in the United States*, J. Lederberg, R. E. Shope, S. C. Oaks Jr., Eds. (National Academy Press, Washington, DC, 1992), pp. 156–157.
6. D. M. Bell *et al*., *Emerg. Infect. Dis.* **12**, 81 (2006).
7. D. M. Bell *et al*., *Emerg. Infect. Dis*.**12**, 88 (2006).
8. A. W. Crosby, *America's Forgotten Pandemic: The Influenza of 1918* (Cambridge Univ. Press, New York, 1989).
9. J. M. Barry, *The Great Influenza* (Viking Penguin, New York, 2004).
10. Institute of Medicine Committee on the Development of Reusable Facemasks for Use During an Influenza Pandemic, *Reusability of Facemasks During an Influenza Pandemic: Facing the Flu* (National Academies Press, Washington, DC, 2006).
11. J. E. Aledort *et al.*, *Non-Pharmacological Public Health Interventions for Pandemic Influenza: Proceedings of an Expert Panel Meeting* (RAND Health Working Paper WR-408-DHHS, 2006).
12. R. Tellier, *Emerg. Infect.* Dis. **12**, 1657 (2006).
13. The "Workshop on personal and workplace protective measures for pandemic influenza," Mailman School of Public Health, Columbia University, and Alfred P. Sloan Foundation, New York, NY, 5 and 6 June 2006.
14. A. C. Lowen *et al.*, *Proc. Natl. Acad. Sci. U.S.A.* **103**, 9988 (2006).
15. R_0 is estimated at about 1.8 to 2 even for the 1918 pandemic (*14*).
16. C. E. Mills, J. M. Robins, M. Lipsitch, *Nature* **432**, 904 (2004).
17. P. J. Hitchcock *et al*., *Biosecur. Bioterror.* **4**, 41 (2006).
18. T. C. Germann, K. Kadau, I. M. Longini Jr., C. A. Macken, *Proc. Natl. Acad. Sci. U.S.A.* **103**, 5935 (2006).
19. Supported by a grant from the Alfred P. Sloan Foundation. S.S.M. is also supported by CDC cooperative agreement U90/CCU224241 (Centers for Public Health Preparedness), by the Arts and Letters Foundation, and by cooperative agreement 5U54AI057158-02 (Northeast Biodefense Center Research Center of Excellence) from NIAID, NIH.

10.1126/science.1135823

ANTHROPOLOGY

A Tool for All Seasons

Stanley H. Ambrose

Laser ablation carbon isotope analysis of robust-australopithecine teeth provides insights into seasonal variations in ancestral diets, while minimizing damage to precious fossils.

Seasonal variations in temperature, rainfall, and food availability drive many animals to hibernate or migrate. Animals that are tethered to their home ranges and remain active in all seasons may need flexible adaptive strategies for survival, especially in arid African savannas, where seasonal and annual rainfall can vary widely. About 2.4 to 1.4 million years ago, our earliest stone tool–making ancestors, *Homo habilis* and *H. erectus*, shared African savannas with their close relatives, commonly referred to as "robust" australopithecines or *Paranthropus* species (*1*). How variable were their environments? How much did their diets overlap in different seasons? And how did these two bipedal hominins manage to coexist for 1 million years?

Enhanced online at www.sciencemag.org/cgi/content/full/314/5801/930

On page 980 of this issue, Sponheimer *et al.* (*2*) document the seasonal variation in diet and climate of four robust australopithecines from Swartkrans Cave in South Africa. The authors use laser ablation of tooth enamel—a method that causes minimal damage to the precious fossils—followed by advanced methods of isotope analysis. They are literally blazing a new trail to answers to fundamental questions about early hominin paleoecology and evolution.

With their huge molar teeth and massive jaw muscles, robust australopithecines are considered dietary specialists that fed mainly on small, hard, tough, fibrous plant foods (see the figure). Their extinction between 1.0 and 1.4 million years ago is often attributed to their low-nutrient, high-fiber diets. However, systematic assessments of the cranial and dental anatomy (*1*) and dental microwear (*3*) suggest that their diets were less specialized than previously thought and more similar to those of their ancestors and hominin competitors.

Dietary niche separation between closely related species is usually greatest when resources are scarce. For example, chimpanzees and lowland gorillas that live in the same area eat similar amounts of fruit for most of the year, but during the leanest season, gorillas rely entirely on herbaceous vegetation (*4*). The powerful teeth and jaws of *Paranthropus* (see the figure) may have been essential for survival only when they resorted to tough "fallback" foods to mitigate competition with *Homo*.

How can stable-isotope variations in teeth provide insight into seasonality in diet and climate? The answer lies in the different $^{13}C/^{12}C$ ratios of different types of plants (*5*). Tropical grasses (and a few herbaceous broadleaf plants) fix atmospheric CO_2 using the C_4 photosynthetic pathway; these plants have high $^{13}C/^{12}C$ ratios. Conversely, most broadleaf plants, including trees, shrubs, and herbs, use the C_3 pathway and have low $^{13}C/^{12}C$ ratios. The isotope ratio of the diet controls that of the consumer, such that grazing (grass-eating) and browsing (broadleaf-eating) herbivores—and the carnivores that prey on them—preserve the isotopic difference at the base of the food web. The carbon-isotope ratios of mixed feeders reflect the proportions of C_3 and C_4 plants in their diets.

Oxygen-isotope ratios can also shed light on diet and climate. The $^{18}O/^{16}O$ ratio of surface water increases with temperature and evaporation and with low humidity. This "enrichment" is amplified in leaf water, which often satisfies most of the water requirements of browsing herbivores.

Tooth enamel exhibits 6- to 12-day growth layers, whose edges are marked by tiny ridges (perikymata) at the tooth surfaces (*6*). Perikymata counts show that formation times of larger mammal crowns usually exceed 1 year. Although time averaging during a few months of enamel maturation mutes short-term variations in the isotopic composition of growth increments, enamel preserves an excellent record of seasonal chemical and isotopic variations (*7*).

Oxygen- and carbon-isotope ratios of tooth

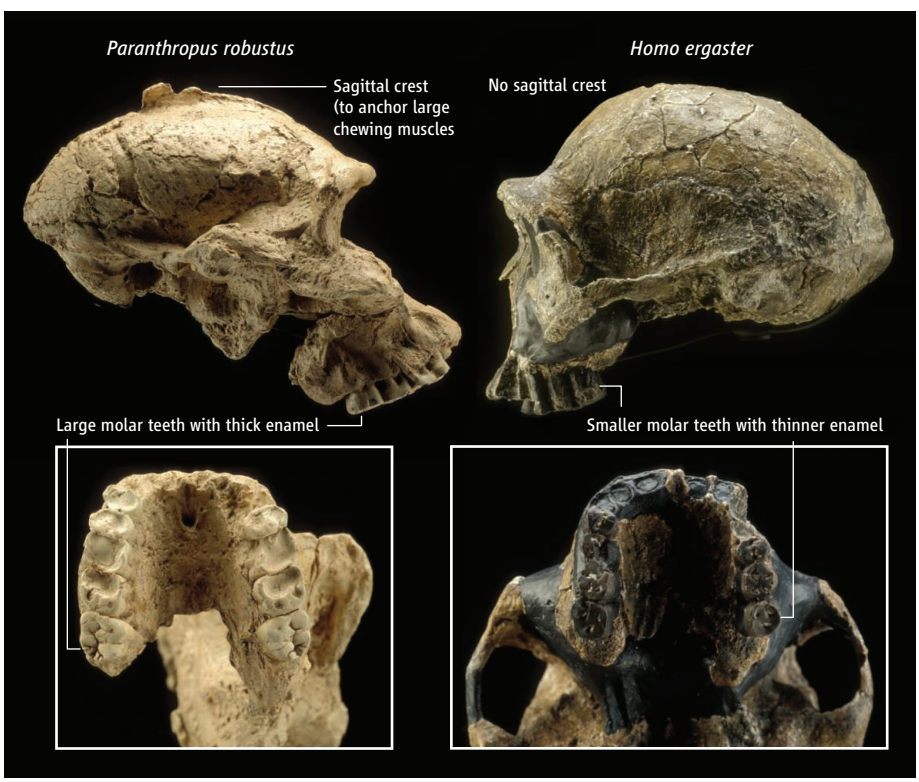

Diet and morphology. Robust australopithecines, like this *Paranthropus robustus* skull from Swartkrans Cave (**left**, specimen SK-46), were well adapted to eating tough fibrous plant foods in southern African savannas. Its bony sagittal crest anchored powerful chewing muscles, and the thick enamel of its massive molar teeth preserves an isotopic record of seasonal variations in diet and climate. *Paranthropus* shared the savanna with early *Homo* species, possibly *H. ergaster* (**right**, specimen ER-3733, from Kenya), whose smaller jaw muscles and smaller molar teeth reflect a softer diet that probably included more ripe fruit and meat.

CREDIT: THE HUMAN ORIGINS PROGRAM/SMITHSONIAN INSTITUTION

The author is in the Department of Anthropology, University of Illinois, Urbana, IL 61801, USA. E-mail: ambrose@uiuc.edu

enamel can be analyzed by conventional mass spectrometry with samples as small as 500 μg. However, seasonality analysis requires drilling a series of deep, ~1-mm-wide grooves parallel to the mineralization/growth plane. The geometry of mineralization does not closely follow that of the incremental growth structures (*7*). Deep drilling may crosscut enamel formed at different times, which could decrease the chronological resolution of seasonal isotopic variation. Moreover, museum curators are often reluctant to allow researchers to drill deep grooves into rare hominin teeth.

In contrast to conventional methods, the laser ablation technique used by Sponheimer *et al.* barely penetrates the enamel surface of an area of less than 0.5 mm^2 and is thus nearly nondestructive (*2*). Laser ablation also avoids the problem of time averaging in large drilled grooves. Moreover, perikymata can be counted, providing a good estimate of the minimum time interval sampled and of the duration of tooth formation.

The *Paranthropus* teeth studied by Sponheimer *et al.* show interesting patterns of seasonal variation in diet and climate. All have the isotopic composition of mixed feeders, and two show at least ~40% variation in the proportions of C_3- and C_4-based resources over 1 year. One individual had a predominantly C_3-based diet and foraged in a cooler, more humid environment; it may have formed its tooth in a very wet year. The others ate more C_4-based foods in a warmer, drier environment. Their average carbon-isotope ratios are similar to those of adaptively versatile savanna baboons (*2*). Analyses of seasonal variation in teeth of modern and fossil baboons and of other hominin species are necessary to evaluate dietary specialization in *Paranthropus* and niche overlap with other hominin species.

High-resolution isotopic records of seasonal variation can provide important insights into the characteristics of annual climate variation during periods of climatic and evolutionary change. For example, the transition from the warm Eocene to the cold Oligocene, 34 million years ago, is marked by a massive wave of marine animal extinctions. Most climatic proxies indicate a drop in ocean temperatures by ~1°C. However, oxygen isotopes from fish otoliths have revealed a substantial increase in the amplitude of intra-annual temperature change, including a decrease in winter temperatures by ~4°C (*8*).

Were changes in patterns of seasonality important for human evolution? Highly variable, often cool and dry climate episodes characterized the end of the Miocene (5 to 7 million years ago) (*9*), when the human, chimpanzee, and gorilla lineages originated. Did greater seasonal variation play a role in their divergence? From 2.6 to 1.0 million years ago, drier, cooler climates predominated, and the lengths of the climate cycles increased from ~21,000 to ~41,000 years. *Homo* and robust australopithecines appeared around 2.5 million years ago. Foley (*10*) has proposed that their divergence and coexistence were achieved by different strategies of adaptation to increased seasonality. More pronounced glacial/interglacial cycles of ~100,000 years characterize the past million years. Potts (*11*) has proposed that the increasing amplitude of climate change through time, including greater seasonal and interannual variation, is a prime mover for the trend of increasing human adaptability.

Seasonality hypotheses for human evolution can be tested most directly by isotopic analysis of fossil teeth. Greater seasonality should result in higher variance in isotope ratios within and between teeth in a fossil assemblage. However, analysis of fossils should be preceded by compilation of a comprehensive modern comparative database of a wide range of species from different climates and environments.

Laser ablation can be a powerful and versatile technique for reconstructing seasonal and interannual variation in diet and climate, and the structure of animal communities. The results reported by Sponheimer *et al.* should persuade museum curators to permit comprehensive surveys of isotopic variations within fossil teeth.

References

1. B. Wood, D. Strait, *J. Hum. Evol.* **46**, 119 (2004).
2. M. Sponheimer *et al.*, *Science* **314**, 980 (2006).
3. R. S. Scott et al., *Nature* **436**, 693 (2005).
4. C. B. Stanford, J. B. Nkurunungi, *Int. J. Primatol.* **24**, 901 (2003).
5. T. E. Dawson, *Annu. Rev. Ecol. Syst.* **33**, 507 (2002).
6. M. C. Dean, *Proc. R. Soc. B* **273**, 2799 (2006).
7. M. Balasse, *Int. J. Osteoarch.* **13**, 3 (2003).
8. L. C. Ivany, W. P. Patterson, K. C. Lohman, *Nature* **407**, 887 (2000).
9. P. B. deMenocal, J. Bloemendal, in *Paleoclimate and Evolution, with Emphasis on Human Origins*, E. S. Vrba, Ed. (Yale Univ. Press, New Haven, CT, 1996), pp. 263–288.
10. R. Foley, *Another Unique Species* (Longman Scientific and Technical, Essex, UK, 1987).
11. R. Potts, *Yrbk. Phys. Anthropol.* **41**, 93 (1998).

10.1126/science.1135741

MICROBIOLOGY

Bacterial Bushwacking Through a Microtubule Jungle

Jean-Pierre Gorvel

The cellular cytoskeleton represents an obstacle to the movement of bacteria inside an infected cell. Certain bacteria have developed virulence factors to remove or sabotage it.

Our view of the cell's cytoplasm has come a long way. Once considered static "free space" between the nucleus and plasma membrane, it is now known to be a highly dynamic cellular entity with limited space for free movement. It is a dense, organized, tightly regulated, and dynamic network of organelles, cytoskeleton (including microtubules, actin, and intermediate filaments), and vesicles that shuttle between organelles. Yet, some pathogenic bacteria move quite efficiently through this cytoplasmic jungle, invading one cell to the next. On page 985 of this issue, Yoshida *et al.* (*1*) report that *Shigella*, the bacteria responsible for dysentary, hacks its way through microtubules by wielding a tubulin-specific protease.

The author is at Centre d'Immunologie INSERM-CNRS-Université de la Méditerranée Parc Scientifique de Luminy Case 906, 13288 Marseille Cedex 9, France.

Cytoplasm-invading pathogens such as *Shigella flexneri* (*2*), *Listeria monocytogenes* (*3*), *Mycobacterium marinum* (*4*), *Rickettsia prowasekii* (*5*), and *Burkholderia pseudomallei* (*6*) recruit and polymerize actin at one pole of the bacterium to give them a propulsive force to move through the host cell's cytoplasm and into adjacent host cells. In the course of *Shigella* infection, the outer membrane protein VirG interacts with host cell proteins CDC42 and neural Wiskott-Aldrich syndrome protein (N-WASP). This leads to the recruitment of the Arp2/3 complex at one pole of the bacterium, which stimulates the local formation of an actin tail that supplies a propulsive force and intracellular motion (*7*).

Despite this powerful propulsive device, movements of pathogenic bacteria are influenced by other cytoskeletal elements and organelles. In the case of *Listeria*, the bacterium recruits stathmin, a microtubule-sequestering protein of the host cell, presumably to destabi-

lize microtubules, thus allowing bacterial movement in the cytoplasm (*8*). The *Shigella* VirA virulence factor is secreted into the cytoplasm by a "syringe and needle" mechanism called a type III secretion system, designed to translocate virulence factors from the bacterial cytoplasm to the host cell cytoplasm. VirA creates a tunnel inside the host cell cytoplasm by breaking down the microtubule infrastructure (see the figure). This not only facilitates a bacterium's movement through the cytoplasm but also helps other bacteria move faster because they are able to follow the same path. Yoshida *et al.* show that VirA is a protease that specifically cleaves alpha-tubulin, a major component of microtubules. *Shigella* mutants lacking VirA not only are unable to move inside host cell cytoplasm but also are deficient in causing bacillary dysentery in a mouse model of infection. In addition, mutants that express an inactive form of VirA protease are also attenuated, demonstrating that specific enyzmatic activity acting on microtubules is absolutely required for *Shigella* virulence. A main question that remains to be answered is the half-life of the *Shigella*-induced tunnels, because microtubules are dynamic structures that regenerate quickly (as fast as 0.18 μm/min).

In other pathogenic microorganisms, proteases play an important role in virulence by acting on the host cell's actin filament rearrangements. Pathogenic *Yersinia* species evade the innate cellular immune response by injecting Yops (*Yersinia* outer proteins) into host cells through a type III secretion system. Among Yops, YopT inactivates RhoA, a host

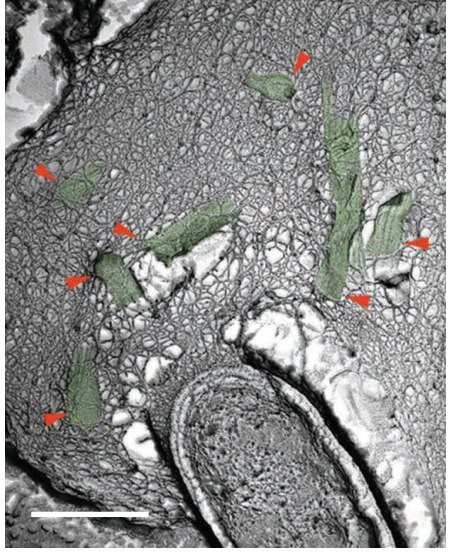

Felling the infrastructure. Freeze-fracture electron micrograph image of a mammalian cell infected with *Shigella*. The bacterium breaks down microtubules (green, red arrowheads) during the course of infection (*1*). Scale bar, 0.2 μm.

cell guanosine triphosphatase. By cleaving RhoA, it prevents the protein's function in regulating the formation of actin stress fibers (*9*).

Although little is known about early stages of the replication cycle of retroviruses, viral proteases appear to be critical. After entry into a cell's cytoplasm, wild-type foamy viruses as well as mutant forms that are defective in an aspartic protease travel along microtubules toward the microtubule-organizing center, the structure from which microtubules radiate. However, whereas the subsequent import of the wild-type retroviral genome and the nucleocapsid protein Gag into the host cell nucleus is observed, incoming nucleocapsids and genome from mutant viruses remain at the microtubule organizing center. This correlates with the detection, only for the wild-type virus, of a specific viral protease–dependent Gag cleavage product early after infection, demonstrating that cleavage of Gag protein by a viral protease, leading to viral core disassembly, is absolutely required for release from microtubules and productive infection (*10*).

Because we are now facing a lack of new antimicrobial molecules, especially of antibiotics, we need further insight into how a microorganism's effector molecules interact with host molecules to usurp host cell function. High-throughput screening chemical libraries has identified small, easy-to-make reagents that can alter or enhance biochemical properties of microbial enzymes, such as inhibitors of the CagA adenosine triphosphatase from *Helicobacter pylori* (*11*) or searching for virulence inhibitors against *Chlamydia pneumoniae* (*12*). Perhaps VirA is such a target.

References

1. S. Yoshida *et al.*, *Science* **314**, 985 (2006).
2. S. Makino, C. Sasakawa, K. Kamata, M. Yoshikawa, *Cell* **46**, 551 (1986).
3. C. Kocks *et al.*, *Cell* **68**, 521 (1992).
4. L. M. Stamm *et al.*, *J. Exp. Med.* **198**, 1361 (2003).
5. E. Gouin *et al.*, *Nature* **427**, 457 (2004).
6. K. Breitbach *et al.*, *Cell Microbiol.* **5**, 385 (2003).
7. C. Egile *et al.*, *J. Cell Biol.* **146**, 1319 (1999).
8. T. Pfeuffer, W. Goebel, J. Laubinger, M. Bachmann, M. Kuhn, *Cell Microbiol.* **2**, 101 (2000).
9. M. Aepfelbacher, R. Zumbihl, J. Heesemann, *Curr. Top. Microbiol. Immunol.* **291**, 167 (2005).
10. J. Lehmann-Che *et al.*, *J. Virol.* **79**, 9244 (2005).
11. M. Hilleringmann *et al.*, *Microbiology* **152**, 2919 (2006).
12. J. K. Alvesalo *et al.*, *J. Med. Chem.* **49**, 2353 (2006).

13.1126/science.1135742

ECOLOGY

A Starving Majority Deep Beneath the Seafloor

The rocks and sediments beneath the seafloor may harbor most of Earth's microorganisms. Molecular approaches are beginning to provide clues regarding the energy sources fueling their metabolic activity.

Bo Barker Jørgensen and Steven D'Hondt

Over the past 20 years, scientific drilling into sediments and basaltic crust all over the world ocean has revealed the omnipresence of microscopic life deep beneath the seafloor. Diverse communities of prokaryotic cells have been discovered in sediments and rock reaching a subsurface depth of 1 km. Most of these microorganisms have no cultured or known relatives in the surface world and are still only characterized by the genetic code of their DNA. Recent studies (*1*–*4*) have shed light on the ways in which they differ from microorganisms in the surface world and on the energy sources that support life in this buried ecosystem.

About 20 years ago, R. John Parkes and Barry Cragg started to systematically enumerate microorganisms in deep cores (*5*). Much later, rigorous contamination tests performed on the drill ship (*6*) showed that the cells detected were indeed indigenous to the deep subsurface. The cell counts were used for a bold extrapolation to the global ocean floor. The astonishing conclusion was that this "unseen majority" of microorganisms accounts for 55 to 85% of Earth's prokaryotic biomass and about 30% of the total living biomass (*7*).

The first drilling expedition focused entirely on deep biosphere exploration was launched in 2002 by the Ocean Drilling Program (ODP, Leg 201) (*1*). The target was the eastern tropical Pacific, with sites ranging from the continental shelf to ocean depths of 5000 m. By drilling through the seafloor and—at open-ocean sites—down to

B. B. Jørgensen is at the Max Planck Institute for Marine Microbiology, 28359 Bremen, Germany. E-mail: bjoergen@mpi-bremen.de S. D'Hondt is at the Graduate School of Oceanography, University of Rhode Island, Narragansett, RI 02882, USA. E-mail: dhondt@gso.uri.edu

the basaltic crust, sediments with ages up to 35 million years old could be sampled (*8*).

At all sites, prokaryotic cells (bacteria and archaea) were detected below the seafloor. Their numbers dropped from more than 10^8 cm^{-3} at the sediment surface to less than 10^6 cm^{-3} just above the ocean crust, with an average density much greater than in the ocean above. Occasional high cell numbers (up to 10^{10} cm^{-3}) coincided with sediment horizons in which more energy was available from counterdiffusing methane and sulfate (*9*).

These large population sizes remain the greatest mystery of the deep biosphere. Although marine sediments harbor Earth's largest reactive carbon pool, the organic matter becomes increasingly unreactive with depth and age and would seem to be practically inaccessible for microorganisms several million years after its burial. How, then, can there be sufficient energy for all these organisms to metabolize and grow?

The metabolic activity of the subsurface populations can be calculated by transport-reaction modeling of pore water solutes that are consumed or excreted by the microorganisms. For example, the mean metabolic activity per cell can be estimated by comparing the bacterial numbers and the predominant bacterial energy metabolism, such as sulfate respiration. For the eastern Pacific seabed, the mean sulfate respiration is 10^{-18} mol per cell per year (*8*, *10*). Because microbial cells must metabolize a certain minimum amount of substrate before they can double their cell size and divide into two daughter cells, their minimum doubling time can also be calculated. On the basis of this calculation, the mean generation time of deep subseafloor microorganisms is more than 1000 years.

This extremely slow growth cannot be reconciled with our understanding of the minimum energy requirements for life. All actively growing organisms must keep their enzymatic machinery going above a critical level to maintain vital cell functions such as replacement of degraded enzymes, repair of DNA damaged by high-energy radiation from natural radionuclides, and, presumably, the maintenance of an electrochemical gradient across the cell membrane (*11*).

A possible explanation for the low apparent rates of deep subsurface metabolism could be that most subseafloor cells are not active but dormant or even dead. However, when a highly sensitive fluorescence technique (catalyzed reporter deposition–fluorescence in situ hybridization or CARD-FISH) was used to detect the presence of ribosomes—a component of all living and active cells that is rapidly degraded upon their death—the results showed that many of the subsurface cells were alive (*12*).

The identity and physiological state of the inhabitants of the deep subsurface are now being elucidated with the powerful toolbox of DNA-, RNA-, and biomarker-based techniques. DNA encoding for 16*S* ribosomal RNA (a key gene for the phylogenetic identification of prokaryotic organisms) extracted from sediments provides thousands of genetic codes that reveal novel lineages of microbial life. Most of the genetic types belong to groups that have no cultured relatives; they are currently classified under provisional names such as "Japan Sea 1 Candidate Group" (bacteria) or "Marine Crenarchaeotic Group I" (archaea) or, even more exotic, "South African Gold Mine Euryarchaeotic Group" (*2*).

The physiology and potential function of these groups in the deep biosphere remain totally obscure, however, and their environment provides little clue as to their physiology. Future genomic research will reveal how 16*S* genes are coupled with key functional genes in the same genome, thereby relating identity and function. Quantitative analyses of intact polar lipids from cell membranes can also be used to identify the active populations of microorganisms (*3*). To date, however, approaches based on DNA, RNA, and biomarkers have provided contradictory conclusions about even the basic question of whether bacteria or archaea dominate the deep biosphere (*3*, *12*, *13*).

A crucial problem is the extremely low energy flux per cell in the deep subsurface. The search for additional energy sources has focused on molecular hydrogen (H_2), which is generated by chemical alterations in young basaltic crust along the mid-oceanic ridges (*14*). However, most of the seabed lies on old, crack-permeable crust, in which the potential oxidants for H_2 (such as oxygen or nitrate) seem to persist long enough to preclude a substantial H_2 supply (*1*). Another possible source of H_2 may come from the decay of natural radionuclides of potassium, thorium, or uranium in the sediments; energy released by this decay dissociates water molecules into free radicals and molecules such as H_2. Hence, this nuclear energy is not only destructive to microbial cells but may also support their metabolic activity.

Lin *et al*. (*15*) have estimated the radiolytic H_2 production rates for a sedimentary basin to be on the order of 10^{-8} nM H_2 s^{-1}. For comparison, sulfate reduction rates fueled by buried organic carbon in subsurface sediments of the eastern tropical Pacific Ocean correspond to H_2 consumption rates of 3 to 60 × 10^{-8} nM H_2 s^{-1} (*1*, *8*). These numbers suggest that water radiolysis

Fresh material from the deep subsurface. A fresh sediment core has just been retrieved from the deep subseafloor in the eastern tropical Pacific Ocean at a water depth of 5000 m during Leg 201 of the Ocean Drilling Program. The 10-m-long core is carried down from the drill deck for microbiological and geochemical sampling on board the drilling vessel JOIDES Resolution. The staff wear gas masks to avoid inhaling toxic hydrogen sulfide and explosive gas hydrate; both are metabolic products of the deep biosphere.

CREDIT: PHOTOGRAPH BY ODP LEG 201 ONBOARD SCIENTIFIC PARTY

could be the principal source of microbial energy in deep-sea sediments that are much more depleted in organic matter than the eastern tropical Pacific sites discussed here. Such sediments with extremely low organic carbon flux cover large regions of the ocean floor, for example, in the central North and South Pacific Ocean.

This potential energy source is particularly interesting in that it is independent of biomass production by photosynthesis. It does not even require an external oxidant. Water radiolysis produces not only H_2 but also oxidants such as H_2O_2 or O_2, which may be directly used for the energy-generating reoxidation of H_2. Although the rich communities at deep-sea hydrothermal vents also live on inorganic chemical energy, for example, from H_2 or H_2S, they depend on O_2 produced from photosynthesis. An extreme low-energy subsurface biosphere driven by radioactivity would be different from all other ecosystems on Earth: It could proceed on a planet without surface life and solar energy.

References

1. S. D'Hondt *et al.*, *Science* **306**, 2216 (2004).
2. F. Inagaki *et al.*, *Proc. Natl. Acad. Sci. U.S.A.* **103**, 2815 (2006).
3. J. F. Biddle *et al.*, *Proc. Natl. Acad. Sci. U.S.A.* **103**, 3846 (2006).
4. J. P. Amend, A. Teske, *Palaeogeogr. Palaeoclimatol. Palaeoecol.* **219**, 131 (2005).
5. R. J. Parkes, B. A. Cragg, P. Wellsbury, *Hydrogeol. J.* **8**, 11 (2000).
6. D. C. Smith *et al.*, *Geomicrobiol. J.* **17**, 207 (2000).
7. W. B. Whitman, D. C. Coleman, W. J. Wiebe, *Proc. Natl. Acad. Sci. U.S.A.* **95**, 6578 (1998).
8. B. B. Jørgensen, S. L. D'Hondt, D. J. Miller, in *Proceedings of the Ocean Drilling Program, Volume 201, Scientific Results,* B. B. Jørgensen *et al.*, Eds. (ODP, College Station, TX, 2006), pp. 1–45 (www-odp.tamu.edu/publications/201_SR/201sr.htm).
9. R. J. Parkes *et al.*, *Nature* **436**, 390 (2005).
10. S. D'Hondt, S. Rutherford, A. J. Spivack, *Science* **295**, 2067 (2002).
11. P. Price, T. Sowers, *Proc. Natl. Acad. Sci. U.S.A.* **101**, 4631 (2004).
12. A. Schippers *et al.*, *Nature* **433**, 861 (2005).
13. L. Mauclaire *et al.*, *Geobiology* **2**, 217 (2004).
14. N. G. Holm, J. L. Charlou, *Earth Planet. Sci. Lett.* **191**, 1 (2001).
15. L.-H. Lin *et al.*, *Geochim. Cosmochim. Acta* **69**, 893 (2005).

10.1126/science.1133796

GEOCHEMISTRY

How Melted Rock Migrates

Magma flows through rock by different mechanisms than previously thought, which may cause a reevaluation of how data from Earth's mantle is interpreted.

Marian Holness

For most nongeologists, the idea of liquids moving through solid rock is a strange one. But liquids of one sort or another are thought to be ubiquitous in the Earth. There are the familiar hydrothermal fluids, dominated by water, which occur in the very shallow crust (the Old Faithful geyser in Yellowstone National Park in the United States is a dramatic example). But in the deeper parts of the Earth there are hydrous and carbon dioxide (CO_2) liquids formed by the heating of rocks as the minerals containing these molecules break down. At still higher temperatures, the rocks start to melt, generating a silicate liquid. The how and why of liquid flow through rocks is a very important problem in geology. This is because movement of liquid within the Earth is one of the primary ways that mass moves around and results in so-called geochemical differentiation. It was the movement of iron-rich liquids down to the center of the Earth that formed the core, for example. On page 970 of this issue, Schiano *et al.* (*1*) report new insights into flow mechanisms and the effects of fluid flow on the rock record .

Our understanding of what happens in the deep Earth is limited by our inability to get down there for a direct look. We are therefore reliant on three different sources of information: remote probing by geophysical methods such as seismic imaging; examining rock fragments that have been ripped off conduit walls and brought up to the surface by erupting lava; and laboratory experiments. All have their limitations. Geophysics can give hints as to what might be happening on a long length-scale, but can say very little about what may be happening on the grain scale. The fragmentary samples of the deep Earth that emerge with erupting lava flows have been separated from their original surroundings, and so the original spatial context is lost. And experiments are hampered by the difficulties of replicating the slow time scales typical of Earth processes within the time scale of a research grant. A further, perhaps not obvious, problem is that sometimes we do not carry out the right experiments. Researchers do not always know what to look for. We design experiments to investigate what we think might be there but sometimes, by chance or a fine instinct, we do something completely different and unexpectedly, serendipitously, happen upon a new and deeper understanding. The problem of silicate melt moving through its source rock provides an excellent example of this (*2*).

Driven by metallurgical insights, we thought for a decade or so that the distribution

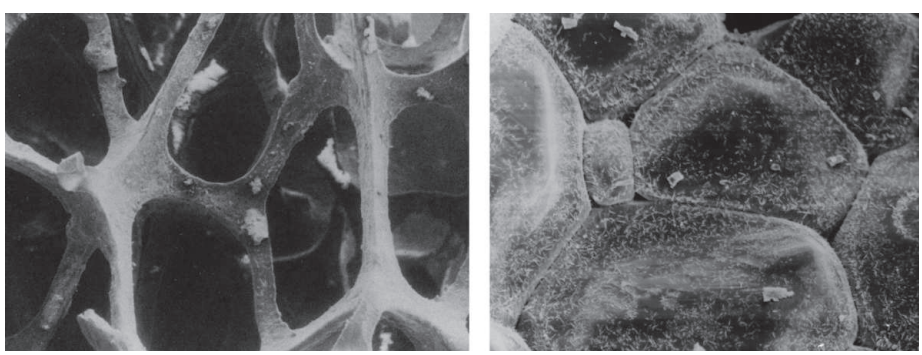

Crystalline yin and yang. Porosity of texturally equilibrated polycrystals revealed in electron microscope images, showing the interplay of liquid and solid. This interconnected geometry of the melt phase was thought to dominate liquid flow in the mantle before Schiano *et al*. demonstrated that transcrystalline melt migration may also be important. (**Left**) A view of the pore structure in aluminum once the solid grains have been removed [reprinted from (*7*) with permission]. The elongated channels that form at three-grain junctions are evident (width of the image is 5 mm). (**Right**) Electron microscope image of quartz grains (with dimensions of about 100 μm) equilibrated with water at 6 kbar and 800°C, showing triangular ends of pores on three-grain junctions.

The author is in the Department of Earth Sciences, University of Cambridge, Cambridge CB2 3EQ, UK. E-mail: marian@esc.cam.ac.uk

of partial melts in the Earth was driven entirely by textural equilibrium, which occurs when the solid grains, and any liquid that might be present, rearrange themselves in the lowest-energy configuration. This generally results in smoothly curved grain boundaries and uniform grain size. In such a situation, the pore geometry is a function of the relative magnitudes of grain boundary energy and the energy of the fluid-solid interface. It is straightforward to demonstrate experimentally (*3*) that this results in a fine network of elongate pores along three-grain junctions and a very high permeability for silicate melts, even for tiny amounts of liquid (see the figure). However, when my colleagues and I started looking at real examples of melt-bearing rock, and in particular rocks from relatively shallow levels in the Earth, it became clear (*4*–*6*) that in the outer parts of the planet the overall temperatures are sufficiently low, and can change sufficiently fast, that textural equilibrium is very rarely achieved. In fact, most liquids flow along fractures formed during chemical reactions (like the process of melting itself) or during deformation.

But what about that part of the Earth that is below the crust and above the iron-dominated core—the mantle? Here the temperature is high, and relatively constant, so that reactions and deformation are probably not able to overtake the rate of textural adjustment driven by interfacial energies. It is therefore possible that partially molten mantle rocks are in, or close to, textural equilibrium, with liquid residing in grain edge channels. However, the new work by Schiano *et al.* shows that if we take temperature gradients into account we get another way of moving melts around that, for small quantities of relatively viscous melts, may be more important than the grain-edge channels.

Fluid inclusions are tiny pockets of liquid (either melt, brines, vapor, or a combination of these) trapped within single crystals. They are common in rocks and are believed to be representative of liquids that passed through the rock along fractures: The inclusions result from the incomplete healing of these fractures. Melt-filled inclusions are common in natural samples of the shallow parts of the mantle that we access. In a fashion similar to the migration of brine inclusions up a thermal gradient in rock salt (NaCl), Schiano *et al*. have shown experimentally that silicate melt-filled inclusions also migrate within single crystals subjected to a thermal gradient—they term this "transcrystalline melt migration." But what is important and exciting about their work is that they found that CO_2 bubbles within the fluid inclusion (formed by the separation of previously homogeneously mixed liquids) do not move. They remain in the same place while the melt of the inclusion moves away, up the temperature gradient. This means that one of the natural records that geologists rely on for discovering what really went on in the Earth may be misleading in some circumstances.

It has previously been assumed that the bulk composition of the inclusion remains constant, unless distinct signs of fracturing are present, but the work of Schiano *et al*. shows that this is not necessarily true and that the fluid-inclusion population may not be representative of the liquid that was present. It begs the question of how widespread this effect may be. How many other fluid-inclusion populations represent the remnants of a melt migration episode? It also poses interesting questions about how we read the rock record to interpret melt migration pathways. Schiano *et al.* show that transcrystalline melt migration can leave distinctively shaped vapor bubbles—will this be enough to detect whether this process operated? Or will the vapor bubbles change to the rounded shape indicative of lower-energy configurations, making it impossible to judge whether they record the movement of vapor alone along now-healed fractures, or whether they record the passage of melt through the grains themselves? This work opens up some exciting new avenues and will provoke much reinterpretation of our current understanding of melt movement, as well as rethinking of the CO_2 content of mantle melts.

References

1. P. Schiano, A. Provost, R. Clocchiatti, F. Faure, *Science* **314**, 970 (2006).
2. D. Laporte, A. Provost, in *Physics and Chemistry of Partially Molten Rocks*, N. Bagdassarov, D. Laporte, A. B. Thompson, Eds. (Kluwer, Dordrecht, 2000), pp. 93–140.
3. C. S. Smith, *Trans. Metall. Soc. AIME* **175**, 15 (1948).
4. M. B. Holness, G. R. Watt, *J. Petrol.* **43**, 511 (2002).
5. M. B. Holness, K. Dane, R. Sides, C. Richardson, M. Caddick, *J. Metamorphic Geol.* **23**, 29 (2005).
6. M. B. Holness, M. J. Cheadle, D. McKenzie, *J. Petrol.* **46**, 1565 (2005).
7. R. M. German, *Liquid Phase Sintering* (Plenum, New York, 1985).

10.1126/science.1135922

VIROLOGY

Sensing Viral RNA Amid Your Own

Viral RNA has a structural modification that cells recognize. This modification could be used in antiviral therapies and to modulate the immune system.

Takashi Fujita

Within hours of infection by a pathogen, our body initiates an arsenal of reactions, collectively known as the innate immune response, to eradicate the invader. In the case of a viral infection, this response involves the expression of numerous cytokine genes, such as type I interferon, to block viral replication and promote acquired immunity days after infection. At the frontline of this defense mechanism is the initial sensing of the virus within an infected cell. How does a cell distinguish viral nucleic acids (DNA or RNA) from its own? On pages 994 and 997 of this issue, Hornung *et al.* (*1*) and Pichlmair *et al.* (*2*) identify an important feature of this surveillance mechanism: Viral RNA is structurally different in a way that marks it as foreign to a host cell.

Creagh and O'Neill recently proposed that a "trinity" of pathogen sensors cooperate in innate immunity (*3*). Cellular NOD-like receptors detect bacteria, whereas viruses are detected by Toll-like receptors (which also recognize bacteria, fungi, and protozoa) and "RIG-like" receptors. The virus-detecting Toll-like receptors operate mainly in plasmacytoid dendritic cells by responding to viral nucleic acids that have been ingested by the cell through phagocytosis and incorporated into endosomal compartments. In these cells, the major immune response is production of type I interferon. But in other cell types, RIG-like receptors are considered the major, and indispensable, viral sensors, responding to viral RNA present in the host cell cytoplasm, which is already replete with self-RNA

Exactly how the RIG-like receptors identify nonself-RNA has not been clear. These

The author is with the Laboratory of Molecular Genetics, Institute for Virus Research, Kyoto University, Kyoto 606-8507, Japan. E-mail: tfujita@virus.kyoto-u.ac.jp

RNA helicases—specifically retinoic acid inducible gene I (RIG-I) and melanoma differentiation–associated gene 5 (MDA5)—play critical roles in sensing viral double-stranded RNA (dsRNA) and controlling infection (*4*, *5*). It is thought that upon binding to dsRNA, they become activated and trigger a chain of signaling events that result in an immune response (see the figure). Helicase activity [unwinding dsRNA into single-stranded RNA (ssRNA)] may not be required to trigger signaling because the amino-terminal portion of RIG-I, which lacks the entire helicase domain by artificial deletion, is constitutively active and can trigger cytokine production without viral infection. Instead, the helicase domain of RIG-I may act as a switch, triggered by a conformational change induced by its helicase-like activity.

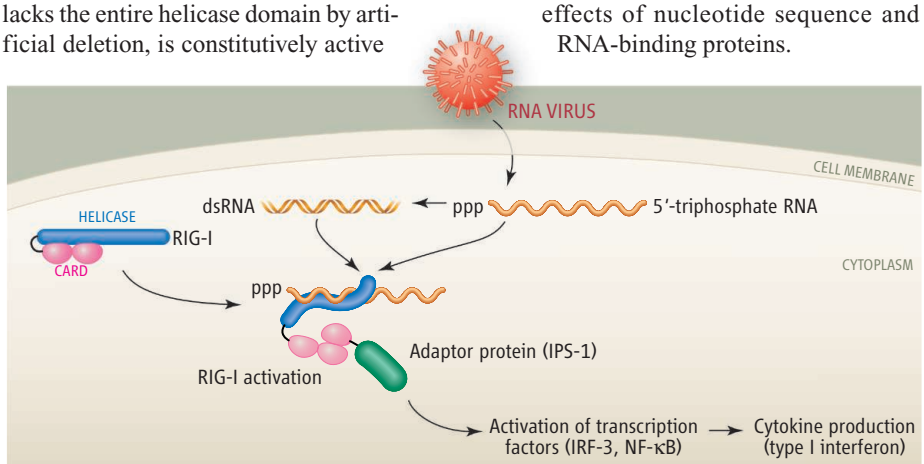

Viral sensing. In the cytoplasm, viral dsRNA or ssRNA containing 5′-triphosphate (ppp) is specifically recognized by RIG-I, initiating interferon production. In some cells, free viral nucleic acids, including those released from infected and killed cells, can be internalized by endocytosis and detected by Toll-like receptors in endosomes, also leading to interferon production. These mechanisms may cooperate to detect invading viruses and thence to initiate immune responses.

dsRNA is virtually absent in mammalian cells, and its molecular structure is considerably different from that of cellular genomic dsDNA. Some RNA viruses, such as encephalomyocarditis virus, generate dsRNA in cells as a by-product of viral replication, but not every virus accumulates such dsRNA. Hornung *et al.* show that ssRNA synthesized in vitro—and thus, that have acquired a 5′-triphosphate—induce interferon production when injected into cultured human cells. Moreover, artificial capping and base modification of 5′-triphosphate ssRNA abrogated detection by RIG-I in injected cells. RIG-I also associated with 5′-triphosphate ssRNA in vitro, suggesting that RIG-I could be a direct viral RNA receptor. But the authors acknowledge that this structure of RNA may only be part of a recognition signal. Cellular primary transcripts contain 5′-triphosphate. However, many self-RNAs undergo various processing steps that remove or mask the 5′-triphosphate moiety: Messenger RNA acquires a 7-methyl-guanosine cap structure at its 5′ end; transfer RNA undergoes 5′ cleavage and a series of nucleotide base modifications; ribosomal RNA readily complexes with ribosomal proteins. But there are also abundant self-RNAs in the cytoplasm that contain 5′-triphosphate, such as 7SL RNA, which is not recognized by RIG-I, indicating that there is more to the molecular signature than 5′-triphosphate. It is necessary to take into account the possible effects of nucleotide sequence and RNA-binding proteins.

This ability to discriminate between self and nonself resembles prokaryotic restriction. In bacteria harboring restriction enzymes that cleave at specific nucleic acid sequences, bacterial genomic DNA is protected from digestion. For example, some recognition sequences are methylated and are thus resistant to cleavage, whereas unmodified invading nuclei acids, such as that of a bacteriophage, are selectively destroyed by restriction enzymes. The common principle underlying these systems is that self-molecules are appropriately modified to avoid being detected.

Pichlmair *et al.* observed that some viruses, including influenza A virus, do not produce appreciable amounts of dsRNA, yet can activate RIG-I (*3*). They also found that ssRNA, such as that of genomic influenza virus, which is uncapped and contains phosphate at the 5′ end, associates with and activates RIG-I. NS1 protein encoded by influenza A virus has been known to affect host immune responses. However, the ability of NS1 to inhibit interferon synthesis in infected cells has been controversial. NS1 contains an RNA-binding domain that is thought to bind to dsRNA and prevent interferon production (*6*). But other work suggests that the RNA-binding activity of NS1 has nothing to do with interferon production (*7*). Pichlmair *et al.* explored a possible connection between a role of NS1 in interferon inhibition and RIG-I function. They found that NS1 forms a complex with RIG-I and propose that this interaction prevents the RIG-I signaling cascade in response to viral infection.

The findings of Hornung *et al.* and Pichlmair *et al.* highlight a new strategy to discriminate viral RNA from the numerous self-RNA species in the host cell cytoplasm. A tight discrimination is crucial because the viruses are replicating inside the cells. On the other hand, endosomal detection is a mechanism to sense a danger signal derived from an infected cell. Apparently, these distinct systems cooperate to maximally respond to the invaders. Some viruses escape 5′-triphosphate detection. The VPg protein of picornavirus covalently attaches to the 5′ end of viral RNA, thus masking it. However, this virus is known to accumulate dsRNA during the course of replication, and this molecular pattern may be detected by another sensor, MDA5 (*5*). The NS3/NS4A protein of hepatitis C virus (*8*) indirectly blocks RIG-I function by destroying its downstream signaling molecule. And influenza A virus may use NS1 protein to thwart host cell detection. Because these immune response blockers are virus encoded, a subtle balance between them and the antiviral activity of host cells will determine the outcome of infection. In this regard, antiviral therapy with either interferon or an interferon inducer could potentially reverse the effect of virus-encoded immune response blockers. The present reports also suggest that designing RNA molecules as a harmless mimicry of a virus could be used as antiviral and immunomodulatory therapies.

References

1. V. Hornung *et al.*, *Science* **314**, 994 (2006); published online 12 October 2006 (10.1126/science.1132505).
2. A. Pichlmair *et al.*, *Science* **314**, 997 (2006); published online 12 October 2006 (10.1126/science.1132998).
3. E. M. Creagh, L. A. J. O'Neil, *Trends Immunol.* **27**, 352 (2006).
4. M. Yoneyama *et al.*, *Nat. Immunol.* **5**, 730 (2004).
5. H. Kato *et al.*, *Nature* **441**, 101 (2006).
6. J. Talon *et al.*, *Proc. Natl. Acad. Sci. U.S.A.* **97**, 4309 (2000).
7. J. Y. Min, R. M. Krug, *Proc. Natl. Acad. Sci. U.S.A.* **103**, 7100 (2006).
8. E. Meylan *et al.*, *Nature* **437**, 1167 (2005).

10.1126/science.1135756

INTRODUCTION

The Glorious Sea Urchin

ANYONE WHO HAS SPENT ANY TIME TAKING COURSES IN DEVELOPMENTAL BIOLOGY has heard about the sea urchin. It has been a major experimental model for over a century, and the elucidation of its genomic sequence described here will be of interest to communities studying everything from economics and ecology in marine ecosystems to fundamental questions in evolution and development.

Davidson (p. 939) introduces us to this organism and to the reasons for its importance. Vertebrates share specific features of embryonic development with the sea urchin (which is the basis for their classification as deuterostomes). The sea urchin genome represents the first full sequence of a nonchordate deuterostome, and as such, makes it possible to identify genes that are truly vertebrate innovations and others that have been lost during evolution. Although much is known about developmental gene regulatory modules, a more detailed picture of these genetic elements and underlying principles of gene regulation that may apply across phyla is now possible. [For further discussion, see *Science*'s Signal Transduction Knowledge Environment site (STKE; www.stke.sciencemag.org)].

To help you visualize the history of sea urchin research and this latest achievement, the section contains a poster, done with the scientific input of A. Cameron and E. Davidson and sure to enrich many walls. An interactive version of the poster, including additional images, video, and Web resources, was created by T. Marathe and S. Wills with images assembled by A. Ransick (www.sciencemag.org/sciext/seaurchin/).

Initial analyses of the 814-megabase genome led to an outpouring of insights, which can be found here in *Science* (Sea Urchin Genome Sequencing Consortium, p. 941), with additional details appearing in a special issue of *Developmental Biology* on 1 December. See also the News article by Elizabeth Pennisi (p. 908). Some of the most striking findings from the sea urchin genome sequence relate to immunity, as described by Rast *et al.* (p. 952). These include an expansion of some innate immune receptors by more than an order of magnitude relative to vertebrates. To complement the genomic sequencing effort, Samanta *et al.* (p. 960) used high-resolution custom tiling arrays to generate a picture of the repertoire of genes expressed during embryogenesis. Having this picture proved to be very valuable to the community in the annotation process.

One fascinating trend is the creative ways in which genomic data can be combined with data from very different disciplines to yield new insights. By examining sequence data for extant sea urchins and combining this information with what is known from the fossil record, it is possible to speculate about the genes that underlie the structural composition of the earliest echinoderms that appeared during the early Cambrian Period. As described by Bottjer (p. 956), paleogenomic analyses of the sea urchin provide insight into genes participating in the generation of fossil-recorded structures. Pearse (p. 940) describes the cause and effect of population fluctuations in this animal, which has economic value as a fishery resource and is a vital component of marine benthic ecosystems. The sequence of the purple sea urchin (and sequences we hope are to come of related species) will help in understanding the basis for variations that affect the cycle between rich kelp forests (on which the urchin grazes) and sea urchin–filled "barrens." The sequencing of the sea urchin moves us a further step away from the past, when the analysis of an individual gene was a breathtaking achievement, toward a future where we will be following multidimensional changes in gene networks and relating them to the world around us.

– BARBARA R. JASNY AND BEVERLY A. PURNELL

Sea Urchin Genome

CONTENTS

See also related News story page 908; Poster; Podcast; Science's STKE material on page 887 or at www.sciencemag.org/sciext/seaurchin/

Science

THE SEA URCHIN

Science

Poster Credits:

Authors
Andrew Cameron
Eric Davidson

Editorial
Barbara R. Jasny

Graphic Design & Art Direction
Joshua Moglia

Production
Marcus Spiegler

THE ANNOUNCEMENT OF THE SEQUENCING of the genome of the sea urchin *Strongylocentrotus purpuratus* is the latest glowing chapter in the long history of contributions from sea urchin researchers to fundamental principles of cell biology, developmental biology, and gene regulation. This poster presents a timeline of the past and a glimpse into the next stage of research that is being opened up through genomic insights. An interactive version of the poster, including additional images, video, and Web resources, can be found online at www.sciencemag.org/sciext/seaurchin/.

–BARBARA R. JASNY

Science

THE SEA URCHIN

Immunology

Innate Immune Receptors

	TLR	NLR	SRCR	PGRP	GNBP
Homo sapiens	10(+1ψ)	20	81(16)	6	0
Ciona intestinalis	3	0	22(8)	6	0
Strongylocentrotus purpuratus	222	203	1095(218)	5	3
Drosophila melanogaster	9	0	14(7)	15	4
Caenorhabditis elegans	1	0	3(1)	0	0

FIGURE CREDIT: SEA URCHIN GENOME SEQUENCING CONSORTIUM/*SCIENCE*

Gene families shown encode toll-like receptors (TLR), NACHT domain and leucine-rich repeat proteins (NLR), scavenger receptor cysteine-rich proteins (SRCR), peptidoglycan recognition proteins (PGRP), and Gram-negative binding proteins (GNBP). ψ indicates pseudogene. SRCR gene statistics are given as number of domains with number of proteins in parentheses for multiple SRCR–containing proteins. Phylogenetic relations among species are indicated by a cladogram at the left.

Network

Endomesoderm specification to 30 hours

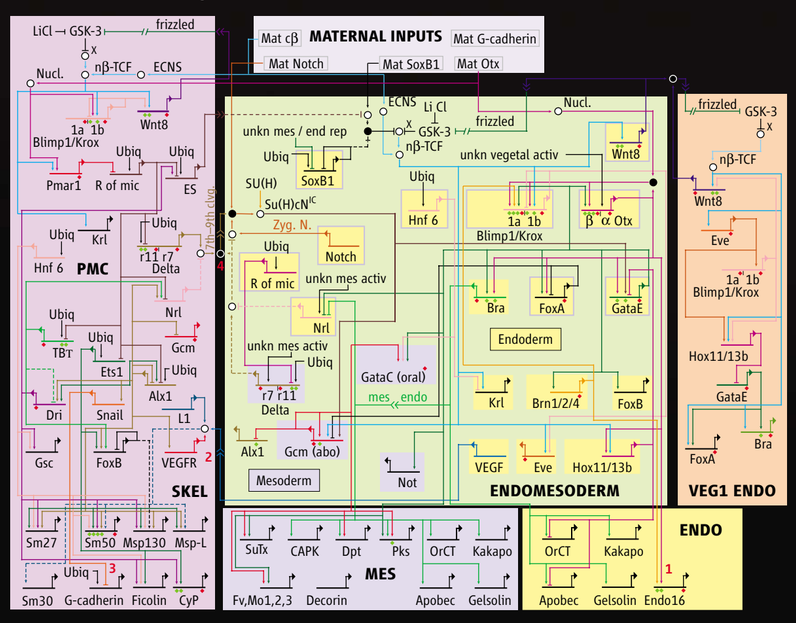

Ubiq = ubiquitous; Mat = maternal; activ = activator; rep = repressor; unkn = unknown; Nucl. = nuclearization; χ = β-catenin source; nβ–TCF = nuclearized b–β–catenin-Tcf1; ES = early signal; ECNS = early cytoplasmic nuclearization system; Zyg. N. = zygotic Notch

FIGURE CREDIT: ADAPTED FROM THE ENDOMESODERM GENE NETWORK AT HTTP://SUGP.CALTECH.EDU/ENDOMES

A triumph of modern biology has been the proof that all complex animals, no matter how different they look, operate their cells the same way and use many of the same genes for transcriptional control and intercellular communication. Ever since the trajectories of modern developmental biology emerged from the observations and logic of late 19th- and early 20th-century embryology, sea urchins have attracted the attention of experimental scientists. The reasons are practical: Sea urchin eggs and embryos are easy to work with. They are almost transparent, lack shells, and produce a relatively small number of cells; they are always available and they develop rapidly, like little machines, in nothing but seawater. By the advent of the First World War, work on sea urchin eggs and embryos had contributed to the realization of two fundamental truths: that the significance of fertilization is the fusion of male and female genomes, and that embryonic development requires the complete genome in every embryonic cell nucleus.

In the late 1950s and 1960s, molecular biology transformed our way of thinking about embryos. Messenger RNAs, regulatory proteins, and regulatory DNA sequences were easy to purify from the sea urchin. Sea urchins were found to have one especially useful attribute as a model organism: If exogenous DNA was injected into the egg cytoplasm (a relatively rapid and easy operation), it would be taken up and incorporated into embryo genomes and could then be expressed during development. The sea urchin embryo has thus become a premier experimental system for exploring the functional importance of regulatory DNA sequence and the encoded interrelationships among regulatory genes, as represented in the sea urchin embryo gene regulatory network shown on the left.

Because of its unique position on the evolutionary tree, the sea urchin is a closer relative to humans than any other nonchordate animal sequenced (such as the fruit fly or nematode), and thus its genomic sequence promised to illuminate the origins and functions of many of our own genes. Obtaining the sequence of such a polymorphic genome posed substantial technical problems that were resolved at the Human Genome Sequencing Center of the Baylor College of Medicine. More than 200 researchers around the world collaborated on the initial annotation of the sequence. The sea urchin (***Strongylocentrotus purpuratus***) genome consists of about 23,300 genes, including representatives of nearly all vertebrate gene families. Some genes thought to be vertebrate-specific were found in the sea urchin, whereas others were identified in the sea urchin but not in the chordate lineage, suggesting loss in the vertebrates.

The sequence will vastly facilitate a multitude of research projects, and in addition it will spawn whole new areas of research. For example, the sea urchin has a diverse and sophisticated immune system mediated by an astonishingly large repertoire of innate pathogen recognition proteins (see figure above). The nervous system of the sea urchin had been poorly understood before the sequencing project; sequence analyses have suggested the usefulness of new reagents that reveal the organization of the nervous system (see figure at left) and have also indicated unexpected complexities. The sea urchin has orthologs for genes associated with vision, hearing, balance, and chemosensation in vertebrates, but lacks genes for gap junction proteins. After a long history of research, the sea urchin genome sequence has thrown open the door on a new vista of opportunities that will connect across the whole biological world.

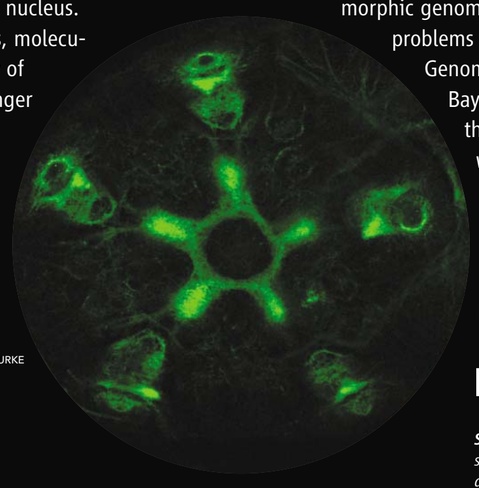

CREDIT: R. BURKE

Neurobiology

Sea urchin nervous system. *Immunofluorescent staining (anti-synaptotagmin) of the rudiment of the adult body that develops enclosed within the larva.*

Milestones in Sea Urchin Research

1876–79

H. Fol and O. Hertwig observed pronuclear fusion, essential to the theory of nuclear genetic determinants.

1891

H. Driesch observed that each blastomere nucleus has all information necessary for development.

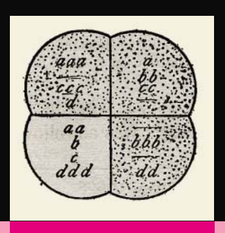

1902–04

T. Boveri demonstrated that only a blastomere with a complete set of chromosomes can develop into a normal embryo.

1926–35

The plasticity of blastomere fates was shown by **S. Horstadius.**

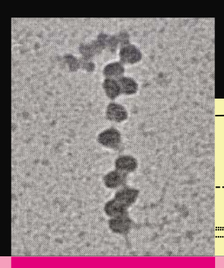

1962–64

Maternal messenger RNA was found in sea urchin eggs by **A. Tyler, A. Monroy,** and colleagues.

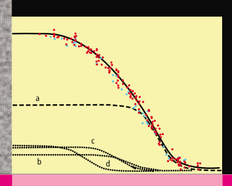

1974

R. Britten, E. Davidson, and colleagues found global interspersion of repetitive sequences in the genome.

1981–82

Synthesis dynamics and complexity of embryo proteins and RNAs were measured in the embryo by many laboratories.

1982

Control of embryonic cell division by cyclin was discovered by **T. Hunt.**

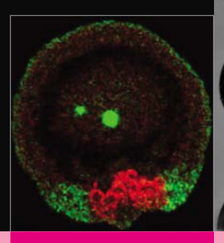

1982–85

Lineage-specific gene expression was found in the embryo by **R. Angerer, E. Davidson, and D. McClay.**

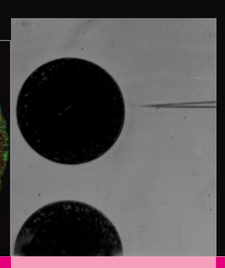

1984–86

Stable incorporation and expression of injected cis-regulatory constructs was demonstrated.

1990–2000

Molecular markers and perturbation reagents were used to reveal signaling systems in development.

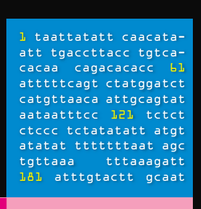

2006

Purple sea urchin sequenced.

TIMELINE CREDITS (LEFT TO RIGHT): G. WESSEL; T. BOVERI, 1902, REDRAWN BY E. B. WILSON, 1925; K. A. MARTIN AND O. L. MILLER JR., REPRINTED FROM *DEV. BIOL.* **98**, 338 (1983)*; D. E. GRAHAM *ET AL.*, ADAPTED FROM *CELL* **1**, 127 (1974)*; P. OLIVERI; A. P. MCMAHON *ET AL.*, REPRINTED FROM *DEV. BIOL.* **108**, 420 (1985)*; *WITH PERMISSION FROM ELSEVIER

PHOTO CREDIT (TOP): JEFFREY ROTMAN/PHOTO RESEARCHERS INC.

PERSPECTIVE

The Sea Urchin Genome: Where Will It Lead Us?

Eric H. Davidson

The sea urchin genome reveals large domains of biology heretofore unexplored at the genome level, as this is the first nonchordate deuterostome sequence. The sequence will accelerate progress toward complete understanding of the genomic regulatory system that controls developmental specification and morphogenetic function, thus illuminating basic developmental process in all animals.

On 1 December 1997, a large male sea urchin of the species *Strongylocentrotus purpuratus*, probably at least 20 years old, donated several milliliters of his sperm in order for a bacterial artificial chromosome (BAC) library to be made of his genome. Immortalized and arrayed in many thousands of small wells, this library contained all the genes and all the hard-wired regulatory instructions required for construction of this sea urchin's body and for his physiological performance in confronting the natural environment (and our laboratory environment), as well as the millions of sequence differences distinguishing his maternal and paternal genomes. This particular library has played an unusually rich role in current bioscience. It provided the sequence base for the first large-scale developmental gene regulatory network to be solved for embryogenesis, the initial version of which was published in these pages in 2002 (*1*), and it was the DNA of this same male and of this same BAC library that have now been sequenced as presented in this issue of *Science* (*2*). The white paper on the basis of which it was decided to proceed with the sequencing effort was written in 2002. This was exactly a century after Boveri concluded from a famous experiment that all chromosomes (i.e., the complete genome) must be present in every cell of a sea urchin embryo for embryonic development to occur normally (*3*).

We now have in digital form the first genome of a nonchordate deuterostome. This is of particular interest because the deuterostomes are the large group of animal species to which both we and sea urchins belong. Sea urchins are hence more closely related to us in evolution than are flies or worms. This is also the first genome of a nonchordate marine animal of any kind to be sequenced. Among the important insights from the genome sequence was the definition of the "deuterostome toolkit," the set of genes particular to this group of animals and not shared with others kinds of animal (*4*). This in turn affords a definition of what genes are truly vertebrate inventions; many genes previously thought to be vertebrate-specific were found in the sea urchin genome. Because of the sea urchin's evolutionary relation to ourselves, its genome provides what evolutionists consider an extremely useful outgroup for the understanding of our own genomes—an intellectual version of Archimedes' idea that with a leverage point removed from Earth he could move the globe. Beyond digesting all this, what will be the more global and far-reaching importance of the sea urchin genome?

We have learned that in the fundamental domain of the genomic control of life, in the genomic organization of development, in genomic explanations of evolutionary process, every animal is in some measure a model for every other animal. The sea urchin embryo has become one of the great model systems in several areas that lie within the domain of genome control. One such area is discovery of the rule set for cis-regulatory design in developmental gene regulatory modules (*5*). These are the discrete genomic units of regulatory function, which determine whether, when, and how much all genes are to be expressed at any given time in any given cell. Cis-regulatory modules usually consist of several hundred base pairs of genomic sequence, in which are clustered multiple specifically recognized target sites for regulatory proteins (transcription factors). Someday we will be able to read the sequence of regulatory modules on which we cannot do experiments, such as our own, and understand on sight the logic functions they execute in response to the sets of transcription factors in given cells at given times. But to do that, we need to know their design principles—which can only be deduced from a deep base of structure-function data obtained by experimentally mutating the module sequence and introducing it back into the egg to see how it works in development. Gene transfer into sea urchin eggs is an uncommonly easy and efficient procedure. For the past several years, most information of this kind has come from the sea urchin and *Drosophila* model systems, and this will continue to be true, although similar experiments in mouse, *Xenopus*, *Caenorhabditis elegans*, chick, and *Ciona* show that there is a universal animal regulatory code remaining to be reduced to principles.

The sea urchin genome will directly contribute to solving the principles of design of gene regulatory networks for embryonic development. These are interacting systems of all the regulatory genes participating in each aspect of development. Such principles can only be obtained by comparing network architecture in different animals developing in similar or different ways. The sea urchin embryo is likely to be the first embryo for which a global network analysis will become available, in which every input into every regulatory gene in the network comes from some other gene in the network—or, put another way, to which the criterion of completeness can be applied everywhere. We will, in the future, be able to account for the course, and hence the outcome, of development—the body plan of each species.

The genome will not only provide the "code" for development but will also contribute to linkage between gene regulatory networks and the actual realization of developmental events. For example, the genomics of gastrulation, epithelium-mesenchyme transitions, and species-specific patterning functions are now accessible. It remains to connect the genes that execute these functions to the control circuitry that specifies their occurrence.

Many other questions will also be approachable if new genome sequences continue to emerge. Just as one example, what is speciation? The large polymorphism of sea urchins invites a direct test of the idea that most genes diverge continuously within and among species, whereas sharper changes

Fig. 1. A sea star, *Pisaster ochraceus*, on a bed of *Strongylocentrotus purpuratus*, the sea urchin species whose genome has now been sequenced. The body plans of these echinoderms are obviously different. But although their genomes no doubt contain a few distinct genes, the root of their different developmental processes lies in their diverse gene regulatory apparatus, which is also encoded in the genomic DNA. The sequence of the sea urchin genome opens the way to experimental analysis of the regulatory code. [Photograph: Robert Potts, California Academy of Sciences]

Division of Biology, 156-29, California Institute of Technology, Pasadena, CA 91125, USA. E-mail: davidson@caltech.edu

in a minor fraction of genes account for the adaptive differences that separate diverging species. If we had the sequence of several additional closely related sea urchin genomes, this model could be directly assessed. Another opportunity would arise if the genome sequences of two other widely used sea urchin species, *Lytechinus variegatus* and *Paracentrotus lividus*, were available: Comparison with the genome of *S. purpuratus* would yield a global map of conserved regulatory modules around every gene. Finally and most essentially, comparative regulatory genomics provides the key to unlock the basic processes of evolution. It has been possible to compare on a small scale the embryonic networks of two animals that have evolved independently for half a billion years, the sea urchin and the sea star (*6*). The comparison revealed both a shocking degree of architectural conservation in certain subcircuits and a shocking level of change of others. This cuts close to the bone of the evolutionary processes by which body plans have diverged in evolution (*7*). Large-scale comparisons of regulatory gene networks between multiple species of different degrees of relatedness will provide a new dimension to our understanding of evolutionary mechanism and of network architecture and system design.

The sea urchin genome sequence did not open the door to a new pathway to knowledge; it opened the door to a nexus of such pathways. They lead in diverse directions, but their central and unifying reference is the genome sequence. Indeed, its central foundation in genomics will characterize a large area of bioscience, a reorganization that is already upon us, the coalescence of what might be called "informational bioscience." This will consist of a scientific continuum over what used to be the distinct disciplines of regulation molecular biology, evolution, developmental biology, and genomics, together with their mathematical and computational support and more traditional descriptive knowledge. The sea urchin research community is now experiencing this intellectual revolution.

References

1. E. H. Davidson *et al.*, *Science* **295**, 1669 (2002).
2. Sea Urchin Genome Sequencing Consortium, *Science* **314**, 941 (2006).
3. T. Boveri, *Verh. D. Phys. Med. Ges. Würzburg* **35**, 67 (1902).
4. S. C. Materna, K. Berney, R. A. Cameron, *Dev. Biol.*, 10.1016/j.dbio.2006.09.033 (2006).
5. E. H. Davidson, *The Regulatory Genome. Gene Regulatory Networks in Development and Evolution* (Academic Press, San Diego, CA, 2006).
6. V. F. Hinman, A. Nguyen, R. A. Cameron, E. H. Davidson, *Proc. Natl. Acad. Sci. U.S.A.* **100**, 13356 (2003).
7. E. H. Davidson, D. H. Erwin, *Science* **311**, 796 (2006).

10.1126/science.1136252

PERSPECTIVE

Ecological Role of Purple Sea Urchins

John S. Pearse

Sea urchins are major components of marine communities. Their grazing limits algal biomass, and they are preyed upon by many predators. Purple sea urchins (*Strongylocentrotus purpuratus*) are among the best studied species. They live in environments that alternate between two stable states: luxuriant, species-rich kelp forests and sea urchin–dominated "barrens." The transition from one state to the other can be initiated by several factors, including the abundance of algal food, predators, storm intensities, and incidence of disease. Purple sea urchins compete with other grazers, some of which are important fishery resources (such as abalones and red sea urchins), and they are harvested for scientific research. Revelations from their genome will lead to a better understanding of how they maintain their ecological importance, and may in turn enhance their economic potential.

Sea urchins are major grazers in shallow seas worldwide (*1*). Purple sea urchins (*S. purpuratus*) and other strongylocentrotid sea urchins of the Northern Hemisphere are particularly important and are the most intensively studied (*2*). A delicate balance between sea urchin grazing and kelp forest productivity leads to stable states that alternate between luxuriant kelp forests and relatively species-depauperate sea urchin "barrens" (*3*). Curiously, the densities of sea urchins are often similar within kelp forests and sea urchin barrens. Within kelp forests, sea urchins are nearly stationary, feeding on captured pieces of kelp litter ("drift kelp") that are produced and shed in high quantities from the kelp plants. However, when the kelps are removed by storms or El Niño events, the remaining sea urchins actively forage on young kelp recruits and on drift kelp brought in from elsewhere, preventing the reestablishment of the kelp forest. The sea urchins can be decimated by storms (*4*) or diseases (*5*), allowing the kelp forest to return to the area.

In addition to the alternation of kelp forests and sea urchin barrens, temporal and spatial variation in recruitment of sea urchins can greatly influence their abundance, and therefore their ecological role, within kelp forests. Infrequent peaks in recruitment can lead to spurts in sea urchin densities (*6*), sometimes triggering intense grazing that removes the kelp, transforming a kelp forest into a sea urchin barren (*7*) (Fig. 1). Recruitment intensity is determined mainly by the supply of sea urchin larvae, which in turn depends on the oceanographic conditions that bring the larvae to suitable areas to settle (*8*).

Predators almost certainly limited the abundance of sea urchins in the past, and the presence of sea urchin barrens around the world is due at least in part to decimation of predators by humans (*9*). In southern California, where sea urchin–dominated barrens are common, major predators such as spiny lobsters, sheephead fish, and sea otters have been greatly reduced during the past century (*10*). Sea otters, in particular, are effective in keeping sea urchin densities low throughout their range (*11*), which often tips the balance toward kelp forests and enhances kelp forest productivity and biodiversity (*12*). Other factors also can favor kelp forests or barrens, even in the absence of major sea urchin predators (*13*). For example, sea urchins compete with other grazers. Purple sea urchins compete in particular with abalones and red sea urchins (*14*). However, because both abalones and red sea urchins have experienced intensive fishing pressure for the past several decades, competitive interactions among these species have probably decreased, perhaps relieving purple sea urchins from adverse competition. On the other hand, juvenile purple sea urchins and abalones often are sheltered from predators under the spines of red sea urchins (*15*), and both may be negatively affected by heavy fishing of red sea urchins. The strengths of these interactions remain poorly known and are complicated by variation in fishing pressures. Red sea urchins have been the basis of a major fishery in the eastern Pacific for the past several decades. However, the U.S. sea urchin fishery has been in decline, mainly because of a decline in demand by the Japanese market ($110 million worth of sea urchins were exported from the United States to Japan in 1993 compared with about $36 million in 2003) (*16*). The smaller, less valuable, purple sea urchins have been a minor component of the fishery but continue to play an extensive role in scientific research (*2*).

Sea urchins are central in structuring marine benthic communities, both as grazers and prey, and are economically valuable in fisheries.

Long Marine Laboratory, University of California, Santa Cruz, 100 Shaffer Road, Santa Cruz, CA 95060, USA. E-mail: pearse@biology.ucsc.edu

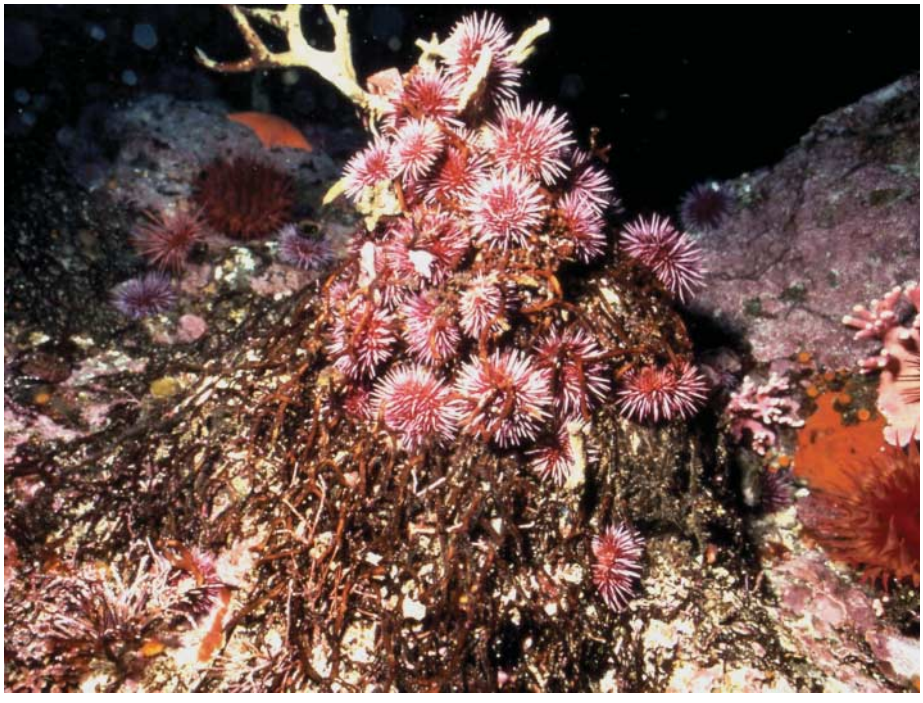

Fig. 1. Purple sea urchins (*S. purpuratus*) grazing on the remains of a giant kelp hold fast after an unusually heavy recruitment in Carmel Bay, California (*7*). [Photo courtesy of J. M. Watanabe]

There are important differences among the different species: Some are more effective as grazers than others, and they vary in their diets, growth rates, longevities, and importance in fisheries. Some show no sign of senility and live for well over a century (*17*). Elucidation of their genomes will open new avenues of research into the underlying genetic and evolutionary bases of these variations.

References and Notes

1. C. Harrold, J. S. Pearse, *Echinoderm Studies* **2**, 137 (1987).
2. L. Rogers-Bennett, in *Edible Sea Urchins: Biology and Ecology*, J. M. Lawrence, Ed. (Elsevier, Amsterdam, Netherlands, 2007), pp. 393–425.
3. P. K. Dayton *et al.*, *Ecol. Monogr.* **62**, 421 (1992).
4. A. W. Ebeling *et al.*, *Mar. Biol.* **84**, 287 (1985).
5. K. D. Lafferty, *Ecol. Appl.* **14**, 1566 (2004).
6. J. S. Pearse, A. H. Hines, *Mar. Ecol. Prog. Ser.* **39**, 275 (1987).
7. J. M. Watanabe, C. Harrold, *Mar. Ecol. Prog. Ser.* **71**, 125 (1991).
8. T. A. Ebert *et al.*, *Mar. Ecol. Prog. Ser.* **111**, 41 (1994).
9. J. B. Jackson *et al.*, *Science* **293**, 629 (2001).
10. P. K. Dayton *et al.*, *Ecol. Appl.* **8**, 309 (1998).
11. J. A. Estes, D. O. Duggins, *Ecol. Monogr.* **65**, 75 (1995).
12. M. H. Graham, *Ecosystems* **7**, 341 (2004).
13. M. S. Foster, *Hydrobiologia* **192**, 21 (1990).
14. M. J. Tegner, P. K. Dayton, *ICES J. Mar. Sci.* **57**, 579 (2000).
15. L. Rogers-Bennett, J. S. Pearse, *Conserv. Biol.* **15**, 642 (2001).
16. D. Sweetnam *et al.*, *Calif. Coop. Oceanic Fish. Invest. Rep.* **46**, 10 (2005).
17. T. A. Ebert, J. R. Southon, *Fish. Bull.* **101**, 915 (2003).

18. I thank J. Watanabe for providing the photo used in Fig. 1, L. Rogers-Bennett for sharing her manuscript with me, V. Pearse and an anonymous reviewer for providing comments on the manuscript, and R. A. Cameron for inviting me to prepare it.

10.1126/science.1131888

RESEARCH ARTICLE

The Genome of the Sea Urchin *Strongylocentrotus purpuratus*

Sea Urchin Genome Sequencing Consortium*†

We report the sequence and analysis of the 814-megabase genome of the sea urchin *Strongylocentrotus purpuratus*, a model for developmental and systems biology. The sequencing strategy combined whole-genome shotgun and bacterial artificial chromosome (BAC) sequences. This use of BAC clones, aided by a pooling strategy, overcame difficulties associated with high heterozygosity of the genome. The genome encodes about 23,300 genes, including many previously thought to be vertebrate innovations or known only outside the deuterostomes. This echinoderm genome provides an evolutionary outgroup for the chordates and yields insights into the evolution of deuterostomes.

The genome of the sea urchin was sequenced primarily because of the remarkable usefulness of the echinoderm embryo as a research model system for modern molecular, evolutionary, and cell biology. The sea urchin is the first animal with a sequenced genome that (i) is a free-living, motile marine invertebrate; (ii) has a bilaterally organized embryo but a radial adult body plan; (iii) has the endoskeleton and water vascular system found only in echinoderms; and (iv) has a nonadaptive immune system that is unique in the enormous complexity of its receptor repertoire. Sea urchins are remarkably long-lived with life spans of *Strongylocentrotid* species extending to over a century [see supporting online material (SOM)] and highly fecund, producing millions of gametes each year; and *Strongylocentrotus purpuratus* is a pivotal component of subtidal marine ecology and an important fishery catch in several areas of the world, including the United States. Although a research model in developmental biology for a century and a half, for most of that time, few were aware of one of the most important characteristics of sea urchins, a character that directly enhances its significance for genomic analysis: Echinoderms (and their sister phylum, the hemichordates) are the closest known relatives of the chordates (Fig. 1 and SOM). A description of the echinoderm body plan, as well as aspects of the life-style, longevity, polymorphic gene pool, and characteristics that make the sea urchin so valuable as a research organism, are presented in the SOM.

The last common ancestors of the deuterostomal groups at the branch points shown in Fig. 1 are of Precambrian antiquity [>540 million years ago (Ma)], according to protein molecular phylogeny. Stem group echinoderms appear in the Lower Cambrian fossil assemblages dating to 520 Ma. Cambrian echinoderms came in many distinct forms, but from their first appearance, the fossil record illustrates certain distinctive features that are still present: their water vascular system, including rows of tube feet protruding through holes in the ambulacral grooves and their calcite endoskeleton (mainly, a certain form of $CaCO_3$),

*Correspondence should be addressed to George M. Weinstock. E-mail: gwstock@bcm.tmc.edu

†All authors with their contributions and affiliations appear at the end of this paper.

which displays the specific three-dimensional structure known as "stereom." The species sequenced, *Strongylocentrotus purpuratus*, commonly known as the "California purple sea urchin" is a representative of the thin-spined "modern" group of regularly developing sea urchins (euechinoids). These evolved to become the dominant echinoid form after the great Permian-Triassic extinction 250 million years ago.

We present here a description of the *S. purpuratus* genome and gene products. The genome provides a wealth of discoveries about the biology of the sea urchin, Echinodermata, and the deuterostomes. Among the key findings are the following:

- The sea urchin is estimated to have 23,300 genes with representatives of nearly all vertebrate gene families, although often the families are not as large as in vertebrates.
- Some genes thought to be vertebrate-specific were found in the sea urchin (deuterostome-specific); others were identified in sea urchin but not the chordate lineage, which suggests loss in the vertebrates.
- Expansion of some gene families occurred apparently independently in the sea urchin and vertebrates.
- The sea urchin has a diverse and sophisticated immune system mediated by an astonishingly large repertoire of innate pathogen recognition proteins.
- An extensive defensome was identified.
- The sea urchin has orthologs of genes associated with vision, hearing, balance, and chemosensation in vertebrates, which suggests hitherto unknown sensory capabilities.
- Distinct genes for biomineralization exist in the sea urchin and vertebrates.
- Orthologs of many human disease–associated genes were found in the sea urchin.

Sequencing and Annotation of the *S. purpuratus* Genome

Sequencing and assembly. Sperm from a single male was used to prepare DNA for all libraries (tables S1 and S2) and whole-genome shotgun (WGS) sequencing. The overall approach was based on the "combined strategy" used for the rat genome (*1*), where WGS sequencing to six times coverage was combined with two times sequence coverage of BAC clones from a minimal tiling path (MTP) (fig. S1). The use of BACs provided a framework for localizing the assembly process, which aided in the assembly of repeated sequences and solved problems associated with the high heterozygosity of the sea urchin genome, without our resorting to extremely high coverage sequencing.

Several different assemblies were produced during the course of the project (see SOM for details). The Sea Urchin Genome Project (SUGP) was the first to produce both intermediate WGS assemblies and a final combined assembly. This was especially useful, not only for the early availability of an assembly for analysis, but also because WGS contigs were used to fill gaps between BACs in the combined assembly. The pure WGS assembly was produced (v 0.5 GenBank accession number range AAGJ01000001 to AAGJ01320773; also referred to as NCBI build 1.1) and released in April 2005. The final combined BAC-WGS assembly was released in July 2006 as version (v) 2.1 and submitted to GenBank (accession number range AAGJ02000001 to AAGJ02220581).

A second innovation in the SUGP was the use of the clone-array pooled shotgun sequencing (CAPSS) strategy (*2*) for BAC sequencing (fig. S2). The MTP consisted of 8248 BACs, and rather than prepare separate random libraries from each of these, the CAPSS strategy involved BAC shotgun sequencing from pools of clones and then deconvoluting the reads to the individual BACs. This allowed the BAC sequencing to be performed in 1/5th the time and at 1/10th the cost.

The principal new challenge in the SUGP was the high heterozygosity in the outbred animal that was sequenced. It was known that single-copy DNA in the sea urchin varied by as much as 4 to 5% [single nucleotide polymorphism (SNP) plus insertion/deletion (indel)], which is much greater than human (~0.5%) (*3*). Moreover, alignment of WGS reads to the early v 0.1 WGS assembly revealed at least one SNP per 100 bases, as well as a comparable frequency of indel variants. This average frequency of a mismatch per 50 bases or higher prevented merging by the assembly module in Atlas, the Phrap assembler, and also made it difficult to determine if reads were from duplicated but diverged sections of the genome or heterozygous homologs. This challenge was met by adding components to Atlas to handle local regions of heterozygosity and to take advantage of the BAC data, because each BAC sequence represented a single haplotype (see SOM). High heterozygosity has been seen in the past with the *Ciona* genomes (*4*, *5*) and is likely to be the norm in the future as fewer inbred organisms are sequenced. Moreover, the CAPSS approach makes BAC sequencing more manageable for large genomes. Thus, the sea urchin project may serve as a paradigm for future difficult endeavors.

Combining the BAC-derived sequence with the WGS sequence generated a high-quality draft with 4 to 5% redundancy that covered more than 90% of the genome while sequencing to a level of 8× base coverage (table S2). The assembly size of 814 Mb is in good agreement with the previous estimate of genome size, 800 Mb ± 5% (*6*). The assembly is a mosaic of the two haplotypes, but it was possible to determine the phase of the BACs on the basis of how many mismatches neighboring BACs had in their overlap regions. This information will be used to create a future version of the genome in which the individual haplotypes are resolved.

Gene predictions. The v 0.5 WGS assembly displayed sufficient sequence continuity (a contig N50 of 9.1 kb) and higher-order organization (a scaffold N50 of 65.6 kb) to allow gene predictions to be produced and the annotation process to begin even while the BAC component was being sequenced. We generated an official gene set (OGS), consisting of ~28,900 gene models, by merging four different sets of gene predictions with the GLEAN program (*7*) (see SOM for details). One of these gene sets, produced from the Ensembl gene prediction software, was created for both v 0.5 and v 2.0 assemblies.

To estimate the number of genes in the *S. purpuratus* genome, we began with the 28,900 gene models in the OGS and reduced this by the 5% redundancy found by mapping to the v 2.0 assembly, then increased it by a few percent for the new genes observed in the Ensembl set from the v 2.0 assembly compared with v 0.5. From manual analysis of well-characterized gene sets (e.g., ciliary, cell cycle control, and RNA metabolism genes), we estimated that, in addition to redundancy, another 25% of the genes in the OGS were fragments, pseudogenes, or otherwise not valid. Finally, whole-genome tiling microarray analysis (see below) showed 10% of the transcriptionally active regions (long open reading frames, not small RNAs) were not represented by genes in the OGS. Taken together, this analysis gave an estimate of about 23,300 genes for *S. purpuratus*. Information on all annotated genes can be found at (*8*).

The overall trends in gene structure were similar to those seen in the human genome. The statistics of the Ensembl predictions from the WGS assembly revealed an average of 8.3 exons and 7.3 introns per transcript (see SOM). The average gene length was 7.7 kb with an average primary transcript length of 8.9 kb. A broad distribution of all exon lengths peaked at around 100 to 115 nucleotides, whereas that for introns at around 750 nucleotides. The smaller average intron size relative to humans' was consistent with the trend that intron size is correlated with genome size.

Annotation process. Manual annotation and analysis of the OGS was performed by a group of over 200 international volunteers, primarily from the sea urchin research community. To facilitate and to centralize the annotation efforts, an annotation database and a shared Web browser, Genboree (*9*), were established at the BCM-HGSC. These tools enabled integrated and collaborative analysis of both precomputed and experimental information (see SOM). A variety of precomputed information for each predicted gene model was made available to the annotators in the browser, including expressed sequence tag (EST) data, the four unmerged gene prediction sets, and transcription data from whole-genome tiling microarray with embryonic RNA (see below) (*10*). Additional resources available to the community are listed in table S4.

Over 9000 gene models were manually curated by the consortium with 159 novel models (gene models not represented in the OGS) added to the official set. If we assume no bias in the curated gene

models, the number of novel models added may imply that the official set contains >98% of the protein-coding genes.

Genome features. A window on the genetic landscape is scaffold-centric in *S. purpuratus*, because linkage and cytogenetic maps are not available. The 36.9% GC content of the genome is uniformly low because assessment of the average GC content by domains is consistent (36.8%), and the distribution is tight (see SOM). Genes from the OGS show no tendency to occupy regions of higher- or lower-than-average GC content. In fact, nearly all genes lie in regions of 35 to 39% GC.

The Echinoderm Genome in the Context of Metazoan Evolution

The sea urchin genetic tool kit lends evolutionary perspective to the gene catalogs that characterize the superclades of the bilaterian animals. The distribution of highly conserved protein domains and sequence motifs provides a view of the expansion and contraction of gene families, as well as an insight into changes in protein function. Examples are enumerated in Table 1, which presents a global overview of gene variety obtained by comparing sequences identified in Interpro, and Table 2, which shows the distribution of specific Pfam database domains associated with selected aspects of cell physiology, including sequences identified in the cnidarian *Nematostella vectensis* (*11*). The Interpro data suggest that about one-third of the 50 most prevalent domains in the sea urchin gene models are not in the 50 most abundant families in the other representative genomes (mouse, tunicate, fruit fly, and nematode), and thus, they constitute expansions that are specific at least to sea urchins, if not to the complex of echinoderms and hemichordates. Two of the most abundant domains make up 3% of the total and mark genes that are involved in the innate immune response. Others define proteins associated with apoptosis and cell death regulation, as well as proteins that serve as downstream effectors in the Toll–interleukin 1 (IL-1) receptor (TIR) cascade. The quinoprotein amine dehydrogenase domain seen in the sea urchin set is 10 times as abundant as in other representative genomes and may be used in the systems of quinone-containing pigments known to occur in these marine animals. The large number of nucleosomal histone domains found agrees with the long-established sea urchin–specific expansion of histone genes. In summary, the distribution of proteins among these conserved families shows the trend of expansion and shrinkage of the preexisting protein families, rather than frequent gene innovation or loss. Gene family sizes in the sea urchin are more closely correlated with what is seen in deuterostomes than what is seen in the protostomes.

Of equal interest are the sorts of proteins not found in sea urchins. The sea urchin gene set shares with other bilaterian gene models about 4000 domains, whereas 1375 domains from other bilaterian genomes are not found in the sea urchin set. In agreement with the lack of morphological evidence of gap junctions in sea urchins, there are no gap junction proteins (connexins, pannexins, and innexins). Also missing are several protein domains unique to insects, such as insect cuticle protein, chitin-binding protein, and several pheromone- or odorant-binding proteins, as well as a vertebrate invention—the Krüppel-associated box or KRAB domain, a repressor domain in zinc finger transcription factors (*12*). Finally, searches for specific subfamilies of G protein–coupled

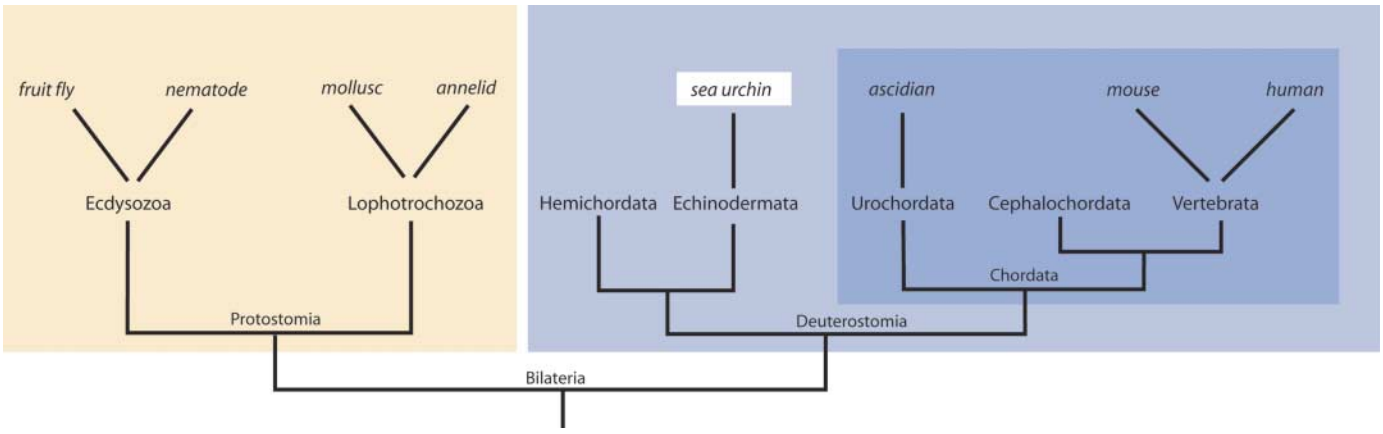

Fig. 1. The phylogenetic position of the sea urchin relative to other model systems and humans. The chordates are shown on the darker blue background overlapping the deuterostomes as a whole on a lighter blue background. Organisms for which genome projects have been initiated or finished are shown across the top.

Table 1. Unique aspects of gene family distribution in sea urchin: Selected examples of the frequency of Interpro domains in the proteome of selected species. ID is the identification number used in the INTERPRO database; the second column shows the name given to the domain or motif family in the database. Species abbreviations: Sp, *Strongylocentrotus purpuratus*; Mm, *Mus musculus*; Ci, *Ciona intestinalis*; Dm, *Drosophila melanogaster*; Ce, *Caenorhabditis elegans*.

ID	Name	Species, total number (percentage of total matches)				
		Sp	Mm	Ci	Dm	Ce
IPR001190	Speract/scavenger receptor	361 (1.79)	14 (0.08)	1 (0.01)	2 (0.02)	0 (0.00)
IPR000157	TIR	248 (1.23)	22 (0.12)	9 (0.09)	9 (0.09)	2 (0.02)
IPR011029	DEATH-like	172 (0.85)	8 (0.05)	19 (0.18)	5 (0.05)	1 (0.01)
IPR007111	NACHT nucleoside triphosphatase	135 (0.67)	16 (0.09)	28 (0.27)	0 (0.00)	0 (0.00)
IPR011044	Quinoprotein amine dehydrogenase, β chain–like	122 (0.60)	7 (0.04)	15 (0.15)	5 (0.05)	6 (0.05)
IPR000558	Histone H2B	110 (0.54)	14 (0.08)	2 (0.02)	100 (1.00)	17 (0.13)
IPR001951	Histone H4	93 (0.46)	7 (0.04)	0 (0.00)	101 (1.01)	16 (0.12)
IPR002119	Histone H2A	87 (0.43)	24 (0.14)	2 (0.02)	104 (1.04)	19 (0.14)
IPR008042	Retrotransposon, Pao	76 (0.38)	0 (0.00)	0 (0.00)	0 (0.00)	6 (0.05)
IPR000164	Histone H3	72 (0.36)	17 (0.10)	5 (0.05)	103 (1.03)	22 (0.17)

receptors (GPCRs) that are known as chemosensory and/or odorant receptors in distinct bilaterian phyla failed to detect clear representatives in the sea urchin genome. However, this failure more likely reflects the independent evolution of these receptors, rather than a lack of chemoreceptive molecules, because the sea urchin genome encodes close to 900 GPCRs of the same superfamily (rhodopsin-type GPCRs), several of which are expressed in sensory structures (*13*). A conservative way to compare gene sets is to count the strict orthologs that give reciprocal BLAST matches. Genes that are genuine orthologs are likely to yield each other as a best hit. Comparison of sea urchin, fruit fly, nematode, ascidian, mouse, and human gene sets (Fig. 2) indicates that the greatest number of reciprocal best matches is observed between mouse and human, which reflects their close relation. The numbers of presumed orthologous genes between the ascidian and the two mammals are about equal, but are less than the number counted between these species and the sea urchin. The difference is consistent with the lower gene number and reduced genome size in the urochordates (*4*).

The number of reciprocal pairs for sea urchin and mouse is about 1.5 times the matches between proteins in sea urchin and fruit fly. The number of nematode proteins matching either sea urchin or fruit fly is even lower. This is likely the result of the more rapid sequence changes in the nematode compared with the other species used in this analysis. More than 75% of the genes that are shared by sea urchin and fruit fly are also shared between sea urchin and mouse. Thus, these genes constitute a set of genes common to the bilaterians, whereas the additional sea urchin–mouse pairs are unique to the deuterostomes.

The sea urchin genome consequently provides evidence for the now extremely robust concept of the deuterostome superclade. A 1908 concept that originated in the form of embryos of dissimilar species (*14*) is demonstrated by genomic comparisons.

Table 2. Distribution among sequenced animal genomes of various Pfam domains associated with selected aspects of eukaryotic cell physiology. In *S. purpuratus*, the number of annotated genes is listed; the number in parentheses is the total number of models (including ones that were not annotated) predicted to contain the Pfam domain. For *Nematostella veciensis* (Nv), numbers were obtained by searching Stellabase (*11*).

Process	Domain	PFAM no.	Sp	Hs	Dm	Ce	Nv
Cell cycle control	Cyclin_N	PF00134	15 (17)	21	11	7	7
	Cyclin_C	PF02984	7 (8)	12	4	5	4
	E2F_TDP	PF02319	3 (5)	11	3	4	3
	RB_A	PF01858	2	3	2	1	0
	RB_B	PF01857	2	3	2	1	0
	P53	PF00870	1	3	1	1	0
	Cullin	PF00888	7	9	8	7	4
	Skp1	PF01466	1	3	5	21	1
Histone metabolism	Histone*	PF00125	49	75	8	?	?
	Linker histone*	PF00538	5	8	2	?	?
	Nucleo-plasmin	PF03066	2	5	2	0	1
	NAP	PF00956	2	24	4	2	0
	HDAC	PF00850	8	11	5	8	3
	DOT1	PF08123	1	1	1	6	1
RNA metabolism	RRM_1	PF00076	140 (178)	245	126	99	41
	TUDOR	PF00567	15	13	15	8	7
	DEAD	PF00270	93 (125)	78	56	65	27
	LSM	PF01423	17	21	17	18	4
	KH-1	PF00013	28 (31)	36	28	28	5
	DSRM	PF00035	14 (15)	21	14	13	8
	3′-5′-Exo-nuclease	PF01612	13 (15)	5	5	9	5
	Exonuc_X-T	PF00929	9 (11)	15	7	10	5
Apoptosis†	Caspase	PF00656	31 (33)	14	7	4	5
	BIR	PF00653	4 (7)	8	4	1	4
	Bcl-2	PF00452	10	11	2	1	7
	TNFR_c6	PF00020	8 (9)	8	1 (no DD)	1 (no DD)	2
	NACHT	PF05729	129 (145)	18	1	1	2
	NB-ARC	PF00931	3	1	1	1	0
	DEATH	PF00531	47 (101)	30	9	6	6
	DED	PF01335	4 (5)	7	1	0	5
	CARD	PF00619	5 (10)	20	1	0	8

Complexity intermediate between that in vertebrates and protostome invertebrate model organisms

Complexity greater than that found in other model organisms

Complexity lower than that found in other model organisms

*Numbers of histone genes refer to distinct core or linker histone genes, as opposed to total gene number as a result of large tandemly repeated arrays (e.g., ~400 clusters of early histone arrays in sea urchin, 100 copies of a tandem array in *Drosophila*, with each array containing a gene for the four core and one H1 histone). †Numbers for Hs, Dm, and Ce obtained from (*53*).

Developmental Genomics

In the 1980s, the sea urchin embryo became the focus of cis-regulatory analyses of embryonic gene expression, and there was a great expansion of molecular explorations of the developmental cell biology, signaling interactions, and regulatory control systems of the embryo. Analysis of the entire genome facilitated the first large-scale correlation of the gene regulatory network for development, which represents the genomic control circuitry for specification of the endoderm and mesoderm of this embryo (*15*–*17*) with the encoded potential of the sea urchin.

The embryo transcriptome and regulome. Because of indirect development in the sea urchin, embryogenesis is cleanly separated from adult body plan formation, in developmental process and in time, and therefore, it is possible to estimate the genetic repertoire specifically required for formation of a simple embryo (*10*). Pooled mRNA preparations from four stages of development, up to the mid-late gastrula stage (48 hours), were hybridized with a whole-genome tiling array. Expression of about 12,000 to 13,000 genes, as conservatively assessed, was seen during this early period, indicating that ~52% of the entire protein-

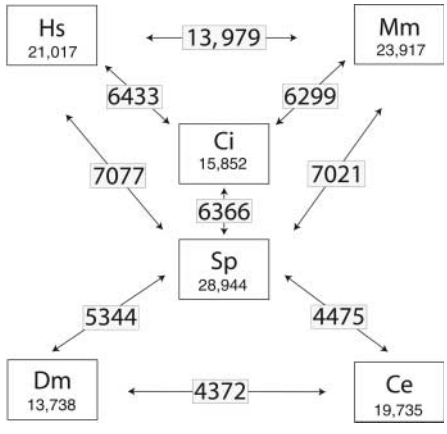

Fig. 2. Orthologs among the Bilateria. The number of 1:1 orthologs captured by BLAST alignments at a match value of $e = 1 \times 10^{-6}$ in comparisons of sequenced genomes among the Bilateria. The number of orthologs is indicated in the boxes along the arrows, and the total number of International Protein Index database sequences is shown under the species symbol. Hs, *Homo sapiens*; Mm, *Mus musculus*; Ci, *Ciona intestinalis*; Sp, *S. purpuratus*; Dm, *Drosophila melanogaster*; Ce, *Caenorhabditis elegans*.

coding capacity of the sea urchin genome is expressed during development to the mid-late gastrula stage. An additional set of microarray experiments extended the interrogation of embryonic expression to the 3-day pluteus larva stage (see SOM) (*18*).

The DNA binding domains of transcription factor families are conserved across the Bilateria, and these protein domain motifs were used to extract the sea urchin homologs (see SOM). For each identified gene, if data were not already available, probes were built from the genome sequence and used to measure transcript concentration by quantitative polymerase chain reaction with a time series of embryo mRNAs, as well as to determine spatial expression by whole-mount in situ hybridization.

All bilaterian transcription factor families were represented in the sea urchin with a few rare exceptions (see below), so the sea urchin data strongly substantiate the concept of a pan-bilaterian regulatory tool kit (*19*) or "regulome." We found that 80% of the whole sea urchin regulome (except the zinc finger genes) was expressed by 48 hours of embryogenesis (*20*), an even greater genetic investment than the 52% total gene use in the same embryo.

Signal transduction pathways. More than 1200 genes involved in signal transduction were identified. Comparative analysis highlights include the protein kinases that mediate the majority of signaling and coordination of complex pathways in eukaryotes. The *S. purpuratus* genome has 353 protein kinases, intermediate between the core vertebrate set of 510 and the fruit fly and nematode conserved sets of ~230. Fine-scale classification and comparison with annotated kinomes (*21*, *22*) reveals a remarkable parsimony. Indeed, with only 68% of the total number of human kinases, the sea urchin has members of 97% of the human kinase subfamilies, lacking just four of those subfamilies (Axl, FastK, H11, and NKF3), whereas *Drosophila* lacks 20 and nematodes 32 (Fig. 3) (*23*). Most sea urchin kinase subfamilies have just a single member, although many are expanded in vertebrates; thus, the sea urchin kinome is largely nonredundant. The sea urchin therefore possesses a kinase diversity surprisingly comparable to that of vertebrates without the complexity. A small number of kinases were more similar to insect than to vertebrate homologs (including the Titin homolog Projection, the Syk-like tyrosine kinase Shark, and several guanylate cyclases), which indicated for the first time the loss of kinase classes in vertebrates (*23*). Expression profiling showed that 87% of the signaling kinases and 80% of the 91 phosphatases were expressed in the embryo (*23*, *24*), which emphasized the importance of signaling pathways in embryonic development.

The small guanosine triphosphatases (GTPases) function as molecular switches in signal transduction, nuclear import and export, lipid metabolism, and vesicle docking. Vertebrate GTPase families were expanded after their divergence from echinoderms, in part by whole-genome duplications (*25*–*27*). The sea urchin genome did not undergo a whole-genome duplication, yet phylogenies for four Ras GTPase families (Ras, Rho, Rab, and Arf) revealed that local gene duplications occurred (Fig. 4), which ultimately resulted in a comparable number of monomeric GTPases in the human and sea urchin genomes (*28*). Thus, expansion of each family in vertebrates and echinoderms was achieved by distinct mechanisms (gene-specific versus whole genome duplication). More than 90% of the small GTPases are expressed during sea urchin embryogenesis, which suggests that the complexity of signaling through GTPases is comparable between sea urchins and vertebrates.

The Wnt family of secreted signaling molecules plays a central role in specification and patterning during embryonic development. Phylogenetic analyses from cnidarian to human indicate that of the 13 known Wnt subfamilies, *S. purpuratus* has 11, missing Wnt2 and Wnt11 homologs (Fig. 5). *S. purpuratus* has WntA, previously reported as being absent from deuterostomes (*29*). Of 126 genes described as components of the Wnt signal transduction machinery, homologs of ~90% were present in the sea urchin genome, which indicates a high level of conservation of all three Wnt pathways (*30*). However, of 94 Wnt transcriptional target genes reported in the literature, mostly from vertebrates (*31*), only 53% were found with high confidence in the sea urchin genome (Fig. 6). The absent Wnt targets include vertebrate adhesion molecules, which were frequently missing from the sea urchin genome (*32*), as well as signaling receptors, which are more divergent and thus more difficult to identify. In contrast, most transcription factor targets of the Wnt pathway are present in the genome, which reflects a higher degree of conservation of transcription factor families (*20*). Taken together, the genomic analysis of signal transduction components indicates that sea urchins have signaling machinery strikingly comparable to that of vertebrates, often without the complexity that arises from genetic redundancy.

Sea Urchin Biology

Analysis of the genome allows understanding of parts of the organism that have not been well studied. Several examples of this follow with further details in the SOM. Additional areas such as intermediary metabolism, metalloproteases, ciliary structure, fertilization, and germline specification are presented in the SOM.

Defense Systems

The need to deal with physical, chemical, and biological challenges in the environment underlies the evolution of an array of defense gene families and pathways. One set of protective mechanisms involves the immune system, which responds to biotic stressors such as pathogens. A second group of genes comprises a chemical "defensome," a network of stress-sensing transcription factors and defense proteins that transform and eliminate many potentially toxic chemicals.

The sea urchin immune system. The sea urchin has a greatly expanded innate immunity repertoire compared with any other animal studied to date (table S5). Three classes of innate receptor proteins are particularly increased (Fig. 7). These make up a vast family of Toll-like receptors (TLRs), a similarly large family of genes that encode NACHT and leucine-rich repeat (LRR)–containing proteins (NLRs), and a set of genes encoding multiple scavenger receptor cysteine-rich (SRCR) domain proteins of a class highly expressed in the sea urchin immune cells or coelomocytes (*33*, *34*). Receptors from each of these families participate in immunity by recognizing nonself molecules that are conserved in pathogens or by responding to self molecules that indicate the presence of infection (*35*). In contrast, homologs of signal transduction proteins and nuclear factor kappa B (NFκB)/Rel domain transcription factors that are known to function further downstream of these genes were present in numbers similar to those in other invertebrate species. One of the more unexpected findings from our analysis of sea urchin immune genes was the identification of a Rag1/2-like gene cluster (*36*). The presence of this cluster, along with other recent findings (*37*), suggested the possibility that these genes had been part of animal genomes for longer than previously considered. Further analysis of the genomic insights into the innate immune system and the underpinnings of vertebrate adaptive immunity can be found in a review in this issue (*38*).

The complement system. The complement system of vertebrates is a complex array of soluble serum proteins and cellular receptors arranged into three activation pathways (classical, lectin, and alternative) that converge and activate the terminal or lytic pathway. This system opsonizes pathogenic cells for phagocytosis and sometimes activates the terminal pathway, which leads to pathogen destruction. An invertebrate complement system was first identified in the sea urchin [for reviews, see (*39*, *40*)], and

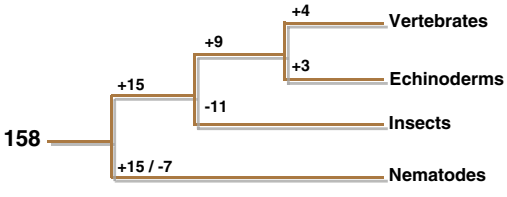

Fig. 3. Protein kinase evolution: Invention and loss of protein kinase subfamilies in metazoan lineages. Deuterostomes share 9 protein kinase subfamilies absent from *C. elegans* and *Drosophila*, and the sea urchin has not lost any of the 158 metazoan primordial kinase classes, unlike insects or nematodes. [From (*23*)]

the analysis of the genome sequence presented a more complete picture of this important immune effector system. In chordates, collectins initiate the lectin cascade through members of the mannose-binding protein (MBP)–associated protease (MASP)/C1r/C1s family. Several genes encoding collectins, C1q and MBP, have been predicted (*39*) and were present in the genome; however, members of the MASP/C1r/C1s family were not identified. There was no evidence for the classical pathway, which links the complement cascade with immunoglobulin recognition in jawed vertebrates. The alternative pathway is initiated by members of the thioester protein family, which, in the sea urchin, was somewhat expanded with four genes. Two of the thioester proteins, SpC3 and SpC3-2, are known to be expressed, respectively, in coelomocytes and in embryos and larvae. Furthermore, there were three homologs of factor B, the second member of the alternative pathway (*41*).

The terminal complement pathway in vertebrates acts to destroy pathogens or pathogen-infected cells with large pores called membrane attack complexes (MACs). Twenty-eight gene models were identified that encode MAC-perforin domains, but none of these had the additional domains expected for terminal complement factors (C6 through C9). Instead, these are members of a novel and very interesting gene family with perforin-like structure. In vertebrates, perforins carry out cell-killing functions by cytotoxic lymphocytes through the formation of small pores in the cell membranes. If the complement system in the sea urchin functions through multiple lectin and alternative pathways in the absence of the lytic functions of the terminal pathway, the major activity of this system is expected to be opsonization.

Homologs of immune regulatory proteins. Cytokines are key regulators of intercellular communication involving immune cells, acting to coordinate vertebrate immune systems. Genes encoding cytokines and their receptors often evolve at a rapid pace, and most families are known only from vertebrate systems. Although members of many cytokine, chemokine, and receptor families were not identified in the sea urchin genome, a number of important immune signaling homologs were present. These included members of the tumor necrosis factor (TNF) ligand and receptor superfamilies, an IL-1 receptor and accessory proteins, two IL-17 receptor–like genes and 30 IL-17 family ligands, and nine macrophage inhibitory factor (MIF)–like genes. Receptor tyrosine kinases (RTKs) included those that bind important growth factors that regulate cell proliferation in vertebrate hematopoietic systems. Of particular note, from the sea urchin genome, were two vascular endothelial growth factor (VEGF) receptor–like genes and a Tie1/2 receptor, all of which were expressed in adult coelomocytes. Many of these genes are homologs of important inflammatory regulators and growth factors in higher vertebrates, and these sea urchin homologs may have similar functions in regulating coelomocyte differentiation and recruitment.

Representatives of nearly all subclasses of important vertebrate hematopoietic and immune transcription factors were present in the sea urchin genome. Notably, the genome contained homologs of immune transcription factors that had not been identified previously outside of chordates, including PU.1/SpiB/SpiC, a member of the Ets subfamily, and a zinc finger gene with similarity to the Ikaros subfamily. Transcript prevalence measurements showed that PU.1, the Ikaros-like gene and homologs of Gata1/2/3, E2A/HEB/ITF2, and Stem

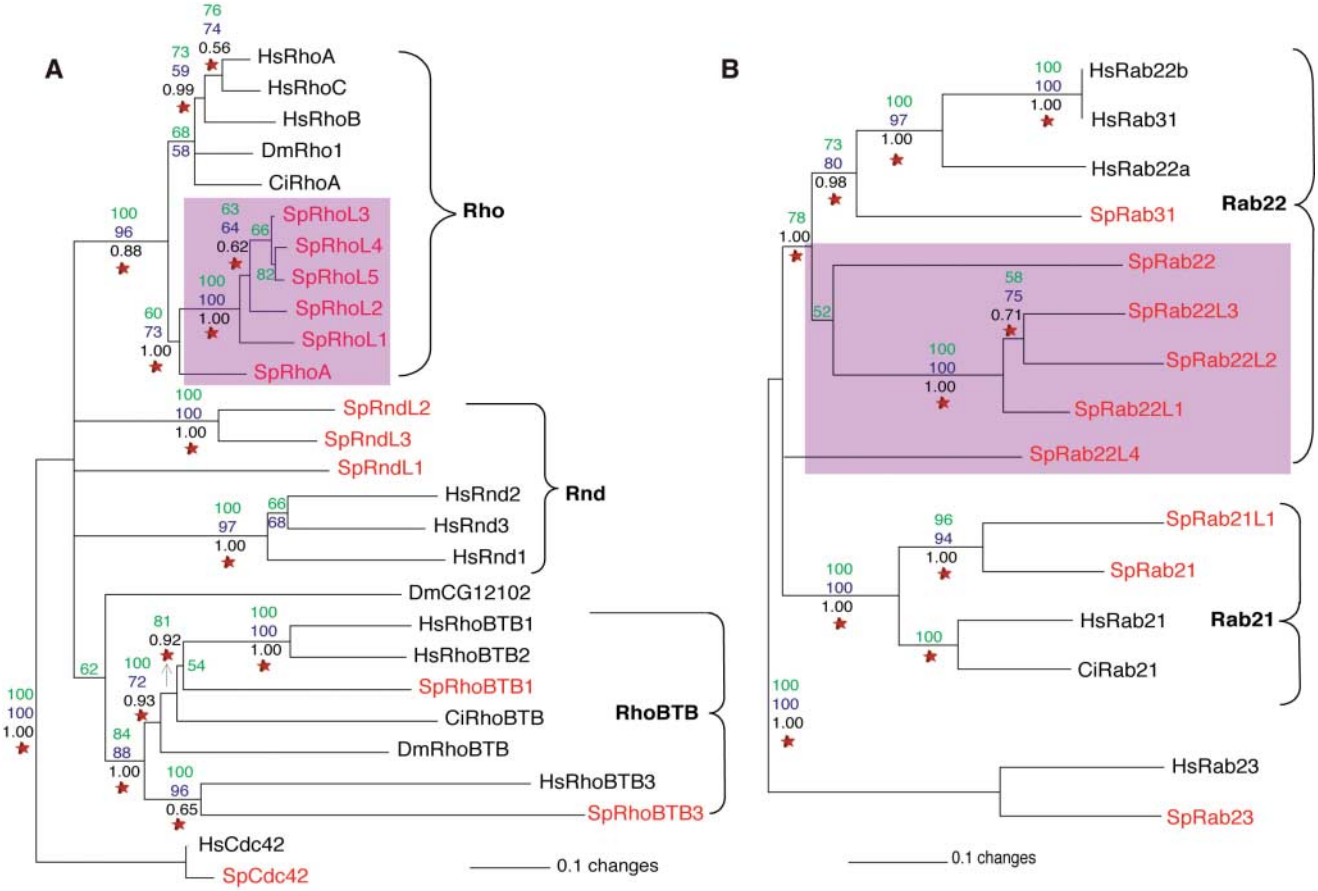

Fig. 4. Partial phylogenies of the Rho (**A**) and the Rab families (**B**) of small GTPases. The pink boxes highlight gene-specific duplications that increased sea urchin GTPase numbers, resulting in a complexity comparable to vertebrates. Numbers at each junction represent confidence values obtained via three independent phylogenetic methods [neighbor-joining (green), maximum parsimony (blue), and Bayesian (black)]; red stars indicate nodes retained by maximum likelihood. [From (*28*)]

Families	Genes	Distribution of the Activators of the Wnt signals throughout the animal kingdom						
		Cnidarians	Ecdysozoans	Lophotrochozoans	Echinoderms	Urochordates	Cephalochordates	Vertebrates
		Sea anemone (*Nematostella vectenesis*)	Fly (*Drosophila melanogaster*)	Annelid and Molluscs (*Platynereis dumerilii and Patella vulgata*)	Sea Urchin (*Strongylocentrotus purpuratus*)	Ascidian (*Ciona intestinalis*)	Amphioxus (*Brachiostoma floridae*)	Human (*Homo sapiens*)
	wnt1	■	■	■	■	?	■	■
	wnt2/13	■	x	■	x	■	■	■
	wnt3	■	x		■	■	■	■■
	wnt4	■	x	■	■	■?	■	■
	wnt5	■	■	■ (D. japonica)	■	■	■	■■
	wnt6	■	■		■	■	■	■
	wnt7	■■	■	■	■	■?	■	■■
	wnt8	■■	x		■	x	■	■■
	wnt9/14/15		■	■	■	■	■■	■■
	wnt10	■	■	■	■	■		■■
	wnt11	■	x		x	x	■	■
	wnt16	■	■ (C.elegans-egl20)		■	?		■■
	wntA	■	■ (A. gambiae)	■	■	x		x

Fig. 5. Survey of the Wnt family of secreted signaling molecules in selected metazoans. Each square indicates a single Wnt gene identified either through genome analyses or independent studies, and squares with a question mark indicate uncertainty of the orthology. Letter X's represent absence of members of that subfamily in the corresponding annotated genome; empty spaces have been left for species for which genomic databases are not yet available. [From (*30*)]

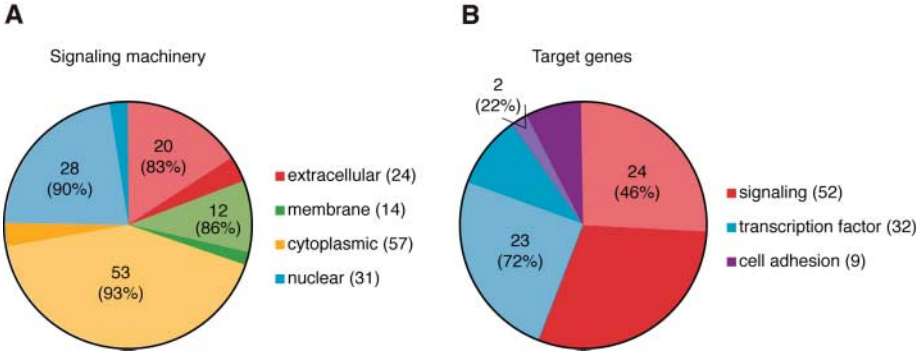

Fig. 6. Presence of Wnt signaling machinery components (**A**) and target genes (**B**) in the *S. purpuratus* genome. (A) The 126 genes involved in the transduction of the Wnt signals have been separated into four categories from the extracellular compartment to the nucleus. Sea urchin homologs are identified by the lighter shade (indicated by both the number and the percentage of homologs that were identified within the chart); the total number of known genes is indicated in the chart legend. (B) The 93 reported Wnt targets have been divided into three categories: signaling molecules, transcription factors, and cell adhesion molecules. Colors and numbers are as in (A).

Cell Leukemia (SCL) were all expressed at substantial levels in coelomocytes (*41*). This was consistent with the presence of conserved mechanisms of regulating gene expression among sea urchin coelomocytes and vertebrate blood cells.

ABC transporters. Many chemicals are removed from cells by efflux proteins known as ATP-binding cassette (ABC) or multidrug efflux transporters. *S. purpuratus* has 65 ABC transporter genes in the eight major subfamilies of these genes [ABC A to H; (*42*)]. The ABCC family of multidrug transporters is about 25% larger than in other deuterostome genomes with at least 30 genes in this family (nearly half of the sea urchin ABC transporters), and 25 of these 30 genes showed substantial mRNA expression in eggs, embryos, or larvae. Much of the expansion is in the Sp-ABCC5 and Sp-ABCC9 families, whereas orthologs of the vertebrate gene ABCC2 (also called MRP2) are absent. Because the ABCC family is known to generally transport more hydrophilic compounds than other transporter families, such as the ABCB genes, sea urchins may have increased need for transport of these compounds. ABCC efflux activity has been described in sea urchin embryos and, consistent with the genomic expansion of the ABCC family, the major activity in early embryos ensues from an ABCC-like efflux mechanism.

Cytochrome P-450 monooxygenase (CYP). Enzymes in the CYP1, CYP2, CYP3, and CYP4 families carry out oxidative biotransformation of chemicals to more hydrophilic products. The sea urchin has 120 CYP genes, and those related to CYP gene families 1 to 4 constitute 80% of the total, which suggests that there has been selective pressure to expand functionality in these gene families (*42*). Eleven CYP1-like genes are present in the sea urchin genome, more than twice the number in chordates. CYP2-like and CYP3-like genes are also present at greater numbers than in other deuterostomes. In addition to the CYPs in families 1 to 4, the sea urchin genome contains homologs of proteins involved in developmental patterning (CYP26), cholesterol synthesis (CYP51), and metabolism (CYP27, CYP46). Homologs of some CYPs with endogenous functions in vertebrates were not found; however, (CYP19, androgen aromatase; CYP8, prostacyclin synthase; CYP11, pregnenolone synthase; CYP7, cholesterol-7α-hydroxylase). These CYP genes in concert with additional expanded defensive gene families represent a large diversification of defense gene families by the sea urchin relative to mammals (*42*).

Oxidative defense and metal-complexing proteins. The metal-complexing proteins include three metallothionein genes and three homologs of phytochelatin synthase genes. Genes for antioxidant proteins include three superoxide dismutase (SOD) genes and a gene encoding ovoperoxidase (an unusual peroxidase with SOD-like activity), along with one catalase, four glutathione peroxidase, and at least three thioredoxin peroxidase genes. Reactive oxygen detoxification genes may be important in conferring the long life-span of sea urchins, because oxidative damage is thought to be a major factor in aging.

Diversity and conservation in xenobiotic signaling. The diversity of genes encoding xenobiotic-sensing transcription factors that regulate biotransformation enzymes and transporters was similar to other invertebrate genomes, but in most cases lower than vertebrates.

For example, the sea urchin genome encoded a single predicted CNC-bZIP protein homologous to the four human CNC-bZIP proteins involved in the response to oxidative stress. There were two sea urchin homologs of the aryl hydrocarbon receptor (AHR), which in vertebrates mediates the transcriptional response to polynuclear and halogenated aromatic hydrocarbons and, in both protostomes and deuterostomes, also regulates specific developmental processes (*43*–*45*). One of the sea urchin AHR homologs was more closely related to the vertebrate AHR; the other shared greatest sequence identity with the *Drosophila* AHR homolog *spineless*. Sea urchins also had two genes encoding hypoxia-inducible factors (HIFα subunits), which regulate adaptive responses to hypoxia, and a gene encoding ARNT, a PAS protein that is a dimerization partner for both AHRs and HIFs.

Strongylocentrotus purpuratus has 32 nuclear receptor (NR) genes (*20*), two-thirds the number in humans, including several with potential roles in chemical defense (*42*). The sea urchin genome also contains two peroxisome proliferator–activated receptor (PPAR, NR1C) homologs and an NR1H gene coorthologous to both liver X receptor (LXR) and farnesoid X receptor (FXR) (*42*). Genes homologous to the vertebrate xenobiotic sensor NR1I genes [pregnane X receptor, PXR; constitutive androstane receptor, CAR (*46*)] are absent, although three NR1H-related genes were found, which possibly form a new subfamily of genes involved in xenobiotic sensing.

Many of the defense genes are expressed during development (*10*, *42*), which suggests that they have dual roles in chemical defense and in developmental signaling. In several cases (CYPs, AHR, NF-E2), the evolution of pathways for chemical defense may have involved recruitment from developmental signaling pathways (*42*).

Nervous System

The echinoderm nervous system is the least well studied of all the major metazoan phyla. For a number of technical reasons, the structure and function of echinoderm nerves have been neglected. Analysis of the sea urchin genome has enabled an unprecedented glimpse into the neural and sensory functions and has revealed several novel molecular approaches to the study of echinoderm nervous systems (Table 3).

The nervous systems of echinoderm larvae and adults are dispersed, but they are not simple nerve nets. This organization differs from both vertebrates, which do not have a dispersed nervous system, and hemichordates, which do have nerve nets (*47*). Adult sea urchins have thousands of appendages, each with sensory neurons, ganglia, and motor neurons arranged in local reflex arcs. These peripheral appendages are connected to each other and to radial nerves, which provide overall control and coordination (*47*, *48*).

Nearly all of the genes encoding known neurogenic transcription factors are present in the sea urchin genome, and several are expressed in neurogenic domains before gastrulation, which indicates that they may operate near the top of a conserved neural gene regulatory network (*47*). Axon guidance molecules known from other metazoans are also expressed in the developing embryo. Unexpectedly, genes encoding the neurotrophin-Trk receptor system that were thought to be vertebrate-specific because they were not found in *Ciona*, are present in sea urchin, which suggests a deuterostome origin and a potential loss in urochordates.

The genes required to construct neurons and to transmit signals are present, but the repertoire of neural genes and the initial characterization of expression of a number of them led to unexpected and surprising conclusions. There appear to be no genes encoding gap junction proteins, which suggests that communication among neurons depends on chemical synapses without ionic coupling. The repertoire of sea urchin neurotransmitters is large, but melatonin and adrenalin are lacking, as they are in ascidians (*4*, *47*). Cannabinoid, lysophospholipid, and melanocortin receptors are not present in urchins, but orthologs were found in ascidians (*4*, *47*). In contrast, some sets of genes thought to be chordate-specific have sea urchin orthologs, for example, insulin and insulin-like growth factors (IGFs) that are more similar to their chordate counterparts than those of other invertebrates (*47*). Overall, the genome contains representatives of all five large superfamilies of GPCRs, including those that mediate signals from neuropeptides and peptide hormones. Both the secretin and rhodopsin superfamilies display marked lineage-specific expansions (*13*, *47*).

Sensory systems. There were 200 to 700 putative chemosensory genes that formed large clusters and lacked introns, which are features of chemosensory genes in vertebrates, but not in *Caenorhabditis elegans* and *Drosophila melanogaster*. Many of these genes encoded amino acid motifs that were characteristic of vertebrate chemosensory and odorant receptors (*13*, *47*). Sea urchins had an elaborate collection of photoreceptor genes that quite surprisingly appeared to be expressed in tube feet (*13*, *47*). These included many genes encoding transcription factors regulating retinal development and a photorhodopsin gene.

Human Usher syndromes are genetic diseases affecting hearing, balance, and retinitis pigmentosa (retinal photoreceptor degeneration). Most of the genes involved have been identified, and they encode a set of membrane and cytoskeletal proteins that form an interacting network that controls the arrangement of mechanosensory stereocilia in hair cells of the mammalian ear. Many or all of the proteins play some roles in photoreceptor organization and/or maintenance. Orthologs of virtually the entire set of membrane and cytoskeletal proteins of the Usher syndrome network were found in the sea urchin genome. These include the very large membrane proteins, usherin and VLGR-1 and large cadherins (Cadh23 and possibly Pcad15), all of which participate in forming links between stereocilia in mammalian hair cells, as well as myosin 7 and 15, two PDZ proteins (harmonin and whirlin) and another adaptor protein (SANS), which participate in linking these membrane proteins to the cytoskeleton. In addition, two membrane transporters, NBC (a candidate Usher syndrome target known to interact with harmonin) and TrpA1 (the mechanosensory channel connected to the tip links containing cadherin 23), have orthologs in the sea urchin genome. Sea urchins do not have ears or eyes, so they must deploy these proteins in

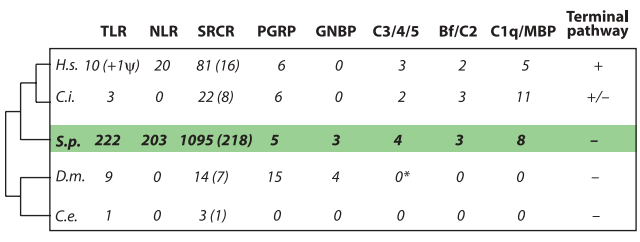

	TLR	NLR	SRCR	PGRP	GNBP	C3/4/5	Bf/C2	C1q/MBP	Terminal pathway
H.s.	10 (+1ψ)	20	81 (16)	6	0	3	2	5	+
C.i.	3	0	22 (8)	6	0	2	3	11	+/–
S.p.	***222***	***203***	***1095 (218)***	***5***	***3***	***4***	***3***	***8***	**–**
D.m.	9	0	14 (7)	15	4	0*	0	0	–
C.e.	1	0	3 (1)	0	0	0	0	0	–

Fig. 7. Gene families encoding important innate immune receptors and complement factors in animals with sequenced genomes. For some key receptor classes, gene numbers in the sea urchin exceeds other animals by more than an order of magnitude. Representative animals include *H.s.*, *Homo sapiens*; *C.i.*, *Ciona intestinalis*; *S.p. Strongylocentrotus purpuratus*; *D.m. Drosophila melanogaster*; and *C.e. Caenorhabditis elegans*. Indicated gene families include TLR, toll-like receptors; NLR, NACHT and leucine-rich repeat (LRR) domain–containing proteins similar to the vertebrate Nod/NALP genes; SRCR, Scavenger receptor cysteine-rich domain genes; PGRP, peptidoglycan recognition protein domain genes; and GNBP, Gram-negative binding proteins. C3/4/5, thioester proteins homologous to vertebrate C3, C4, and C5; Bf/C2, complement factors homologous to vertebrate C2 and factor B; C1q/MBP, homologs of vertebrate lectin pathway receptors; and Terminal pathway, homologs of vertebrate C6, C7, C8, and C9. SRCR gene statistics are given as domain number/gene number for multiple SRCR-containing proteins (numbers for *C. intestinalis* includes all SRCR proteins). Asterisk in the *D. melanogaster* C3/4/5 column is meant to denote the presence of related thioester genes (TEPs) and a true C3/4/5 homolog from another arthropod. +/– for *C. intestinalis* Terminal pathway column indicates the presence of genes with similarity to C6 only (Nonaka and Yoshizaki 2004). Phylogenetic relations among species are indicated by a cladogram at the left.

other sensory processes. Sea urchins respond to light, touch, and displacement and probably use some of same sensory genes used by vertebrates.

The Echinoderm Adhesome

The *S. purpuratus* genome contained representatives of all the standard metazoan adhesion receptors (table S7), but the emphasis on different classes of receptors differed substantially from that used by vertebrates. The integrin family was intermediate in size between those of protostomes and vertebrates—several chordate-specific expansions of the integrin repertoire were absent, and there were some expansions unique (so far) to echinoderms. The cadherin repertoire was also small relative to vertebrates (a dozen or so instead of over a hundred), and many chordate-specific expansions were missing. Specialized large cadherins shared by protostomes and vertebrates were present, as well as some specialized large cadherins previously thought to be chordate-specific, but overall, the cadherin repertoire was more invertebrate than vertebrate in character. Sea urchins lacked the integrins and cadherins that link to intermediate filaments in vertebrates.

In contrast, sea urchins had large repertoires of adhesion molecules containing immunoglobulin superfamily, fibronectin type 3 repeat (FN3), epidermal growth factor (EGF), and LRR repeats. In addition to the expansion of TLRs and NLRs mentioned above, there are large expansions of other LRR receptor families, including GPCRs (*32*). The key neural adhesion systems involved in regulating axonal outgrowth were present (netrin/Unc5/DCC; Slit/Robo; and semaphorins/plexins), as were adhesion molecules involved in synaptogenesis (Agrin/MUSK; and neurexin/neuroligins). This was not surprising because these molecules were known in both protostomes and vertebrates. However, structurally, the synapses of echinoderms are unusual because there are no direct synaptic contacts (*49*). Some of them were expressed in sea urchin embryos before there are any neurons, suggesting that they may have other roles as well.

The basic metazoan basement membrane extracellular matrix (ECM) tool kit was present—two alpha-IV collagen genes, perlecan, laminin subunits, nidogen, and collagen XV/XVIII. There did not appear to be much, if any, expansion of these gene families, as is found in vertebrates, which suggests that there is less diversity among basement membranes. Quite a few ECM proteins present in chordates, but not protostomes, were also missing in sea urchins, including fibronectins, tenascins, von Willebrand factor, vitronectin, most vertebrate-type matrix proteoglycans, and complex VWA/FN3 collagens among others (*32*). Absence of these genes may be related to the absences of neural crest migration, a high shear endothelial-lined vasculature and, of course, cartilage and bone.

In addition to the components of Usher syndromes mentioned above, it was surprising to find a clear ortholog of reelin, a large ECM protein involved in establishing the layered organization of neurons in the vertebrate cerebral cortex. Reelin is mutated in the *reeler* mouse, and mutations in the *reeler* gene in humans have been associated with Norman-Roberts-type lissencephaly syndrome. Reelin has a unique domain

Table 3. Genomic insights into sea urchin neurobiology.

Neural process	Revelations from the genome	Genes
Neural development	Neurogenic ectoderm is specified in early embryonic development.	Sp-Achaete-scute, Sp-homeobrain, Sp-Rx (retinal anterior homeobox), Sp-Zic2
Synapse structure and function	Echinoderm synapses are structurally unusual, despite the presence of many genes encoding proteins involved in synapse function.	Sp-Neurolignin, Sp-neurexin, Sp-agrin, Sp-MUSK, Sp-thrombospondin, Sp-Rim2, Sp-Rab3, exocyst complex, Snares, SM, synaptotagmins
Electrical signaling and coupling	Neurons have ion channel proteins, but lack electrical coupling via gap junctions.	Voltage-gated K^+, Ca^{2+}, and Na^+ channels, but no connexins or pannexins/innexins
Neurotransmitter/neuromodulatory diversity	Neurons use the same neurotransmitters as vertebrates, but lack melatonin and adrenalin.	Enzymes involved in synthesis, transport, reception, and hydrolysis of serotonin, dopamine, noradrenaline, γ-aminobutryic acid (GABA), histamine, acetycholine, glycine, and nitric oxide
GPCR signaling	Identification of GPCRs that are unique to chordates and identification of expanded GPCR families.	Orthologs of vertebrate cannabinoid, lysophospholipid, and melanocortin receptors are absent; 162 secretin receptor-like genes
Peptide signaling	G protein–coupled peptide receptors indicate diversity in peptide signaling systems, but only a few sea urchin neuropeptides or peptide hormones identified.	37 G protein–coupled peptide receptors. Precursors for SALMFamides, NGFFFamide, and a vasotocin-like peptide
Neurotrophins	Neurotrophins and neurotrophin receptors are not unique to chordates.	Sp-Neurotrophin, Sp-Trk, Sp-p75NTR, ependymins
Insulin and IGFs	More similar to vertebrate forms than invertebrate insulin-like molecules.	Sp-IGF1, SpIGF2
Chemosensory functions	A large family of predicted chemoreceptor genes, some expressed in tube feet or pedicellariae, indicates a complex chemosensory system.	Over 600 genes encoding putative G protein–coupled chemoreceptors, many tandemly repeated and lacking introns
Photoreception functions	Genes associated with photoreception are expressed in tube feet.	Photorhodopsins, Sp-Pax6, retinal transcription factors
Mechanosensory functions	Orthologs of vertebrate mechanosensory genes are present.	Sp-Usherin, Sp-VLGR-1, Sp-cadherins, Sp-myosin 7, Sp-myosin 15, Sp-harmonin, Sp-whirlin, Sp-NBC, Sp-TrpA1

composition and organization (Reeler, EGF, BNR) that has not been found outside chordates, but the sea urchin genome included a very good homolog of reelin. Receptors for reelin are believed to include low-density lipoprotein receptor–related proteins (LRPs), and there are a number of these receptors in *S. purpuratus* although it is as yet unclear whether they are reelin receptors, lipoprotein receptors, or something else. Similar receptors are also involved in human disease (atherosclerosis).

Biomineralization Genes

Among the deuterostomes, only echinoderms and vertebrates produce extensive skeletons. The possible evolutionary relations between biomineralization processes in these two groups have been controversial. Analysis of the *S. purpuratus* genome revealed major differences in the proteins that mediate biomineralization in echinoderms and vertebrates (*50*). First, there were few sea urchin counterparts of extracellular proteins that mediate biomineral deposition in vertebrates. For example, in vertebrates, an important class of proteins involved in biomineralization is the family of secreted, calcium-binding phosphoproteins, or SCPPs. Sea urchins did not have counterparts of SCPP genes, which supports the hypothesis that this family arose via a series of gene duplications after the echinoderm-chordate divergence (*51*). Second, almost all of the proteins that have been directly implicated in the control of biomineralization in sea urchins were specific to that clade. The echinoderm skeleton consists of magnesium calcite (as distinct from the calcium phosphate skeletons of vertebrates) in which is occluded many secreted matrix proteins. The sea urchin spicule matrix proteins were encoded by a family of 16 genes that are organized in small clusters and likely proliferated by gene duplication. Counterparts of sea urchin spicule matrix genes were not found in vertebrates, amphioxus, or ascidians. Likewise, other genes that have been implicated in biomineralization in sea urchins, including genes that encode the transmembrane protein P16 and MSP130, a glycosylphosphatidylinositol-linked glycoprotein, were members of small clusters of closely related genes without apparent homologs in other deuterostomes. The members of all three of these sea urchin–specific gene families were expressed specifically by the biomineral-forming cells of the embryo, the primary mesenchyme cells [see (*50*)]. As a whole, these findings highlighted substantial differences in the primary sequences of the proteins that mediate biomineralization in echinoderms and vertebrates.

Cytoskeletal genes. In addition to identifying genes for all previously known *S. purpuratus* actins and tubulins, one δ- and two ε-tubulin genes were found (*52*). Newly identified motor protein genes include members of four more classes of myosin, and eight more families of kinesins. The first dynein cloned and sequenced was from sea urchin, and although most *S. purpuratus* dynein heavy chain genes mapped one-to-one to mammalian homologs, Sp-DNAH9 mapped one-to-three, as it was equidistant between the closely similar mammalian genes DNAH9, DNA11, and DNAH17 (*52*).

Conclusions

Our estimate of 23,300 genes is similar to estimates for vertebrates, despite the fact that two whole-genome duplications are believed to have occurred in the chordate lineage after divergence from the lineage leading to the echinoderms (*25*–*27*). From the analysis presented here, it seems likely that many mechanisms shaped the final genetic content of these genomes. On the one hand, there are cases of gene families that are expanded in vertebrates compared with sea urchin, including examples of the expected 4:1 ratio from two duplications (*15*). However other patterns are also found. The nuclear receptor family is only slightly reduced in sea urchin compared with that of humans, which suggests gene loss followed the vertebrate duplications. The unprecedented expansions of innate immune system diversity contrast sharply with the much smaller sets of counterparts that are present in the sequenced genomes of protostomes, *Ciona*, and vertebrates, an example of independent expansion in the sea urchin, whereas the GTPases described here have expanded in sea urchin to about the same numbers as in vertebrates. Thus, whereas the duplications of the chordate lineage were a contributor to the increased complexity of vertebrates, regional expansions clearly play a large role in the evolution of these animals.

The refinement of the inventory of vertebrate-specific or protostome-specific genes likewise benefits from the sea urchin genome. Many more human genes have shared ancestry across the deuterostomes, and in fact, bilaterian genes are more broadly shared than had been inferred from comparison of the previously limited genome sequences. The new biological niche sampled by the sea urchin genome provides not only a clearer view of the deuterostome and bilaterian ancestor, but has also provided a number of surprises. The finding of sea urchin homologs for sensory proteins related to vision and hearing in humans may lead to interesting new concepts of perception, and the extraordinary organization of the sea urchin immune system is different from any animal yet studied. From a practical standpoint, the sea urchin may be a treasure trove. Because of the many pathways shared by sea urchin and human, the sea urchin genome includes a large number of human disease gene orthologs. Many of the genes described in the preceding sections fall into this category (see tables S8 and S9) and cover a surprising diversity of systems such as nervous, endocrine, and blood systems, as well as muscle and skeleton, as exemplified by the Huntington and muscular dystrophy genes. Continued exploration of the sea urchin immune system is expected to uncover additional variations for protection against pathogens. The immense diversity of pathogen-binding motifs encoded in the sea urchin genome provides an invaluable resource for antimicrobial applications and the identification of new deuterostome immune functions with direct relevance to human health. These exciting possibilities show that much biodiversity is yet to be uncovered by sampling additional evolutionary branches of the tree of life.

References and Notes

1. R. A. Gibbs *et al.*, *Nature* **428**, 493 (2004).
2. W. W. Cai, R. Chen, R. A. Gibbs, A. Bradley, *Genome Res.* **11**, 1619 (2001).
3. R. J. Britten, A. Cetta, E. H. Davidson, *Cell* **15**, 1175 (1978).
4. P. Dehal *et al.*, *Science* **298**, 2157 (2002).
5. J. P. Vinson *et al.*, *Genome Res.* **15**, 1127 (2005).
6. R. T. Hinegardner, *Anal. Biochem.* **39**, 197 (1971).
7. C. G. Elsik, A. J. Mackey, J. T. Reese, N. V. Milshina, D. S. Roos, G. M. Weinstock, *Genome Biol*,. in press.
8. Sea Urchin Genome Project (http://sugp.caltech.edu/resources/annotation.php).
9. Genboree (www.genboree.org).
10. M. Samanta *et al.*, *Science* **314**, 960 (2006).
11. J. C. Sullivan *et al.*, *Nucleic Acids Res.* **34**, D495 (2006).
12. S. C. Materna, M. Howard-Ashby, R. F. Gray, E. H. Davidson, *Dev. Biol.* 10.1016/j.ydbio.2006.08.032, in press.
13. F. Raible *et al.*, *Dev. Biol.*, in press.
14. K. Grobben, *Verh. Zool. Bot. Ges. Wien* **58**, 491 (1908).
15. E. H. Davidson, in *Gene Regulatory Networks in Development and Evolution* (Academic Press/Elsevier, San Diego, CA, 2006).
16. E. H. Davidson *et al.*, *Science* **295**, 1669 (2002).
17. E. H. Davidson *et al.*, *Dev. Biol.* **246**, 162 (2002).
18. Z. Wei, R. C. Angerer, L. M. Angerer, *Dev. Biol.* 10.1016/j.ydbio.2006.08.034, in press.
19. D. H. Erwin, E. H. Davidson, *Development* **129**, 3021 (2002).
20. M. Howard-Ashby, C. T. Brown, S. C. Materna, L. Chen, E. H. Davidson, *Dev. Biol.*, in press.
21. G. Manning, G. D. Plowman, T. Hunter, S. Sudarsanam, *Trends Biochem. Sci.* **27**, 514 (2002).
22. G. Manning, D. B. Whyte, R. Martinez, T. Hunter, S. Sudarsanam, *Science* **298**, 1912 (2002).
23. C. Bradham *et al.*, *Dev. Biol.* 10.1016/j.ydbio.2006.08.074, in press.
24. C. Byrum *et al.*, *Dev. Biol.*, in press.
25. P. Dehal, J. L. Boore, *PLoS Biol.* **3**, e314 (2005).
26. X. Gu, Y. Wang, J. Gu, *Nat. Genet.* **31**, 205 (2002).
27. A. McLysaght, K. Hokamp, K. H. Wolfe, *Nat. Genet.* **31**, 200 (2002).
28. W. Beane, E. Voronina, G. M. Wessel, D. R. McClay, *Dev. Biol.* 10.1016/j.ydbio.2006.08.046, in press.
29. A. Kusserow *et al.*, *Nature* **433**, 156 (2005).
30. J. Croce *et al.*, *Dev. Biol.*, in press.
31. The Wnt homepage (www.stanford.edu/~rnusse/wntwindow.html).
32. C. A. Whittaker *et al.*, *Dev. Biol.* 10.1016/j.ydbio.2006.07.044, in press.
33. Z. Pancer, *Proc. Natl. Acad. Sci. U.S.A.* **97**, 13156 (2000).
34. Z. Pancer, J. P. Rast, E. H. Davidson, *Immunogenetics* **49**, 773 (1999).
35. S. Akira, S. Uematsu, O. Takeuchi, *Cell* **124**, 783 (2006).
36. S. D. Fugmann, C. Messier, L. A. Novack, R. A. Cameron, J. P. Rast, *Proc. Natl. Acad. Sci. U.S.A.* **103**, 3728 (2006).
37. V. V. Kapitonov, J. Jurka, *PLoS Biol.* **3**, e181 (2005).
38. J. P. Rast *et al.*, *Science* **314**, 952 (2006).
39. L. C. Smith, K. Azumi, M. Nonaka, *Immunopharmacology* **42**, 107 (1999).

40. L. C. Smith, L. A. Clow, D. P. Terwilliger, *Immunol. Rev.* **180**, 16 (2001).
41. T. Hibino *et al.*, *Dev. Biol.* 10.1016/j.ydbio.2006.08.065, in press.
42. J. Goldstone *et al.*, *Dev. Biol.* 10.1016/j.ydbio.2006.08.066, in press.
43. H. Qin, J. A. Powell-Coffman, *Dev. Biol.* **270**, 64 (2004).
44. J. A. Walisser, E. Glover, K. Pande, A. L. Liss, C. A. Bradfield, *Proc. Natl. Acad. Sci. U.S.A.* **102**, 17858 (2005).
45. D. M. Duncan, E. A. Burgess, I. Duncan, *Genes Dev.* **12**, 1290 (1998).
46. W. Xie, R. M. Evans, *J. Biol. Chem.* **276**, 37739 (2001).
47. R. D. Burke *et al.*, *Dev. Biol.* 10.1016/j.ydbio.2006.08.007, in press.
48. J. L. S. Cobb, in *Nervous Systems of Invertebrates*, M. A. Ali, Ed. (Plenum, New York, 1987), pp. 483–525.
49. J. L. Cobb, V. W. Pantreath, *Tissue Cell* **9**, 125 (1977).
50. B. T. Livingston *et al.*, *Dev. Biol.* 10.1016/j.ydbio.2006.07.047, in press.
51. K. Kawasaki, T. Suzuki, K. M. Weiss, *Proc. Natl. Acad. Sci. U.S.A.* **101**, 11356 (2004).
52. R. L. Morris *et al.*, *Dev. Biol.* 10.1016/j.ydbio.2006.08.052, in press.
53. E. V. Koonin, L. Aravind, *Cell Death Differ.* **9**, 394 (2002).

54. We gratefully acknowledge the following support: BCM-HGSC, National Human Genome Research Institute (NIH) grant 5 U54 HG003273; Naples Workshop, Stazione Zoologica Naples and the Network of Excellence "Marine Genomics Europe" (GOCE-04-505403); M. Elphick, Biotechnology and Biological Sciences Research Council (BBSRC), UK, grant S19916; J. Rast laboratory, Natural Sciences and Engineering Research Council (NSERC) of Canada, Canadian Institutes of Health Research (CIHR), and the Uehara Memorial Foundation; J. A. Coffman, **Mount Desert Island Biological Laboratory** (MDIBL), NIH grant GM070840; M. C. Thorndyke, K. H. Wilson, F. Hallböök, R. P. Olinski, Swedish Science Research Council, Network of Excellence Marine Genomics Europe (GOCE-04-505403), European Union Research Training Networks FP5 Trophic Neurogenome HPRN-ct-2002-00263, and the Royal Swedish Academy of Sciences, STINT; E. H. Davidson, R. A. Cameron, the Center for Computational Regulatory Genomics (E. H. Davidson, principal investigator) was supported by the NIH grant RR-15044, NSF IOB-0212869, and the Beckman Institute; also, support for the E. H. Davidson laboratory is from NIH grants HD-37105 and GM61005 and U.S. Department of Energy (DOE) grant DE-FG02-03ER63584; P. Oliveri, Camilla Chandler Frost Fellowship; G. M. Wessel laboratory supported by NSF IOB-0620607 and NIH grant R01 HD028152; B. Brandhorst, K. Bergeron, and N. Chen, NSERC; K. R. Foltz, NSF, IBN-0415581; M. Hahn, NIH grant R01ES006272; D. Burgess, NIH grant GM058231; L. C. Smith, NSF (MCB-0424235); R. O. Hynes, Howard Hughes Medical Institute and National Cancer Institute (NCI) (MIT Cancer Center core grant P30-CA14051); D. McClay, NIH grants GM61464, HD039948, and HD14483; V. D. Vacquier (group leader), G. W. Moy, H. J. Gunaratne, M. Kinukawa, M. Nomura, A. T. Neill, and Y.-H. Su, NIH grant R37-HD12896; R. D. Burke, NSERC and CIHR; L. M. Angerer, National Institute of Dental and Craniofacial Research (NIDCR), R. C. Angerer (NIDCR), Z. Wei (NIDCR), G. Humphrey, National Institute of Child Health and Human Development (NICHD), M. Landrum, National Center for Biotechnology Information (NCBI), O. Ermolaeva (NCBI), P. Kitts (NCBI), K. Pruitt (NCBI), V. Sapojnikov (NCBI), A. Souvorov (NCBI), W. Hiavina (NCBI), S. Fugmann, National Institute on Aging (NIA), M. Dean, National Cancer Institute–Frederick (NCIFCRF) Intramural Research Program of the NIH; P. Cormier, Association pour la Recherche contre la Cancer (ARC), France, grants 4247 and 3507 to P.C., Ligue Nationale contre le Cancer to P.C., Conseil Régional de Bretagne and Conseil Général du Finistère; W. H. Klein, National Eye Institute, NIH grant EY11930, NICHD HD66219, and the Robert A. Welch Foundation (G-0010); N. Adams, NSF grant IBN 0417003 and the Department of the Navy, Office of Naval Research, under Award N00014-05-1-0855; D. Epel, NSF 0417225; A. Hamdoun, F32-HD47136; C. Byrum, American Heart Association grant 0420074Z; K. Walton, U.S. Army Medical Research and Materiel Command grant W81XWH-04-1-0324; J. Stegeman, NIH 2P42 ESO7381; and J. Goldstone, NIH F32 ESO12794.

Sea Urchin Genome Sequencing Consortium

Overall project leadership: Erica Sodergren,[1,2] George M. Weinstock,[1,2] Eric H. Davidson,[3] R. Andrew Cameron[3]

Principal investigators: Richard A. Gibbs,[1,2] George M. Weinstock[1,2]

Annotation section leaders: Robert C. Angerer,[4] Lynne M. Angerer,[4] Maria Ina Arnone,[5] David R. Burgess,[6] Robert D. Burke,[7] R. Andrew Cameron,[3] James A. Coffman,[8] Eric H. Davidson,[3] Michael Dean,[9] Maurice R. Elphick,[10] Charles A. Ettensohn,[11] Kathy R. Foltz,[12] Amro Hamdoun,[13] Richard O. Hynes,[14] William H. Klein,[15] William Marzluff,[16] David R. McClay,[17] Robert L. Morris,[18] Arcady Mushegian,[19,20] Jonathan P. Rast,[21] Erica Sodergren,[1,2] L. Courtney Smith,[23] Michael C. Thorndyke,[24] Victor D. Vacquier,[24] George M. Weinstock,[1,2] Gary M. Wessel,[26] Greg Wray,[27] Lan Zhang[1,2]

Annotation: Gene list: Erica Sodergren[1,2] (leader), George M. Weinstock[1,2] (leader), Robert C. Angerer,[4] Lynne M. Angerer,[4] R. Andrew Cameron,[3] Eric H. Davidson,[3] Christine G. Elsik,[27] Olga Ermolaeva,[29] Wratko Hlavina,[29] Gretchen Hofmann,[30] Paul Kitts,[28] Melissa J. Landrum,[28] Aaron J. Mackey,[32*] Donna Maglott,[28] Georgia Panopoulou,[33] Albert J. Poustka,[33] Kim Pruitt,[28] Victor Sapojnikov,[29] Xingzhi Song,[1,2] Alexandre Souvorov,[28] Victor Solovyev,[34] Zheng Wei,[4] Charles A. Whittaker,[35] Kim Worley,[1,2] Lan Zhang[1,2]

Assembly of genome: Erica Sodergren[1,2] (leader), George M. Weinstock[1,2] (leader), K. James Durbin,[1,2] Richard A. Gibbs,[1,2] Yufeng Shen[1,2] (v 2.1), Xingzhi Song[1,2] (v 0.5), Kim Worley,[1,2] Lan Zhang[1,2]

Basal transcription apparatus proteins and polymerases chromatin proteins: Greg Wray[27] (leader), Olivier Fedrigo,[26] David Garfield,[27] Ralph Haygood,[17] Alexander Primus,[26] Rahul Satija,[26] Tonya Severson[27]

BCM-HGSC annotation database and Genboree: Lan Zhang[1,2] (leader), Erica Sodergren[1,2] (leader), George M. Weinstock[1,2] (leader), Manuel L. Gonzalez-Garay,[1,2] Andrew R. Jackson,[1,2] Aleksandar Milosavljevic,[1,2] Xingzhi Song,[1,2] Mark Tong,[1,2] Kim Worley[1,2]

Biomineralization: Charles A. Ettensohn[11] (leader), R. Andrew Cameron,[3] Christopher E. Killian,[36] Melissa J. Landrum,[31] Brian T. Livingston,[37] Fred H. Wilt[36]

Cell physiology: James A. Coffman[8] (leader), William Marzluff[16] (leader), Arcady Mushegian[19,20] (leader), Nikki Adams,[37] Robert Bellé,[38,39] Seth Carbonneau,[8] Rocky Cheung,[16] Patrick Cormier,[38,39] Bertrand Cosson,[38,39] Jenifer Croce,[17] Antonio Fernandez-Guerra,[40,41] Anne-Marie Genevière,[40,41] Manisha Goel,[19] Hemant Kelkar,[42] Julia Morales,[38,39] Odile Mulner-Lorillon,[39,40] Anthony J. Robertson[8]

Cellular defense: Amro Hamdoun[13] (leader), Jared V. Goldstone[42] (leader), Nikki Adams,[36] Bryan Cole,[13] Michael Dean,[9] David Epel,[13] Bert Gold,[9] Mark E. Hahn,[43] Meredith Howard-Ashby,[3] Mark Scally,[9] John J. Stegeman[43]

Ciliogenesis and ciliary compounds: Robert L. Morris[18] (leader), Erin L. Allgood,[18] Jonah Cool,[18] Kyle M. Judkins,[18] Shawn S. McCafferty,[18] Ashlan M. Musante,[18] Robert A. Obar,[44]† Amanda P. Rawson,[18] Blair J. Rossetti[18]

Cytoskeletal and organelle genes: David R. Burgess[6] (leader), Erin L. Allgood,[18] Jonah Cool,[18] Ian R. Gibbons,[45] Matthew P. Hoffman,[6] Kyle M. Judkins,[18] Andrew Leone,[6] Shawn S. McCafferty,[18] Robert L. Morris,[18] Ashlan M. Musante,[18] Robert A. Obar,[44]† Amanda P. Rawson,[18] Blair J. Rossetti,[18] Gary M. Wessel[26]

Embryonic transcriptome: Eric H. Davidson[3] (leader), R. Andrew Cameron,[3] Sorin Istrail,[46] Stefan C. Materna,[3] Manoj P. Samanta,[47,48] Viktor Stolc,[47] Waraporn Tongprasit,[47] Qiang Tu[3]

Embryonic temporal expression pattern list: Robert C. Angerer[4] (leader), Lynne M. Angerer[4] (leader), Zheng Wei[4]

Echinoderm adhesome: Richard O. Hynes[14] (leader), Karl-Frederik Bergeron,[49] Bruce P. Brandhorst,[50] Robert D. Burke,[7] Charles A. Whittaker,[35] James Whittle[51]

Echinoderm evolution: R. Andrew Cameron[3] (leader), Kevin Berney,[3] David J. Bottjer,[51] Cristina Calestani,[53] Eric H. Davidson,[3] Kevin Peterson,[54] Elly Chow,[55] Qiu Autumn Yuan[55]

Genome analysis [GC content]: Eran Elhaik,[56] Christine G. Elsik,[28] Dan Graur,[56] Justin T. Reese[28]

Genome FPC map: Ian Bosdet,[57] Shin Heesun,[57] Marco A. Marra,[57] Jacqueline Schein[57]

Human genetic disease orthologs: Michael Dean[9] (leader), Amro Hamdoun[13] (leader), The Sea Urchin Genome Sequencing Consortium

Immunity: Jonathan P. Rast[21] (leader), L. Courtney Smith[23] (leader), Michele K. Anderson,[22] Kevin Berney,[3] Virginia Brockton,[23] Katherine M. Buckley,[23] R. Andrew Cameron,[3] Avis H. Cohen,[58] Sebastian D. Fugmann,[59] Taku Hibino,[21] Mariano Loza-Coll,[21] Audrey J. Majeske,[23] Cynthia Messier,[21] Sham V. Nair,[60] Zeev Pancer,[61] David P. Terwilliger[22]

Neurobiology and sensory systems: Robert D. Burke[7] (leader), Maurice R. Elphick[10] (leader), William H. Klein[15] (leader), Michael C. Thorndyke[24] (leader), Cavit Agca,[62] Lynne M. Angerer,[4] Enrique Arboleda,[5] Maria Ina Arnone,[5] Bruce P. Brandhorst,[50] Nansheng Chen,[50] Allison M. Churcher,[63] F. Hallböök,[64] Glen W. Humphrey,[65] Richard O. Hynes,[14] Mohammed M. Idris,[5] Takae Kiyama,[15] Shuguang Liang,[15] Dan Mellott,[60] Xiuqian Mu,[15] Greg Murray,[48] Robert P. Olinski,[64] Florian Raible,[66,67] Matthew Rowe,[10] John S. Taylor,[63] Kristin Tessmar-Raible,[66] D. Wang,[63] Karen H. Wilson,[24] Shunsuke Yaguchi[7]

Reproduction: Kathy R. Foltz[12] (leader), Victor D. Vacquier[25] (leader), Gary M. Wessel[26] (leader), Terry Gaasterland,[25] Blanca E. Galindo,[67] Herath J. Gunaratne,[25] Meredith Howard-Ashby,[3] Glen W. Humphrey,[65] Celina Juliano,[26] Masashi Kinukawa,[25] Gary W. Moy,[25] Anna T. Neill,[25] Mamoru Nomura,[25] Michael Raisch,[12] Anna Reade,[12] Michelle M. Roux,[12] Jia L. Song,[25] Yi-Hsien Su,[3] Ian K. Townley,[12] Ekaterina Voronina,[26] Julian L. Wong[26]

Sea Urchin Genome Annotation Workshop in Naples: Maria Ina Arnone[5] (leader), Michael C. Thorndyke[24] (leader), Gabriele Amore,[5] Lynne M. Angerer,[4] Enrique Arboleda,[5] Margherita Branno,[5] Euan R. Brown,[5] Vincenzo Cavalieri,[69] Véronique Duboc,[70] Louise Duloquin,[70] Maurice R. Elphick,[10] Constantin Flytzanis,[70,71] Christian Gache,[70] Anne-Marie Genevière,[40,41] Mohammed M. Idris,[5] François Lapraz,[70] Thierry Lepage,[70] Annamaria Locascio,[5] Pedro Martinez,[73,74] Giorgio Matassi,[75] Valeria Matranga,[76] David R. McClay,[17] Julia Morales,[38,39] Albert J. Poustka,[33] Florian Raible,[66,67] Ryan Range,[70] Francesca Rizzo,[5] Eric Röttinger,[70] Matthew Rowe,[10] Kristin Tessmar-Raible,[66] Erica Sodergren,[1,2] George M. Weinstock,[1,2] Karen Wilson[24]

Signal transduction: David R. McClay[17] (leader), Lynne M. Angerer,[4] Maria Ina Arnone,[5] Wendy Beane,[17] Cynthia Bradham,[17] Christine Byrum,[17,78] Jenifer Croce,[17] Veronique Duboc,[70] Louise Duloquin,[70] Christian Gache,[70] Anne-Marie Genevière,[40,41] Tom Glenn,[17] Taku Hibino,[22] Sofia Hussain,[37] François Lapraz,[70] Thierry Lepage,[70] Brian T. Livingston,[37] Mariano Loza,[21] Gerard Manning,[76] Esther Miranda,[17] Ryan Range,[70] Francesca Rizzo,[5] Eric Röttinger,[70] Rebecca Thomason,[17,78] Katherine Walton,[17] Zheng Wei,[4] Gary M. Wessel,[26] Athula Wikramanayke,[77] Karen H. Wilson,[23] Charles Whittaker,[35] Shu-Yu Wu,[17] Ronghui Xu[78]

Transcription regulatory factors: Eric H. Davidson[3] (leader), Maria Ina Arnone,[5] Margherita Branno,[5] C. Titus Brown,[3] R. Andrew Cameron,[3] Lili Chen,[3] Rachel F. Gray,[3] Meredith Howard-Ashby,[3] Sorin Istrail,[46] Pei Yun Lee,[3] Annamaria Locascio,[5] Pedro Martinez,[73,74] Stefan C. Materna,[3] Jongmin Nam,[3] Paola Oliveri,[3] Francesca Rizzo,[5] Joel Smith[3]

DNA sequencing: Donna Muzny[1,2] (leader), Erica Sodergren[1,2] (leader), Richard A. Gibbs[1,2] (leader), George M. Weinstock[1,2] (leader), Stephanie Bell,[1,2] Joseph Chacko,[1,2] Andrew Cree,[1,2] Stacey Curry,[1,2] Clay Davis,[1,2] Huyen Dinh,[1,2] Shannon Dugan-Rocha,[1,2] Jerry Fowler,[1,2] Rachel Gill,[1,2] Cerrissa Hamilton,[1,2] Judith Hernandez,[1,2] Sandra Hines,[1,2] Jennifer Hume,[1,2] LaRonda Jackson,[1,2] Angela Jolivet,[1,2] Christie Kovar,[1,2] Sandra Lee,[1,2] Lora Lewis,[1,2] George Miner,[1,2] Margaret Morgan,[1,2] Lynne V. Nazareth,[1,2] Geoffrey Okwuonu,[1,2] David Parker,[1,2] Ling-Ling Pu,[1,2] Yufeng Shen,[1,2] Rachel Thorn,[1,2] Rita Wright[1,2]

[1]Human Genome Sequencing Center, Baylor College of Medicine, One Baylor Plaza, Houston, TX 77030, USA. [2]Department of Molecular and Human Genetics, Baylor College of Medicine, One Baylor Plaza, Houston, TX 77030, USA. [3]Division of Biology, California Institute of Technology, Pasadena, CA 91125, USA. [4]National Institute of Dental and Craniofacial Research, NIH, Bethesda, MD

20892, USA. [5]Stazione Zoologica Anton Dohrn, Villa Comunale, 80121 Napoli, Italy. [6]Department of Biology, Boston College, Chestnut Hill, MA 02467, USA. [7]Department of Biology, Department of Biochemistry and Microbiology, University of Victoria, Victoria, BC, Canada, V8W 3N5. [8]Mount Desert Island Biological Laboratory, Salisbury Cove, ME 04672, USA. [9]Human Genetics Section, Laboratory of Genomic Diversity, National Cancer Institute–Frederick, Frederick, MD 21702, USA. [10]School of Biological and Chemical Sciences, Queen Mary, University of London, London E1 4NS, UK. [11]Department of Biological Sciences, Carnegie Mellon University, Pittsburgh, PA, 15213, USA. [12]Department Molecular, Cellular and Developmental Biology and the Marine Science Institute, University of California, Santa Barbara, Santa Barbara, CA 93106–9610, USA. [13]Hopkins Marine Station, Stanford University, Pacific Grove, CA 93950, USA. [14]Howard Hughes Medical Institute, Center for Cancer Research, Massachusetts Institute of Technology (MIT), Cambridge, MA 02139, USA. [15]Departments of Biochemistry and Molecular Biology, University of Texas, M. D. Anderson Cancer Center, Houston, TX, 77030, USA. [16]Molecular Biology and Biotechnology, University of North Carolina at Chapel Hill, Chapel Hill, NC 27599, USA. [17]Department of Biology, Duke University, Durham, NC 27708, USA. [18]Department of Biology, Wheaton College, Norton, MA 02766, USA. [19]Stowers Institute for Medical Research, Kansas City, MO 64110, USA. [20]Department of Microbiology, Kansas University Medical Center, Kansas City, KS 66160, USA. [21]Sunnybrook Research Institute and Department of Medical Biophysics, University of Toronto, Toronto, Ontario, Canada M4N 3M5. [22]Department of Immunology, University of Toronto, Toronto, Ontario, Canada, M4N 3M5. [23]Department of Biological Sciences, George Washington University, Washington, DC 20052, USA. [24]Royal Swedish Academy of Sciences, Kristineberg Marine Research Station, Fiskebackskil, 450 34, Sweden. [25]Marine Biology, Scripps Institution of Oceanography, University of California San Diego, La Jolla, CA 92093–0202, USA. [26]Department of Molecular and Cellular Biology and Biochemistry, Brown University Providence, RI 02912, USA. [27]Department of Biology and Institute for Genome Sciences and Policy, Duke University, Durham, NC 27708, USA. [28]Department of Animal Science, Texas A&M University, College Station, TX 77843, USA. [29]National Center for Biotechnology Information, National Library of Medicine, NIH, Bethesda, MD 20894, USA. [30]Department of Ecology, Evolution, and Marine Biology, University of California Santa Barbara, Santa Barbara, CA 93106, USA. [31]National Center for Biotechnology Information, NIH, Bethesda, MD 20892, USA. [32]Penn Genomics Institute, University of Pennsylvania, Philadelphia, PA 19104, USA. [33]Evolution and Development Group, Max-Planck Institut für Molekulare Genetik, 14195 Berlin, Germany. [34]Royal Holloway, University of London, Egham, Surrey TW20 0EX, UK. [35]Center for Cancer Research, MIT, Cambridge, MA 02139, USA. [36]Department of Molecular and Cell Biology, University of California, Berkeley, Berkeley, CA 94720–3200, USA. [37]Department of Biology, University of South Florida, Tampa, FL 33618, USA. [38]Université Pierre et Marie Curie (Paris 6), UMR 7150, Equipe Cycle Cellulaire et Développement, Station Biologique de Roscoff, 29682 Roscoff Cedex, France. [39]CNRS, UMR 7150, Station Biologique de Roscoff, 29682 Roscoff Cedex, France. [40]CNRS, UMR7628, Banyuls-sur-Mer, F-66650, France. [41]Université Pierre et Marie Curie (Paris 6), UMR7628, Banyuls-sur-Mer, F-66650, France. [42]Center for Bioinformatics, University of North Carolina at Chapel Hill, Chapel Hill, NC 27599, USA. [43]Biology Department, Woods Hole Oceanographic Institution, Woods Hole, MA 02543, USA. [44]Tethys Research, LLC, 2115 Union Street, Bangor, Maine 04401, USA. [45]Department of Molecular, Cellular, and Developmental Biology, University of California, Berkeley, Berkeley, CA 94720, USA. [46]Center for Computational Molecular Biology, and Computer Science Department, Brown University, Providence, RI 02912, USA. [47]Genome Research Facility, National Aeronautics and Space Administration, Ames Research Center, Moffet Field, CA 94035, USA. [48]Systemix Institute, Cupertino, CA 95014, USA. [49]Department of Molecular Biology and Biochemistry, Simon Fraser University, Burnaby, British Columbia, Canada, V5A 1S6. [50]Department of Molecular Biology and Biochemistry, Simon Fraser University, Burnaby, BC, Canada, V5A 1S6. [51]Department of Biology, Center for Cancer Research, MIT, Cambridge, MA 02139, USA. [52]Department of Earth Sciences, University of Southern California, Los Angeles, CA 90089–0740, USA. [53]Department of Biology, University of Central Florida, Orlando, FL 32816–2368, USA. [54]Department of Biological Sciences, Dartmouth College, Hanover, NH 03755, USA. [55]Center for Computational Regulatory Genomics, Beckman Institute, California Institute of Technology, Pasadena, CA 91125, USA. [56]Department of Biology and Biochemistry, University of Houston, Houston, TX 77204, USA. [57]Genome Sciences Centre, British Columbia Cancer Agency, Vancouver, BC, Canada, V5Z 4E6. [58]Department of Biology and the Institute of Systems Research, University of Maryland, College Park, MD 20742, USA. [59]Laboratory of Cellular and Molecular Biology, National Institute on Aging, NIH, Baltimore, MD 21224, USA. [60]Department of Biological Sciences, Macquarie University, Sydney NSW 2109, Australia. [61]Center of Marine Biotechnology, UMBI, Columbus Center, Baltimore, MD 21202, USA. [62]Department of Cell Biology and Anatomy, Louisiana State University Health Sciences Center, New Orleans, LA 70112, USA. [63]Department of Biology, University of Victoria, Victoria, BC, Canada, V8W 2Y2. [64]Department of Neuroscience, Uppsala University, Uppsala, Sweden. [65]Laboratory of Cellular and Molecular Biophysics, National Institute of Child Health and Development, NIH, Bethesda, MD 20895, USA. [66]Developmental Unit, EMBL, 69117 Heidelberg, Germany. [67]Computational Unit, EMBL, 69117 Heidelberg, Germany. [68]Biotechnology Institute, Universidad Nacional Autónoma de Mexico (UNAM), Cuernavaca, Morelos, Mexico 62250. [69]Department of Cellular and Developmental Biology "Alberto Monroy," University of Palermo, 90146 Palermo, Italy. [70]Laboratoire de Biologie du Développement (UMR 7009), CNRS and Université Pierre et Marie Curie (Paris 6), Observatoire Océanologique, 06230 Villefranche-sur-Mer, France. [71]Department of Biology, University of Patras, Patras, Greece. [72]Department of Molecular and Cellular Biology, Baylor College of Medicine, One Baylor Plaza, Houston, TX 77030, USA. [73]Departament de Genetica, Universitat de Barcelona, 08028–Barcelona, Spain. [74]Institució Catalana de Recerca i Estudis Avancats (ICREA), Barcelona, Spain. [75]Institut Jacques Monod, CNR-UMR 7592, 75005 Paris, France. [76]Consiglio Nazionale delle Ricerche, Istituto di Biomedicina e Immunologia Molecolare "Alberto Monroy," 90146 Palermo, Italy. [77]Razavi-Newman Center for Bioinformatics, Salk Institute for Biological Studies, La Jolla, CA 92186, USA. [78]Department of Zoology, University of Hawaii at Manoa, Honolulu, HI 96822, USA.

*Present address: GlaxoSmithKline, 1250 South Collegeville Road, Collegeville, PA 19426, USA.
†Present address: Massachusetts General Hospital Cancer Center, Charlestown, MA 02129, USA.

Supporting Online Material
www.sciencemag.org/cgi/content/full/314/5801/941/DC1
Materials and Methods
SOM Text
Figs. S1 to S6
Tables S1 to S8
Reference

8 August 2006; accepted 17 October 2006
10.1126/science.1133609

REVIEW

Genomic Insights into the Immune System of the Sea Urchin

Jonathan P. Rast,[1]* L. Courtney Smith,[2] Mariano Loza-Coll,[1] Taku Hibino,[1] Gary W. Litman[3,4]

Comparative analysis of the sea urchin genome has broad implications for the primitive state of deuterostome host defense and the genetic underpinnings of immunity in vertebrates. The sea urchin has an unprecedented complexity of innate immune recognition receptors relative to other animal species yet characterized. These receptor genes include a vast repertoire of 222 Toll-like receptors, a superfamily of more than 200 NACHT domain–leucine-rich repeat proteins (similar to nucleotide-binding and oligomerization domain (NOD) and NALP proteins of vertebrates), and a large family of scavenger receptor cysteine-rich proteins. More typical numbers of genes encode other immune recognition factors. Homologs of important immune and hematopoietic regulators, many of which have previously been identified only from chordates, as well as genes that are critical in adaptive immunity of jawed vertebrates, also are present. The findings serve to underscore the dynamic utilization of receptors and the complexity of immune recognition that may be basal for deuterostomes and predicts features of the ancestral bilaterian form.

Animal immune mechanisms are classified as acquired (adaptive), in which immune recognition specificity is the product of somatic diversification and selective clonal proliferation, or as innate, in which recognition specificity is germline encoded. Collectively, these systems act to protect the individual from invasive bacteria, viruses, and eukaryotic pathogens by detecting molecular signatures of infection and initiating effector responses. Innate immune mechanisms probably originated early in animal phylogeny and are closely allied with wound healing and tissue maintenance functions. In many cases, their constituent elements are distributed throughout the cells of the organism. In bilaterally symmetrical animals (Bilateria), immune defense is carried out and tightly coordinated by a specialized set of mesoderm-derived cells that essentially are committed to this function (*1*–*3*). Overlaid onto this conserved core of developmental and immune programs are a variety of rapidly evolving recognition and

ERRATUM

Post date 9 February 2007

Research Articles: "The genome of the sea urchin *Strongylocentrotus purpuratus*" by Sea Urchin Genome Sequencing Consortium (10 Nov. 2006, p. 941). On pages 951 and 952, errors were made in renumbering authors' affiliations: Some changes were missed, and the affiliation for Nikki Adams was omitted. C. G. Elsik, T. Hibino, and V. D. Vacquier appear twice. C. G. Elsik is at Texas A&M University; T. Hibino is at the Sunnybrook Research Institute and Department of Medical Biophysics, University of Toronto; V. D. Vacquier is at the Scripps Institution of Oceanography. Corrected group affiliations, then individuals alphabetically: P. Kitts, M. J. Landrum, D. Maglott, K. Pruitt, A. Souvorov, National Center for Biotechnology Information, National Library of Medicine, Bethesda, MD 20894, USA. O. Fedrigo, A. Primus, R. Satija, Department of Biology and Institute for Genome Sciences and Policy, Duke University, Durham, NC 27708, USA. Nikki Adams, Biology Department, California Polytechnic State University, San Luis Obispo, CA 93407, USA. C. Flytzanis, Department of Biology, University of Patras, Patras, Greece, and the Department of Molecular and Cellular Biology, Baylor College of Medicine, One Baylor Plaza, Houston, TX 77030, USA. B. E. Galindo, Biotechnology Institute, Universidad Nacional Autónoma de Mexico (UNAM), Cuernavaca, Morelos, Mexico 62250. J. V. Goldstone, Department of Molecular, Cellular, and Developmental Biology, University of California, Berkeley, Berkeley, CA 94720, USA. G. Manning, Razavi-Newman Center for Bioinformatics, Salk Institute for Biological Studies, La Jolla, CA 92186, USA. D. Mellott, Center of Marine Biotechnology, University of Maryland Biotechnology Institute, Columbus Center, Baltimore, MD 21202, USA. J. Song, Department of Molecular and Cellular Biology and Biochemistry, Brown University, Providence, RI 02912, USA. D. P. Terwilliger, Department of Biological Sciences, George Washington University, Washington, DC 20052, USA. A. Wikramanayake, Department of Zoology, University of Hawaii at Manoa, Honolulu, HI 96822, USA.

effector mechanisms, which likely are responsive to the dynamic nature of host-pathogen interactions (*4*) and are among the most rapidly evolving animal systems (*5*).

For a variety of reasons, the field of immunology has been overwhelmingly focused on the rearranging adaptive immune system, which is based on the activities of immunoglobulin and T cell–antigen receptors (TCR) and which, at this point, seems to be restricted to the jawed vertebrates (*6*). Interest in comparative approaches to immunity was broadened by the recognition of common features of innate immunity between *Drosophila melanogaster* (fruit fly) and mammals (*7*, *8*). Recent findings suggest that somatic mechanisms of receptor diversification analogous to those of the acquired system of jawed vertebrates may be a more widespread feature of animal immunity than previously supposed. Examples of these include a gene conversion–like process that diversifies variable leucine-rich repeat (LRR)–containing receptor (VLR) proteins in jawless vertebrates (*9*, *10*), somatic mutation of fibrinogen-related protein (FREP) receptors in a mollusc (*11*), and extensive alternative splicing of the Down syndrome cell adhesion molecule (DSCAM), a molecule that principally guides neuronal patterning, to generate immune reactive isoforms in insects (*12*, *13*). On the basis of this narrow sampling, it is likely that a universe of novel and dynamic immune mechanisms exists among the invertebrates, further validating their role as significant immune models.

Of the ~30 bilaterian phyla that are recognized, only chordates, molluscs, nematodes, arthropods, and echinoderms have been the subject of extensive molecular immune research (Fig. 1). The overwhelming majority of functional and genetic data regarding immune systems comes from just two animal phyla: Chordata (mainly from mammals) and Arthropoda (*D. melanogaster*). Comprehensive genomic analyses of immunity also have been conducted in three other invertebrate species, the sea squirt (*Ciona intestinalis*) (*14*), the mosquito (*Anopheles gambiae*) (*15*), and the nematode worm (*Caenorhabditis elegans*) (*16*). More focused molecular studies include investigations of an immunelike transplantation reaction in *Botryllus schlosseri* (a urochordate) (*17*) and the immune response of a gastropod mollusc, *Biomphalaria glabrata,* to trematode parasites (*11*). Here we describe highlights from a community-wide genome analysis effort (*18*) on the purple sea urchin, *Strongylocentrotus purpuratus*, a member of the phylum Echinodermata, with both biological and phylogenetic attributes that are of compelling interest from an immune perspective.

[1]Sunnybrook Research Institute and Department of Medical Biophysics, University of Toronto, 2075 Bayview Avenue, Room S-126B, Toronto, Ontario M4N 3M5, Canada. [2]Department of Biological Sciences, George Washington University, 2023 G Street, NW, Washington, DC 20052, USA. [3]Department of Pediatrics, University of South Florida (USF) College of Medicine, USF/ACH (All Children's Hospital) Children's Research Institute, St. Petersburg, FL 33701, USA. [4]H. Lee Moffitt Cancer Center and Research Institute, Tampa, FL 33612, USA.

*To whom correspondence should be addressed. E-mail: jrast@sri.utoronto.ca

Genes Related to Immune Function in the Sea Urchin

It is likely that between 4 and 5% of the genes identified in the sea urchin genome are involved directly in immune functions (*18*). Considering only those components that exhibit distinct homology to forms found in other phyla, the repertoire of immune-related genes (*18*) that has been shown to participate in the recognition of conserved pathogen-associated molecular patterns (PAMPs) includes 222 Toll-like receptor (TLR) genes, 203 NACHT domain–LRR (NLR) genes with similarity to vertebrate nucleotide-binding and oligomerization domain (NOD)/NALP cytoplasmic receptors (*19*), and a greatly expanded superfamily of 218 gene models encoding scavenger receptor cysteine-rich (SRCR) proteins (*20*, *21*). In considering these estimates, it is critical to note that the sea urchin genome sequence was derived from sperm taken from a single animal (*18*). Although in certain cases inadvertent inclusion of both haplotypes in genome assembly may artificially inflate estimations of complexity of multigene families, this risk is likely to be small for the gene sets that we report here and, in any event, would not change the major conclusion of the findings [see supporting online material (SOM) for a more detailed explanation]. Furthermore, gene expansion is not a uniform characteristic of immune genes in sea urchin. Other classes of immune mediators, such as key components of the complement system, peptidoglycan-recognition proteins (PGRPs), and Gram-negative binding proteins (GNBPs) are equivalent in numbers to their homologs in protostomes and other deuterostomes.

Of the three major expansions of multigene families encoding immune genes, the TLRs are particularly informative. Two broad categories of these genes can be recognized: a greatly expanded multigene family consisting of 211 genes and a more limited group of 11 divergent genes (*22*), which includes 3 genes with ectodomain structures characteristic of most protostome TLR proteins, such as *Drosophila Toll* (*23*) (Fig. 2A). The latter findings suggest that TLRs of this form were present in the common bilaterian ancestor and subsequently were lost in the vertebrate lineage. The expanded set of sea urchin TLRs (211 genes) consists of vertebrate-like structures, of which many appear to have been duplicated recently. Within subfamilies of these vertebrate-like genes [defined by clustering in phylogenetic analysis (Fig. 2B)], hypervariability is regionalized in particular LRRs (*22*). These patterns of intergenic variation and the high prevalence of apparent pseudogenes (25 to 30%) suggest that the evolution of the sea urchin TLR genes is dynamic with a high gene turnover rate and could reflect rapidly evolving recognition specificities. By comparison, the relatively few TLR genes found in vertebrates derive from an ancient vertebrate diversification that appears to have been stabilized by selection for binding to invariant PAMPs (*24*).

It is unclear at present what aspects of sea urchin biology drive the differences in size and diversity of the expanded multigene families of innate receptors (we speculate on this below), but the characteristics of the TLR genes and their putative downstream signal mediators may have some bearing on their mode of function. It is likely that such a large and variable family recognizes pathogens directly rather than through intermediate molecules, as reported in insects (*25*). The moderate expansion of immediate downstream adaptors of TLR signaling that contain the Toll–interleukin 1 receptor (TIR) domain (four Myd88-like and 22 other cytoplasmic TIR domain adaptor genes) may serve to partition cellular responses after recognition by different classes of TLR proteins. In contrast, the lack of multiplicity of genes encoding the kinases and of transcription factors further downstream in the TLR signaling pathway resembles that observed in other species (*22*). This narrowed molecular complexity from the cell surface to the nucleus may mean that specificity of downstream cellular responses with respect to activation by different TLRs (if it exists) arises within the context of their restricted expression, as is the case for diversity in vertebrate adaptive systems. In certain general respects, the patterns of variation (Fig. 2B), the apparently rapid gene turnover rate, and the tandem genetic linkage of TLRs (Fig. 2C) resemble the multiplicity and diversity of the germline components of somatically variable adaptive immune receptors of vertebrates (*6*) and, taken together, they suggest that similar selective forces have molded their function.

Diverse TLRs are expressed by coelomocytes in the sea urchin (*22*). Furthermore, marked variation in the relative levels of expression is seen for different TLR subfamilies that is not strictly correlated with gene family size (fig. S1). In principle, restricted combinatorial expression of TLRs on individual immunocytes could generate a highly diverse range of individual functional specificities and, if shown to be the case, would provide one explanation for the observed patterns of TLR diversity. Combinatorial utilization within the more limited range of TLRs has been shown for mammals (*26*).

Some sea urchin TLR subgroup members are linked in large tandem arrays of identically oriented genes that appear to have been duplicated and diversified recently (Fig. 2C). Within this genomic context, the possibility exists for exclusive regulatory control. Both the linkage in direct tandem arrays and intergenic sequence

identity of the TLRs may promote gene diversification through duplication and/or deletion, gene conversion, recombination, and meiotic mispairing of alleles, followed by unequal crossovers as has been shown for plant disease resistance genes (*27*). The clustered genomic organization of sea urchin TLR genes resembles that seen in olfactory receptors, which exhibit clonal restriction in the absence of DNA-level rearrangement (*28*, *29*). As innate immune systems reach higher levels of complexity, it is plausible that increased evolutionary pressure would drive the immune response toward regulation through isotype- and/or allele-restricted expression, cellular selection, and expansion, characteristics that we traditionally ascribe to adaptive immune receptors in vertebrates. The boundaries between germline-encoded innate receptors (e.g., vertebrate and insect TLRs) and the somatically variable adaptive immune receptors of vertebrates are becoming increasingly less distinct (*30*, *31*).

Whereas the TLRs are the most readily characterized family of diversified innate receptors in sea urchin genome sequence and thus the focus of discussion here, a similar expansion is seen in other multigene families encoding immune proteins (Fig. 2A). NLR genes, which have been described previously only from vertebrates, serve as pathogen recognition receptors (PRRs) that detect cytoplasmic PAMPs (*19*) and are associated with immunity and autoimmune disease in the gut (*32*). The number and complexity of the more than 200 sea urchin NLR genes stand in distinct contrast to the ~20 NLR proteins in vertebrates. The gut is a major site of transcription of the NLRs in sea urchin (*22*), and gut-related immunity is likely a driving force behind expansion of this gene family. *S. purpuratus* is an herbivore, and much of its diet is kelp; various symbionts likely degrade complex carbohydrates and toxic compounds. Specific NLR-types and possibly TLR-types, as has been shown for vertebrates (*33*), may play a role in maintaining a balance with symbionts. Like the TLRs and NLRs, the multidomain SRCR genes of the sea urchin are expanded to unprecedented degrees (Fig. 2A). These genes encode proteins with structural similarity to some vertebrate scavenger receptors that have been ascribed roles in innate immune recognition (*34*). More than 1000 SRCR domains are encoded in 218 gene models, exceeding by 10-fold the number of SRCR domains seen in humans. Diverse members of this gene family are expressed in coelomocytes and exhibit dynamic shifts in transcription after immune challenge (*21*).

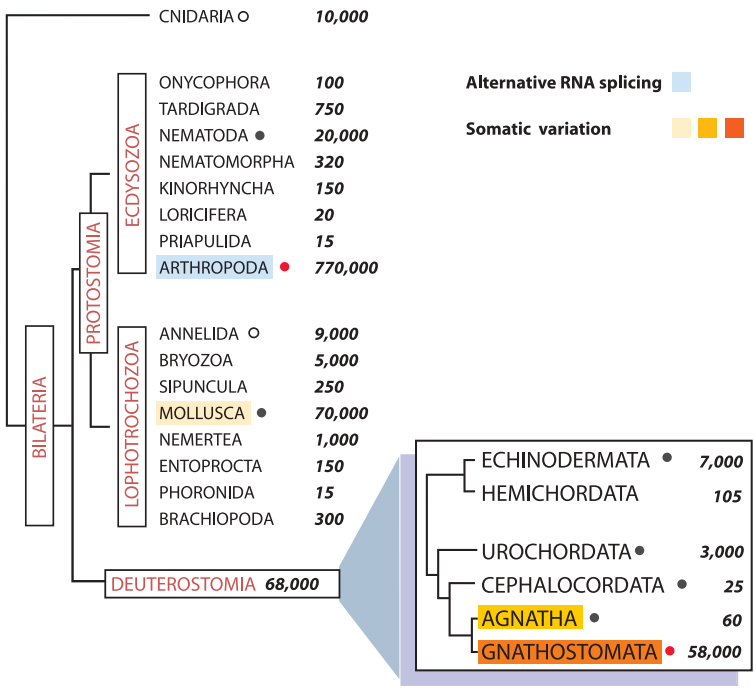

Fig. 1. A simplified phylogenetic tree depicting the general relationships of the major bilaterian phyla and chordate subphyla, highlighting select species that use different somatic mechanisms of immune receptor diversification. Red dots designate animal groups where the vast majority of immune data have been derived. Solid black dots denote taxa in which species have been the subject of extensive molecular immune research. Circles denote phyla where some molecular data are available. Color variation (see key) over specific phyla denotes the presence of a major somatic mechanism of receptor diversification in at least one representative member (*6*) and is not intended to be mutually exclusive. In the case of somatic variation, shade intensity indicates the level of empirically established diversity. Innate immune receptors, including TLRs, are likely present in all of the phyla. Numbers given beside taxa names are approximate estimates of species diversity and are presented to underscore the immense variety of immune mechanisms that have not yet been investigated [primarily taken from the Tree of Life Web project (*44*)]. Cnidarians (e.g., jellyfishes and sea anemones) are shown as an outgroup to the Bilateria. This view is not intended to represent all known species in which immune-type mediators have been identified.

There are a number of additional expanded gene families in the sea urchin genome that encode proteins with immune-related functions. The *185/333* genes were first noted because they are sharply up-regulated in response to whole bacteria and lippolysaccharide (*2*, *35*). Transcripts of the *185/333* genes constitute up to 6.5% of message prevalence in activated coelomocytes (*36*). The encoded novel proteins are highly diversified and are secreted from and localized to the surface of a subset of coelomocytes (*37*). The *185/333* genes represent another family of tightly linked and diverse immune-type genes (*35, 38*). Another large gene family that is implicated in the response of the sea urchin to immune challenge includes ~100 small C-type lectin and galectin genes. These examples, in addition to the TLRs, NLRs, and SRCRs, underscore a complex immune system in the sea urchin where large gene families, many with closely linked members, may be of significant importance.

The Origins of Vertebrate Immune Systems

Some of the most intriguing questions facing evolutionary immunology concern our limited understanding of the deuterostome underpinnings of the jawed-vertebrate immune system. The sea urchin genome, which encodes mediators of immunity that are shared with vertebrates but are absent in those protostomes for which whole-genome information is available, fills an essential gap in our recently broadened view of the immune system. As emphasized elsewhere in this issue, the overall complexity of the regulatory control networks, as well as the structures and genomic organization of their constituent elements, are highly significant in understanding the evolution of complex integrated systems such as those regulating immunity. Representatives of all important lymphocyte transcription factor subfamilies can be identified, including a deuterostome-restricted PU.1/SpiB/SpiC Ets transcription factor (a gene family that is intimately connected to blood cell functions in vertebrates) and an Ikaros/Aiolos/Helios/Eos-related gene (*22*). Immune signaling mediators, including a family of interleukin (IL)–17 genes, the IL receptors IL-1R and IL-17R, and tumor necrosis factor family members that were previously known only from chordates or vertebrates, are present in the sea urchin genome (*22*). It seems that the gene regulatory tool kit encoded in the sea urchin is remarkably complete as compared with immunity in the jawed vertebrates, which raises new questions about alternative functions of regulatory elements that we tend to associate with the basic development and differentiation of vertebrate immunocytes.

Rag1 and Rag2 represent the principle mediators of the somatic rearrangement process that is common to both immunoglobulin and T cell–antigen receptor gene families that effect adaptive immunity in jawed vertebrates. Whereas a number of conventional approaches failed to identify homologs of these genes in jawless vertebrates and invertebrates, genomic analysis has identified Rag1 core region–like transposable elements and partial Rag1-like genes in a variety of invertebrates (*39*). The identification of a homologous, Rag1/2-like functional gene cluster was one of the most unexpected findings from the sea urchin genome (*40*), as the transposon-like character of the vertebrate Rag genes suggests that they may have been acquired through a process of horizontal gene transfer at the time of the emergence of rearranging TCR and immunoglobulin gene systems in a jawed-vertebrate common ancestor. Although it is unclear at present whether or not these genes are active in immunity, it is improbable that they emerged independently in an echinoderm. The most parsimonious explanation for the distribution of Rag1/2-like clusters in two major deuterostome clades is that it represents a shared genetic feature present in a common ancestral deuterostome. Alternatively, the Rag1/2-like gene cluster may represent the independent cooption of an as yet unknown transposon that encoded both Rag1- and Rag2-like genes.

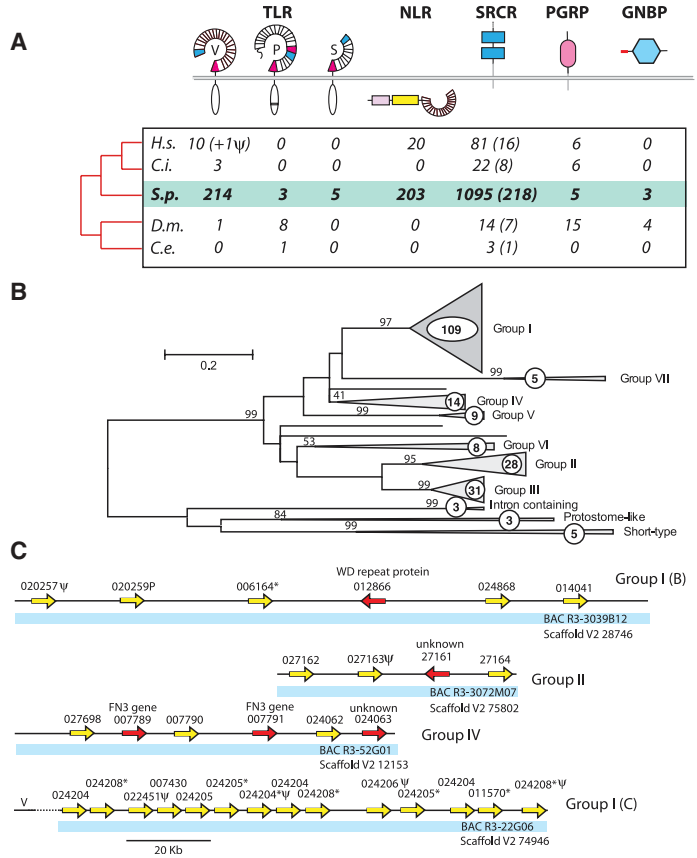

Fig. 2. Innate immune receptor multiplicity in the sea urchin genome sequence. (**A**) Comparison of gene families encoding innate immune receptors in representative animals with sequenced genomes to *S. purpuratus* (bold, hereafter designated sea urchin). For some key receptor classes, gene numbers in the sea urchin exceed those of other animals by more than an order of magnitude. Representative animals are *Homo sapiens*, *H.s.*; *C. intestinalis*, *C.i.*; *S. purpuratus*, *S.p.*; *D. melanogaster*, *D.m.*; and *C. elegans*, *C.e.* Gene families include TLRs, NLRs, SRCRs, PGRPs, and GNBPs. Specifically, TLR diagrams show V, vertebrate-like, P, protostome-like; and S, short type; oval indicates TIR domain; and segmented partial circles indicate LRR regions; LRR-NT, blue; and LRR-CT, red. NLR diagram shows death family domain in pink, NACHT domain in yellow, and the LRR region, for which horizontal orientation implies cytoplasmic function. The other diagrams show multiple SRCR genes (both secreted and transmembrane), PGRP genes (PFAM: Amidase_2 domain–containing, secreted or transmembrane); and GNBP proteins (PFAM: Glyco_hydro_16–containing, secreted). For multiple SRCR genes, representative values are domain number (gene number in parentheses). For *C. intestinalis*, numbers correspond to all annotated SRCR proteins. Phylogenetic relations among species are indicated by the red cladogram at the left of the table; diagrams of molecules are not intended to imply specific structural features. (**B**) Unrooted neighbor-joining tree showing interrelations of TIR domains of TLRs in sea urchin. TLRs can be classified into three divergent classes (protostome-like, intron-containing, and short) and a large sea urchin lineage-specific family, which distributes into seven (I to VII) subgroups; numbers of member genes indicated in circles. Group I can be further subdivided [I(A) to I(E)]. Numbers beside branches indicate % bootstrap support for each subgroup. Efforts to relate vertebrate and other TLRs to the sea urchin genes result in low-confidence affinities with the divergent groups as described for other TLR comparisons (*24*). (**C**) Clustering of representative sea urchin TLR genes (yellow arrows) from high-confidence regions of the assembly supported by bacterial artificial chromosome (BAC) sequence (indicated by blue bar). Clusters segregate according to groups [I(B) and I(C) are subgroups of group I]. Gene model numbers are indicated above arrows. Model numbers with asterisks are close matches to annotated gene models and likely represent the second haplotype to that which was used to create models from the previous assembly. Red arrows indicate non-TLR genes. V indicates putative position of a V-type immunoglobulin domain cluster. Verification of cluster organization will require further independent genomic analysis. ψ signifies pseudogene. Scale is indicated in kb (kilobase pairs).

In addition to the Rag1/2-like cluster, several other components related to those that function in the somatic reorganization and diversification of immunoglobulin and TCR also have been identified, including a polymerase that is homologous to the common ancestor of terminal deoxynucleotidyl transferase (TdT) and polymerase μ. Finally, several families of immunoglobulin domain genes (a total of about 50) have been identified that are predicted to encode immunoglobin variable-type (V) domains similar to those used by adaptive immune receptors of jawed vertebrates, and also the VCBPs, a diversified family of nonrearranging immune-type receptors in cephalochordates (*31*). Notably a cluster of V-type immunoglobulin genes is encoded adjacent to a large cluster of TLR genes (Scaffold_V2_74946; Fig. 2C) in the current assembly, although this will need to be independently verified (fig. S2). These V-type immunoglobulin domain structures uniformly lack canonical recombination signal sequences, which represent an integral component of DNA-mediated recombination and, thereby, the generation of a complex immune repertoire. Elucidating the function of these genes in a species where Rag1/2-like genes are present, but the process of variable-(diversity)-joining [V(D)J] segmental recombination of antigen binding receptors is absent, is potentially useful for understanding the origins of the segmental rearrangements of immunoglobulin domains in the adaptive immune receptors of jawed vertebrates.

Conclusions

The current data inform us about the evolution of immunity from multiple perspectives. First, this genome sequence significantly refines our understanding of deuterostome immunity. Immune factors previously known only from chordates and often only from vertebrates (e.g., IL-1R, IL-17, PU.1/SpiB/SpiC, NOD/NALP-like receptors) can be attributed now to the common deuterostome ancestor shared by echinoderms and chordates. Next, this genome is informative in comparison with

protostomes as protostome-like TLRs are present in the sea urchin genome and likely were present in the common bilaterian ancestor. Another perspective is defined by those components of the sea urchin genome that are related to the basic structural units of the antigen-binding receptors, as well as to the genes encoding the molecular machinery that effects somatic diversification of immunoglobulin and TCRs in jawed vertebrates. Finally, the genome sequence reveals adaptations that appear to be specific to the sea urchin lineage. Most strikingly, the expansion of gene families encoding innate immune recognition receptors is unlike that seen in any species characterized to date. Not only are the numbers of genes increased, but they reveal distinct patterns of variation, suggesting that they function through gradations in specificity that, in turn, may reflect differences in either the pathogens they recognize and/or the manner in which they cope with nonself on a systemwide basis.

The complexity of the sea urchin innate immune receptor superfamilies may be driven by the same selective forces that mold the vertebrate adaptive system. Alternatively, this innate complexity may relate to unique aspects of sea urchin biology. It is difficult to ignore that sea urchins are particularly long-lived [*S. purpuratus* lives to >30 years, and a closely related congener has been dated to more than 100 years (*41*)] and that their body size is large relative to other invertebrates with sequenced genomes. Other aspects of its basic biology may also be important, including its nonreduced genome, enormous numbers of progeny, and a biphasic life history. Finally, features of its life-style, including the complex relationship it probably exhibits with symbionts, could factor in the specialization of immune mechanisms as discussed for vertebrate systems (*33*, *42*) and for other physiological adaptations in marine organisms (*43*). One clear conclusion to be derived from the sea urchin genome is that the complexity of immunological mechanisms among unexplored animal phyla (Fig. 1) is likely to rival that found across the vertebrate-invertebrate (or agnathan-gnathostome) divergence.

Despite the entirely likely and intriguing links between sea urchin and vertebrate immunity, genomics only can take us so far in understanding complex regulatory and functional relations. However, the dichotomy observed in the complexity of genes encoding innate receptors within the deuterostomes provides a particularly well-defined starting point for further investigations. Clearly, the LRR proteins (TLRs and NLRs) have proven to be evolutionarily malleable in the context of sea urchin immunity. Many features of the organization and regulation of the particularly large diversified multigene families of immune receptors are consistent with potential restricted expression of individual genes in coelomocytes, which are basic characteristics of the lymphocyte- and natural killer cell–based immune systems of vertebrates (*42*). The experimental accessibility of the sea urchin will allow ready answers to questions of restricted expression and the nature of the regulatory interface between the apparently ancient networks that underpin animal immunocyte specification and the more evolutionarily labile immune mechanisms that mediate their differentiated functions.

References and Notes

1. E. H. Davidson, D. H. Erwin, *Science* **311**, 796 (2006).
2. J. P. Rast, Z. Pancer, E. H. Davidson, *Curr. Top. Microbiol. Immunol.* **248**, 3 (2000).
3. C. J. Evans, V. Hartenstein, U. Banerjee, *Dev. Cell* **5**, 673 (2003).
4. P. M. Murphy, *Cell* **72**, 823 (1993).
5. A. L. Hughes, *Mol. Biol. Evol.* **14**, 1 (1997).
6. G. W. Litman, J. P. Cannon, L. J. Dishaw, *Nat. Rev. Immunol.* **5**, 866 (2005).
7. J. A. Hoffmann, *Nature* **426**, 33 (2003).
8. C. A. Janeway Jr., R. Medzhitov, *Annu. Rev. Immunol.* **20**, 197 (2002).
9. Z. Pancer *et al.*, *Nature* **430**, 174 (2004).
10. M. N. Alder *et al.*, *Science* **310**, 1970 (2005).
11. S. M. Zhang, C. M. Adema, T. B. Kepler, E. S. Loker, *Science* **305**, 251 (2004).
12. F. L. Watson *et al.*, *Science* **309**, 1874 (2005).
13. Y. Dong, H. E. Taylor, G. Dimopoulos, *PLoS Biol.* **4**, e229 (2006).
14. K. Azumi *et al.*, *Immunogenetics* **55**, 570 (2003).
15. G. K. Christophides *et al.*, *Science* **298**, 159 (2002).
16. A. C. Millet, J. J. Ewbank, *Curr. Opin. Immunol.* **16**, 4 (2004).
17. A. W. De Tomaso *et al.*, *Nature* **438**, 454 (2005).
18. Sea Urchin Genome Sequencing Consortium, *Science* **314**, 941 (2006).
19. T. A. Kufer, J. H. Fritz, D. J. Philpott, *Trends Microbiol.* **13**, 381 (2005).
20. Z. Pancer, J. P. Rast, E. H. Davidson, *Immunogenetics* **49**, 773 (1999).
21. Z. Pancer, *Proc. Natl. Acad. Sci. U.S.A.* **97**, 13156 (2000).
22. T. Hibino *et al.*, *Dev. Biol.* 10.1016/j.ydbio.2006.08.065 (2006).
23. F. L. Rock, G. Hardiman, J. C. Timans, R. A. Kastelein, J. F. Bazan, *Proc. Natl. Acad. Sci. U.S.A.* **95**, 588 (1998).
24. J. C. Roach *et al.*, *Proc. Natl. Acad. Sci. U.S.A.* **102**, 9577 (2005).
25. S. Akira, S. Uematsu, O. Takeuchi, *Cell* **124**, 783 (2006).
26. A. Ozinsky *et al.*, *Proc. Natl. Acad. Sci. U.S.A.* **97**, 13766 (2000).
27. S. H. Hulbert, C. A. Webb, S. M. Smith, Q. Sun, *Annu. Rev. Phytopathol.* **39**, 285 (2001).
28. J. Li, T. Ishii, P. Feinstein, P. Mombaerts, *Nature* **428**, 393 (2004).
29. B. M. Shykind *et al.*, *Cell* **117**, 801 (2004).
30. M. F. Flajnik, L. Du Pasquier, *Trends Immunol.* **25**, 640 (2004).
31. J. P. Cannon, R. N. Haire, N. Schnitker, M. G. Mueller, G. W. Litman, *Curr. Biol.* **14**, R465 (2004).
32. J. P. Ting, D. L. Kastner, H. M. Hoffman, *Nat. Rev. Immunol.* **6**, 183 (2006).
33. S. Rakoff-Nahoum, J. Paglino, F. Eslami-Varzaneh, S. Edberg, R. Medzhitov, *Cell* **118**, 229 (2004).
34. S. Mukhopadhyay, S. Gordon, *Immunobiology* **209**, 39 (2004).
35. D. P. Terwilliger, K. M. Buckley, D. Mehta, P. G. Moorjani, L. C. Smith, *Physiol. Genomics* **26**, 134 (2006).
36. S. V. Nair, H. Del Valle, P. S. Gross, D. P. Terwilliger, L. C. Smith, *Physiol. Genomics* **22**, 33 (2005).
37. K. M. Brockton, L. C. Smith, unpublished observations.
38. V. Buckley, L. C. Smith, unpublished observations.
39. V. V. Kapitonov, J. Jurka, *PLoS Biol.* **3**, e181 (2005).
40. S. D. Fugmann, C. Messier, L. A. Novack, R. A. Cameron, J. P. Rast, *Proc. Natl. Acad. Sci. U.S.A.* **103**, 3728 (2006).
41. T. A. Ebert, J. R. Southon, *Fish. Bull. (Washington, DC)* **101**, 915 (2003).
42. Z. Pancer, M. D. Cooper, *Annu. Rev. Immunol.* **24**, 497 (2006).
43. E. S. Loker, C. M. Adema, S. M. Zhang, T. B. Kepler, *Immunol. Rev.* **198**, 10 (2004).
44. Tree of Life Web project (www.tolweb.org).

45. We thank the Human Genome Sequencing Center at the Baylor College of Medicine for assistance throughout this analysis. We greatly appreciate helpful discussions with C. Messier, Z. Pancer, S. Fugmann, D. Philpott, and S. Girardin. We thank K. M. Buckley for comments on the manuscript, B. Pryor for editorial assistance, B. Jasny for very helpful input on the organization of these findings, and two anonymous reviewers for enlightening observations. This work was made possible by support from the NSF (MCB-0424235) to L.C.S.; the Uehara Memorial Foundation to T.H.; the Canadian Institutes for Health Research (MOP74667), and National Science and Engineering Research Council of Canada (458115/211598) to J.P.R.; and the NIH (AI23338) to G.W.L.

Supporting Online Material

www.sciencemag.org/cgi/content/full/314/5801/952/DC1
Materials and Methods
SOM Text
Figs. S1 and S2
Table S1
References

10.1126/science.1134301

REVIEW

Paleogenomics of Echinoderms

David J. Bottjer,[1]* Eric H. Davidson,[2] Kevin J. Peterson,[3] R. Andrew Cameron[2]

Paleogenomics propels the meaning of genomic studies back through hundreds of millions of years of deep time. Now that the genome of the echinoid *Strongylocentrotus purpuratus* is sequenced, the operation of its genes can be interpreted in light of the well-understood echinoderm fossil record. Characters that first appear in Early Cambrian forms are still characteristic of echinoderms today. Key genes for one of these characters, the biomineralized tissue stereom, can be identified in the *S. purpuratus* genome and are likely to be the same genes that were involved with stereom formation in the earliest echinoderms some 520 million years ago.

Paleogenomics is the addition of the component of deep time to the field of genomics (*1*). Initial studies have concentrated on reconstructing regions of the ancestral mammalian genome (*2*) or sequencing preserved DNA of recently extinct organisms, such as the wooly mammoth (*3*). Although such studies present many exciting possibilities,

the prospects for paleogenomics are much broader.

Genomics offers the opportunity of identifying genes that are responsible for the evolution of key shared characters of organisms, or synapomorphies, which are ultimately used to reconstruct the tree of life. Paleogenomics thus allows for both the geologic and genetic fossil records to shed light on the origin and subsequent evolution through time of key genes and the key synapomorphies that they encode.

Echinoderm Paleogenomics and the Stereom Skeleton

The initial appearance of biomineralized skeletal tissues in the fossil record (*4*), just before the beginning of the Cambrian ~542 million years ago (Ma), coincides with the start of the rapid increase in the diversity of metazoans termed the Cambrian explosion (*5*). Later in the Early Cambrian, by 520 Ma, a variety of biomineralized skeletal structures had appeared. Among the most distinctive is a major echinoderm synapomorphy: the unique endoskeletal tissue called stereom.

Stereom is composed of calcite organized into a meshlike structure (Fig. 1, A to D), the pores of which in life are populated with dermal cells and fibers (*6*). Much is known about this structure from studies of representatives of the approximately 7000 species that constitute the five clades of living echinoderms (crinoids or sea lilies, ophiuroids or brittle stars, asteroids or sea stars, holothuroids or sea cucumbers, and echinoids or sea urchins), all of which produce stereom endoskeletons (*6*). Stereom forms structural elements (Fig. 1) that can be embedded in soft tissues or may be fused together to form larger compound plates, generating the various types of echinoderm skeletons (*6*).

Because the high-magnesium calcite of which stereom is constructed is stable, echinoderm skeletons are very durable during the process of fossil preservation, and this has led to an abundant and well-understood echinoderm fossil record (*6*, *7*).

Echinoderm Phylogeny and the History of Stereom

Echinoderms, one of the three major phyla of the Deuterostomia, make their first appearance in the fossil record during the Early Cambrian, about 520 Ma, but the most primitive echinoderms are the stylophorans, a bizarre group first recorded in the fossil record in the Middle Cambrian (~510 Ma) (*8*) (Figs. 2 and 3A). Stylophorans are recognized as echinoderms because they possess stereom (Fig. 1, C and D). Another major echinoderm synapomorphy is the water vascular system (*8*, *9*), a closed circulatory system that uses ambient seawater to provide the hydraulic force necessary to extend the tube feet of living forms. The water vascular system first made its appearance in another group of Cambrian forms, the solutes (Figs. 2 and 3B). Both stylophorans and solutes are "stem-group" echinoderms (*8*) because they are more closely related to living echinoderms than they are to living hemichordates, the closest living relatives of modern echinoderms, but they are not descended from the last common ancestor of the living echinoderms (Fig. 2).

Other stem-group echinoderms that produced both a biomineralized stereom skeleton and plate morphologies indicating the presence of a water vascular system appear in the stratigraphic record from about 520 Ma (*10*). These include the helicoplacoids, eocrinoids, and edrioasteroids (Fig. 3, C to E). Pentameral symmetry of the adult body, a highly characteristic echinoderm synapomorphy of crown-group echinoderms, makes its initial appearance in the edrioasteroids and the eocrinoids (*10*).

Crown-group echinoderm fossils (Fig. 2) occur in the earliest Ordovician at about 485 Ma, in the form of primitive crinoids, another immobile filter-feeding group (*11*) (Figs. 2 and 3F). The remaining crown-group echinoderms have mobile life habits on and in the seafloor and as a group are termed eleutherozoans (asteroids, ophiuroids, holothuroids, and echinoids) (Fig. 3, G and H). Eleutherozoans with biomineralized stereom ossicles also first appear in the earliest Ordovician about 475 to 480 Ma (*12*), with the earliest occurrence of a fossil sea star (asteroid). Sea urchins (echinoids) do not occur in the fossil record until the Late Ordovician (~450 Ma) (*13*) (Fig. 3H). The modern forms trace their roots back to the Late Permian, when the first cidaroid echinoids ("pencil-spined" sea urchins) appeared (*14*). Perhaps only two echinoid lineages survived the end-Permian mass extinction ~252 Ma. *Strongylocentrotus purpuratus*, the modern sea urchin whose genome sequence is now available, is a regular euechinoid.

Echinoderm Biomineralization: Cell Biology and Genes

The process by which the biomineralized stereom skeleton is formed in echinoids is coming to light, through combined approaches of cell, molecular, and developmental biology (*15*). First, embryonic mesenchymal cells secrete the earliest portions of the skeleton to appear. The larval spicules (Fig. 1E) and additional independent sites in the larva are the starting points for the adult plates. The biomineral is composed of calcite ($CaCO_3$) containing 5% $MgCO_3$. It is

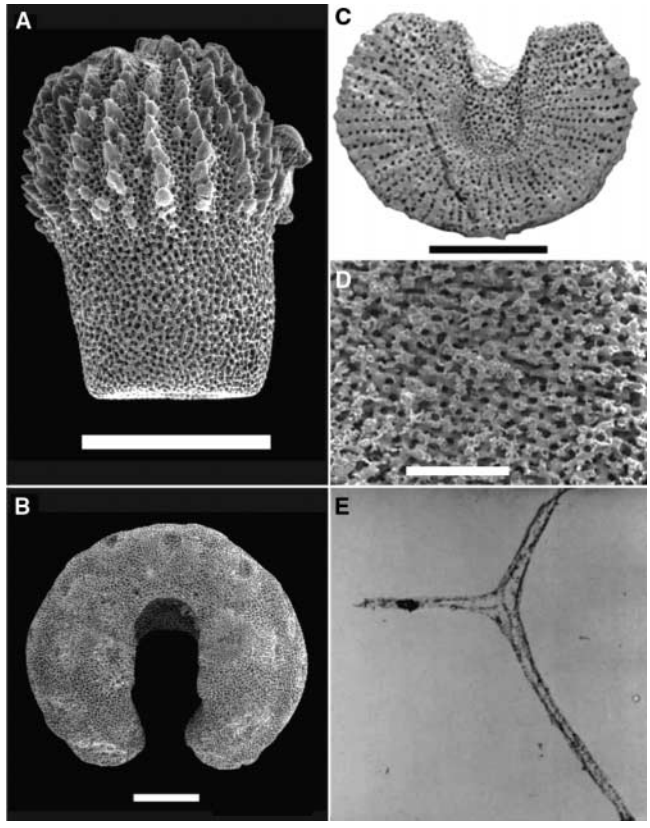

Fig. 1. Stereom formation in modern and fossil echinoderms. (**A**) A spine of the modern sea star *Asterias* with soft tissue removed, constructed of meshlike stereom. (**B**) An occular plate of the modern sea star *Asterias* with soft tissue removed, constructed of meshlike stereom. (**C**) Median cross section of the stylocone from the Middle Cambrian stylophoran *?Ceratocystis*, showing stereom construction. (**D**) Detail of stereom from the inner face in external view of the stylocone from the Middle Cambrian stylophoran *?Ceratocystis*. (**E**) Larval spicule of *S. purpuratus* with biomineralized stereom (calcite) dissolved away, showing the distribution of spicule matrix proteins. [(A) and (B) are used with permission from C. Sumrall; (C) and (D) are reprinted by permission from Macmillan Publishers Ltd. (*Nature*) (*11*), copyright (2005); (E) is reprinted from (*27*), copyright 1983, with permission from Elsevier.] Scale bars in (A) to (C), 500 μm; scale bar in (D), 100 μm; magnification of (E) is ×3000.

[1]Department of Earth Sciences, University of Southern California, Los Angeles, CA 90089–0740, USA. [2]Division of Biology 156-29, California Institute of Technology, Pasadena, CA 91125, USA. [3]Department of Biological Sciences, Dartmouth College, Hanover, NH 03755, USA.

*To whom correspondence should be addressed. E-mail: dbottjer@usc.edu

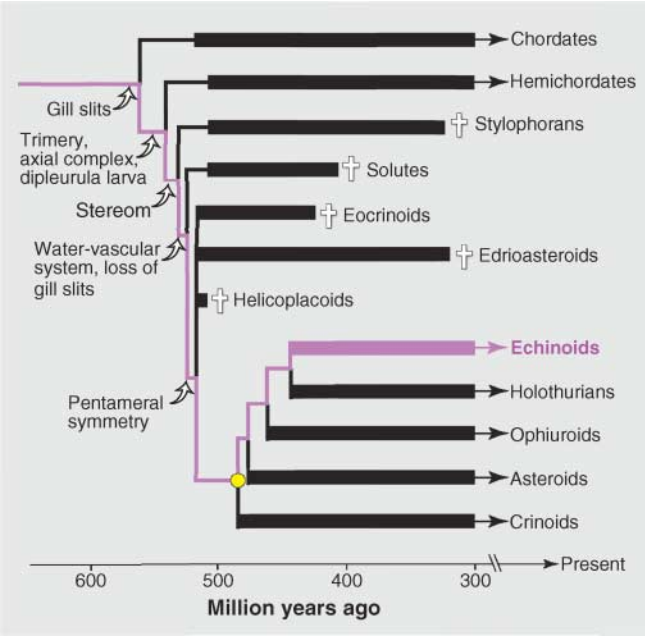

Fig. 2. Evolutionary history of the major echinoderm groups. Deuterostomia consists of three major groups: the chordates, hemichordates, and echinoderms, all with fossil representatives in the Cambrian. Cambrian echinoderms are recognized by the possession of stereom, but the phylogenetically most basal groups (such as stylophorans) lack the water vascular system, are highly asymmetrical, and possess gill slits. Pentameral symmetry is seen in two major Early Cambrian lineages, the edrioasteroids and eocrinoids; a third Early Cambrian taxon, the helicoplacoids, have an unusual threefold symmetry thought to be derived from the ancestral pentameral arrangement (*10*). All stem-group echinoderm lineages became extinct by the Carboniferous (indicated with crosses). Crown-group echinoderms, indicated by the yellow circle, consist of the five major extant lineages in addition to numerous extinct lineages not shown. Most class-level crown groups first appear in the latest Paleozoic–early Mesozoic, including echinoids. The lineage leading to echinoids, and hence to *S. purpuratus*, is indicated in purple. Known stratigraphic ranges are shown with thick lines, and inferred range extensions are shown with thin lines.

secreted into an extracellular space, probably sequestered from the surrounding environment, initially as amorphous calcium carbonate, which then undergoes a regulated transition to the crystalline form (*16*).

Occluded within the calcite is an organic matrix of proteins that make up about 0.1% of the mass, and the birefringent optical properties of the skeletal elements result from the regular alignment of the crystals in the matrix (*17*). As shown in Fig. 1E (*18*), which portrays a skeletal element after demineralization, the triradiate physical form is a property of the matrix proteins, which originally were deposited with the biomineral. Additionally, there is an envelope of proteins around the mineral portion. Initial surveys indicate that a large number of separable proteins or protein derivatives is associated with the mineral (*15*). Something is known of the structure and deployment of seven of these proteins, and four have been studied in detail, namely SM50, SM30, SM37, and PM27 (*15*).

The multiplicity of the spicule matrix proteins is reflected by structural and functional variety within this sample, though all have a C-type lectin domain, which is a calcium-dependent carbohydrate binding motif. SM30 and SM37 are glycosylated. SM30 is known to occupy the occluded protein compartment, whereas SM50 and PM27 are found occluded and in the extracellular matrix around the spicule. SM50 contains an unusual proline- and glycine-rich repeat sequence similar to the pericardin repeat motif (*19*). Little is known, though, about the exact functions of these proteins except that interference with the expression of SM50 inhibits spicule formation in *S. purpuratus* embryos (*20*).

The sea urchin genome project revealed the seven known spicule matrix genes and eight new ones as well (*21*). Furthermore, the genome sequence provides the opportunity to observe the arrangement of the spicule matrix protein genes, and the results illuminate an aspect of their evolution. These genes occur in small clusters and thus are likely to be the related products of local gene family expansions. For example, four related SM30 genes were found to be arranged in tandem on a single assembly scaffold (*21*). In addition, the SM37 gene is closely linked to the SM50 gene (*21–23*).

The *S. purpuratus* sequence also contains homologs of many of the signaling molecules and extracellular matrix proteins involved in vertebrate biomineralization (*21*). But in contrast to these, the sea urchin C-lectin spicule matrix proteins share little similarity with the well-characterized vertebrate skeletogenic proteins. Nor are they similar to any sequences present in current databases of expressed sequence tags (ESTs) from the hemichordate *Saccoglossus kowalewsaki* or the cephalochordate *Branchiostoma floridae.* With respect to any other known genome, the spicule matrix proteins of echinoids are encoded by a clade-specific set of genes. This may be true for echinoderms in general, but there is too little sequence data from other classes to make the conclusion definitive. The stereom structure is so similar among the classes that it would be remarkable if these proteins were not a character of the phylum.

The molecular and cell biology of stereom biomineralization in the sea urchin offers a fascinating glimpse into the genetic underpinnings of an echinoderm synapomorphy that arose in the Early Cambrian. A suite of identifiable unique genes (except that they have in common a domain encoding a calcium-dependent lectin) evolved to construct the unique biomineral structure of the stereom. The basic pattern of fenestration in the stereom (Fig. 1) is the property of a single differentiated cell type, defined by the expression of a battery of matrix genes, which first appeared in echinoderms at least 520 Ma.

Discussion

Paleogenomics adds a genomic dimension to the paleontological description of synapomorphies. Stereom is an iconic synapomorphy for echinoderms, much as bone is for the vertebrates, and it was the first to arise in the divergence of echinoderms from the other major deuterostome lineages. Thus, we hypothesize that the evolution of the spicule matrix genes occurred after the Precambrian-Cambrian boundary (542 Ma), but before the time in the Early Cambrian when stereom-containing fossils first appear (~520 Ma) (Fig. 2). The specific prediction is that a unique echinoderm synapomorphy, a definitive property not shared with phylogenetic sister groups, will be the genomic constituents of the calcite/stereom differentiation gene battery (Table 1). That is, echinoderms will in general share variants of the same biomineralization genes and use the same transcriptional regulatory controllers of these genes. This is of course open to experimental verification by comparative molecular analysis of biomineralization in modern forms of echinoderm. Were it found that the genetic repertoire used to produce stereom in the diverse echinoderm classes is indeed similar, then it would be indisputable that their stem-group ancestors used the same genetic apparatus.

Paleogenomics is a knife that cuts two ways: We gain insights not only into the genes that built the structures of our fossils, but also into the evolutionary origin of the gene networks that operate in the construction of modern animal body parts. In this case, we propose that the specific stereom matrix gene battery (that is, the variety of structural functions encoded in its diverse proteins, plus its regulatory controls) must have been assembled as such in Early Cambrian time. It has remained a feature of echinoderm genomes ever since. Something is already known of the regulatory network apparatus controlling spicule matrix protein expression in the *S. purpuratus* embryo. The differentiation genes of the biomineralization gene battery of this embryo are

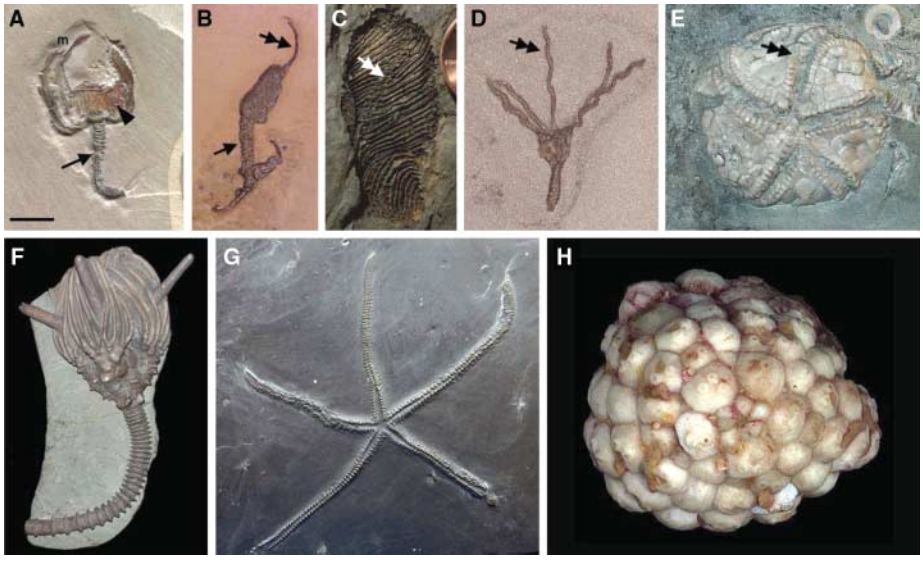

Fig. 3. Stem-group (**A** to **E**) and crown-group (**F** to **H**) echinoderms. (A) The stylophoran *Cothurnocystis bifida* (Middle Cambrian, Utah, USA). The putative gill skeletons as viewed from the back side are indicated with an arrowhead. M is the putative mouth. The arrow indicates the posterior appendage. (B) The solute *Coleicarpus sprinklei* (Middle Cambrian, Utah, USA). The arrow indicates the posterior appendage, and the double arrow points to the single ambulacrum. (C) The helicoplacoid *Helicoplacus* (Early Cambrian, California, USA). The double arrow points to one of the ambulacral grooves. (D) The eocrinoid *Gogia spiralis* (Middle Cambrian, Utah, USA). The double arrow points to one of the five arms. (E) The edrioasteroid *Edriophus bigsbyi* (Ordovician, Ontario, Canada). It displays conspicuous pentameral symmetry; one of the arms is indicated by the double arrow. (F) The crinoid *Dorycrinus mississippiensis* (Mississippian, Indiana, USA). (G) The asteroid *Furcaster palaeozoicus* (Devonian, Budenbach, Germany). (H) The echinoid *Bothriocidaris* (Ordovician, Estonia) [reprinted with permission from A. B. Smith, from (*30*)]. Scale bar, 0.5 cm in (A); 0.75 cm in (B) to (E); 2 cm in (F); 1.3 cm in (G); and 0.15 cm in (H). Part of a penny is shown for scale in (C).

Table 1. Predicted features of the echinoderm biomineralization gene battery extrapolated from *S. purpuratus.*

Functions	Characteristics
Regulatory apparatus	Multiple specific regulatory genes (such as *Alx1*, *Ets1*, *Dr*, and *Hnf6*) with feed-forward input into biomineralization genes (*31*)
Cellular biology	Non–echinoderm-specific molecules used for secretion and motility (*21*)
Biomineralization genes	Echinoderm-specific genes featuring glycine- and proline-rich repeats on the same protein with C-type lectin domains (*15*, *21*)

together regulated by a specific small set of transcriptional control genes (*24*, *25*).

Paleogenomic approaches can be extended to other clades for which there is both a sequenced genome and a well-preserved fossil record. The objective is the identification of clade-specific gene batteries that encode clade-specific features of the body plan. What emerges will add a time dimension to specific parts of the underlying gene regulatory networks. Thus we will be able to "age-date" portions of the functional genome to determine parts of genomes that are relatively young, in contrast to others that are extraordinarily old.

It is unusual in the consideration of body plan evolution to be able to cite a phylum-specific set of structural or differentiation genes, of which it can literally be said that their evolution underlay a phylum-specific morphological feature. The organization of body plans obviously depends in general on the regulatory control of the developmental process, which in turn depends at the genomic level on the organization of developmental gene regulatory networks. In general, therefore, the evolution of diversity of body plans depends on changes in the architecture of gene regulatory networks. But the regulatory genes constituting these networks, which encode transcription factors and intercellular signaling components, are notoriously not clade-specific: They are largely pan-bilaterian (*26*–*28*), if not pan-metazoan. Similarly, the downstream differentiation genes that produce the proteins from which major components of the body plan are constructed are often not clade-specific either. For example, muscles, nervous systems, and hearts use many orthologous genes across the Bilateria. Clade-specific sets of genes that are often noted in animal genome sequences, such as genes of the immune system or smell receptor genes, are not very likely to produce signatures in the fossil record.

In temporal and historical aspects, as well as in architectural and functional terms, genetic systems for the control of development are internally inhomogeneous (*27*). Some subcircuits are very ancient and have changed little since their early evolution hundreds of millions of years ago; others are of more recent origin and have arisen in given evolutionary branches. This view is, of course, inconsistent with the microevolutionary presumption of temporal uniformity in evolutionary processes. The broad objectives of paleogenomics are convergent with those of "regulatory phylogenetics" [for example, gene regulatory network comparisons (*29*)], in that both result in the association of given genetic components with specific time-resolved evolutionary nodes. A distinction, as in the example described in this paper, is the direct relation between genes producing a structure and the fossil record, rather than the indirect relation between the regulatory genes and the body plan. It is satisfying to be able to apply genomic data directly to the origins of a character that arose over half a billion years ago and is found in animals present on Earth today.

References and Notes

1. D. Birnbaum, F. Coulier, M.-J. Pebusque, P. Pontarotti, *J. Exp. Zool.* **288**, 21 (2000).
2. M. Blanchette, E. D. Green, W. Miller, D. Haussler, *Genet. Res.* **14**, 2412 10.1101/gr.2800104 (2004).
3. H. N. Poinar *et al.*, *Science* **311**, 392 (2006).
4. J. P. Grotzinger, W. A. Watters, A. H. Knoll, *Paleobiology* **26**, 334 (2000).
5. K. J. Peterson, M. A. McPeek, D. A. D. Evans, *Paleobiology* **31** (suppl.), 36 (2005).
6. A. B. Smith, in *Skeletal Biomineralization: Patterns, Processes and Evolutionary Trends.* vol. I, J.G. Carter, Ed. (Van Nostrand, New York, 1990), pp. 413–443.
7. E. Flügel, *Microfacies of Carbonate Rocks* (Springer-Verlag, Berlin, 2004).
8. A. B. Smith, *Geol. J.* **40**, 255 (2005).
9. S. Clausen, A. B. Smith, *Nature* **438**, 351 (2005).
10. J. Sprinkle, B. C. Wilbur, *Geol. J.* **40**, 281 (2005).
11. T. E. Guensburg, J. Sprinkle, *Geology* **29**, 131 (2001).
12. D. B. Blake, T. E. Guensberg, *J. Paleontol.* **79**, 395 (2005).
13. A. B. Smith, J. J. Savill, *Trans. R. Soc. Edinb. Earth Sci.* **92**, 137 (2001).
14. A. B. Smith, N. T. J. Hollingworth, *Proc. Yorkshire Geol. Soc.* **48**, 47 (1990).
15. F. H. Wilt, *Dev. Biol.* **280**, 15 (2005).
16. E. Beniash, J. Aizenberg, L. Addadi, S. Weiner, *Proc. R. Soc. London Ser. B* **264**, 461 (1997).
17. A. Berman *et al.*, *Science* **250**, 664 (1990).
18. S. Benson, E. M. E. Jones, N. Crise-Benson, F. Wilt, *Exp. Cell Res.* **148,** 249 (1983).
19. Y. Katoh-Fukui *et al.*, *Dev. Biol.* **145**, 201 (1991).
20. M. Peled-Kamar, P. Hamilton, F. H. Wilt, *Exp. Cell Res.* **272**, 56 (2002).
21. B. T. Livingston *et al.*, *Dev. Biol.* 10.1016/j.ydbio.2006.07.047 (2006).
22. Y.-H. Lee, R. J. Britten, E. H. Davidson, *Dev. Growth Differ.* **41**, 303 (1999).

23. M. R. Illies, M. T. Peeler, A. M. Dechtiaruk, C. A. Ettensohn, *Dev. Genes Evol.* **212**, 419 (2002).
24. P. Oliveri, E. H. Davidson, *Curr. Opin. Genet. Dev.* **14**, 351 (2004).
25. G. Amore, E. H. Davidson, *Dev. Biol.* **293**, 555 (2006).
26. V. F. Hinman, A. T. Nguyen, R. A. Cameron, E. H. Davidson, *Proc. Natl. Acad. Sci. U.S.A.* **100**, 13356 (2003).
27. D. H. Erwin, E. H. Davidson, *Development* **129**, 3021 (2002).
28. E. H. Davidson, D. H. Erwin, *Science* **311**, 796 (2006).
29. E. H. Davidson, *The Regulatory Genome. Gene Regulatory Networks in Development and Evolution* (Academic Press/Elsevier, San Diego, CA, 2006).
30. The Echinoid Directory (www.nhm.ac.uk/research-curation/projects/echinoid-directory).
31. G. Amore, E. H. Davidson, *Dev. Biol.* **293**, 555 (2006).
32. This work was partially supported by NSF grant IOB-0212869 (to R.A.C.), NIH grant RR-15044 (to E.H.D.), and the Caltech Beckman Institute. D.J.B. is supported by NASA, NSF, and the University of Southern California; K.J.P. is supported by NSF, NASA-Ames, and Dartmouth College.

10.1126/science.1132310

REPORT

The Transcriptome of the Sea Urchin Embryo

Manoj P. Samanta,[1] Waraporn Tongprasit,[2,3] Sorin Istrail,[4,5] R. Andrew Cameron,[5] Qiang Tu,[5] Eric H. Davidson,[5] Viktor Stolc[2]*

The sea urchin *Strongylocentrotus purpuratus* is a model organism for study of the genomic control circuitry underlying embryonic development. We examined the complete repertoire of genes expressed in the *S. purpuratus* embryo, up to late gastrula stage, by means of high-resolution custom tiling arrays covering the whole genome. We detected complete spliced structures even for genes known to be expressed at low levels in only a few cells. At least 11,000 to 12,000 genes are used in embryogenesis. These include most of the genes encoding transcription factors and signaling proteins, as well as some classes of general cytoskeletal and metabolic proteins, but only a minor fraction of genes encoding immune functions and sensory receptors. Thousands of small asymmetric transcripts of unknown function were also detected in intergenic regions throughout the genome. The tiling array data were used to correct and authenticate several thousand gene models during the genome annotation process.

Embryogenesis in the sea urchin occurs rapidly and is relatively simple in form (*1*). By 2 days after fertilization, when the embryo is in the late gastrula stage, there are about 800 cells and 10 to 15 cell types. Thus, genes expressed in individual cell types or territories represent a larger fraction of the total number of transcripts than do genes expressed in adult organs of vertebrates or in more complex embryos such as that of *Drosophila*. Earlier studies have provided extensive quantitative evidence on transcript prevalence for sea urchin embryos, both for populations of mRNA (and nuclear RNA) and for many individual transcripts, measured by quantitative polymerase chain reaction (QPCR) (*2–4*). The genome sequence of *Strongylocentrotus purpuratus* (*5*) enabled these advantages to be exploited for a whole-genome tiling array analysis of the embryonic transcriptome.

Transcriptome analysis by whole-genome tiling array (*6–9*) has three advantages relative to standard microarray analysis with oligonucleotide probes constructed on the basis of known or predicted protein-coding genes: (i) The genes identified are not limited a priori by the gene predictions used to design the probes and therefore are not biased in favor of more prevalent or more conserved sequences; (ii) the transcripts detected will include noncoding as well as protein-coding RNAs; and (iii) intron-exon boundaries plus untranslated regions (UTRs) are revealed. In comparison with expressed sequence tag (EST) or cDNA-based approaches, whole-genome tiling arrays offer an unbiased and complete view of the transcriptional activity of the genome in the developmental state examined and in addition display the intron and exon structures of expressed genes. In itself, tiling array data cannot assign a distant exon to its gene, but this shortcoming can be overcome by integrating tiling and EST/cDNA data for genome annotation.

Tiling array experiments have traditionally been performed only several years after genome sequencing (*9*). However, maskless array synthesizer technology permitted us to develop custom arrays from preliminarily assembled draft sequence. This initiative enhanced the genome project while it was still in process, by substantially reducing the gap between sequencing and comprehensive annotation of the genome.

To sample transcriptional activity throughout early sea urchin development on a single set of high-density microarrays, we prepared polyadenylated RNA from egg, early blastula (15 hours), early gastrula (30 hours), and late gastrula stage (45 hours) embryos. Samples were mixed in equal quantities, reverse transcribed, fluorescently labeled, and hybridized. The tiling array probes were designed from the initial draft assembled sequence, which at that time was based on 6× whole-genome shotgun sequence coverage (*5*). A total of 10,133,868 50-nucleotide (nt) probes were selected to uniformly represent the entire sea urchin genome, maintaining an average spacing of 10 nt between consecutive probes (table S1). Repetitive sequences and simple sequence tracts were excluded. The probes were synthesized on 27 glass-based microarrays. To avoid any potential bias due to cutoff selection based on unexpressed genomic probes, we also added a set of 1000 random sequences not represented anywhere in the genome to each array. The cutoff was such that only 1% of those random probes were falsely expressed. Additionally, each array included a small (2000) identical set of genomic control probes used for normalization purposes. After hybridization, data from all arrays were normalized according to the control probes, mapped back to the latest genome sequence assembly, and mounted on a genome browser together with the optimal set of computationally derived gene models [OGS set in (*5*); for visual presentation of all transcriptome results as in Fig. 1A, see www.systemix.org/sea-urchin]. Details of the methods used are available in the Supporting Online Material (*10*), and the microarray designs and experimental data have been deposited in the National Center for Biotechnology Information (NCBI) Gene Expression Omnibus (GEO) (www.ncbi.nlm.nih.gov/geo) under the accession code GSE6031.

Analysis of signals for 28 well-characterized genes (*11*) (table S2) showed that the array measurements were highly sensitive. When mapped against the known structure of these genes, it was apparent that transcribed regions were clearly distinguished from silent regions, and no intronic transcripts were detected. Intron-exon boundaries of expressed genes were thus clearly distinguishable (e.g., Fig. 1A, fig. S1). To establish a conservative statistical criterion of expression, we first established the background variance and chose a cutoff value about 2.5 times that of the mean background. At this value, about 1% of random control probes displayed apparently artifactual noise, e.g., single-point peaks over background surrounded by probes at the background level (as in the single-

[1]Systemix Institute, Los Altos, CA 94024, USA. [2]NASA Ames Genome Research Facility, Moffet Field, CA 94035, USA. [3]Eloret Corporation, Sunnyvale, CA 94086, USA. [4]Brown University, Providence, RI 02912, USA. [5]California Institute of Technology, Pasadena, CA 91125, USA.

*To whom correspondence should be addressed. E-mail: vstolc@arc.nasa.gov

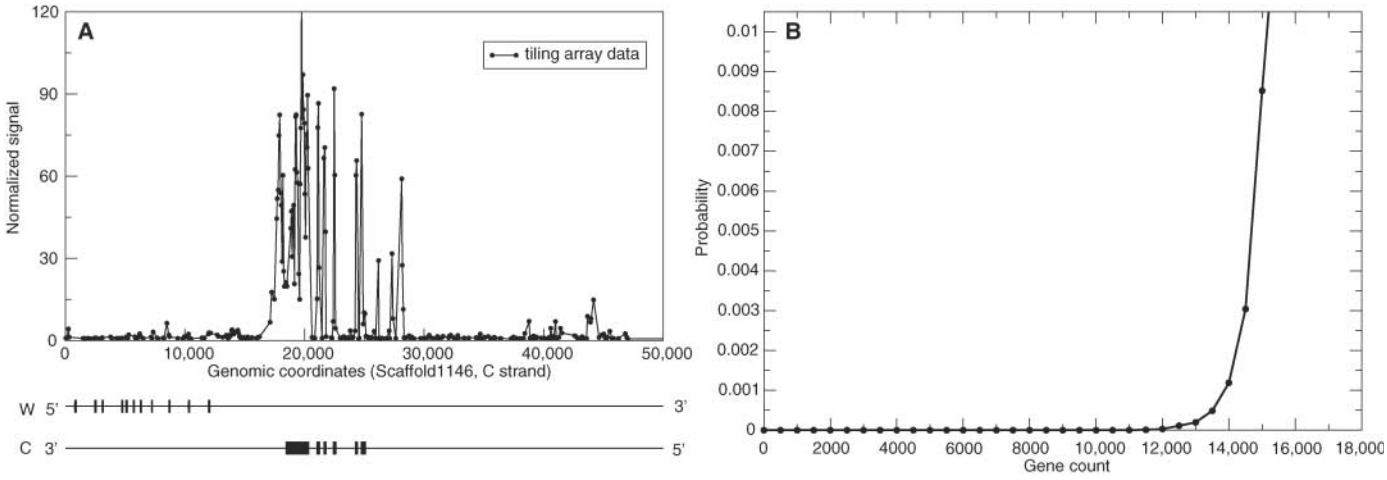

Fig. 1. Visualization of transcription profiles in protein-coding genes and probability of false-positives. (**A**) An active and an inactive gene. The protein-coding regions of the genes are indicated by the bars, and the orientation of the genes by the DNA strands (W, C) on which they are portrayed. Hybridization of each chip in the array is shown in arbitrary units (ordinate). The active gene is *Sp-gcm*, for which complete cDNA sequence is also available (*21*), transcribed from right to left. The activity profile includes the 3′-UTR, extending beyond the terminal codogenic region in the last exon. The inactive gene encodes an adenosine 5′-diphosphate ribosylation factor related protein. The peaks preceding the first exon of *gcm*, at 26,000 to 28,000, and at 45,000, are of the short noncoding RNA class. (**B**) Poisson probabilities of occurrence of falsely positive expression assignment, as a function of the total of number of apparently expressed genes. The probability that the expression profile of each gene could have been generated from adventitiously noisy probes was computed as described in the text.

probe intron peak of fig. S1A). We determined whether a gene is actually expressed in the 0- to 45-hour embryo by assessing the significance of transcriptional activity in the set of probes that lie within the predicted exons of that gene (*10*). For each gene in the OGS set (*5*), a Poisson calculation was performed, based on the number of probes in the array overlying the exons of the gene that score as active, to estimate the probability that the observed profile was artifactual. Above about 12,000 to 13,000 active gene models, the probability of false-positives rose rapidly (Fig. 1B, table S3). Some genuinely active genes are no doubt excluded by this cutoff—for example, genes that consist entirely of very small exons, or genes that are represented by very few probes (<3) because of sequence features that precluded choice of those sequence elements for representation in the probe set (*10*), or genes not represented in the genome assembly.

To estimate the number of genes expressed in the embryo up to the late gastrula stage, several corrections were required. Of the approximately 12,000 to 13,000 OGS gene models unequivocally scored as expressed (Fig. 1B), 1400 were duplicates, an artifact of high genomic polymorphism in the initial assembly process (*5*). A further 250 active gene models were excluded, because they are single-exon reverse transcriptase genes (mobile elements). On the other hand, this measurement detected a number of active open reading frames not represented in the gene model set used in this study (*5*). Where these were near one another, they were clustered, and the probability of accidental occurrence of these open reading frames in an 800-Mb genome was calculated. In total, ~1000 such putative genes were identified with a false-positive rate of <1% (table S4).

We may compare the end result, about 11,000 to 12,000 genes expressed, to the conclusion derived a quarter of a century ago from saturation single-copy sequence hybridization of embryo polysomal mRNA (*2*). This conclusion was that the same embryo uses about 8500 different genes (counting all the members of any given repetitive class of genes as 1) at the gastrula stage and, if other stages are added in (as they are here), about 10% more. Given that genes with high sequence similarity in large (more than 100-member) gene families would have been excluded from the earlier hybridization results, the two values are reasonably consistent. In any case, these measurements demonstrate that even by conservative estimates, a very large number of protein-coding informational units are required for the construction of this embryo, simple as it is, amounting to at least half of the total number of genes predicted in the *S. purpuratus* genome (12,000 out of 23,500) (*5*).

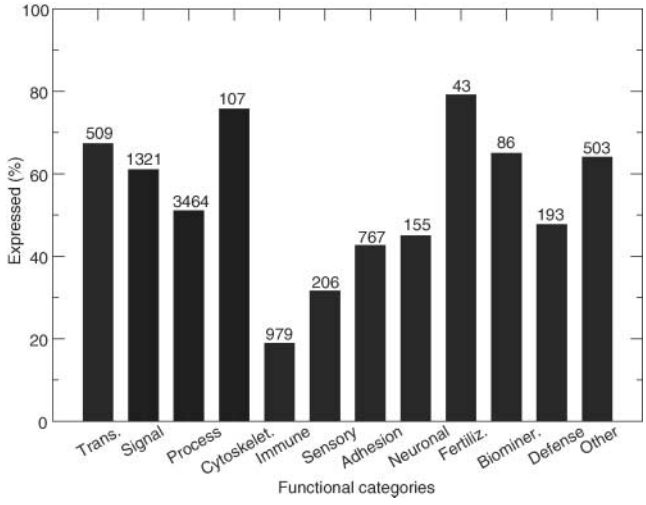

Fig. 2. Functional distribution of genes expressed in the embryo. The bar chart displays the percentage of annotated genes of different functional categories expressed in the sea urchin embryo. The functional categories are derived from a manual curation database (*5*) and are shown in table S3. The number at the top of each bar represents the total number of annotated genes in the corresponding category, including all expressed and unexpressed ones. Trans., transcription factors; Signal, signaling genes; Process, basic cellular processes such as metabolism; Cytoskelet., cytoskeletal; Fertiliz., fertilization; Biominer., biomineralization.

In *S. purpuratus*, the embryo gives rise to a larva after 3 days of development, within which the adult form develops during the successive weeks of larval feeding. By the late gastrula stage, only some small patches of undifferen-

tiated cells set aside from the processes of embryonic specification for adult body formation (*12*), and the midgut, will contribute to the adult body plan in the postembryonic period. The descendants of most of the 48-hour embryo cells will be jettisoned at metamorphosis. In contrast, in other embryos for which we have array-based transcriptome measurements, such as *Drosophila* (*9*) and *Caenorhabditis elegans* (*13*), the development of adult body parts begins immediately upon gastrulation, and there is no point after the very earliest stage at which embryonic gene use per se can be separated from gene use to construct the adult body plan.

More than 9200 OGS gene models were functionally annotated in the course of the genome project (*5*). In Fig. 2 we report the fractions of these genes expressed during embryogenesis, according to their functional classes (table S3). Most notable is the high embryonic usage of transcription factor and signaling genes. In other work (*14*), Howard-Ashby *et al.* showed by QPCR measurements that nearly 80% of all genes encoding transcription factors other than putative Zn-finger transcription factors are expressed by 48 hours [in Fig. 2, Zn finger proteins in the "Trans." category are probably not all transcription factors (*15*)]. Thus, it requires most of the "regulome" just to construct the single-cell-thick gastrula embryo. These same genes must, in general, be used repeatedly in the construction of the far more complex adult body plan. Genes related to basic cellular processes (e.g., intermediary metabolism) and cytoskeletal structure (e.g., actins and myosins) were also highly expressed; these would be expected to be required in cells of both embryo and adult tissues. This is true as well of detoxification and other xenobiotic defense molecules—the price of existence in the marine environment—and of biomineralization and neuronal molecules partially shared by the respective embryonic and adult differentiated cell types. By contrast, the immune genes (*5*, *16*) are largely expressed in the coelomocytes, which are the adult immune effector cell types. There is an elemental embryonic and larval immune defense system as well, mediated by certain embryonic mesenchymal cells, and this may account for the ~20% usage of immune genes in the embryo transcriptome (*16*). Sensory genes, such as G-coupled sensory receptors, are expressed in adult structures, the tubefeet and the pedecellaria (*17*), although again there is a rudimentary larval sensory system, about which very little is known. Little genomewide data are currently available on gene expression in adult bodies of the sea urchin. An experiment similar to this one is not meaningful for entire adult bodies made of large numbers of different tissues, because transcripts present in rare tissues will not be visible. Expression in each tissue will need to be measured individually.

Qualitatively, the transcription profiles enabled thousands of the >9200 gene models annotated by the Consortium (*5*) to be directly checked or corrected. Table S5 presents the results of our comparison between each predicted gene model and the transcribed regions derived from the tiling data. The gene models were mainly accurate, but missing exons were often identified by reference to these profiles. On average, the OGS genes expressed in the sea urchin embryo were 15.8 kb long and contained 9 exons, whereas the OGS genes on average were 11.9 kb long with 6.6 exons. Lack of tiling probes on short OGS genes with few exons may have contributed to the difference. The transcriptome data also indicated the dimensions of the 3′-UTR sequences (table S3), as well as the approximate transcription start sites. Many of the subgroups of sea urchin annotators used the high-resolution array data to manually curate their genes of interest (*5*). It was thus particularly useful for the subsequent analysis that the transcriptome measurements were carried out at a relatively early stage of the genome sequencing project as a whole, as soon as the initial assembly permitted.

Finally, as in all other whole-genome array hybridizations, many enigmatic transcripts were observed that are not included in protein-coding genes (table S6). A major class of these is composed of short ($\leq$ 200 nt) asymmetrically represented transcripts, of which some 51,000 were recorded (table S7). Only a small fraction (about 2000) represent sequences that also occur in active, protein-coding genes (including 3′-UTRs), and these repetitive sequences were excluded. Nor is any appreciable fraction complementary to other short noncoding sequences, again excluding the possibility that they are repetitive sequences transcribed elsewhere. Similarly, there was little homology to any known microRNAs (miRNAs), and the short transcripts are smaller than typical pre-miRNAs (>1 kb). Nearly 170 of the 51,000 transcribed regions are conserved in the human genome (BLAST cutoff 1×10^{-5}, table S7) and could potentially represent noncoding RNAs. Statistically, these 51,000 transcripts are exactly as likely to occur far from any active gene, in a distant intergenic domain, as near a gene or in its introns. To determine if these could in general be transcripts produced in cis-regulatory modules [e.g., (*18*)], we first manually examined a number of known examples, but in almost no instance observed the authenticated cis-regulatory modules we used as probes to be represented by these transcripts. We also compared the locations of the short transcripts in the vicinity of 28 well-characterized genes (table S2) to those of all interspecifically conserved sequence patches. There were about 500 such patches in introns or within 30 kb of these genes in either direction (*3*, *4*, *19*), and many have cis-regulatory activity [e.g., (*20*)]. Only 21 of these patches overlapped regions included in the short transcripts, a result not different from random expectation, and with one exception the termini of the patches and the transcripts were noncoincident. We therefore believe that these transcripts do not represent cis-regulatory modules, although experimental verification will be necessary.

The number of active genes sets in concrete terms the dimensions of the regulatory task of the genomic control apparatus driving embryogenesis. It cannot be said that the transcriptome is functionally understood until the individual roles and interactions of each component are revealed. Assessment of transcriptional activity across the whole genome represents the essential beginning of that process.

References and Notes

1. E. H. Davidson, A. Ransick, R. A. Cameron, *Development* **125**, 3269 (1998).
2. E. H. Davidson, *Gene Activity in Early Development* (Academic Press, San Diego, 1986).
3. H. Bolouri, E. H. Davidson, *Proc. Natl. Acad. Sci. U.S.A.* **100**, 9371 (2003).
4. For a large current compilation focused upon regulatory genes, see http://sugp.caltech.edu/endomes/.
5. Sea Urchin Genome Sequencing Consortium, *Science* **314**, 941 (2006).
6. P. Kapranov *et al.*, *Science* **296**, 916 (2002).
7. P. Bertone *et al.*, *Science* **306**, 2242 (2004).
8. V. Stolc *et al.*, *Science* **306**, 655 (2004).
9. F. Biemar *et al.*, *Proc. Natl. Acad. Sci. U.S.A.* **103**, 12763 (2006).
10. Materials and Methods, figs. S1 and S2, and tables S1 to S7 are available as supporting materials on *Science* Online.
11. It is a set of regulatory genes for which full-length cDNA sequences are available. Their embryonic expressions were previously confirmed by QPCR measurement (*3*, *4*).
12. K. J. Peterson, R. A. Cameron, E. H. Davidson, *Bioessays* **19**, 623 (1997).
13. M. N. Arbeitman *et al.*, *Science* **297**, 2270 (2002).
14. M. Howard-Ashby *et al.*, *Dev. Biol.* 10.1016/j.ydbio.2006.10.016, in press.
15. S. C. Materna, M. Howard-Ashby, R. Gray, E. H. Davidson, *Dev. Biol.* 10.1016/j.ydbio.2006.08.32, in press.
16. T. Hibino *et al.*, *Dev. Biol.* 10.1016/j.ydbio.2006.08.065, in press.
17. F. Raible *et al.*, *Dev. Biol.* 10.1016/j.ydbio.2006.08.070, in press.
18. M. Ronshaugen, M. Levine, *Dev. Cell* **7**, 925 (2004).
19. Conserved patches were derived on the basis of sequence homology between two distant sea urchin species (*3*, *4*).
20. C.-H. Yuh *et al.*, *Dev. Biol.* **246**, 148 (2002).
21. A. Ransick *et al.*, *Dev. Biol.* **246**, 132 (2002).

22. This work was supported by grants to V.S. from the NASA Center for Nanotechnology, the NASA Fundamental Biology Program, the Computing, Information, and Communications Technology programs (contract NAS2-99092), NIH grant HD-37105 (to E.H.D.), and Brown University (to S.I.).

Supporting Online Material

www.sciencemag.org/cgi/content/full/314/5801/960/DC1
Materials and Methods
Fig. S1
Tables S1 to S7
References

29 June 2006; accepted 23 October 2006
10.1126/science.1131898

Predators Accelerate Nutrient Cycling in a Bromeliad Ecosystem

Jacqueline T. Ngai* and Diane S. Srivastava

The availability of nutrients in ecosystems is determined by resource supply and recycling rates and affects important ecosystem properties (*1*–*3*). The relative roles of abiotic supply and food web configuration in determining resource-processing rates remain contentious and poorly understood. Under anthropogenic pressure, ecosystems are predicted to lose predators disproportionately, affecting ecosystem processes (*4*). Current ecological theory predicts that predator loss will affect nutrient cycling by changing prey abundance (density-mediated effects, as in a trophic cascade) (*5*) or prey foraging efficiency (trait-mediated effects) (*6*). These changes can further affect nutrient cycling by altering the species composition or size structure of the prey community. In this study, we examined the effects of predators on nutrient cycling by using the detritus-based insect community in bromeliads. We demonstrate that predation can have counterintuitive effects on nutrient cycling.

Leaves of tank-forming bromeliads (e.g., *Vriesea* and *Guzmania* genera) are tightly interlocking, forming wells that collect water and leaf litter and provide habitat for aquatic insect larvae. The detritus not only supports the insect community but also provides a source of nutrients for the bromeliad. A natural gradient also exists in predation where the major predator, a damselfly larva (*Mecistogaster modesta*), becomes more abundant as the plant grows. Although it has been hypothesized that aquatic insects increase nutrient flux to the bromeliad, this relationship has never been documented.

First, we ran fertilization experiments to determine whether nitrogen (N) or phosphorus (P) limit the productivity of the plant and insect components of this ecosystem (*7*). Both tissue nutrient ratios and fertilization experiments showed that N, rather than P, primarily limits productivity of bromeliads and can limit insect productivity [Supporting Online Material (SOM) text and tables S1 and S2], so we focused on the effects of trophic structure on N cycling. Leaf detritus enriched in ^{15}N was used to trace the movement of N through the food web in bromeliads containing either no insects, detritivores only, or detritivores and predators.

The presence of detritivores alone did not affect the amount of N entering bromeliads from the enriched detritus (Fig. 1A). However, in the presence of both detritivores and predators, there was a significant enrichment in ^{15}N in bromeliad leaves compared with plants containing detritivores alone, indicating that the presence of predators increased the flow of N from litter to bromeliads. This is surprising given that previous studies, consistent with the predictions of density- or trait-mediated effects, have shown that predators decrease litter decomposition by reducing detritivore abundance (*8*) or by decreasing the foraging rate (*9*) of detritivorous arthropods.

We hypothesize that the detritivorous insects, which pupate relatively rapidly, constitute a loss of litter-derived N for bromeliads when they emerge. A survey indicated that detritivorous insects generally have higher N:P ratios than those found in typical litter (Fig. 1B), suggesting that, as leaf litter is consumed, the insects will preferentially retain N in their body tissues and release P. Predation by longer-lived damselfly larvae converts the mobile pool of N contained in detritivores into fecal pellets that can be decomposed by microbes or leached to release N in a form available to the bromeliad. Thus, insects facilitate nutrient uptake by the plant, but only if both predators and detritivores are present.

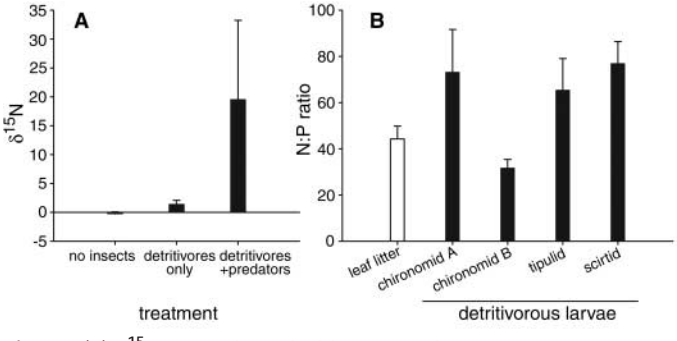

Fig. 1. (**A**) $\delta^{15}N$ in new bromeliad leaves for plants containing no insects, detritivore insects only, or detritivore and predatory insects (mean ± SEM). Bonferroni-corrected *t* test (detritivores alone versus control, $z = 0.478$ and $P = 0.63$; detritivores plus predators versus detritivores alone, $z = 2.36$ and $P = 0.018$). (**B**) Comparison of N:P ratios (by atom) for detritivore larvae and for leaf litter (mean ± SEM). Larger detritivores (chironomid A, scirtids, and tipulids) have N:P ratios higher than that of leaf litter [$F_{1,\ 20} = 5.05$, $P = 0.04$ for linear contrast following significant analysis of variance ($F_{4,20} = 3.66$, $P = 0.02$)]. Chironomid B is a smaller detritivore that accounts for only a small proportion of detritivore biomass in bromeliads.

These results emphasize the importance of the temporal and spatial scales of dispersal for nutrient flux. The emergence of adult insects means that, although detritivores increase resource flux over larval time scales by releasing nutrients from litter, these insects act as a nutrient sink for bromeliads over their entire life span. The faster emergence rate of detritivores compared with that of predators allows predation to reduce the loss of N from the bromeliad. Although we use insects in bromeliads to examine biotic effects on nutrient cycling, our results can give insights into other systems where mobility differs between trophic levels. Some trophic interactions, for instance, involve migratory and nonmigratory species or species that undergo ontogenetic niche shifts. This mechanism may also apply if the prey species has a very different range size than its predator. Given the increased extinction risk of higher trophic levels, understanding the mechanisms whereby predators drive important ecosystem processes is critical in predicting anthropogenic impacts on natural systems.

References and Notes

1. R. Aerts, F. S. Chapin, *Adv. Ecol. Res.* **30**, 1 (2000).
2. S. E. Hobbie, P. M. Vitousek, *Ecology* **81**, 1867 (2000).
3. A. Tewfik, J. B. Rasmussen, K. S. McCann, *Ecology* **86**, 2726 (2005).
4. E. J. Duffy, *Ecol. Lett.* **6**, 680 (2003).
5. M. E. Power, *Science* **250**, 811 (1990).
6. E. E. Werner, S. D. Peacor, *Ecology* **84**, 1083 (2003).
7. Materials and methods are available as supporting material on *Science* Online.
8. C. R. Ruetz, R. M. Newman, B. Vondracek, *Oecologia* **132**, 307 (2002).
9. T. M. Short, J. R. Holomuzki, *Freshwater Biol.* **27**, 91 (1992).
10. We thank R. Conner, A. Pelletier, M. Rios, and E. Umaña Canales for field assistance; the Área de Conservación Guanacaste, C. Moraga Medina, P. Rios Castro, R. Blanco, and M. Chavarría for logistical support; B. Gilbert, K. Kirby, and B. Starzomski for comments on the manuscript and help in the field; and L. Harmon, D. Irwin, J. Shurin, M. Vellend, K. Venter, and two anonymous reviewers for comments on earlier drafts. Funding was provided by the Natural Sciences and Engineering Research Council (Canada).

Supporting Online Material

www.sciencemag.org/cgi/content/full/314/5801/963/DC1
Materials and Methods
SOM Text
Tables S1 and S2
References

17 July 2006; accepted 30 August 2006
10.1126/science.1132598

Department of Zoology, University of British Columbia, 6270 University Boulevard, Vancouver, British Columbia V6T 1Z4, Canada.

*To whom correspondence should be addressed. E-mail: ngai@zoology.ubc.ca

Low-Field Magnetic Separation of Monodisperse Fe_3O_4 Nanocrystals

Cafer T. Yavuz,[1] J. T. Mayo,[1] William W. Yu,[1] Arjun Prakash,[2] Joshua C. Falkner,[1] Sujin Yean,[3] Lili Cong,[3] Heather J. Shipley,[3] Amy Kan,[3] Mason Tomson,[3] Douglas Natelson,[4] Vicki L. Colvin[1]*

Magnetic separations at very low magnetic field gradients (<100 tesla per meter) can now be applied to diverse problems, such as point-of-use water purification and the simultaneous separation of complex mixtures. High–surface area and monodisperse magnetite (Fe_3O_4) nanocrystals (NCs) were shown to respond to low fields in a size-dependent fashion. The particles apparently do not act independently in the separation but rather reversibly aggregate through the resulting high-field gradients present at their surfaces. Using the high specific surface area of Fe_3O_4 NCs that were 12 nanometers in diameter, we reduced the mass of waste associated with arsenic removal from water by orders of magnitude. Additionally, the size dependence of magnetic separation permitted mixtures of 4- and 12-nanometer–sized Fe_3O_4 NCs to be separated by the application of different magnetic fields.

The removal of particles from solution with the use of magnetic fields is more selective and efficient (and often much faster) than centrifugation or filtration (*1*–*3*) and, as a result, magnetic separations are used in areas as diverse as biotechnology and ore refinement (*4*–*7*). Central to the process is the generation of magnetic forces on particles large enough to overcome opposing forces, such as Brownian motion, viscous drag, and sedimentation (*8*). In biotechnology, magnetic separators use relatively low field gradients in a batch mode to concentrate surface-engineered magnetic beads from a suspension (*9*, *10*). In manufacturing, magnetic materials are typically recovered from waste streams under flow conditions with high-gradient magnetic separators (HGMS) that use larger fields (up to 2 T) and columns filled with ferromagnetic materials (*11*, *12*).

Decreasing the particle sizes used in magnetic separations from micrometers to nanometers would increase the available sorptive areas by 100 to 1000 times. Such material optimization, however, is not generally practical, because the magnetic force acting on a particle in a field gradient is proportional to the particle volume. If the particles are too small, their magnetic tractive forces in a field gradient will not be large enough to overcome Brownian motion, and no separation will occur (*13*–*15*). For iron oxide, extrapolations from the behavior of the bulk material suggest that the critical size for separation is ~50 nm for the case of an isolated (nonaggregated) particle (*13*). This treatment assumes very large applied fields and the latest designs for extremely high-gradient separators, both features that make magnetic separations prohibitively expensive in many settings (*3*, *16*). For simpler and less costly low-gradient separators, the critical size for capture in magnetic gradients increases substantially.

Extrapolations from bulk properties to nanoscale materials are frequently problematic, and a more comprehensive analysis of nanoscale magnetic behavior suggests that nanocrystals (NCs) could offer substantial opportunities for low-field magnetic separations. Below 50 nm in diameter, nanoscale magnets exhibit a complex range of size-dependent behaviors, including a transition below ~40 nm in size to single-domain character (*17*, *18*), magnetic susceptibilities greater than that of the bulk material (*19*, *20*), and the emergence of superparamagnetic behavior (*17*). Such systems could experience larger than expected magnetic forces from bulk behavior due to larger moments. Hutten and co-workers have suggested the advantages of higher-susceptibility materials, such as FeCo, in which an increased magnetic moment could in principle enable high-gradient separations with isolated NCs (*7*, *21*). Additionally, in external fields, the large surface gradients present at the surfaces of single-domain materials could induce transient aggregation, effectively forming larger and more magnetically responsive particles. Laibinis and co-workers suggested nanoparticle aggregation, even before field application, to explain their observation of the magnetic capture of polydisperse NCs in a high-gradient separation (>1000 T/m) using fields of 1 to 2 T (*16*, *22*).

We show that magnetite (Fe_3O_4) particles of a critical size (20 nm) can be removed from solution at very low field gradients (<100 T/m) and present evidence that aggregation, caused by the high field gradients at the nanoparticle surfaces, helps drive this process. To determine whether a critical size exists for this low-field separation, we have prepared Fe_3O_4 NCs that are highly monodisperse in size and nonaggregated in both aqueous and organic solutions (figs. S1 to S5) (*23*–*25*). Having previously established that the surfaces of nanocrystalline Fe_3O_4 particles are useful in the context of As removal from solution, we will use this problem as an example of a high-throughput separation (*26*).

Nanocrystalline Fe_3O_4 particles could be removed from solution with a low-gradient separator (23 T/m) like those applied to the recovery of micrometer-sized beads in protein purification. The initial rust-colored solution contained 16-nm-diameter Fe_3O_4 NCs homogeneously dispersed in water (Fig. 1A). Once placed in the separator, the solution became clear within minutes, and a deposit of particles formed at the back of the vial, where the field gradient was the largest (Fig. 1B). After removal from the separator, the solution could be restored to its initial state with a vigorous shake. Similar behavior was observed for all NCs larger than ~10 nm in diameter, but the time for complete separation varied with solution concentration and NC size.

The removal of NCs cannot be explained with a simple model of noninteracting particles. If we assume that the iron oxide particles act independently, we may calculate a size threshold below which NCs will not be removed. For a field gradient ∇B of 23 T/m, the largest magnetic force F_{mag} that can be applied to a single particle

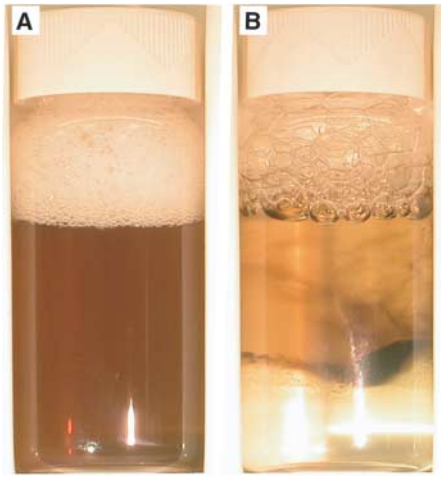

Fig. 1. Magnetic batch separation of 16-nm water-soluble Fe_3O_4 NCs with a conventional separator (Dexter Magnetic LifeSep 50SX). The field gradient at full field was 23.3 T/m. (**A**) Appearance of the solution immediately after placement in the separator. (**B**) After several minutes, the initially homogeneous solution became heterogeneous, and a black deposit formed on the back wall where the field gradient was the highest.

[1]Department of Chemistry, Rice University, 6100 Main Street, Houston, TX 77005, USA. [2]Department of Chemical and Biomolecular Engineering, Rice University, 6100 Main Street, Houston, TX 77005, USA. [3]Department of Civil and Environmental Engineering, Rice University, 6100 Main Street, Houston, TX 77005, USA. [4]Department of Physics and Astronomy, Rice University, 6100 Main Street, Houston, TX 77005, USA.

*To whom correspondence should be addressed. E-mail: colvin@rice.edu

of diameter d is $F_{mag} = \frac{4\pi}{3}\left(\frac{d}{2}\right)^3 M_{sat}\nabla B$, where M_{sat} is the saturation magnetization of the material. In order for these particles to separate effectively, this force must exceed the typical Brownian force $F_B \sim \frac{k_B T}{d}$, where T is temperature and k_B is Boltzmann's constant. For Fe_3O_4, with $M_{sat} = 4.69 \times 10^5$ A/m, at 300 K, this implies that independent particles smaller than ~160 nm in diameter will not separate in the low field gradients that were used. The previous analysis ignores the fact that the application of an external field will generate extremely large field gradients (up to $\mu_0 M_{sat}/d$, where μ_0 is the permeability of free space) at the surfaces of single-domain particles. Even in the absence of a field, magnetic NCs may interact as a result of magnetic dipole-dipole interactions (*27*). In the presence of a field, these surface gradients could generate chains or aggregates of NCs. Once the field is removed, surface gradients would disappear and particle interactions would diminish. This reversible aggregation provides the advantages of a high–surface area nanocrystalline sorbent, without sacrificing the ability to separate the materials in a reasonable field gradient.

We characterized the size dependence of the NC separation process using an HGMS. Unlike the simple batch separator used in Fig. 1, this system uses an electromagnet to generate external fields of variable strength around a column packed with ferromagnetic wire. Exact measures of the field gradients in such a system are challenging to obtain, but most treatments predict that the gradient and the applied external field are proportional and that, at fields in excess of 1 T, gradients of 10^4 T/m are possible (*28*, *29*). Fe_3O_4 NCs of varying sizes were gravity-fed into the 22.3-cm-long column at various field strengths, and the effluent was collected and analyzed for iron content by means of inductively coupled plasma atomic emission spectroscopy (ICP-AES). From such experiments, we calculated the fraction of material retained in the column at increasing magnetic field strengths and compared these retention efficiencies between samples (Fig. 2A).

The size dependence of the retention of NCs in the magnetized column is shown in Fig. 2A. The amount of material retained in the column increased as the external field strength increased. For example, nearly 100% of the 12-nm-diameter NCs were retained in the column at applied fields of only 0.2 T, well below the saturation field for stainless steel. This same field, however, could not capture NCs less than 8.0 nm in diameter. Figure 2B shows that for all particles, as the particle size became smaller, more field was required to ensure their complete separation. This result parallels the observation (fig. S1C) that, at low field strengths, small NCs are not fully aligned. Without complete alignment, the magnetic moments of NCs would be quite small and would not generate enough tractive force with external field gradients (*19*, *30*).

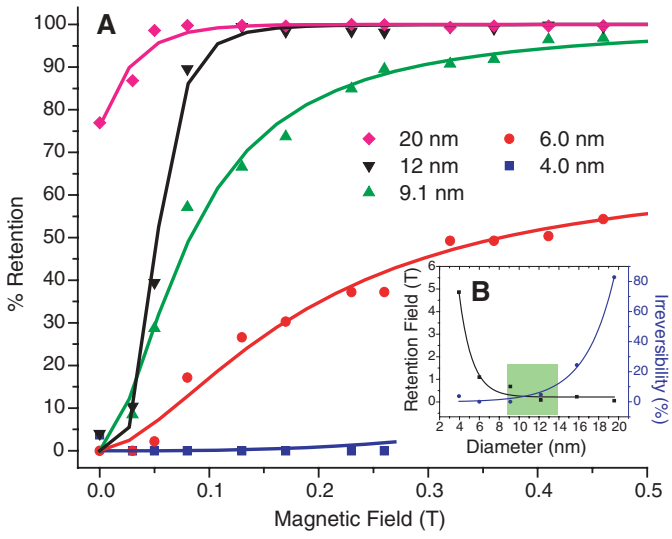

Fig. 2. (**A**) Size-dependent magnetic separation of 4.0-, 6.0-, 9.1-, 12-, and 20-nm Fe_3O_4 NCs in a column separator. A hexane dispersion of NCs was passed through a stainless steel column packed with 15 g of stainless steel wool; solutions were introduced at 20 ml/min by way of a gravity feed. The column was held in an S. G. Frantz canister separator (tunable field 0 to 1.6 T). After each data point was taken, the packing was removed, and the column was washed thoroughly, dried in an oven (at 60°C), and packed with clean, unused, stainless steel wool. Fractions collected at each data point were digested in concentrated HNO_3 and diluted to 5.5% HNO_3 before iron content analysis by means of ICP-AES. The percent retention was calculated by dividing the atomic iron concentration in a solution by the concentration found for the starting (unseparated) suspension. The curves presented are complex polynomials meant to guide the display and are not reflective of any physical model. These data illustrate that the smaller the NC, the greater the magnetic field required to retain the NC in the column. The 20-nm-diameter particles permanently affixed to the column after removal of the field. (**B**) The absolute field required to retain 100% of the NCs loaded to the stainless steel column (black points and curve) versus the diameter of Fe_3O_4 NCs. Also shown (blue points and curve) are the fractions of material that were unrecoverable after washing the column. The shaded area represents the optimal size for magnetic separations. For 4.0- and 6.0-nm particles, materials that were not completely retained, the absolute field for complete retention was estimated from their low-field behavior.

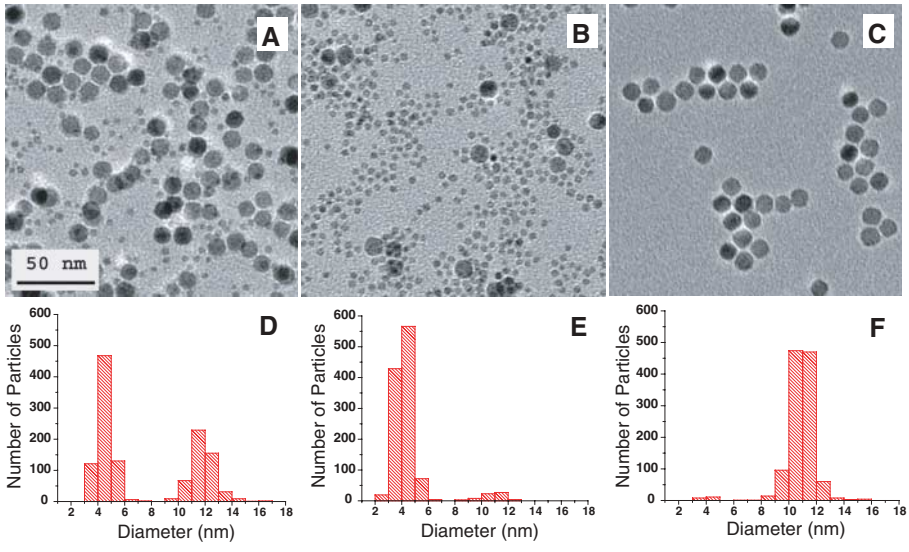

Fig. 3. Multiplexed separation of NC mixtures. 4.0- and 12-nm Fe_3O_4 NC solutions (both in hexane dispersions) were mixed in a 1:3 ratio (volume/volume) to achieve a particle mixture that contained roughly the same concentration of each size. With the use of an S. G. Frantz canister separator (Model L1-CN), the mixture separated into two size fractions, depending on the field. (**A**) Transmission electron microscopic (TEM) micrograph of the initial bimodal mixture. Scale bar in (A) is for (A) to (C). (**B**) TEM micrograph of the high-field (0.3 T) fraction. 94.4% of the 4.0-nm particles and <3% of the 12-nm particles were recovered. (**C**) TEM micrograph of low-field (0.03 T) fraction. 98.3% of larger (12 nm) NCs were collected. (**D** to **F**) Size-distribution histograms for particles counted in (A) to (C), respectively. In (A), two different populations were observed. In (B), the smaller size range was apparent as observed in the TEM micrograph. In (C), the larger sizes were successfully recovered after separation. For all size histograms, >1000 particles were counted in multiple images and measured automatically with the use of the software package ImagePro.

The size of NCs can also influence their recovery after magnetic capture. As seen in Fig. 2A, at zero external field (after the columns were magnetized), NCs that were 20 nm in diameter could not be removed from the column matrix even after repeated washes. This irreversible interaction is analogous to the fouling of a physical filter and would limit the use of larger magnetic sorbents in a commercial setting. Smaller NCs, however, did not show such behavior and could be concentrated and reused quite easily (Fig. 2B). This observation stems from the fact that iron oxide NCs less than ~16 nm in diameter behave as superparamagnets (*17*, *30*–*33*). In this limit, NCs have no net magnetization (fig. S1E) and thus experience no interactions with the very small stray fields present in the ferromagnetic column matrix (*34*). This result is consistent with observations of commercial magnetic beads, which found that, even in micrometer-sized systems, there was much value in the use of magnetic materials that were superparamagnetic (*35*, *36*). The data shown here reveal that superparamagnetism is only one of several properties that should be considered in material design. Indeed, if NCs are too small, then magnetic separations require very large critical field strengths to affect any capture of particles (Fig. 2B). For optimal NC magnetic separations at low fields, one should use the largest NCs that still show superparamagnetic properties.

Table 1. A comparison of As removal efficiency, assuming a treatment of 2 liters of As solution (500 μg/liter) with 1 g of Fe_3O_4.

Particle size (nm)	As(V) or As(III)	Residual As concentration (μg/liter)	% removal
12	As(III)	3.9	99.2
20	As(III)	45.3	90.9
300	As(III)	375.7	24.9
12	As(V)	7.8	98.4
20	As(V)	17.3	96.5
300	As(V)	354.1	29.2

The size dependence of NC capture (Fig. 2A) now makes it possible to develop magnetic separation processes that can, in one process, remove several different types of materials. Such capability is particularly important in biotechnology, in which the simultaneous treatment of mixtures requires more sophisticated multiplexed separations (*37*). Figure 3 demonstrates the principle for magnetic separations, in which different field strengths recovered different populations of bimodally distributed iron oxide NCs. Initially, the sample consisted of two monodisperse fractions of NCs, intentionally combined to create a test solution (Fig. 3A); at low applied fields (0.3 T), the effluent from the column contained >90% of the smaller particles, and the larger particles were retained in solution (Fig. 3B). After the field was turned off, a column wash recovered the larger particles (Fig. 3C). With the use of monodisperse iron oxide NCs, it is thus possible to use magnetic separations in a multiplexed mode and recover different components of a mixture in one treatment.

Because NCs can be removed from batch solutions with the use of permanent handheld magnets, we explored whether these NCs could act as effective magnetic sorbents for the removal of As from water. Arsenic is a good model contaminant for these materials, because its interaction with iron oxides is strong and irreversible, even on nanoscale particles (*26*, *38*). Its practical and effective removal from groundwater remains an important and intractable problem in water treatment (*39*, *40*). Conventional HGMSs operating at ≥1T are already used in water treatment processes, primarily to induce the aggregation of intrinsically magnetic waste products that are not easily amenable to other methods of coagulation (*12*, *26*, *41*, *42*).

Both As(III) and As(V) exhibit strong adsorption onto iron oxide nanocrystalline surfaces; as the concentration of As increased in the standard solution, the amount of As bound to NCs increased as well, until the capacity of the material was reached (Fig. 4). The interactions between iron oxide and As are also irreversible, so Fe_3O_4 NCs that have bound As should not release the material back into the environment during storage and further treatment. These data show clearly that as the size of sorbent NCs decreases, sorption capacities increase substantially because of the increased surface areas in the samples.

Once As was sorbed onto NC surfaces, magnetic separations provided a way to remove the materials from solution. The As concentrations in test solutions before and after the removal of particles by means of a column magnetic separator (Table 1 and table S1) showed that As(III) and As(V) could be reduced to well below the current U.S. standards for drinking water (*43*). Also, because the test NCs are very small (12 nm), their very high specific surface areas provide extremely concentrated waste materials. For example, 300-nm-sized iron oxide particles have a sorption capacity of only 0.002% by weight, and thus, treating 50 liters of solution with 500 μg of As per liter generates 1.4 kg of waste; in contrast, for an equivalent treatment, only 15 g of 12-nm-sized iron oxide sorbent is required.

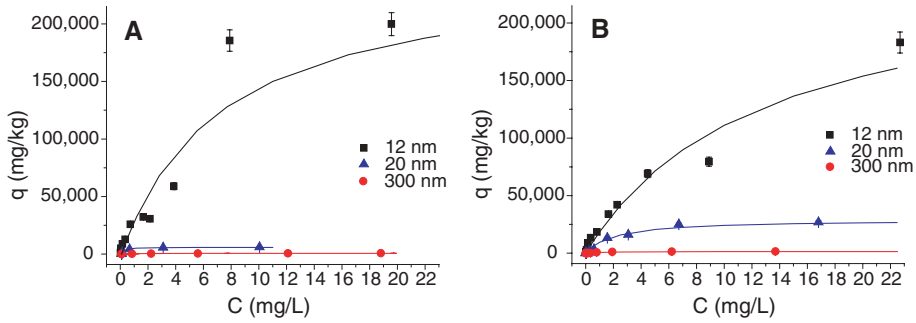

Fig. 4. Arsenic adsorption studies with nanocrystalline (12 nm) and commercially available (20 and 300 nm) Fe_3O_4. The smaller (12 nm) Fe_3O_4 particles were made water-soluble by means of a surfactant; for this, the NC solution was sonicated with an aqueous dispersion of a secondary surfactant, Igepal CO 630, and then purified by sedimentation [50,000 revolutions per minute (141,000*g*)]. Arsenic adsorption experiments were performed with 25 μg/liter to 25 mg/liter of As(III) and As(V) solutions, prepared in an electrolyte solution containing 0.01 M NaCl, 0.01 M tris(hydroxymethylamino)methane buffer, and 0.01 M NaN_3 at pH 8. All experiments were performed in batches with 10 and 100 mg of Fe_3O_4 per liter of solution for the 12- and 20-nm particles, respectively, and 2.5 g of Fe_3O_4 per liter of solution for the 300-nm particles. Equilibrium time was 24 hours, with constant tumbling. The solution was separated from Fe_3O_4 by a magnetic field column separator [S. G. Frantz canister separator (Model L1-CN)]. After the effluent was collected, the magnet was turned off, and 40 ml of deionized water was passed through the separator to elute Fe_3O_4. All effluents were acidified with trace-metal grade HNO_3 to contain 1% HNO_3 in solution. Arsenic concentration was measured with inductively coupled plasma mass spectrometry (ICP-MS). The nanoscale Fe_3O_4 was acid-digested, and the Fe and As concentrations in the digest were measured by ICP-AES and ICP-MS, respectively. (**A**) As(V) adsorption to magnetites of different size; (**B**) As(III) adsorption. C, arsenic concentration in solution; q, adsorption capacity. Errors bars in (A) and (B) indicate 5% error in the measurement of arsenic.

References and Notes

1. S. C. Chang *et al.*, *J. Ind. Microbiol. Biotechnol.* **32**, 629 (2005).
2. J. J. Hubbuch, D. B. Matthiesen, T. J. Hobley, O. R. T. Thomas, *Bioseparation* **10**, 99 (2001).
3. B. L. Hirschbein, D. W. Brown, G. M. Whitesides, *Chemtech* **12**, 172 (1982).
4. C. G. Gunther, *Electro-Magnetic Ore Separation* (Hill, New York, 1909).
5. R. Gerber, R. R. Birss, *High Gradient Magnetic Separation* (Research Studies, New York, 1983).
6. J. Oberteuffer, *IEEE Trans. Magn.* **10**, 223 (1974).
7. G. Reiss, A. Hutten, *Nat. Mater.* **4**, 725 (2005).
8. J. H. P. Watson, *J. Appl. Phys.* **44**, 4209 (1973).
9. M. Lewin *et al.*, *Nat. Biotechnol.* **18**, 410 (2000).

10. J. M. Nam, C. S. Thaxton, C. A. Mirkin, *Science* **301**, 1884 (2003).
11. C. H. Setchell, *J. Chem. Technol. Biotechnol. B Biotechnol.* **35**, 175 (1985).
12. C. Delatour, *IEEE Trans. Magn.* **9**, 314 (1973).
13. D. Fletcher, *IEEE Trans. Magn.* **27**, 3655 (1991).
14. D. R. Kelland, *IEEE Trans. Magn.* **34**, 2123 (1998).
15. G. B. Cotten, H. B. Eldredge, *Sep. Sci. Technol.* **37**, 3755 (2002).
16. G. D. Moeser, K. A. Roach, W. H. Green, T. A. Hatton, P. E. Laibinis, *Am. Inst. Chem. Eng. J.* **50**, 2835 (2004).
17. H. U. Worm, *Geophys. J. Int.* **133**, 201 (1998).
18. R. F. Butler, *Paleomagnetism: Magnetic Domains to Geologic Terranes* (Blackwell Scientific, Boston, 1992).
19. D. Horak, F. Lednicky, E. Petrovsky, A. Kapicka, *Macromol. Mater. Eng.* **289**, 341 (2004).
20. G. F. Goya, T. S. Berquo, F. C. Fonseca, M. P. Morales, *J. Appl. Phys.* **94**, 3520 (2003).
21. A. Hutten *et al.*, *J. Biotechnol.* **112**, 47 (2004).
22. A. Ditsch, S. Lindenmann, P. E. Laibinis, D. I. C. Wang, T. A. Hatton, *Ind. Eng. Chem. Res.* **44**, 6824 (2005).
23. See the supporting material on *Science* Online for supplementary data.
24. W. W. Yu, J. C. Falkner, C. T. Yavuz, V. L. Colvin, *Chem. Commun.* **2004**, 2306 (2004).
25. S. H. Sun, H. Zeng, *J. Am. Chem. Soc.* **124**, 8204 (2002).
26. S. Yean *et al.*, *J. Mater. Res.* **20**, 3255 (2005).
27. K. Butter, P. H. H. Bomans, P. M. Frederik, G. J. Vroege, A. P. Philipse, *Nat. Mater.* **2**, 88 (2003).
28. M. R. Parker, *Phys. Technol.* **12**, 263 (1981).
29. G. Iacob, A. Ciochina, O. Bredetean, *Eur. Cell. Mater.* **3**, 167 (2002).
30. A. R. Muxworthy, *Geophys. J. Int.* **144**, 441 (2001).
31. S. Bucak, D. A. Jones, P. E. Laibinis, T. A. Hatton, *Biotechnol. Prog.* **19**, 477 (2003).
32. R. F. Butler, S. K. Banerjee, *J. Geophys. Res.* **80**, 4049 (1975).
33. J. A. Dearing *et al.*, *Geophys. J. Int.* **124**, 228 (1996).
34. R. D. Ambashta, P. K. Wattal, S. Singh, D. Bahadur, *J. Magn. Magn. Mater.* **267**, 335 (2003).
35. B. I. Haukanes, C. Kvam, *Nat. Biotechnol.* **11**, 60 (1993).
36. G. P. Hatch, R. E. Stelter, *J. Magn. Magn. Mater.* **225**, 262 (2001).
37. G. Liu, J. Wang, J. Kim, M. R. Jan, G. E. Collins, *Anal. Chem.* **76**, 7126 (2004).
38. S. R. Kanel, B. Manning, L. Charlet, H. Choi, *Environ. Sci. Technol.* **39**, 1291 (2005).
39. M. A. Hossain *et al.*, *Environ. Sci. Technol.* **39**, 4300 (2005).
40. L. G. Twidwell, J. McCloskey, P. Miranda, M. Gale, in *Proceedings of the Global Symposium on Recycling, Waste Treatment and Clean Technology Conference*, San Sebastian, Spain, 5 to 9 September 1999 (The Minerals, Metals, and Materials Society, Warrendale, PA, 1999), pp. 1715–1726.
41. Y. Kakihara, T. Fukunishi, S. Takeda, S. Nishijima, A. Nakahira, *IEEE Trans. Appl. Supercond.* **14**, 1565 (2004).
42. A. Chiba *et al.*, *IEEE Trans. Appl. Supercond.* **12**, 952 (2002).
43. U.S. Environmental Protection Agency Arsenic Rule, *Fed. Regist.* **66**, 6976 (22 January 2001) [40 Code of Federal Regulations] (www.epa.gov/safewater/arsenic/regulations.html).
44. We thank NSF for its support of the Center for Biological and Environmental Nanotechnology (EEC-0647452). We also acknowledge with gratitude the Office of Naval Research (N00014-04-1-0003), and the U.S. Environmental Protection Agency Star Program (RD-83253601-0) for funding. C.T.Y. thanks the Robert A. Welch Foundation (C-1349) for a graduate fellowship. D. M. Mittleman provided invaluable help in developing this manuscript. Finally, the authors appreciate the efforts of J. Jones and W. Guo, who provided support for the supporting figures included on *Science* Online.

Supporting Online Material
www.sciencemag.org/cgi/content/full/314/5801/964/DC1
Figs. S1 to S5
Table S1
References

19 June 2006; accepted 20 September 2006
10.1126/science.1131475

Localized Temporal Change of the Earth's Inner Core Boundary

Lianxing Wen

Compressional waves of an earthquake doublet (two events occurring in the South Sandwich Islands on 1 December 1993 and 6 September 2003), recorded at three seismic stations in Russia and Kyrgyzstan and reflected off Earth's inner core boundary, arrived at least from 39 to 70 milliseconds earlier in the 2003 event than in the 1993 event. Such changes indicate that Earth's inner core radius enlarged locally beneath middle Africa by 0.98 to 1.75 kilometers between the times of these two events. Changes of the inner core radius may be explained by either a differential motion of the inner core, assuming that irregularities are present at the inner core boundary and fixed to the inner core, or a rapid growth of the inner core by this amount.

Earth's inner core grows from the solidification of the outer core (*1*). The growth of the inner core releases latent heat and dispels light elements, providing driving forces for the outer core convection (*2*) and power for generating the geodynamo (*3*, *4*). The inner core growth process is thought to be geologically slow (*5*–*10*) and geographically uniform because of the presumed extremely small variation in temperature in the outer core (*11*). Here, I used PKiKP [a compressional wave reflected off the inner core boundary (Fig. 1A)] waveforms of an earthquake waveform doublet discovered by Zhang *et al*. (*12*) to study temporal change of the inner core boundary.

Earthquake waveform doublets are earthquakes occurring at different times but in almost exactly the same location and generating similar waveforms (*12*–*18*). Because the relative travel time and waveform difference between the waveform doublets is sensitive only to the relative change of event location and/or the temporal change of seismic properties, it is powerful to use waveform doublets to study high-resolution relative locations of the earthquakes (*13*–*15*) and to detect temporal change of seismic properties (*12*, *16*–*18*). The similarities of the doublet waveforms also allow accurate travel time measurement to be made. Zhang *et al*. (*12*) reported the existence of 19 waveform doublets in the South Sandwich region over a period of 35 years and showed that the PKP(DF) (PKIKP) phases [a compressional wave propagating through the inner core (Fig. 1A)] are in misalignment to each other between the doublets. Their study provided compelling evidence for the reported temporal changes in PKIKP travel time (*19*–*21*). They further proposed that the observed temporal changes can be explained by an inner core differential motion over a lateral velocity gradient in the inner core (*20*).

I used the best doublet reported in Zhang *et al*. (*12*) (table S1). The doublet consists of two events occurring on 1 December 1993 (event 93) and 6 September 2003 (event 03). I used the observed difference in absolute arrival time of various seismic phases that are not associated with the inner core (non-IC phases) between the doublet to determine the relative location and origin time of the two events. I used event 93 as the master event [i.e., fixed its origin time and location to those reported in the earthquake catalog (table S1)] and searched for the best-fitting relative location and origin time for event 03 that minimize the travel time residuals of the non-IC phases between the two events. I then studied the temporal changes of travel time and waveform of the PKiKP-PKIKP or PKiKP phases between the doublet based on the best-fitting relative hypocenter location and origin time of the two events. To do so, the PKiKP and PKiKP-PKIKP waveforms of the doublet were superimposed on the basis of the relative arrival times of these phases between the doublet, estimated using the best-fitting relative location and origin time of the two events. The PKiKP travel time residuals between the doublet are further calculated by subtracting the predicted relative arrival times of the seismic phases from the measured arrival time differences between the doublet. If the superimposed waveforms are in misalignment between the doublet, or if a travel time residual is larger than the relocation error bar, it would mean that the arrival times of the seismic phases between the doublet cannot be explained by the relative origin time and hypocenter location of the doublet, and these phases exhibit temporal change in time.

The detailed relocation analysis places the doublet within 0.37 km in horizontal space and 0.7 km in depth (*22*). The inferred best-fitting relative origin time and hypocenter location between the doublet yield, for the non-IC phases,

Department of Geosciences, State University of New York at Stony Brook, NY 11794, USA. E-mail: Lianxing.Wen@sunysb.edu

a minimal root mean square travel time residual of 0.016 s and a maximal travel time residual of 0.031 s in the individual stations (fig. S1B) (*22*). The maximal travel time residual in the individual stations (0.031 s) is considered as the relocation error bar.

Superimposed PKiKP-PKIKP waveforms and PKiKP waveforms observed at stations ARU (Arti, Russia), AAK (Ala Archa, Kyrgyzstan), and OBN (Obninsk, Russia) reveal that the PKiKP phases observed at these stations are in misalignment and that they arrived earlier in event 03 than in event 93, even after the travel time differences due to the relative hypocenter position of the two events are taken into account (Fig. 1, B to E). The PKiKP and PKIKP phases recorded at station ARU arrived 0.11 s earlier and the PKIKP phase about 0.04 s earlier in event 03 than in event 93. Moreover, the PKiKP-PKIKP differential travel time was about 0.07 s smaller in event 03 than in event 93 (Fig. 1C). Station AAK is closer, and the separation of the PKiKP and PKIKP phases is not clear, but the later portion of the waveforms (energy primarily associated with the PKiKP phases) is clearly in misalignment and arrived about 0.07 s earlier in event 03 than in event 93, whereas the earlier portion of energy appears to have arrived at about the same time (Fig. 1D). The PKiKP waveforms observed at station OBN exhibit two characteristics: (i) the PKiKP main phases are evidently in misalignment between the two events, with the phase in event 03 arriving about 0.07 s earlier than in event 93 and (ii) the PKiKP coda waves show waveform dissimilarities between the two events (Fig. 1E).

The observed smaller differential PKiKP-PKIKP travel times of about 0.07 s at stations ARU and AAK in event 03 further confirm that the PKiKP travel time residuals were not caused by relative event location or origin time of the doublet but by temporal changes of PKiKP travel time between the occurrences of the two events (*22*). The temporal changes in PKiKP travel time are at least 0.07 s at ARU and AAK, using their PKIKP arrival times as reference, and 0.039 s at OBN taking into account the maximal possible error of relocation, with the PKiKP phases arriving earlier in event 03 than in event 93.

No discernible temporal change of PKiKP travel time is observed for other stations. Superimposed PKiKP-PKIKP or PKiKP waveforms of the doublet recorded at other stations show excellent agreements in both absolute arrival time and differential travel time of the two phases (Fig. 2, A and B). The best-fitting relative location and origin time of event 03, obtained using the arrival times of the non-IC phases, also reduce the travel time residuals of the PKiKP and PKIKP phases within the relocation error bar for all other stations (Figs. 2 and 3). For the data available, the temporal changes in the PKiKP travel times are only observed for the phases recorded at ARU, AAK, and OBN, which sampled a localized region of the inner core boundary beneath middle Africa (Fig. 3).

The temporal changes of travel time for the PKiKP phases recorded at stations ARU, AAK, and OBN between the doublet are not likely to have been caused by temporal changes of seismic properties near the hypocenters or in the mantle (*22*).They indicate a localized change of the inner core radius beneath middle Africa between the occurrences of the doublet. A larger radius would produce an earlier PKiKP arrival, because the PKiKP phase would be reflected at a shallower depth. An inner core radius enlarged by 0.98 to 1.75 km would fit the travel time changes of about 0.039 to 0.07 s observed at stations OBN, ARU, and AAK between 1 December 1993 and 6 September 2003.

The localized change of the inner core radius can be explained by a differential inner core rotation, if the inner core boundary has localized topography (Fig. 4A) or locally deviates away from the equilibrium position with a slope of topography (Fig. 4B). In the former case, the PKiKP phases recorded at OBN, ARU, and AAK may sample the topographically low regions in event 93 and the topographically high regions in event 03 that are moved into the sampling points by the inner core differential motion (Fig. 4A). In the latter case, the PKiKP phases recorded at stations OBN, ARU, and AAK in event 03 may sample relatively elevated positions of the nonequilibrium sloped boundary that is moved eastward by the differential rotation of the inner core (Fig. 4B). For these mechanisms to work, it would also require the localized topography or the nonequilibrium slope to be geographically fixed to the inner core as the inner core differentially rotates.

The localized change of inner core radius can also be explained by a rapid localized growth of the inner core by 0.98 to 1.75 km between the occurrences of the doublet, either in the PKiKP sampling points (Fig. 4C) or in a regional scale beneath middle Africa (Fig. 4D). The position of the inner core boundary is controlled by the temperature and the outer core composition (iron and its companion light elements) (*10*). The localized growth may be caused by something unknown (for example, Earth's magnetic field) or by a regional perturbation of temperature and/or composition near the inner core boundary through mechanisms such as a heterogeneous heat-flow flux at the bottom of the outer core induced near the core-mantle boundary (*23*) or small-scale compositional convection in the top of the inner core (*24*).

Both interpretations indicate that the inner core boundary has irregular topography and that the growth of the inner core and the energy release associated with the growth are not geo-

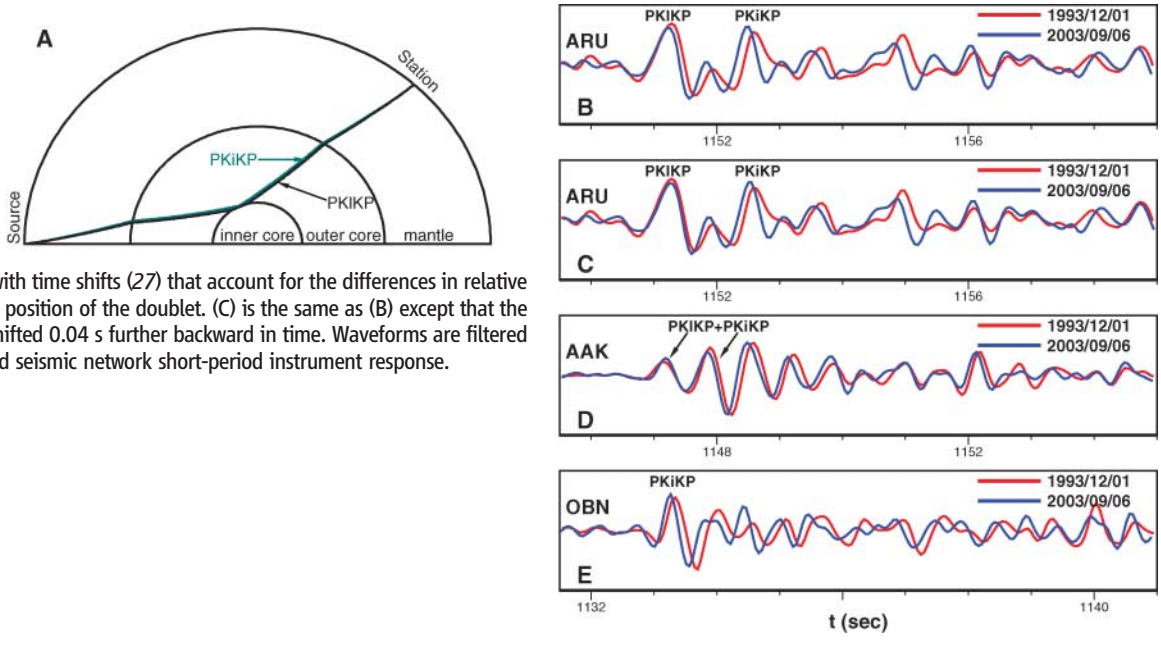

Fig. 1. (**A**) Ray paths of PKIKP (black) and PKiKP (light blue) waves. (**B** to **E**) Superimposed PKiKP-PKIKP waveforms of the doublet recorded at stations ARU (B and C) and AAK (D), and PKiKP waveforms at OBN (E). Waveforms in (B), (D), and (E) are superimposed with time shifts (*27*) that account for the differences in relative origin time and hypocenter position of the doublet. (C) is the same as (B) except that the waveform for event 03 is shifted 0.04 s further backward in time. Waveforms are filtered with the worldwide standard seismic network short-period instrument response.

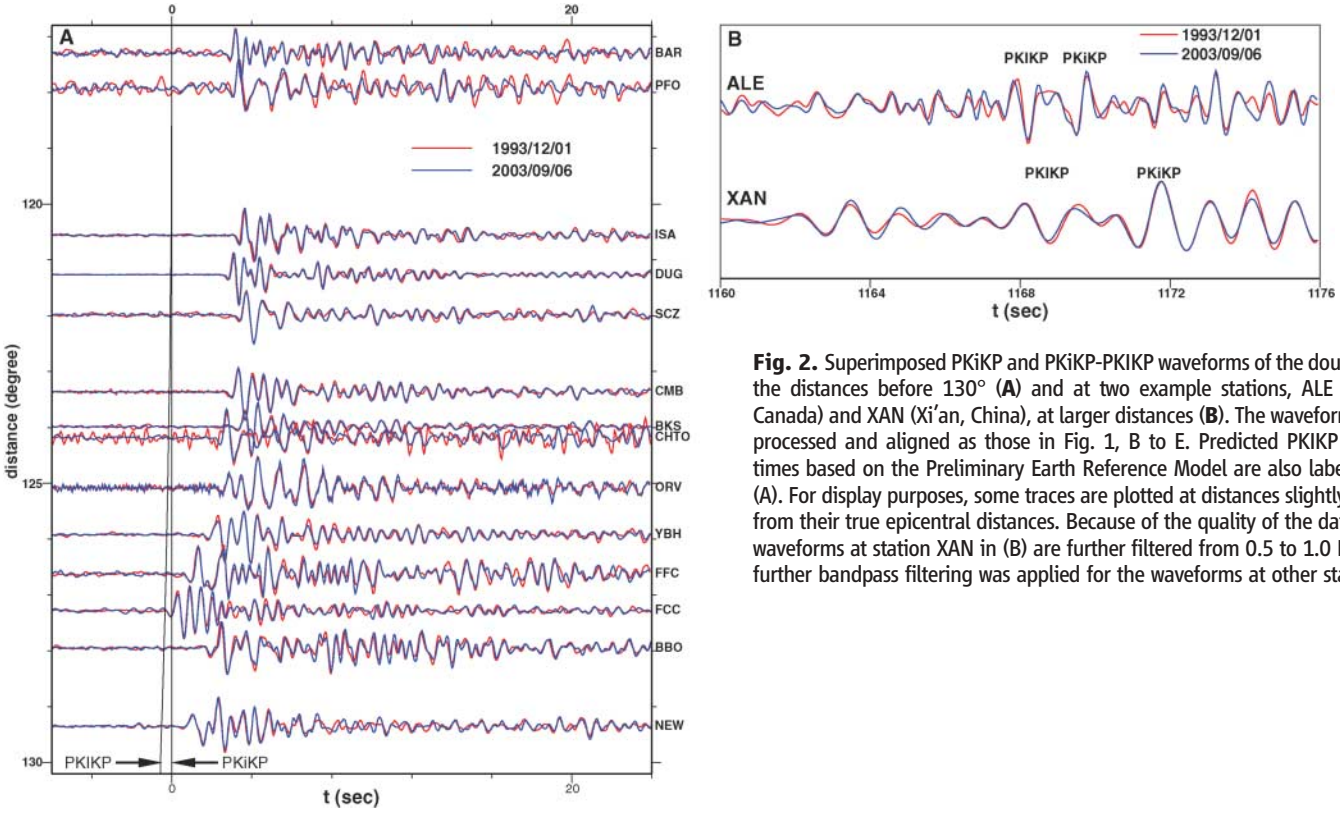

Fig. 2. Superimposed PKiKP and PKiKP-PKIKP waveforms of the doublet at the distances before 130° (**A**) and at two example stations, ALE (Alert, Canada) and XAN (Xi'an, China), at larger distances (**B**). The waveforms are processed and aligned as those in Fig. 1, B to E. Predicted PKIKP travel times based on the Preliminary Earth Reference Model are also labeled in (A). For display purposes, some traces are plotted at distances slightly away from their true epicentral distances. Because of the quality of the data, the waveforms at station XAN in (B) are further filtered from 0.5 to 1.0 Hz. No further bandpass filtering was applied for the waveforms at other stations.

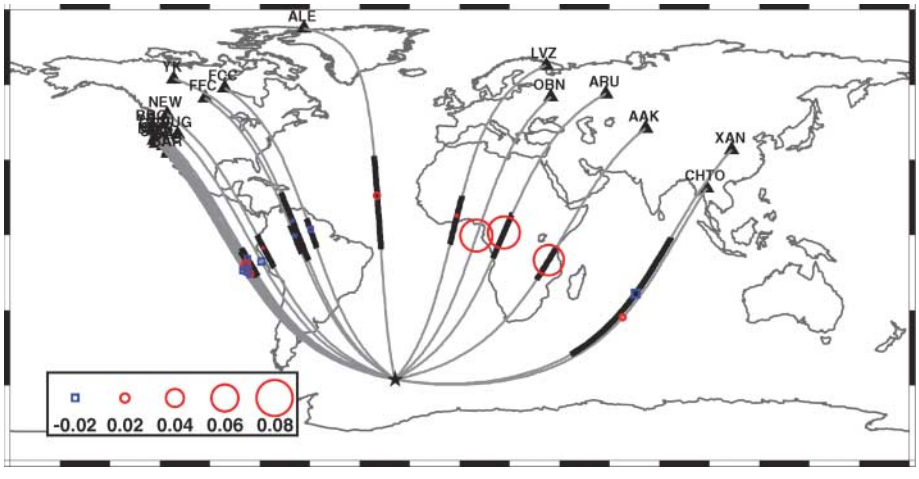

Fig. 3. Travel time residuals (*27*) of the PKiKP phases or differences in differential PKiKP-PKIKP travel time between the doublet, plotted at the reflected points of the inner core, along with the great circle paths from the doublet (star) to stations (triangles) and PKIKP ray paths in the inner core (heavy lines). Positive values indicate that the PKiKP arrives earlier or the differential PKiKP-PKIKP travel time is smaller for event 03, whereas negative values indicate the opposite. The differences in PKiKP-PKIKP differential travel time for those with heavy lines are also close to zero, except for stations ARU and AAK, in which only the differences in PKiKP-PKIKP differential travel time are shown. The great circle path to YK (Yellowknife, Canada) array comprises a total of 18 observational pairs.

graphically uniform. Furthermore, the existence of irregular topography of the inner core boundary would require the existence of small-scale variations of temperature or/and outer core composition near the inner core boundary. Because the time scale of the outer core convection is short, the required existence of small-scale variations of temperature and/or outer core composition would suggest that the rapid localized growth of the inner core is a plausible interpretation for the observed localized enlarged inner core radius. If the temporal change of the inner core boundary position is caused by rapid localized growth of the inner core, it would further suggest that the growth of the inner core and the energy release due to the solidification of the outer core are rapid and episodic. To maintain a geologically slow growth rate, the inner core growth process would also be required to be constructive for some localized regions in some time periods and destructive in other regions or in other time periods.

The above inference of the conditions near the inner core boundary would have considerable implications for the convection in the outer core and geodynamo. The inner core region with the enlarged radius corresponds to where the anomalously strong small-scale magnetic field changes in the top of the outer core are inferred at the present time (*25*) and where most of Earth's reversed magnetic polarity field has been produced in the past 400 years (*26*).

References and Notes

1. J. A. Jacobs, *Nature* **172**, 297 (1953).
2. S. I. Braginsky, *Dokl. Akad. Nauk SSSR* **149**, 1311 (1963).
3. D. Gubbins, *J. Geophys.* **43**, 453 (1977).
4. D. E. Loper, *Geophys. J. R. Astron. Soc.* **54**, 389 (1978).

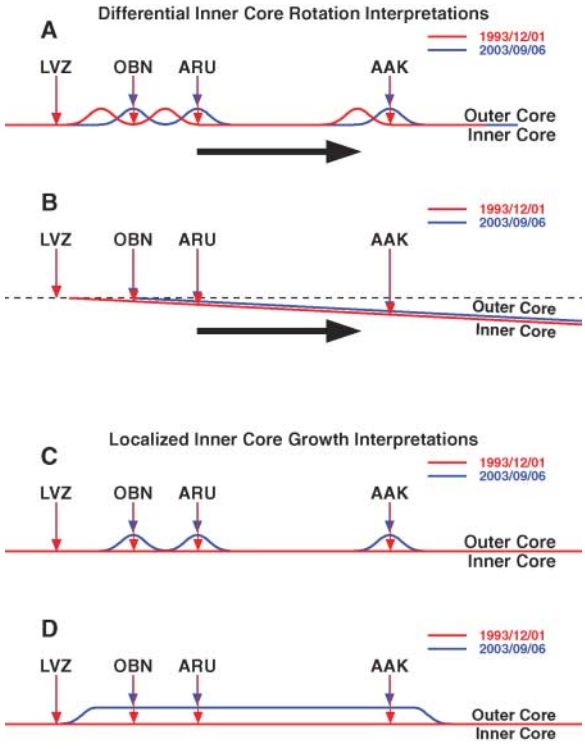

Fig. 4. Illustration of possible scenarios to change the inner core boundary at PKiKP reflected points between the occurring times of the doublet. (**A** and **B**) The inner core boundary has irregular topography and is changed by a differential inner core rotation. The dashed line in (B) is the equilibrium position of the inner core boundary. (**C** and **D**) The inner core boundary is changed by rapid localized inner core growth.

5. G. F. Davies, Paper 10/30, *XVII General Assembly. IUGG*. Canberra (1979).
6. D. E. Loper, P. H. Roberts, *Phys. Earth Planet. Int.* **24**, 302 (1981).
7. D. J. Stevenson, T. Spohn, G. Schubert, *Icarus* **54**, 466 (1983).
8. B. A. Buffett, in *Earth's Deep Interior: Mineral Physics and Tomography from the Atomic to the Global Scale*, S.-I. Karato *et al.*, Eds., Geophysical Monograph **117**, 37, American Geophysical Union, Washington, DC (2000).
9. S. Yoshida, I. Sumita, M. Kumazawa, *J. Geophys. Res.* **101**, 28085 (1996).
10. D. R. Fearn, D. E. Loper, P. H. Roberts, *Nature* **292**, 232 (1981).
11. D. J. Stevenson, *Geophys. J. R. Astron. Soc.* **89**, 311 (1987).
12. J. Zhang *et al.*, *Science* **309**, 1357 (2005).
13. G. Poupinet, A. Souriau, O. Coutant, *Phys. Earth Planet. Int.* **118**, 77 (2000).
14. G. Poupinet, W. L. Ellsworth, J. Frechet, *J. Geophys. Res.* **89**, 5719 (1984).
15. D. P. Schaff, P. G. Richards, *Science* **303**, 1176 (2004).
16. A. Y. Li, P. G. Richards, *Geochem. Geophys. Geosys.* **4**, 1072 10.1029/2004GL021240 (2003).
17. X. D. Song, *Phys. Earth Planet. Inter.* **124**, 269 (2001).
18. G. Poupinet, A. Souriau, *Phys. Earth Planet. Inter.* **124**, 275 (2001).
19. X. D. Song, P. G. Richards, *Nature* **382**, 221 (1996).
20. K. C. Creager, *Science* **278**, 1284 (1997).
21. J. E. Vidale, D. A. Dodge, P. S. Earle, *Nature* **405**, 445 (2000).
22. Materials and methods are available as supporting material on *Science* Online.
23. I. Sumita, P. Olson, *J. Geophys. Res.* **107**, 2169 10.1029/2001JB000548 (2002).
24. M. G. Worster, *J. Fluid Mech.* **237**, 649 (1992).
25. G. Hulot, C. Eymin, B. Langlais, M. Mandea, N. Olsen, *Nature* **416**, 620 (2002).
26. J. Bloxham, D. Gubbins, A. Jackson, *Philos. Trans. R. Soc. Lond. A* **329**, 415 (1989).
27. Time shifts in Fig. 1, B, D, and E, and Fig. 2, and travel time residuals in Fig. 3, are defined as $T^{pre}_{03-93,k,p}$ and $T^{res}_{03-93,k,p}$ in (*22*), respectively. They are estimated using the best-fitting relative origin time (6 September 2003, 15:47:00.205) and hypocenter position of event 03 (fig. S2A).

28. I thank two anonymous reviewers for constructive reviews and W.-C Yu for assistance in collecting the seismic data. This work is supported by the National Science Foundation.

Supporting Online Material
www.sciencemag.org/cgi/content/full/1131692/DC1
Materials and Methods
Figs. S1 to S3
Table S1
References

23 June 2006; accepted 23 August 2006
Published online 28 September 2006;
10.1126/science.1131692
Include this information when citing this paper.

Transcrystalline Melt Migration and Earth's Mantle

Pierre Schiano,[1]* Ariel Provost,[1] Roberto Clocchiatti,[2] François Faure[1]†

Plate tectonics and volcanism involve the formation, migration, and interaction of magma and gas. Experiments show that melt inclusions subjected to a thermal gradient migrate through olivine crystals, under the kinetic control of crystal-melt interface mechanisms. Exsolved gas bubbles remain fixed and eventually separate from the melt. Scaled to thermal gradients in Earth's mantle and geological times, our results account for the grain-scale segregation of primitive melts, reinterpret CO_2-rich fluid inclusions as escaped from melt, and question the existence of a free, deeply percolating fluid phase. Melt migration experiments also allow us to quantify crystal growth kinetics at very low undercoolings in conditions appropriate to many natural systems.

Deciphering the physical processes by which melts (silicate-rich liquids) and "fluids" (CO_2- or H_2O-rich gases or supercritical fluids) form, migrate, and interact is necessary to fully understand the dynamics of Earth's mantle and volcanism. It has long been believed, for instance, that the migration of magma has two modes: porous flow through small channels along grain boundaries followed by flow through a fracture network. Also, melt and fluid inclusions in mantle minerals are supposed to be the direct expressions of independent, deeply percolating fluid and melt phases (*1*). Here, we present experimental results that introduce transcrystalline melt migration as a mechanism occurring in Earth and suggest that most fluid inclusions in mantle minerals represent natural remnants of transcrystalline melt migration rather than samples of a free, fluid phase that pervades the mantle.

The samples used in this study are olivine crystals collected from lapilli levels at Piton Vincendo (Piton de la Fournaise Volcano, Reunion Island, Indian Ocean) and La Sommata

[1]Laboratoire Magmas et Volcans, Observatoire de Physique du Globe, Université Blaise Pascal et CNRS, 5 rue Kessler, 63038 Clermont-Ferrand Cedex, France. [2]Laboratoire Pierre Süe, Centre d'Etudes Nucléaires de Saclay, Commissariat à l'Energie Atomique et CNRS, 91191 Gif-sur-Yvette Cedex, France.

*To whom correspondence should be addressed. E-mail: schiano@opgc.univ-bpclermont.fr

†Present address: Centre de Recherches Pétrographiques et Géochimiques, Université Henri Poincaré et CNRS, 15 rue Notre-Dame des Pauvres, 54501 Vandoeuvre-lès-Nancy, France.

(Piano Caldera, Vulcano Island, Aeolian Arc) scoria cones (*2*–*4*). The selected crystals contain subspherical vitreous inclusions (30 to 300 μm in diameter) consisting only of glass and a bubble containing CO_2, as verified by laser-Raman analyses. The distribution of inclusions is not controlled by healed fractures (as might be expected for inclusions of secondary origin), and gas bubbles readily dissolve into the melt at magmatic temperatures (which would not happen systematically if inclusions were originally multiphase). These inclusions represent droplets of the parental liquid, captured during the growth of their host crystal. Vitreous inclusions in Fo_{83-84} olivine from Piton Vincendo have homogeneous, H_2O-poor (0.74 ± 0.07 weight %, where the error = 2 SD) alkali basalt compositions with 8.68 ± 0.60 wt % MgO and 0.68 ± 0.11 wt % K_2O, whereas inclusions in Fo_{90-91} olivine from La Sommata have homogeneous, H_2O-rich (3.70 ± 0.10 wt %) basalt compositions of the shoshonitic series (10.16 ± 0.95 wt % MgO and 1.83 ± 0.26 wt % K_2O) (table S1).

The experiments were performed in a microscope 1-atm heating stage (*5*, *6*) and a purified He atmosphere. The oxygen fugacity was monitored in the outgoing gas flux with a zirconia probe, calibrated with an Ar + 1% H_2 gas, and calculated to be kept at 10^{-10} to 10^{-9} atm at 1100°C. The mean temperature was monitored with a Pt-$Pt_{90}Rh_{10}$ thermocouple directly welded to the sample holder. The temperature gradient inside the working zone (0.03 to 0.06 K/μm) was mapped by melting small pieces of gold disseminated on the olivine plate; it was further checked on each run by melting two pieces of gold placed on the extremities of the studied melt inclusion. In some experimental runs, the crystals were first heated up (52 K/min) to the temperature at which the inclusions homogenize to a single, uniform melt phase (1170° to 1230°C for La Sommata inclusions, 1200° to 1280°C for Piton Vincendo), then cooled down (30 K/min) to the temperature of bubble nucleation (about 20 to 50 K below the homogenization temperature) and maintained at these conditions for 1 to 20 hours. In other runs, the crystals were carried straight to the final temperature. We observed the same behavior regardless of procedure.

At the onset of an experiment, the fluid bubble moves toward the cold side of the working zone (this reduces free energy because gases have greater expansion coefficients than melts), reaching and wetting the inclusion cavity wall almost instantaneously (Fig. 1A). While the melt slowly and continuously shifts toward the hot side, the bubble front end is dragged by the melt, but the rear end remains motionless (Fig. 1, B to F). The bubble stretches and distorts to a dumbbell shape and a fixed, crystal-hosted bulge develops at the expense of the moving, melt-hosted bulge (Fig. 1G). The fluid is thus progressively extracted from the melt and engulfed by the host crystal. The fluid wake ultimately pinches off [possibly through dislocation creep (*7*) given that no crystal rupture is detected], leaving one or more isolated, subspherical fluid inclusions (Fig. 2, A and B). In brief, the melt migrates toward the hot spot of the working zone, leaving the fluid bubble behind, which ultimately forms a separate, motionless fluid inclusion. Segregation of fluid inclusions generally occurs after a displacement of about twice the size of the parent inclusion.

While moving, the melt inclusion gradually changes from subspherical to a faceted, negative-crystal shape (it also lengthens and narrows slightly). Indeed, this shape reveals that migration is not strictly parallel to the thermal gradient but proceeds along a small-index crystallographic direction ([001] in the case of Fig. 1). Melt migration was monitored from the bubble rear end and other fixed reference marks such as small crystal defects. Migration rate, obtained by measuring the bubble track on successive photographs, stays constant during an experiment (Fig. 3A). In La Sommata samples, migration rates varied from 1 to 3.2 nm/s for 0.03 to 0.06 K/μm thermal gradients and 1134° to 1175°C mean temperatures (Table 1). Lower migration rates were obtained for Piton Vincendo: 0.3 to 1.3 nm/s for 0.03 to 0.04 K/μm and 1190° to 1196°C.

At the end of the experiments, the samples were quenched, mounted in epoxy, and polished for microprobe analysis. Representative composition profiles are shown in fig. S1. Host olivine displays no zoning, and its composition is the same at the front, back, and sides. Although the glass of Piton Vincendo inclusions is not zoned either, La Sommata inclusions display a uniform, ~10-μm wide, outer region in which CaO content increases and MgO decreases toward the crystal wall. Otherwise, the glasses are homogeneous and compositionally similar to unheated vitreous

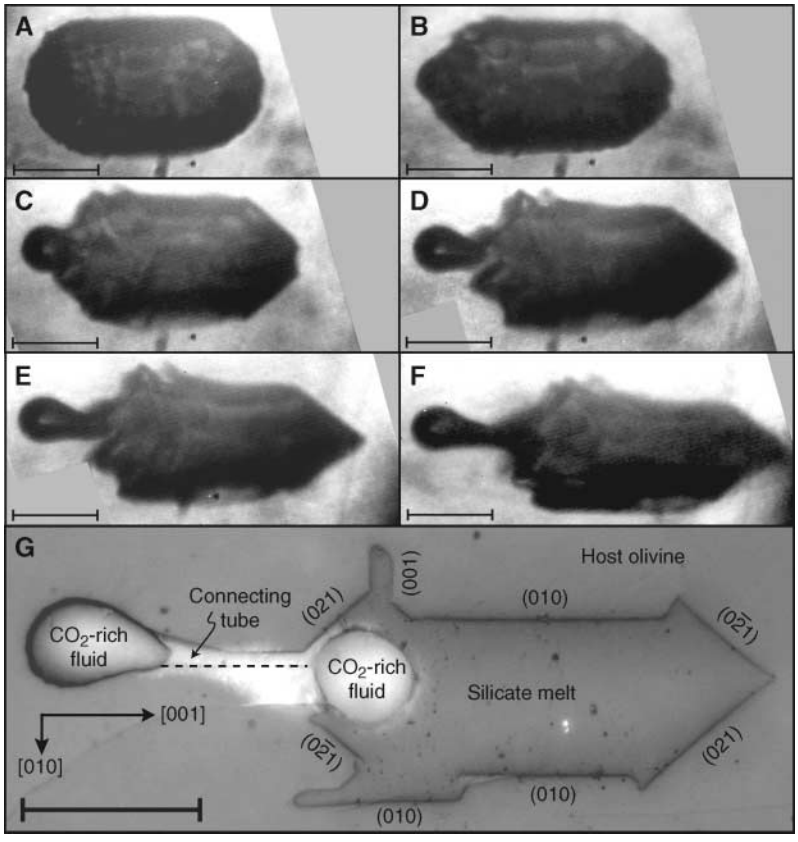

Fig. 1. Morphological evolution of melt-and-bubble inclusions. (**A** to **F**) Transmitted-light images of an olivine-hosted, CO_2-oversaturated melt inclusion during run Som1 (Table 1). Melt inclusion migrates toward the working-zone hot spot (to the right of each image, beyond the edge) and takes a faceted shape. A CO_2 bubble is initially hosted by the melt but wets the crystal at the inclusion cold end. It later stretches and constricts, developing a motionless, crystal-hosted bulge. (**G**) Reflected-light microphotograph of the inclusion after quenching and polishing for exposure. A thin, fluid-filled tube still connected the growing, crystal-hosted and residual, melt-hosted bulges at the end of experiment, but polishing has scraped the tube walls (one edge of the tube section, discernible on photograph enlargements, is indicated by dashes). Also shown are the crystallographic axes and Miller indices of host olivine. Scale bars, 50 μm.

inclusions from the same samples. The zoning pattern of La Sommata quenched glasses is typical of diffusion-limited crystal growth, accounting for the inward crystallization of a ~1-μm olivine layer. It is not a result of melt migration but represents a quench artifact [La Sommata melts are more difficult to quench than Piton Vincendo melts because of their lower viscosities (*8*, *9*)].

We interpreted the thermal migration of melt inclusions as due to olivine dissolution ahead and crystallization astern, because creep would not maintain a faceted shape. Inclusions are delimited by the commonly observed {021} and (010) faces of olivine (Fig. 1G), but also by the less common (001) faces at the back. Faces (001) are typical of olivine crystals showing a polyhedral habit (*10*), a morphology thought to develop during slow crystal growth governed by molecular attachment, when the uptake and rejection of chemical components at the interface of solids and liquids are slower than their diffusion in the melt (*11*). Indeed, diffusion-controlled migration would occur parallel to the thermal gradient whatever the orientation of the host crystal, whereas melt inclusions actually migrate along a low-index crystallographic direction (Fig. 1). Diffusion-limited dissolution (*12*) and crystallization would also require MgO melt content to decrease, and CaO content to increase, from front to back; microprobe analyses failed to detect concentration gradients associated with the migration, which is another indication that interface detachment and attachment are the rate-controlling processes. Given that no discernible chemical modification of the trapped melt or host olivine was observed either, inclusion volume is left constant during migration, showing that dissolution and crystallization rates are equal.

Quantitative interpretation of the observed migration rates requires a thermodynamic analysis of the process of dissolution and crystallization. For the sake of simplicity, we modeled a melt inclusion geometrically as a prism of length L (30 to 130 μm) and chemically as a binary mixture of dissolved host olivine and MgO-free solvent [olivine mole fraction $\overline{C}$ = 0.203 for La Sommata samples and 0.190 for Piton Vincendo (table S2)]. Inclusion migrates by crystallizing olivine at the cooler rear end (with a temperature T_1 and a molar fraction C_1) while host olivine melts at the hotter front end (T_2 and C_2). Latent heat is transported from rear to front by conduction, and dissolved olivine travels in the other direction by diffusion. The binary diffusion coefficient D, taken as the self-diffusion coefficient of the slowest cation (Si), is greater than 10^{-12} m^2/s at the temperatures and compositions we studied (*13*, *14*), whereas thermal diffusivity (*15*) κ is on the order of 10^{-6} m^2/s. The time scale for attainment of steady state is L^2/D = a few minutes for diffusion, and much less for conduction (i.e., boundary layers merge within minutes and the whole inclusion behaves as a diffusion layer). Migration velocity V is on the order of 10^{-9} m/s, $VL/\kappa << VL/D < 0.1$; thus, both T and C steady-state profiles are linear: $T = T_1 + \theta x$ and $C = C_1 + \gamma x$, where x is the distance from rear and $\theta = (T_2 - T_1)/L$, $\gamma = (C_2 - C_1)/L$. Notably, latent heat negligibly affects the imposed thermal gradient θ_0: $\theta \approx \theta_0 \cos\alpha$, where α is the angle of thermal gradient and migration path ($\cos\alpha \approx 1$ in our experiments).

Migration is governed by the interplay of boundary condition $V = D\gamma/(1 - \overline{C})$ and interface kinetics $V = f(\Delta\mu)$, where Δμ is the driving force for fusion and crystallization. Function f depends on the dominant interface mechanism (*11*), which could be continuous detachment and attachment, the propagation of screw dislocations, or surface nucleation [$f(u) = k_c u$, $k_s u^2$, or $k_n \exp(-a/u)$, where k_c, k_s, k_n, and a are constants]. $\Delta\mu = \mu_{liq}(T_1,P,C_1) - \mu^0_{sol}(T_1,[\sigma]) = \mu^0_{sol}(T_2,[\sigma]) - \mu_{liq}(T_2,P,C_2)$, where μ^0_{sol} is the molar free enthalpy of host olivine; [σ] stands for the three invariants of the stress tensor, the same at both ends; and μ_{liq} is the chemical potential of the olivine component in the melt (at pressure P). Classical thermodynamic relations give $\Delta\mu = \Delta\mu_T - \Delta\mu_C$, where $\Delta\mu_T = \frac{1}{2}(S^0_{liq} - S^0_{sol})\theta L$ and $\Delta\mu_C = \frac{1}{2}R\,\overline{T}\gamma L/\overline{C}$, assuming a constant activity coefficient of the olivine component [where S^0_{sol} is molar entropy of host olivine, S^0_{liq} is partial molar entropy of the olivine component, R is the gas constant, and $\overline{T} = \frac{1}{2}(T_1 + T_2)$]. Equating the two expressions for V fixes γ and, thus, fixes V. Two endmember cases appear: diffusion control $\Delta\mu << \Delta\mu_T \rightarrow V \approx V_D = D\,\overline{C}(S^0_{liq} - S^0_{sol})\theta/(1 - \overline{C})R\overline{T}$, and interface kinetics control $\Delta\mu_C << \Delta\mu_T \rightarrow V \approx V_K = f(\Delta\mu_T)$. In practice, $V \approx V_D$ if $V_D << V_K$ and $V \approx V_K$ if $V_K << V_D$. Control by chemical diffusion makes V proportional to thermal gradient θ and independent of inclusion length L. Control by interface kinetics

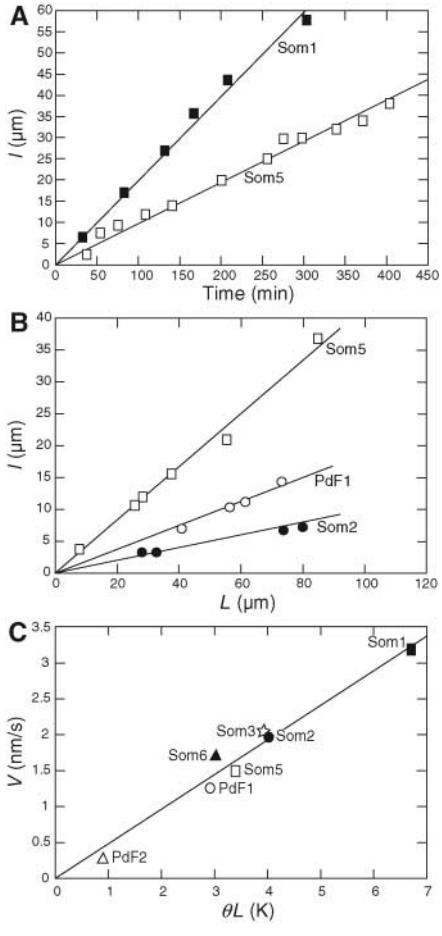

Fig. 3. Kinetics of transcrystalline melt migration (experimental runs Som1 to Som6, PdF1, and PdF2, see Table 1). (**A**) Bubble track length l (a measure of melt migration distance) versus time, showing that migration rate is constant for a given inclusion in given experimental conditions. (**B**) Final bubble track length l versus inclusion length L for crystals with several melt inclusions, showing that the different inclusions of a given crystal migrate at rates proportional to their lengths. (**C**) Migration rate V versus the product of thermal gradient θ and inclusion length L, showing that the same, linear kinetic law applies to different experimental conditions and different crystals from two different geological settings. Best-fit slope is 0.48 ± 0.07 nm s^{-1} K^{-1} (where error = 2 SD). V does not depend only (or even mainly) on θ, as diffusion control would demand (fig. S2).

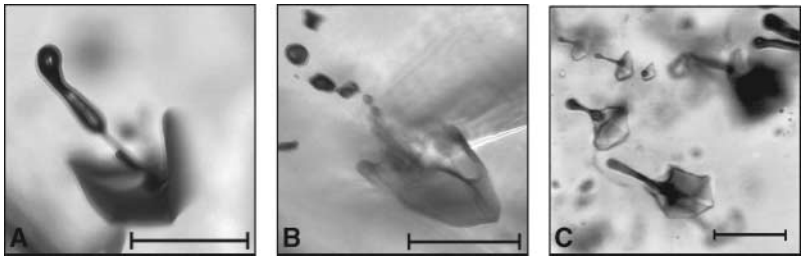

Fig. 2. (**A** and **B**) Transmitted-light microphotographs showing how a CO_2 bubble (upper left), left over by a migrating melt inclusion, pinches off (A) and converts into a trail of isolated fluid inclusions (B). (**C**) Transmitted-light microphotograph of an olivine crystal with several melt-and-bubble inclusions (run PdF1; see Table 1). Scale bars, 50 μm.

gives $V = f(\Delta\mu_T)$, where $\Delta\mu_T$ is proportional to θ and L. Depending on the dissolution and crystallization mechanism (continuous detachment and attachment, screw dislocation growth, or surface nucleation), V is proportional to $\Delta\mu_T$, $(\Delta\mu_T)^2$, or $\exp(-a/\Delta\mu_T)$, and hence to θL, $\theta^2 L^2$, or $\exp(-b/\theta L)$ [where $b = 2a/(S^0_{liq} - S^0_{sol})$].

Some olivine crystals host several melt inclusions of different sizes (Fig. 2C). Subjected to the same thermal gradient, these inclusions migrate along parallel paths but at different speeds, serving as further evidence that chemical diffusion is not the rate-controlling process. Moreover, migration rate is proportional to inclusion length (Fig. 3B), which points to continuous detachment and attachment as the controlling mechanism at the interface. Finally, migration rates obtained for different crystals with different experimental conditions are plotted as a function of θL in Fig. 3C: They define a single straight line running through the origin, which supports the kinetic law $V = k\theta L$ (i.e., continuous detachment and attachment). It also shows that the kinetic constant k is not very sensitive to temperature or melt composition: $k \approx 0.5$ nm s^{-1} K^{-1}. Notably, control by interface kinetics, not diffusion, has also been obtained for the thermal migration of brine droplets in synthetic halides (*16*) and natural ice (*17*, *18*).

That dissolution and crystallization are governed by continuous detachment and attachment may seem perplexing, given that continuous growth is usually associated with large local undercoolings (i.e., the difference between liquidus and actual temperatures at the interface) and nonfaceted shapes (*11*) and that it is explained by uniform face attachment (UFA) on rough interfaces. Actually, as discussed thoroughly by Tiller (*19*), two other continuous regimes exist at low undercoolings: uniform ledge attachment (ULA), when growth units can only attach onto the crystal at layer edges, and kink-only attachment (KOA), when they can join the crystal only at kink sites. Both apply to faceted shapes and are reversible (with the same constant k applying to both dissolution and crystallization), and KOA at least applies down to zero driving force.

It is a classical result of crystal growth theory (*19*) that growth (or dissolution) rate control shifts from thermal and/or chemical diffusion at large bulk disequilibrium to interface kinetics at lower disequilibrium (of two processes acting in series, the slower process is in control). With decreasing disequilibrium at the interface, the governing interface-kinetics mechanism shifts from two-dimensional–island nucleation to screw dislocation growth to ULA to KOA (of several processes competing in parallel, the fastest is in control). Here, the bulk undercooling at rear (and overheating at front) reads $\Delta T = \theta L/2$. Our results show no dependence on L (for a given ΔT) and a linear dependence of growth (and dissolution) rates on ΔT for ΔT ranging from 1.6 down to 0.5 K (Fig. 3C). This observation and the evidence that KOA is normally valid down to zero undercooling allow us to extrapolate our results to the lower bulk undercoolings and therefore lower thermal gradients that apply in natural conditions, even if our experiments lie in the ULA regime ($k_{KOA} < k_{ULA}$, but they have the same order of magnitude).

This process of melt migration and associated fluid separation may have important implications. First, melt migration experiments permit the acquisition of basic quantitative data for crystal growth kinetics at bulk undercoolings <1 K. Such conditions are more appropriate to many natural systems [e.g., magma chambers (*20*)] than classical crystal growth experiments, which are generally done at large bulk undercoolings (tens of K) (*21*). Our experiments provide an unambiguous determination of a crystal-growth kinetic constant for a magmatic system, with no interference from nucleation delay, chemical diffusion, melt convection, or statistical hypotheses.

Second, the separation of fluid inclusions from parent melt inclusions is relevant to Earth's mantle on geological time scales. Temperature and pressure are known to stimulate most reaction kinetics, but no systematic study is available for liquid-solid systems, so we use our experimental kinetic constant k as a conservative estimate. Horizontal (*22*) and vertical (*23*, *24*) gradients on the order of 0.5 and 5 K/km, respectively, are known to prevail in the shallow continental mantle. Taking 5 K/km, complete melt-fluid separation is achieved in 25,000 years. Silicate melt and CO_2-rich fluid inclusions in olivines and pyroxenes of ultramafic xenoliths have already been recognized as cogenetic (*25*) (because of their systematic spatial association, the occurrence of multiphase inclusions, and that of melt inclusions and fluid inclusions joined by necks), but a physical explanation was lacking. The morphological resemblance of deformed, necking-down melt-and-fluid inclusions and rows of residual fluid inclusions in our experiments to dumbbell-shaped melt-and-fluid inclusions and fluid inclusion arrays commonly observed in mantle xenoliths (*1*) further suggests that the latter represent remnants of transcrystalline melt migration. If this interpretation is correct, little basis remains for the current hypothesis that fluid inclusions in mantle xenoliths are trapped samples of a free, deeply percolating fluid phase (*1*).

Third, transcrystalline melt migration provides a previously unrecognized mechanism for the grain-scale segregation of magma. Current models of thermal structure and flow field beneath mid-ocean ridges (*26*, *27*) and hot spots (*28*) predict gradients up to hundreds or thousands of K/km, locally. For a typical SiO_2-rich mantle melt inclusion 20 μm long (*25*), $\theta = 100$ K/km translates into $V = 10^{-15}$ m/s; i.e., it migrates by 30 μm in 1000 years. This is faster than buoyancy-driven interconnected porous flow (*29*) for such viscous melts ($\eta \approx 3000$ Pa s) (*30*) at all melt fractions less than 0.1%. This may answer the questions as to why very primitive [less than 1% partial melting (*31*, *32*)] SiO_2-rich melts are only encountered as melt inclusions in mantle olivines (never as magma bodies), whereas less primitive (1 to 10% partial melting) basaltic melts are only encountered as magma bodies (never as melt inclusions in mantle olivines). Only the most primitive droplets formed at fertile grain corners (or edges) have time (if melting does not proceed rapidly to higher degrees) to enter the crystals by thermally driven migration, instead of escaping by buoyancy-driven flow along grain edges. Less primitive melts form interconnected wetted-edge networks and escape rapidly to higher levels where grain-scale channels are relayed by fracture networks [or chemically formed channels (*33*)] and collection into magma bodies.

Table 1. Summary of melt migration experiments. $\overline{T}$ is mean temperature (maximum error $\delta = 5$°C), θ is thermal gradient ($\delta = 5$ mK/μm), t_f is run duration ($\delta = 30$ s), L is inclusion length (measured at the end of experiment, $\delta = 0.5$ μm), l is final bubble track length ($\delta = 0.5$ μm), V is migration rate (l/t_f, $\delta = 0.5$ nm/s). For crystals with several melt inclusions (runs Som2, Som5, and PdF1), the reported L, l, and V stand for the longest. n.d., not determined.

Run no.	$\overline{T}$ (°C)	θ(K/μm)	t_f (min)	L (μm)	l (μm)	V (nm/s)
			La Sommata (Vulcano Island)			
Som1	1155	0.05	304	134	58	3.2
Som2	1175	0.05	60	80	7	1.9
Som3	1140	0.06	300	65	37	2.1
Som4	1126	0.05	964	n.d.	55	1.0
Som5	1134	0.04	403	85	37	1.5
Som6	1170	0.03	362	100	36	1.7
			Piton Vincendo (Reunion Island)			
PdF1	1190	0.04	180	73	14	1.3
PdF2	1196	0.03	1200	30	19	0.3

References and Notes

1. E. Roedder, Ed., *Fluid Inclusions*, vol. 12 of *Reviews in Mineralogy* (Mineralogical Society of America, Washington, DC, 1984).
2. H. Bureau, F. Pineau, N. Metrich, M. Semet, M. Javoy, *Chem. Geol.* **147**, 115 (1998).
3. A. Gioncada *et al.*, *Bull. Volcanol.* **60**, 286 (1998).
4. D. Massare, N. Métrich, R. Clocchiatti, *Chem. Geol.* **183**, 87 (2002).
5. A. V. Sobolev, L. V. Dmitriev, V. L. Barsukov, V. N. Nevsorov, A. B. Slutsky, in *Igneous Processes and Remote Sensing,* vol. 11 of *Proceedings of the Lunar and Planetary Science Conference*, P. R. Criswell, R. B. Merrill, Eds. (Pergamon, New York, 1980), pp. 105–116.
6. P. Schiano, *Earth Sci. Rev.* **63**, 121 (2003).
7. B. J. Wanamaker, B. Evans, *Contrib. Mineral. Petrol.* **102**, 102 (1989).
8. D. B. Dingwell, K. U. Hess, C. Romano, *Earth Planet. Sci. Lett.* **158**, 31 (1998).
9. Y. Zhang, Z. Xu, Y. Liu, *Am. Mineral.* **88**, 1741 (2003).
10. W. A. Deer, R. A. Howie, J. Zussman, *Orthosilicates* (Longman, London, 1962).
11. A. Baronnet, *Fortschr. Miner.* **62**, 187 (1984).
12. L. C. Kuo, R. J. Kirkpatrick, *Am. J. Sci.* **285**, 51 (1985).
13. C. H. Donaldson, *Lithos* **8**, 163 (1975).
14. J. E. Mungall, C. Romano, D. B. Dingwell, *Am. Mineral.* **83**, 685 (1998).
15. D. Snyder, E. Gier, I. Carmichael, *J. Geophys. Res.* **99**, 15503 (1994).
16. D. R. Olander, A. J. Machiels, M. Balooch, S. K. Yagnik, *J. Appl. Phys.* **53**, 669 (1982).
17. H. E. Cline, T. R. Anthony, *J. Appl. Phys.* **43**, 10 (1972).
18. D. R. H. Jones, *J. Cryst. Growth* **20**, 145 (1973).
19. W. A. Tiller, *The Science of Crystallization: Microscopic Interfacial Phenomena* (Cambridge Univ. Press, Cambridge, UK, 1991).
20. G. Brandeis, C. Jaupart, C. J. Allègre, *J. Geophys. Res.* **89**, 10161 (1984).
21. R. J. Kirkpatrick, in *Reviews in Mineralogy vol 8*, A. C. Lasaga, R. J. Kirkpatrick, Eds. (Mineralogical Society of America, Washington, DC, 1981), pp. 321–398.
22. J. C. Mareschal, C. Jaupart, *Earth Planet. Sci. Lett.* **223**, 65 (2004).
23. S. V. Sobolev *et al.*, *Tectonophysics* **275**, 143 (1997).
24. N. M. Shapiro, M. H. Ritzwoller, J. C. Mareschal, C. Jaupart, in *Geological Prior Information: Informing Science and Engineering*, A. Curtis, R. Wood, Eds. (Geological Society of London Special Publication, London, 2004), vol. 239, pp. 175–194.
25. P. Schiano, R. Clocchiatti, *Nature* **368**, 621 (1994).
26. M. J. Cordery, J. P. Morgan, *J. Geophys. Res.* **98**, 19477 (1993).
27. Y. J. Chen, J. Lin, *Earth Planet. Sci. Lett.* **221**, 263 (2004).
28. C. G. Farnetani, B. Legras, P. J. Tackley, *Earth Planet. Sci. Lett.* **196**, 1 (2002).
29. T. J. Henstock, *Geophys. Res. Lett.* **29**, 1137 (2002).
30. J. Maumus, D. Laporte, P. Schiano, *Contrib. Mineral. Petrol.* **148**, 1 (2004).
31. P. Schiano *et al.*, *Earth Planet. Sci. Lett.* **160**, 537 (1998).
32. M. M. Hirschmann, M. B. Baker, E. M. Stolper, *Geochim. Cosmochim. Acta* **62**, 883 (1998).
33. E. Aharonov, J. A. Whitehead, P. B. Kelemen, M. Spiegelman, *J. Geophys. Res.* **100**, 20433 (1995).

34. We thank B. Thellier and D. Massare for technical assistance. Financial support was provided by the European Community's Human Potential Programme under contract HPRN-CT-2002-00211 (Euromelt).

Supporting Online Material

www.sciencemag.org/cgi/content/full/314/5801/970/DC1
Figs. S1 and S2
Tables S1 and S2
Reference

13 July 2006; accepted 10 October 2006
10.1126/science.1132485

Selective Etching of Metallic Carbon Nanotubes by Gas-Phase Reaction

Guangyu Zhang,* Pengfei Qi,* Xinran Wang, Yuerui Lu, Xiaolin Li, Ryan Tu, Sarunya Bangsaruntip, David Mann, Li Zhang, Hongjie Dai†

Metallic and semiconducting carbon nanotubes generally coexist in as-grown materials. We present a gas-phase plasma hydrocarbonation reaction to selectively etch and gasify metallic nanotubes, retaining the semiconducting nanotubes in near-pristine form. With this process, 100% of purely semiconducting nanotubes were obtained and connected in parallel for high-current transistors. The diameter- and metallicity-dependent "dry" chemical etching approach is scalable and compatible with existing semiconductor processing for future integrated circuits.

Carbon nanotubes have shown promise for future electronics (*1*–*6*). However, a major roadblock to the scaling up of single-walled carbon nanotube (SWNT) field-effect transistors (FETs) has been the difficulty in obtaining purely semiconducting SWNTs (S-SWNTs) without electrical short by metallic SWNTs (M-SWNTs). Parallel S-SWNTs are necessary to enable high-current and high-speed nanotube FETs to surpass modern silicon devices. Various approaches have been developed for selective synthesis of S-SWNTs (*7*, *8*), electrical breakdown of M-SWNTs (*9*, *10*), solution-phase chemical separation (*11*, *12*) and selective chemical modification (*13*–*15*). For large-scale circuits, much remains to be done to achieve full semiconductor yield, high scalability of metallic SWNT removal, optimum nanotube diameter and length, and highly preserved electrical properties of SWNTs.

Here, we demonstrate a methane plasma followed by an annealing process to selectively hydrocarbonate M-SWNTs and retain S-SWNTs grown on substrates. The retained S-SWNTs are free of covalent alterations, are stable at high temperatures, and exhibit electrical properties similar to pristine materials. The distribution of diameters of the S-SWNTs is narrowed down to a window (~1.3 to 1.6 nm) that provides sufficient band gaps for high on/off ratios and allows for good electrical contacts (*16*), both of which are important in high-performance electronics. The dual effects of selective metal removal and diameter distribution narrowing combined with compatibility with microfabrication technology make the method promising for large-scale SWNT electronics.

We first fabricated an array (Fig. 1A) of 98 "few-tube" electrical devices on SiO_2(67 nm)/Si (as back-gate) (Fig. 1A, bottom) substrates, with each device comprising 0 to 3 as-grown SWNTs [by patterned chemical vapor deposition (CVD) growth (*17*) at 800°C] bridging source-drain (S-D) Ti/Au electrodes (S-D distance ~ 400 nm) (Fig. 1A). The particular CVD recipe produced SWNTs in a broad diameter (d) range of d = 1 to 2.8 nm, measured by atomic force microscopy (AFM). About 55% of the as-fabricated devices (out of 244 measured on six chips) were found to be "depletable" (D) by sweeping gate-voltage with on/off conductance ratios $\geq 10^3$. These were devices fortuitously composed of one or multiple (two or three) as-grown S-SWNTs. The other 45% of the devices contained at least one M-SWNT (with or without S-SWNT) and were "nondepletable" (ND) with on/off ratios ≤ 10.

We treated hundreds of as-made few-tube device arrays by exposure to a methane plasma at 400°C, followed by 600°C annealing in vacuum in a 4-inch quartz-tube furnace equipped with a remote plasma system (*18*). The use of methane plasma instead of hydrogen plasma was found key to selective M-SWNT etching because of milder reactivity and higher controllability. After the treatment, the percentage of depletable devices increased from ~55% (out of 244) to ~93% (out of 78 that survived), with only a few nondepletable devices remaining (Fig. 2A), indicating that selective removal of metallic SWNTs over semiconducting ones was occurring.

We observed five different behaviors with the 244 few-tube devices after the treatments, including ND→D (i.e., non-

Department of Chemistry and Laboratory for Advanced Materials, Stanford University, Stanford, CA 94305, USA.

*These authors contributed equally to this work.
†To whom correspondence should be addressed. E-mail: hdai@stanford.edu

depletable became depletable, ~10%) (Fig. 1B); D→D (20% remained depletable) (Fig. 1C); ND→ND (2%) (Fig. 1D); ND→LOST (34% became electrically insulating (Fig. 1E); and D→LOST (34%) (Fig. 1F). In all ND→D devices, AFM revealed at least one (metallic) tube etched into pieces or nearly removed from the substrate and the existence of fully intact S-SWNTs (Fig. 1B, inset). Intact tubes were observed in ND→D and D→D devices (Fig. 1, B and C, insets), respectively, and etched tubes were observed in the LOST devices (Fig. 1, E and F, insets).

The semiconducting SWNTs in D→LOST devices (with only S-SWNTs) were "miskilled" by the plasma treatment. Notably, we found that these devices when as-made all exhibited low on-state conductance ($G < \sim 5$ μS) (Fig. 2B) and were composed of predominantly small-diameter S-SWNTs with $d \leq$ 1.4 nm (Fig. 2E), as revealed by AFM. The low on-conductance was consistent with small-diameter, large band gap ($E_g \sim 1/d$), high Schottky barriers at the metal-tube contacts, and thus with high resistances (*16*). The surviving semiconductor D→D devices mostly exhibited higher conductance (Fig. 2C) and contained larger-diameter ($d \geq 1.4$ nm) tubes observed by AFM (Fig. 2G). These results showed that small-diameter S-SWNTs were selectively etched over large S-SWNTs. On the other hand, analysis of the ND→LOST devices (with M-SWNTs) found a wider span of conductance (Fig. 2D), with tube diameters mainly in the range of 1 to 2 nm (Fig. 2F). This suggested that metallic SWNTs with small and medium diameters ($d < 2$ nm) were all etched in the ND→LOST devices. For the few ND→ND devices remaining, we imaged all tubes in these devices and always observed the existence of large tubes ($d > \sim 2$ nm) (Fig. 2H and Fig. 1D, inset), suggesting that large metallic tubes could survive the plasma. Taken together, our data revealed that in the small-diameter regime ($d \leq 1.4$ nm), M- and S-SWNTs were etched nondiscriminately (Fig. 3A). In the medium-diameter regime ($d \sim 1.4$ to 2 nm), M-SWNTs were selectively etched/removed over semiconducting ones. In the large-diameter regime ($d > 2$ nm), both M- and S-SWNTs were not etched by the plasma (Fig. 3A).

Etching of SWNTs in the methane plasma is attributed to hydrocarbonation, with SWNTs irreversibly etched (*19*) into hydrocarbon gas species as a result of reactions with neutral and positive ions of H and CH_3 species in a methane plasma (*20*). The results above show that diameter is an important factor for the chemical reactivity of a SWNT toward hydrocarbonation. Smaller-diameter SWNTs are preferentially etched over larger ones because of the higher radius of curvature and higher strain in the C-C bonding configuration, as in other chemical reactions [e.g., oxidation (*21*)] of SWNTs. In the small- and large-diameter regimes, respectively, SWNTs are either etched or unaffected without selectivity over metallicity (Fig. 3A). In the medium-diameter range, metallic tubes are selectively etched over semiconducting ones (Fig. 3A). This is consistent with first-principles calculations (*22*, *23*) that the formation energies of same-diameter S-SWNTs are lower than M-SWNTs because of the electronic energy gain resulting from the band gap opening (*22*) and the higher chemical reactivity of M-SWNTs due to more abundant delocalized electronic states (*23*). The difference diminishes for SWNTs with large diameters (*22*), consistent with reduced chemical etching selectivity seen here for large tubes. It is notable that the window of selective M-SWNT etching is small and exploitable only with methane plasma treatment. With pure hydrogen-generated plasma, we observed diameter-dependent etching (*19*) but failed to etch M-SWNT selectively and enrich depletable nanotube FETs. Pure hydrogen

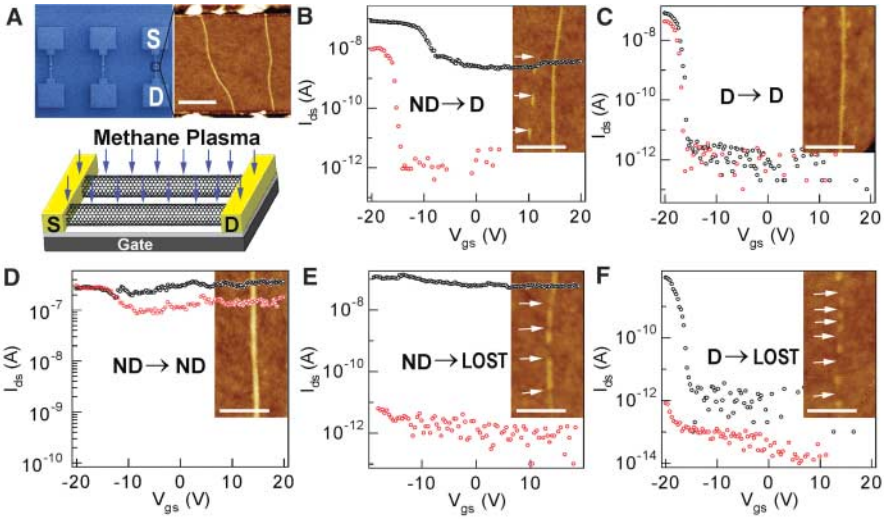

Fig. 1. Selective etching of metallic carbon nanotubes from the gas phase. (**A**) (Top) A scanning electron microscope (SEM) image of an array of few-tube (0 to 3) devices and an AFM image of two SWNTs bridging S-D electrodes. (Bottom) Schematic of the methane plasma treatment step [see (*18*) for details]. (**B** to **F**) Current (I_{ds}) versus gate voltage (V_{gs}) characteristics (V_{ds} = 10 mV) showing five different evolutions before (black) and after (red) the plasma and annealing treatment. Inset in each graph is an AFM image showing nanotubes in each device recorded after the treatment. White arrows highlight etched tubes in the devices. Scale bars, 100 nm.

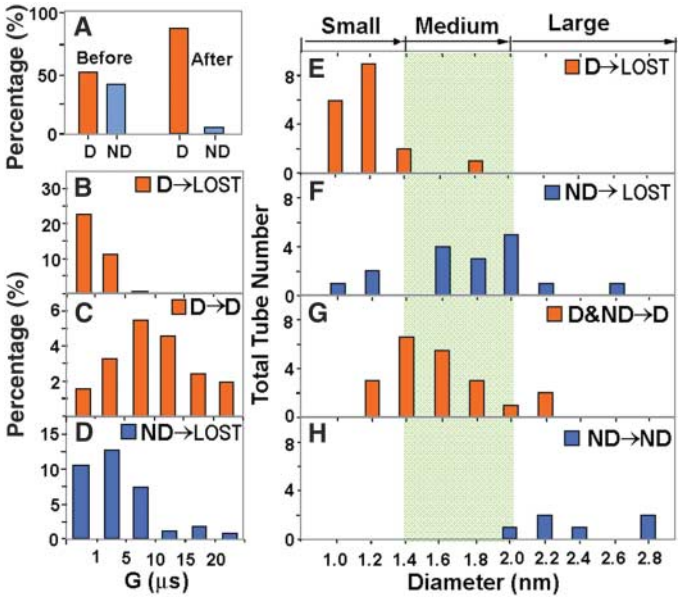

Fig. 2. Diameter- and metallicity-dependent SWNT hydrocarbonation. (**A**) Percentage of D and ND devices (total number, 244) before and after the treatment. (**B** to **D**) Electrical conductance (before treatment) distribution for devices exhibiting D→LOST, D→D, and ND→LOST evolutions, respectively. (**E** to **H**) Diameter distribution (measured by AFM topography) for SWNTs in devices exhibiting different evolutions. (E) shows that the semiconducting SWNTs, mainly in the small-diameter regime [defined at the top of (E) to (H)], are etched, or "lost," by the treatment. (F) shows that metallic SWNTs (in the ND devices), predominantly in the small and medium regimes, are etched. (H) shows that large-diameter metallic tubes can survive the plasma treatment and are responsible for the devices remaining ND.

plasma appeared too reactive to control experimentally, causing nondiscriminating etching effects.

Covalent chemical groups on nanotubes cause sp^3 hybridization (tetrahedral bonding) and degrade electrical properties and device performance. We carried out infrared (IR) spectroscopic experiments with ensembles of SWNTs to check the chemical effects of our treatment. After the 400°C methane plasma treatment step, we detected IR vibrational modes that can be assigned to covalent C-H_x groups (*24*) on nanotubes at either sidewalls or ends (Fig. 3, B and C). These species vanished upon 600°C vacuum annealing, indicating the elimination of covalently bound groups through demethylation and dehydrogenation. Thus, the 600°C annealing step ensured that the semiconducting SWNTs in the final FET devices were free of covalently attached species. This is further evidenced by retained electrical properties of nonetched S-SWNTs (*18*) (Fig. 1C and fig. S2).

Next, we showed that our method is reliable and can provide a 100% yield of semiconductors in an ensemble of SWNTs. For demonstration of FETs with large numbers of S-SWNTs in parallel, we fabricated arrays of micro devices (Fig. 4, A and B) with 40 to 50 CVD-grown SWNTs bridging S-D electrodes (channel length ~700 nm) on SiO_2(67 nm)/Si substrates. The catalyst islands and electrodes widths were designed to be ~100 to 200 μm for growth and for wiring up large numbers of tubes (Fig. 4A). We optimized CVD growth by lowering the growth temperature to 750°C to produce SWNTs with diameters predominantly in the 1- to 1.8-nm range. As-made devices were all nondepletable, with negligible on/off ratios due to metallic tubes (Fig. 4C, black curve). After our treatment steps, all devices exhibited improved on/off ratios, affording FETs with on/off of 10^4 to 10^5 at V_{ds} = 1 V (Fig. 4C, blue curve) and high on-currents (I_{ds} ~ 140 μA at V_{ds} = 2 V) (Fig. 4D). AFM revealed ~20 intact semiconducting SWNTs in parallel in such devices (together with residues of etched M-SWNTs) (Fig. 4B) without any metallic short (a single M-SWNT mixed with ~20 S-SWNTs would degrade on/off to ~10). The properties of our macro-FETs (on-current, ~5 to 7 μA per tube) are comparable to the best ~700-nm-long channel devices of similar diameter (~1.4 nm) S-SWNTs in as-grown forms (*16*). Multitube FETs were reproducibly obtained with large numbers of devices (fig. S3) (*18*), providing strong evidence for the effectiveness of our method.

Our present work focuses on only one of the ingredients needed for eventual manufacturing of nanotube electronics. Other important elements are still required, including assembly of SWNTs in a closely packed manner on wafer substrates. Hydrocarbonation etching can then be used to permanently remove metallic tubes from the wafers, which will then reduce the packing between the retained S-SWNTs. This reduced packing will be acceptable and could favor electrostatics gate control over SWNTs in the assembly (*25*). Our gas-phase reaction can be easily integrated into fabrication processes and is advantageous over wet chemical treatments, as the latter tend to involve excessively short SWNTs caused by sonication, too-small-diameter tubes in the starting materials, or covalent groups remaining on the SWNTs. The starting nanotube materials for future electronics should have diameters of 1.3 to 1.6 nm, beyond which the nanotubes will be too small for high performance or too large to attain pure semiconductors. An important benefit of narrow-diameter distribution (~1.5 nm) is that fewer SWNTs (up to about one-third, which is the metallic fraction) will need to be etched or sacrificed. Thus, with suitable starting materials and advances in assembly and selective-etching chemistry, a road map can be envisioned for manufacturable nanotube electronics.

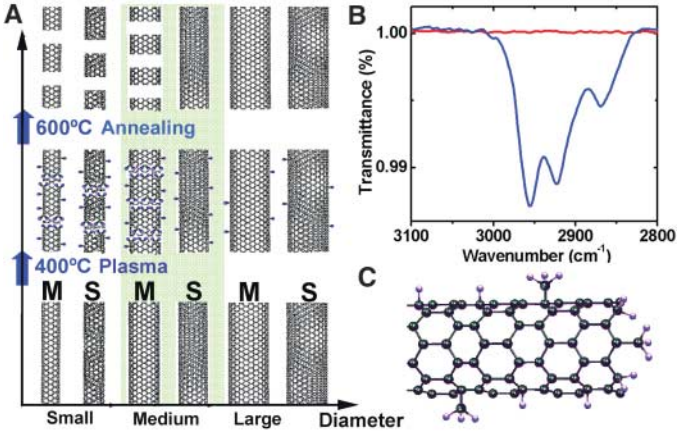

Fig. 3. Chemical and structural evolutions of SWNTs and diameter and metallicity dependence. (**A**) Illustrations of the fate of metallic and semiconducting SWNTs in different diameter regimes. In all cases, the annealing step reverses covalent functionalization (represented by species drawn on the tubes after the plasma step) on the retained SWNTs. (**B**) Infrared transmittance spectra of a film of SWNTs after plasma and annealing, respectively. IR absorption peaks (blue curve) at 2960 cm^{-1}, 2920 cm^{-1}, and 2850 cm^{-1} are assigned to C–CH_3, C–H or C–H_2, and C–H_2, respectively, covalently attached to the C atoms on nanotube ends and/or sidewalls. These peaks vanish after annealing. (**C**) A schematic of the possible chemical groups on a SWNT after the plasma step.

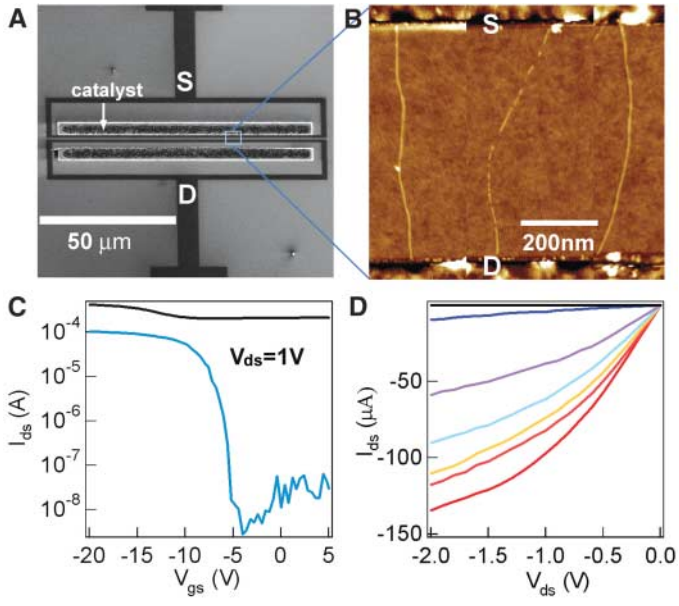

Fig. 4. High-current FETs with all-semiconducting nanotubes in parallel. (**A**) An SEM image of a macro-SWNT device composed of ~50 SWNTs bridging S-D electrodes (S-D distance ~700 nm). (**B**) An AFM image zoomed into a region between S-D showing three SWNTs (with one severely etched) after the plasma and annealing treatment. (**C**) Current versus gate-voltage (I_{ds}-V_{gs}) characteristics (V_{ds} = 1 V) of the device shown in (A) and (B) before (ND, black curve) and after (D, on/off ~5 × 10^4, blue curve) treatment. (**D**) Current-voltage (I_{ds}-V_{ds}) characteristics of the resulting FET composed of ~20 semiconducting tubes with on-current of 0.14 mA. The curves were recorded at several gate-voltages from V_{gs} = –20 V to –5 V in steps of 2.5 V from on to off.

References and Notes

1. C. Dekker, *Phys. Today* **52**, 22 (1999).
2. P. L. McEuen, M. S. Fuhrer, H. K. Park, *IEEE Trans. Nanotechnology* **1**, 78 (2002).
3. A. Javey, J. Guo, Q. Wang, M. Lundstrom, H. J. Dai, *Nature* **424**, 654 (2003).
4. A. Javey *et al.*, *Nano Lett.* **4**, 1319 (2004).
5. Y. M. Lin *et al.*, *IEEE Elec. Dev. Lett.* **26**, 823 (2005).
6. J. Appenzeller, Y. M. Lin, J. Knoch, Z. H. Chen, P. Avouris, *IEEE Trans. Elec. Dev.* **52**, 2568 (2005).

7. S. M. Bachilo *et al.*, *J. Am. Chem. Soc.* **125**, 11186 (2003).
8. Y. M. Li *et al.*, *Nano Lett.* **4**, 317 (2004).
9. P. Collins, M. Arnold, P. Avouris, *Science* **292**, 706 (2001).
10. R. Seidel *et al.*, *Nano Lett.* **4**, 831 (2004).
11. D. Chattopadhyay, L. Galeska, F. Papadimitrakopoulos, *J. Am. Chem. Soc.* **125**, 3370 (2003).
12. M. Zheng *et al.*, *Science* **302**, 1545 (2003).
13. M. S. Strano *et al.*, *Science* **301**, 1519 (2003).
14. K. Balasubramanian, R. Sordan, M. Burghard, K. A. Kern, *Nano Lett.* **4**, 827 (2004).
15. L. An, Q. A. Fu, C. G. Lu, J. Liu, *J. Am. Chem. Soc.* **126**, 10520 (2004).
16. W. Kim *et al.*, *Appl. Phys. Lett.* **87**, 1 (2005).
17. J. Kong, H. Soh, A. Cassell, C. F. Quate, H. Dai, *Nature* **395**, 878 (1998).
18. Materials and methods are available as supporting materials on *Science* Online.
19. G. Y. Zhang *et al.*, *J. Am. Chem. Soc.* **128**, 6026 (2006).
20. G. Drabner, A. Poppe, H. Budzikiewicz, *Int. J. Mass Spectrom. Ion Process.* **97**, 1 (1990).
21. W. Zhou *et al.*, *Chem. Phys. Lett.* **350**, 6 (2001).
22. Y. Li *et al.*, *J. Phys. Chem. B* **109**, 6968 (2005).
23. H. Park, J. Zhao, J. P. Lu, *Nanotechnology* **16**, 635 (2005).
24. T. Heitz, B. Drevillon, C. Godet, J. E. Bouree, *Phys. Rev. B* **58**, 13957 (1998).
25. J. Guo, S. Goasguen, M. Lundstrom, S. Datta, *Appl. Phys. Lett.* **81**, 1486 (2002).

26. We thank Intel and MARCO Center for Materials, Structures, and Devices for support of this work.

Supporting Online Material
www.sciencemag.org/cgi/content/full/314/5801/974/DC1
Materials and Methods
Figs. S1 to S3

11 August 2006; accepted 3 October 2006
10.1126/science.1133781

Metamaterial Electromagnetic Cloak at Microwave Frequencies

D. Schurig,[1] J. J. Mock,[1] B. J. Justice,[1] S. A. Cummer,[1] J. B. Pendry,[2] A. F. Starr,[3] D. R. Smith[1]*

A recently published theory has suggested that a cloak of invisibility is in principle possible, at least over a narrow frequency band. We describe here the first practical realization of such a cloak; in our demonstration, a copper cylinder was "hidden" inside a cloak constructed according to the previous theoretical prescription. The cloak was constructed with the use of artificially structured metamaterials, designed for operation over a band of microwave frequencies. The cloak decreased scattering from the hidden object while at the same time reducing its shadow, so that the cloak and object combined began to resemble empty space.

A new approach to the design of electromagnetic structures has recently been proposed, in which the paths of electromagnetic waves are controlled within a material by introducing a prescribed spatial variation in the constitutive parameters (*1*, *2*). The recipe for determining this variation, based on coordinate transformations (*3*), enables us to arrive at structures that would be otherwise difficult to conceive, opening up the new field of transformation optics (*4*, *5*).

One possible application of transformation optics and media is that of electromagnetic cloaking, in which a material is used to render a volume effectively invisible to incident radiation. The design process for the cloak involves a coordinate transformation that squeezes space from a volume into a shell surrounding the concealment volume. Maxwell's equations are form-invariant to coordinate transformations, so that only the components of the permittivity tensor ε and the permeability tensor μ are affected by the transformation (*5*), becoming both spatially varying and anisotropic. By implementing these complex material properties, the concealed volume plus the cloak appear to have the properties of free space when viewed externally. The cloak thus neither scatters waves nor imparts a shadow in the transmitted field, either of which would enable the cloak to be detected. Other approaches to invisibility either rely on the reduction of backscatter or make use of a resonance in which the properties of the cloaked object and the cloak itself must be carefully matched (*6*, *7*).

It might be of concern that we are able to achieve two different solutions to Maxwell's equations that both have, in principle, the exact same field distributions on a surface enclosing the region of interest. Indeed, the uniqueness theorem would suggest that these two solutions would be required to have the exact same medium within the surface. The uniqueness theorem, however, applies only to isotropic media (*8*, *9*); the required media that result from our coordinate transformations are generally anisotropic. Such media have been shown to support sets of distinct solutions having identical boundary conditions (*10*, *11*).

The effectiveness of a transformation-based cloak design was first confirmed computationally in the geometric optic limit (*1*, *5*) and then in full-wave finite-element simulations (*12*). Advances in the development of metamaterials (*13*), especially with respect to gradient index lenses (*14*, *15*), have made the physical realization of the specified complex material properties feasible. We implemented a two-dimensional (2D) cloak because its fabrication and measurement requirements were simpler than those of a 3D cloak. Recently, we have demonstrated the capability of obtaining detailed spatial maps of the amplitude and phase of the electric field distribution internal to 2D negative-index metamaterial samples at microwave frequencies (*16*). Using this measurement technique, we confirmed the performance of our cloak by comparing our measured field maps to simulations.

In both the cloaking simulations and the measurements presented here, the object being cloaked is a conducting cylinder at the inner radius of the cloak; this is the largest and most strongly scattering object that can be concealed in a cloak of cylindrical geometry.

For the cloak design, we start with a coordinate transformation that compresses space from the cylindrical region $0 < r < b$ into the annular region $a < r' < b$, where r and r' are the radial coordinates in the original and transformed system, respectively, a is the cloak inner radius, and b is the cloak outer radius. A simple transformation that accomplishes this goal is

$$r' = \frac{b-a}{b} r + a \quad \theta' = \theta \quad z' = z \qquad (1)$$

where θ and z are the angular and vertical coordinates in the original system, and θ' and z' are the angular and vertical coordinates in the transformed system. This transformation leads to the following expression for the permittivity and permeability tensor components

$$\varepsilon_r = \mu_r = \frac{r-a}{r} \quad \varepsilon_\theta = \mu_\theta = \frac{r}{r-a}$$

$$\varepsilon_z = \mu_z = \left(\frac{b}{b-a}\right)^2 \frac{r-a}{r} \qquad (2)$$

Equation 2 shows that all of the tensor components have gradients as a function of radius, implying a very complicated metamaterial design. However, because of the nature of the experimental apparatus, in which the electric field is polarized along the z axis (cylinder axis), we benefit from a substantial simplification in that only ε_z, μ_r, and μ_θ are relevant. Moreover, if we wish to primarily demonstrate the wave trajectory inside the cloak, which is solely determined by the dispersion relation, we gain even more flexibility in choosing the functional forms for the electromagnetic ma-

[1]Department of Electrical and Computer Engineering, Duke University, Box 90291, Durham, NC 27708, USA. [2]Department of Physics, The Blackett Laboratory, Imperial College, London SW7 2AZ, UK. [3]SensorMetrix, 5695 Pacific Center Boulevard, San Diego, CA 92121, USA.

*To whom correspondence should be addressed. E-mail: drsmith@ee.duke.edu

terial parameters. In particular, the following material properties

$$\varepsilon_z = \left(\frac{b}{b-a}\right)^2 \quad \mu_r = \left(\frac{r-a}{r}\right)^2 \quad \mu_\theta = 1 \quad (3)$$

have the same dispersion as those of Eq. 2, implying that waves will have the same dynamics in the medium. In the geometric limit, for example, rays will follow the same paths in media defined by Eqs. 2 or 3, and refraction angles into or out of the media will also be the same (*12*). The only penalty for using the reduced set of material properties (Eq. 3) is a nonzero reflectance.

To implement the material specification in Eq. 3 with a metamaterial, we must choose the overall dimensions, design the appropriate unit cells, and specify their layout, which for our implementation represents a pattern that is neither cubic nor even periodic. All three of these design elements share parameters, making it advantageous and necessary to optimize them all at once. Equation 3 shows that the desired cloak will have constant ε_z and μ_θ, with μ_r varying radially throughout the structure. This parameter set can be achieved in a metamaterial in which split-ring resonators (SRRs), known to provide a magnetic response that can be tailored (*17*), are positioned with their axes along the radial direction (Fig. 1).

As can be seen from Eq. 3, the transformed material properties depend strongly on the choice of a and b . Because of constraints from the unit cell design and layout requirements, we chose the seemingly arbitrary values a = 27.1 mm and b = 58.9 mm. The resulting material properties are plotted in Fig. 1.

All metamaterials reported to date have consisted of elements repeated in cubic or other standard lattice configurations and are usually diagonal in the Cartesian basis. The layout of our cylindrical cloak, however, uses cells that are diagonal in a cylindrical basis and has "unit cells" that are curved sectors with varied electromagnetic environments. The correct retrieval procedure that would obtain the effective medium properties from such irregular unit cells is not yet available. Given that the curvature is not extreme in this cloak design, however, we modeled the unit cells as right-rectangular prisms in a periodic array of like cells, with the assumption that the actual cells will produce minor corrections in the effective medium properties.

Because of constraints of the layout, we chose a rectangular unit cell with dimensions $a_\theta = a_z$ = 10/3 mm and a_r = 10/π mm. We were able to obtain both the desired ε_z and $\mu_r(r)$ from an SRR by tuning two of its geometric parameters: the length of the split s and the radius of the corners r (Fig. 2). The parameters r and s shift the frequency of the electric and magnetic resonance, respectively, though there is some cross-coupling that must be compensated for.

Using commercial, full-wave, finite-element simulation software (Microwave Studio, Computer Simulation Technology), we performed a series of scattering (*S*) parameter simulations for the SRR unit cells over a discrete set of the parameters r and s covering the range of interest. A standard retrieval procedure (*18*, *19*) was then performed to obtain the effective material properties ε_z and μ_r from the *S* parameters. The discrete set of simulations and extractions was interpolated to obtain the particular values of the geometric parameters that yielded the desired material properties. We chose an operating frequency of 8.5 GHz, which yields a reasonable effective medium parameter $\lambda/a_\theta > 10$, where λ is the wavelength in free space.

The layout consisted of 10 concentric cylinders, each of which was three unit cells tall. The evenly spaced set of cylinder radii was chosen so that an integral number of unit cells fit exactly around the circumference of each cylinder, necessitating a particular ratio of radial-to-circumferential unit cell size. We chose to increase the number of unit cells in each successive cylinder by six, enabling us to use six supporting radial spokes that can intersect each of the cylinders in the spaces between the SRRs. This led to the requirement $a_r/a_\theta = 3/\pi$. Additionally, to minimize the magnetoelectric coupling inherent in single-split SRRs (*20*), we alternated their orientation along the z direction (Fig. 1).

The overall scale of the cloak is such that a complete field mapping of the cloak and its immediate environment is feasible (Fig. 3). By the same reasoning, numerical simulations of the cloak are also feasible, so long as the cloak is approximated by continuous materials. A complete simulation of the actual cloak structure, including the details of the thousands of SRRs, would be impractical for general optimization studies.

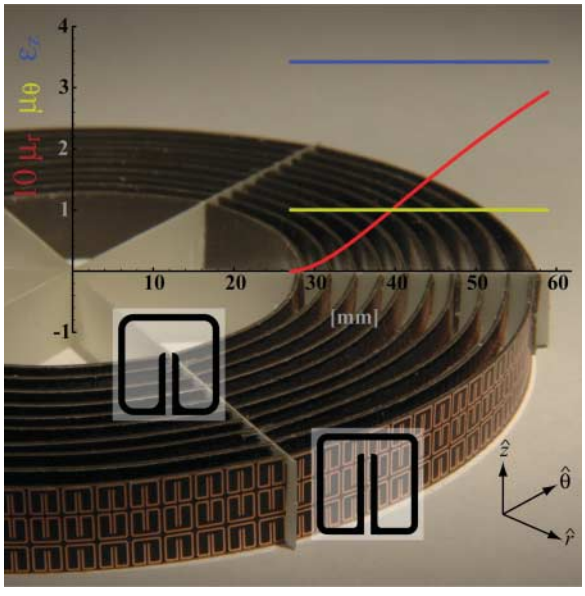

Fig. 1. 2D microwave cloaking structure (background image) with a plot of the material parameters that are implemented. μ_r (red line) is multiplied by a factor of 10 for clarity. μ_θ (green line) has the constant value 1. ε_z (blue line) has the constant value 3.423. The SRRs of cylinder 1 (inner) and cylinder 10 (outer) are shown in expanded schematic form (transparent square insets).

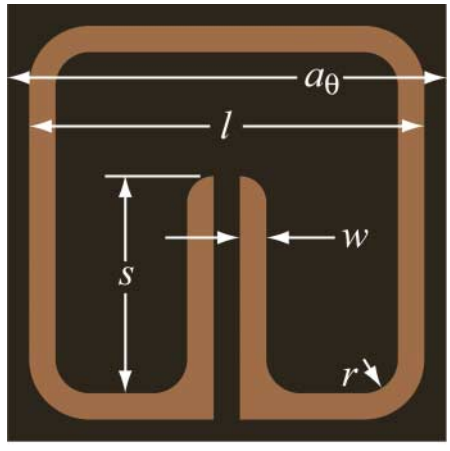

cyl.	r	s	μ_r
1	0.260	1.654	0.003
2	0.254	1.677	0.023
3	0.245	1.718	0.052
4	0.230	1.771	0.085
5	0.208	1.825	0.120
6	0.190	1.886	0.154
7	0.173	1.951	0.188
8	0.148	2.027	0.220
9	0.129	2.110	0.250
10	0.116	2.199	0.279

Fig. 2. SRR design. The in-plane lattice parameters are $a_\theta = a_z$ = 10/3 mm. The ring is square, with edge length l = 3 mm and trace width w = 0.2 mm. The substrate is 381-μm-thick Duroid 5870 (ε = 2.33, t_d = 0.0012 at 10 GHz, where t_d is the loss tangent). The Cu film, from which the SRRs are patterned, is 17 μm thick. The parameters r and s are given in the table together with the associated value of μ_r. The extractions gave roughly constant values for the imaginary parts of the material parameters, yielding 0.002 and 0.006 for the imaginary part of ε_z and μ_r, respectively. The inner cylinder (cyl.) is 1 and the outer cylinder is 10.

Continuous medium simulations of cloaking structures were performed by means of the COMSOL Multiphysics finite-element–based electromagnetics solver (*12*). The simulation result of the ideal case is shown in Fig. 4A, with material properties as in Eq. 2, and no absorption loss. Several real-world effects were incorporated into another simulation (Fig. 4B) to match experimental conditions as much as possible. In the latter simulation, the reduced material properties of Eq. 3 were used, and $\mu_r(r)$ was approximated by a 10-step piecewise constant function to mimic the concentric rings of the fabricated cloak. Additionally, absorption loss was added corresponding to that found in the unit cell simulations (and given in Fig. 2).

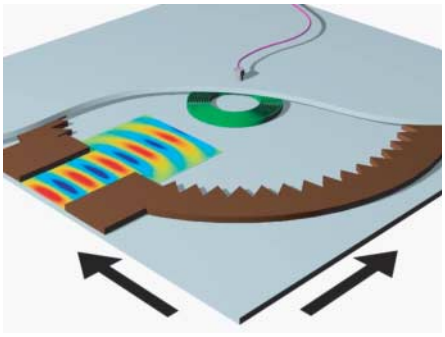

Fig. 3. Cutaway view of the planar waveguide apparatus. Microwaves (red and yellow patterns) are introduced by means of a coaxial-to-waveguide transition (not shown) attached to the lower plate (lined with a circular sawtooth-shaped microwave absorber). An antenna mounted in the fixed upper plate measures the phase and amplitude of the electric field. To perform field maps, we stepped the lower plate in the lateral directions (black arrows).

For the experimental confirmation, we measured the metamaterial cloak in a parallel-plate waveguide comprising two flat conducting (Al) plates spaced 11 mm apart (Fig. 3). Microwaves were introduced through an X-band (8 to 12 GHz) coax-to-waveguide adapter that was attached to the lower plate and were incident on the cloak, which rested on the lower plate and was nearly of the same height (10 mm) as the plate separation.

A field-sensing antenna was formed from a coaxial fixture inserted into a hole drilled through the upper plate. The center conductor and dielectric of the coaxial connector extended to a position flush with the lower surface of the upper plate and did not protrude into the chamber volume. The lower plate was mounted on two orthogonal linear translation stages, so that the lower plate (including the cloak, waveguide feed, and absorber) could be translated with respect to the upper plate and to the detector. By stepping the lower plate in small increments and recording the field amplitude and phase at every step, a full 2D spatial field map of the microwave scattering pattern could be acquired both inside the cloak and in the surrounding free-space region. Further experimental details can be found in (*16*) and in the supporting online material.

Both the cloak surrounding a 25-mm-radius Cu cylinder (Fig. 4D) and the bare Cu cylinder (Fig. 4C) were measured. The samples were placed on the lower plate in the center of the mapping region and illuminated with microwaves over a discrete set of frequencies that included the expected operating frequency of the cloak. At each frequency, the complex electric field was acquired, and the process was repeated for all x and y positions in the scan range. After reviewing the field maps at all frequencies, the optimal frequency for the cloak sample was determined to be 8.5 GHz, in near-exact agreement with the design target. The optimal frequency was selected as that which best matched the simulated field plots. The acquired real part of the electric field distribution is shown (Fig. 4, C and D).

Comparison of Fig. 4, C and D, shows that the cloak reduces both backscatter (reflection) and forward scatter (shadow). The backscatter is particularly evident in movie S3 as a strong standing-wave component. Comparison of Fig. 4, B and D, shows that the field plots found through full-wave simulations are in marked agreement with the experimental data. The underlying physics of the cloaking mechanism can be studied even further by viewing the field animations (movies S1 to S5). As the waves propagate through the cloak, the center section of the wavefront begins to lag as it approaches the inner radius, exhibiting a compression in wavelength and a reduction in intensity. The wavefront then separates to pass around the cloak hole and reforms on the opposite side, where its center section initially leads the wavefront. The wavefronts at the boundary of the cloak match the wavefronts outside the cloak, which essentially correspond to those of empty space. The scattering is thus minimized, though not perfectly, as a result of the reduced parameter implementation. The fields on the exit side are noticeably attenuated because of the absorption of the cloak material.

The agreement between the simulation and the experiment is evidence that metamaterials can indeed be designed to detailed and exacting specifications, including gradients and non-rectangular geometry. Though the invisibility is imperfect because of the approximations used and material absorption, our results do provide an experimental display of the electromagnetic cloaking mechanism and demonstrate the feasibility of implementing media specified by the transformation optics method with metamaterial technology.

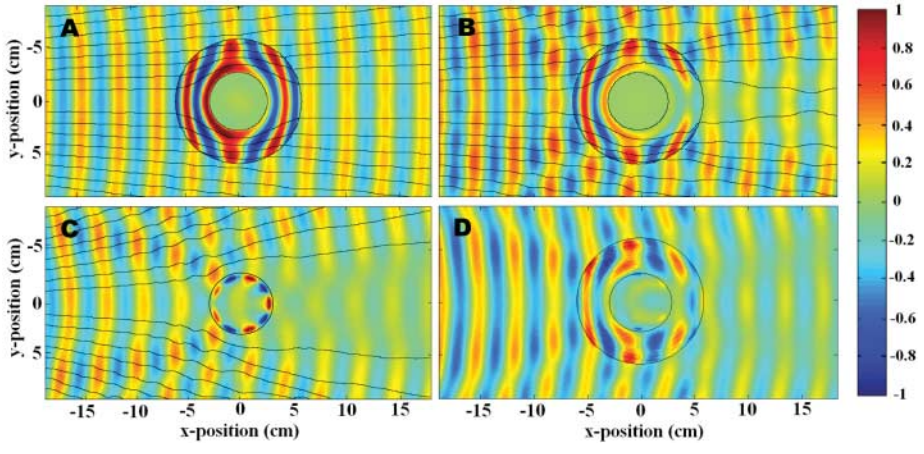

Fig. 4. Snapshots of time-dependent, steady-state electric field patterns, with stream lines [black lines in (A to C)] indicating the direction of power flow (i.e., the Poynting vector). The cloak lies in the annular region between the black circles and surrounds a conducting Cu cylinder at the inner radius. The fields shown are (**A**) the simulation of the cloak with the exact material properties, (**B**) the simulation of the cloak with the reduced material properties, (**C**) the experimental measurement of the bare conducting cylinder, and (**D**) the experimental measurement of the cloaked conducting cylinder. Animations of the simulations and the measurements (movies S1 to S5) show details of the field propagation characteristics within the cloak that cannot be inferred from these static frames. The right-hand scale indicates the instantaneous value of the field.

References and Notes

1. J. B. Pendry, D. Schurig, D. R. Smith, *Science* **312**, 1780 (2006).
2. U. Leonhardt, *Science* **312**, 1777 (2006).
3. A. J. Ward, J. B. Pendry, *J. Mod. Opt.* **43**, 773 (1996).
4. U. Leonhardt, T. G. Philbin, *N. J. Phys.* **8**, 247 (2006).
5. D. Schurig, J. B. Pendry, D. R. Smith, *Opt. Express* **14**, 9794 (2006).
6. A. Alu, N. Engheta, *Phys. Rev. E Stat. Nonlin. Soft Matter Phys.* **72**, 016623 (2005).
7. G. W. Milton, N.-A. P. Nicorovici, *Proc. R. Soc. London Ser. A* **462**, 1364 (2006).
8. A. I. Nachman, *Ann. Math.* **128**, 531 (1988).
9. G. Gbur, *Prog. Opt.* **45**, 273 (2003).
10. A. Greenleaf, M. Lassas, G. Uhlmann, *Physiol. Meas.* **24**, 413 (2003).
11. A. Greenleaf, M. Lassas, G. Uhlmann, *Math. Res. Lett.* **10**, 1 (2003).

12. S. A. Cummer *et al.*, *Phys. Rev. E* **74**, 036621 (2006).
13. D. R. Smith, J. B. Pendry, M. C. K. Wiltshire, *Science* **305**, 788 (2004).
14. R. B. Greegor *et al.*, *Appl. Phys. Lett.* **87**, 091114 (2005).
15. T. Driscoll *et al.*, *Appl. Phys. Lett.* **88**, 081101 (2006).
16. B. J. Justice *et al.*, *Opt. Express* **14**, 8694 (2006).
17. J. B. Pendry, A. J. Holden, D. J. Roberts, W. J. Stewart, *IEEE Trans. Micr. Theory Techniques* **47**, 2075 (1999).
18. D. R. Smith, S. Schultz, P. Markoš, C. M. Soukoulis, *Phys. Rev. B* **65**, 195104 (2002).
19. X. Chen, T. M. Grzegorczyk, B.-I. Wu, J. Pacheco, J. A. Kong, *Phys. Rev. E Stat. Nonlin. Soft Matter Phys.* **70**, 016608 (2004).
20. R. Marqués, F. Medina, R. Rafii-El-Idrissi, *Phys. Rev. B* **65**, 14440 (2002).
21. D.S. acknowledges support from the Intelligence Community Postdoctoral Research Fellowship program. L. Guo was instrumental in establishing our data acquisition and motion-control capabilities. J.B.P. thanks the Engineering and Physical Sciences Research Council for a Senior Fellowship.

Supporting Online Material
www.sciencemag.org/cgi/content/full/1133628/DC1
SOM Text
Figs. S1 to S3
Movies S1 to S5

8 August 2006; accepted 3 October 2006
Published online 19 October 2006;
10.1126/science.1133628
Include this information when citing this paper.

Isotopic Evidence for Dietary Variability in the Early Hominin *Paranthropus robustus*

Matt Sponheimer,[1] Benjamin H. Passey,[2] Darryl J. de Ruiter,[3] Debbie Guatelli-Steinberg,[4] Thure E. Cerling,[2,5] Julia A. Lee-Thorp[6]

Traditional methods of dietary reconstruction do not allow the investigation of dietary variability within the lifetimes of individual hominins. However, laser ablation stable isotope analysis reveals that the $\delta^{13}C$ values of *Paranthropus robustus* individuals often changed seasonally and interannually. These data suggest that *Paranthropus* was not a dietary specialist and that by about 1.8 million years ago, savanna-based foods such as grasses or sedges or animals eating these foods made up an important but highly variable part of its diet.

Both dental microwear texture analysis (*1*) and stable carbon isotope analysis (*2*–*5*) have demonstrated that the diets of South African australopiths were variable on the whole, but it has not been clear how the diets of individual hominins varied during their lifetimes. Here we provide evidence for short-term (seasonal and interannual) dietary change within the lifetimes of individual hominins, using a laser ablation method for stable isotope analysis (*6*). This method allows analysis along the growth axis of hominin teeth at submillimeter increments, making it possible to trace an individual's dietary history.

In tropical environments, virtually all trees, bushes, shrubs, and forbs use the C_3 photosynthetic pathway, whereas grasses and some sedges use the C_4 photosynthetic pathway (*7*, *8*). C_3 plants are depleted in ^{13}C [~ –27 per mil (‰)] as compared to C_4 plants (~ –12‰). The carbon isotopes in plants are incorporated into the tissues of consumers, with some additional fractionation (*9*, *10*), and consequently carbon isotope ratios of tooth enamel can reveal the degree to which an animal consumed C_3 or C_4 resources. This allows determination of whether a hominin ate C_3 foods, such as the forest fruits and leaves consumed by extant apes, or if they supplemented their diets with savanna-based C_4 foods, such as grasses or animals eating those plants (*2*).

We analyzed the enamel of four permanent teeth of *Paranthropus robustus* from Swartkrans, South Africa [found in member 1 at the site, dated ~1.8 million years ago (Ma)] using laser ablation stable isotope analysis (*11*). We also analyzed enamel of three contemporaneous browsing herbivores (*Raphicerus* sp.) from Swartkrans to control for postmortem alteration of carbon isotope ratios. We also counted the tooth growth increments (perikymata) that outcropped to the enamel surface between and adjacent to each ablation track on the hominin specimens to temporally constrain the isotope data where possible (Fig. 1). The number of days represented by perikymata is 9 days in humans and extant apes, with ranges from 6 to 12 days in humans and extant apes (*12*). Because the actual periodicities of perikymata in fossil teeth cannot be known without sectioning them, we assumed that the periodicity for *Paranthropus* was 7 days for this study (*12*).

The mean of all carbon isotopic analyses for *Raphicerus* demonstrates that diagenesis has not obliterated the biogenic carbon isotopic compositions, because it indicates a C_3 diet like that of *Raphicerus'* modern congeners (*13*) and of other known browsing herbivores from the site (Table 1 and table S1; $\delta^{18}O$ values are discussed in fig. S1) (*2*). Moreover, the expected small range in variation within individual *Raphicerus* teeth (a maximum of 0.9‰) shows that fossilization has not induced significant carbon isotopic variation at the spatial resolution of our analyses (Fig. 2). In contrast, there is strong variability within individual hominin teeth. The mean range of variation within individual teeth is 3.4‰ for *Paranthropus*, whereas the mean range for *Raphicerus* is only 0.7‰ ($P < 0.05$, Mann-Whitney *U* test, Table 1), showing that these hominins had more variable diets. In two out of four hominin teeth, the amplitude exceeds 4‰, which, at face value, suggests that their consumption of C_4 resources (tropical grasses or sedges or animals eating these foods) varied by ~40%. However, this isotopic signal is attenuated because of protracted mineral uptake during amelogenesis and our sampling protocol, which required some mixing of enamel layers (*14*).

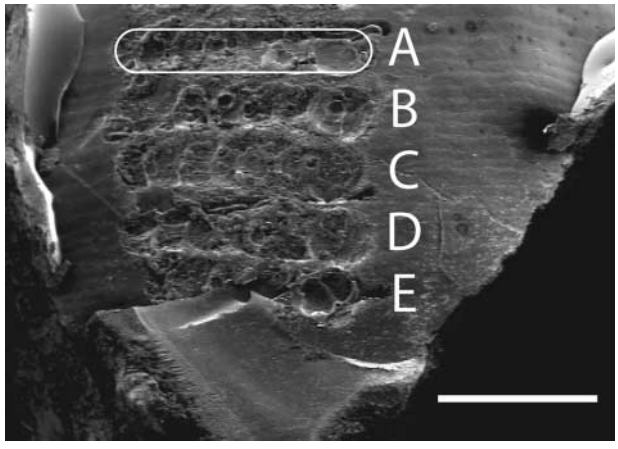

Fig. 1. A portion of the imbricational enamel of SKX 5939, on which the total number of perikymata between the first and last ablation samples shown (**A** to **E**) is 22, meaning that the interval represented by these samples is approximately 154 days (22 × 7). The day counts are only intended to be rough approximations sufficient to differentiate seasonal from interannual variability. The first visible ablation track is outlined in white. Perikymata are visible as faint horizontal lines across the tooth's surface. Scale bar, 1 mm.

[1]Department of Anthropology, University of Colorado at Boulder, Boulder, CO 80309, USA. [2]Department of Geology and Geophysics, University of Utah, Salt Lake City, UT 84112, USA. [3]Department of Anthropology, Texas A&M University, College Station, TX 77843, USA. [4]Department of Anthropology, The Ohio State University, Columbus, OH 43210, USA. [5]Department of Biology, University of Utah, Salt Lake City, UT 84112, USA. [6]Department of Archeological Sciences, University of Bradford, Bradford BD1 7DP, UK.

Thus, a change of 5.2‰, as seen in specimen SKX 5939, probably signifies a change from a diet dominated by C_4 resources to one of predominantly C_3 foods. Our data do not allow us to determine which C_4 resources *Paranthropus* consumed, although it is likely that grasses (seeds and roots), sedges (tubers and pith), and animal foods were all consumed to varying degrees.

Although all of the *Paranthropus* specimens show evidence of seasonal variability, there is also evidence of interannual variation that might reflect yearly differences in rainfall-related food availability (Fig. 2). Another possible explanation is that these individuals were migrating between more wooded habitats (favoring C_3 food consumption) and more open savannas (favoring C_4 resource consumption). Regardless, these results are very unlike what has been observed in our close relative the chimpanzee (*Pan troglodytes*). Some chimpanzees inhabit savanna woodland environments that are believed to be similar to those inhabited by early hominins [such as Mt. Assirik in Senegal (*15*)]. However, they do not consume C_4 resources to any measurable extent (*16*, *17*), and the carbon isotope compositions of their hair are not known to vary significantly from season to season (fig. S2) (*17*). Baboons (*Papio* spp.), in contrast, consume significant quantities of C_4 resources such as grass seeds and roots in some regions and some have variable $\delta^{13}C$ values (*18*). Thus, eurytopic *Papio* might be a more appropriate ecological analog for *P. robustus* (*19*).

A dental microwear study of the earlier (3.0 to 3.7 Ma) hominin *Australopithecus afarensis* found no evidence that its diet changed over time or in different habitats (*20*). In contrast, stable carbon isotope (*3*, *4*) and dental microwear texture analyses (*1*) of the slightly younger (~3.0 to ~2.4 Ma) hominin *A. africanus* demonstrated that its diet was far more variable. This suggests the possibility that a major increase in hominin dietary breadth was broadly coincident with the onset of increasing African continental aridity and seasonality after 3 Ma (*21*, *22*) and only shortly antedated the first probable members of the genera *Homo* and *Paranthropus* (*23*–*25*) and the earliest stone tools (*26*). The undoubted toolmaker *Homo* is thought to have been a dietary generalist that consumed novel foods such as large ungulate meat and tubers that are abundant in savanna environments (*27*–*30*). *Paranthropus*, in contrast, with its extremely large and flat cheek teeth, thick enamel, robust mandible, and heavily buttressed facial architecture, is often portrayed as a dietary specialist (*27*–*29*). Further, it has been argued that this specialization contributed to its extinction when confronted with increasingly dry and seasonal environments later in the Pleistocene, whereas *Homo*'s generalist adaptation was crucial for its success (*28*, *29*). Our results suggest that *Paranthropus* had an extremely flexible diet, which may indicate that its derived masticatory morphology signals an increase, rather than a decrease, in its potential foods. Thus, other biological, social, or cultural differences may be needed to explain the different fates of *Homo* and *Paranthropus* (*31*).

Table 1. Carbon isotope means, ranges, perikymata counts (PKM), and estimated number of days (perikymata × 7) for the total sampling intervals of specimens in this study. Oxygen isotope compositions are produced in tandem with the carbon isotope data and are further discussed in fig. S1. SD, standard deviation; na, not applicable.

Specimen	$\delta^{13}C$ (‰)	$\delta^{13}C$ range (‰)	PKM (*n*)	Days (*n*)
Paranthropus				
SK 24605	−7.3	1.3	47	329
SK 24606	−6.1	4.4	70	490
SKX 5939	−5.4	5.2	92	644
SKW 6427	−8.6	2.5	63	441
Mean	−6.9	3.4	68	467
SD	1.4	1.8	19	131
Raphicerus				
SKX 14150	−9.9	0.6	na	na
SKX 8494	−9.8	0.5	na	na
SKX 8535a	−8.6	0.9	na	na
Mean	−9.4	0.7	na	na
SD	0.7	0.2	na	na

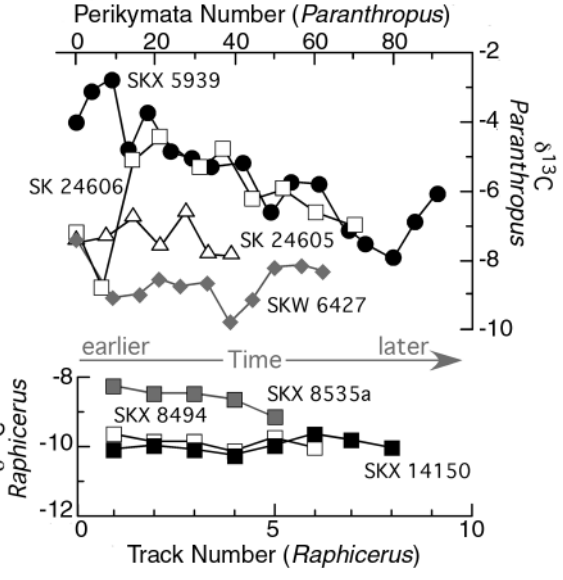

Fig. 2. $\delta^{13}C$ of multiple ablation samples along the growth axes of teeth of the early hominin *P. robustus* (top) and the browsing bovid *Raphicerus* sp. (bottom). Precision as gauged by reproducibility of internal enamel and CO_2 standards analyzed concurrently with each specimen was found to be 0.2, 1.1, 0.3, and 0.5‰ for SKX 5939 (black circles), SK 24606 (white squares), SK 24605 (white triangles), and SKW 6427 (gray diamonds), respectively. A perikymata count of 50 should be roughly equivalent to 1 year's crown formation. It is also important to note that each sample could incorporate carbon consumed over many months because of protracted mineral uptake during amelogenesis (*14*). This effectively attenuates the primary dietary signal, meaning that the intratooth variability observed here significantly underestimates actual dietary variability. Determination of the full amplitude of diet change awaits further study of enamel maturation parameters in hominoids [as in (*14*)]. The lack of variability within the *Raphicerus* teeth suggests that temporal differences in C_3 vegetation $\delta^{13}C$ values were very small and would not have contributed significantly to the variability in *Paranthropus*.

References and Notes

1. R. S. Scott *et al.*, *Nature* **436**, 693 (2005).
2. J. A. Lee-Thorp, N. J. van der Merwe, C. K. Brain, *J. Hum. Evol.* **27**, 361 (1994).
3. M. Sponheimer, J. A. Lee-Thorp, *Science* **283**, 368 (1999).
4. N. J. van der Merwe, J. F. Thackeray, J. A. Lee-Thorp, J. Luyt, *J. Hum. Evol.* **44**, 581 (2003).
5. M. Sponheimer *et al.*, *J. Hum. Evol.* **48**, 301 (2005).
6. B. H. Passey, T. E. Cerling, *Chem. Geol.* 10.1016/j.chemgeo.2006.07.002 (2006).
7. B. N. Smith, S. Epstein, *Plant Physiol.* **47**, 380 (1971).
8. J. C. Vogel, A. Fuls, R. P. Ellis, *S. Afr. J. Sci.* **74**, 209 (1978).
9. S. H. Ambrose, L. Norr, in *Prehistoric Human Bone: Archaeology at the Molecular Level*, J. B. Lambert, G. Grupe, Eds. (Springer-Verlag, Berlin, 1993).
10. B. H. Passey *et al.*, *J. Archaeol. Sci.* **32**, 1459 (2005).
11. Materials and methods are available as supporting material on *Science* Online.
12. R. J. Lacruz, F. R. Rozzi, T. G. Bromage, *J. Hum. Evol.*, 10.1016/j.jhevol.2006.05.007 (2006).
13. M. Sponheimer *et al.*, *J. Mammal.* **84**, 471 (2003).
14. B. H. Passey, T. E. Cerling, *Geochim. Cosmochim. Acta* **66**, 3225 (2002).
15. W. C. McGrew, P. J. Baldwin, C. E. G. Tutin, *J. Hum. Evol.* **10**, 227 (1981).
16. M. J. Schoeninger, J. Moore, J. M. Sept, *Am. J. Primatol.* **49**, 297 (1999).
17. M. Sponheimer *et al.*, *J. Hum. Evol.* **51**, 128 (2006).
18. D. Codron, J. A. Lee-Thorp, M. Sponheimer, D. De Ruiter, J. Codron, *Am. J. Phys. Anthropol.* **129**, 204 (2006).
19. C. J. Jolly, *Yearb. Phys. Anthropol.* **44**, 177 (2001).
20. F. E. Grine, P. S. Ungar, M. F. Teaford, S. El-Zaatari, *J. Hum. Evol.* **51**, 297 (2006).
21. T. E. Cerling, *Paleogeogr. Paleoclimatol. Paleoecol.* **97**, 241 (1992).
22. P. B. deMenocal, *Science* **270**, 53 (1995).
23. A. Hill, S. Ward, A. Deino, G. Curtis, R. Drake, *Nature* **355**, 719 (1992).
24. F. Schrenk, T. Bromage, C. Betzler, U. Ring, Y. Juwayeyi, *Nature* **365**, 833 (1993).
25. A. Walker, R. E. Leakey, J. M. Harris, F. H. Brown, *Nature* **322**, 517 (1986).
26. S. Semaw *et al.*, *Nature* **385**, 333 (1997).
27. J. T. Robinson, *Evol. Int. J. Org. Evol.* **8**, 324 (1954).
28. R. Foley, *Another Unique Species* (Longman Scientific & Technical, Essex, UK, 1987), pp. 210–255.
29. E. S. Vrba, in *Evolutionary History of the "Robust" Australopithecines*, F. E. Grine, Ed. (Aldine de Gruyter, New York, 1988), pp. 405–426.
30. J. F. O'Connell, K. Hawkes, N. G. Blurton Jones, *J. Hum. Evol.* **36**, 461 (1999).

31. B. Wood, D. Strait, *J. Hum. Evol.* **46**, 119 (2004).
32. We thank T. Kearney, S. Potze, and F. Thackeray for their help and access to specimens; S. Copeland, B. Covert, Y. Rahman, D. VanGerven, and three anonymous reviewers for their comments on the manuscript; and L. Ayliffe, C. Dean, D. Dufour, F. Grine, J. Moggi-Cecchin, K. Reed, and P. Ungar for help and discussions related to this manuscript. This work was funded by NSF, the National Research Foundation, and the Dean's Fund of the University of Colorado at Boulder.

Supporting Online Material
www.sciencemag.org/cgi/content/full/314/5801/980/DC1
Materials and Methods
Figs. S1 and S2
Table S1
References

14 August 2006; accepted 2 October 2006
10.1126/science.1133827

Human Hair Growth Deficiency Is Linked to a Genetic Defect in the Phospholipase Gene *LIPH*

Anastasiya Kazantseva,[1,2] Andrey Goltsov,[2,3] Rena Zinchenko,[4] Anastasia P. Grigorenko,[1,2] Anna V. Abrukova,[5] Yuri K. Moliaka,[1,2] Alexander G. Kirillov,[6] Zhiru Guo,[7] Stephen Lyle,[7] Evgeny K. Ginter,[4] Evgeny I. Rogaev[1,2,3,8]*

The molecular mechanisms controlling human hair growth and scalp hair loss are poorly understood. By screening about 350,000 individuals in two populations from the Volga-Ural region of Russia, we identified a gene mutation in families who show an inherited form of hair loss and a hair growth defect. Affected individuals were homozygous for a deletion in the *LIPH* gene on chromosome 3q27, caused by short interspersed nuclear element–retrotransposon–mediated recombination. The *LIPH* gene is expressed in hair follicles and encodes a phospholipase called lipase H (alternatively known as membrane-associated phosphatidic acid–selective phospholipase A1α), an enzyme that regulates the production of bioactive lipids. These results suggest that lipase H participates in hair growth and development.

Mammalian hair follicles are self-renewing organs that represent interesting models for the regulation of stem cells. Hair follicles cycle through periods of growth (anagen), involution (catagen), and rest (telogen) before regenerating at the onset of a new anagen growth phase (*1*–*3*). Hair follicle stem cells, permanent residents of the stem cell niche called the "bulge," communicate with the underlying dermal papilla cells and proliferate at anagen onset to generate the progenitor matrix cells required for new hair growth (*4*). The molecules that control morphogenesis and cycling of hair follicles and the mechanisms underlying hair loss are poorly understood. However, genetic studies of rare familial cases of alopecia (hair loss on the scalp) and hypotrichosis (deficiencies of hair growth) have yielded important information about some of the genes controlling hair growth, including human *hairless*, desmoglein 4 (*DSG4*), and corneodesmosin (*CDSN*) (*5*–*7*).

Previously, we described individuals within the aboriginal Finno-Ugric population of Russia with a genetic form of hair growth deficiency (*8*, *9*). To identify the genetic defect for this condition, we have now studied two ethnic groups of mixed Caucasian and Mongoloid origin living in the Volga-Ural region of Russia (Mari El and Chuvash). The Mari population belongs to the Finno-Ugric linguistic group and the Chuvash population to the Turks linguistic group. The ancestors of the Chuvash population were probably Volga Bulgars, extruded by Mongols from Volga Bulgaria, who settled in the territory occupied by the Mari ancestral populations. We analyzed 50 families with hypotrichosis (14 from Mari and 36 from Chuvash) identified in a genetic epidemiological study of 171,500 Mari individuals and 178,722 Chuvash individuals (see supporting online material).

Affected individuals were characterized by deficiencies of hair growth on the scalp and body starting at birth, but showed no other pathologies. The growth of scalp hairs was retarded or arrested, leading to short hair length. Hair loss on the scalp was occasionally seen in children and progressed with age (Fig. 1A and fig. S1). Histopathological analysis revealed abnormal morphology of hair follicles and dystrophy and fragility of the hairs in analyzed individuals (Fig. 1, B to D).

The parents of affected individuals were normal, and the segregation frequency suggested an autosomal-recessive form of inheritance. We conducted primary genotyping in Mari families with a set of STR (simple tandem repeat) markers

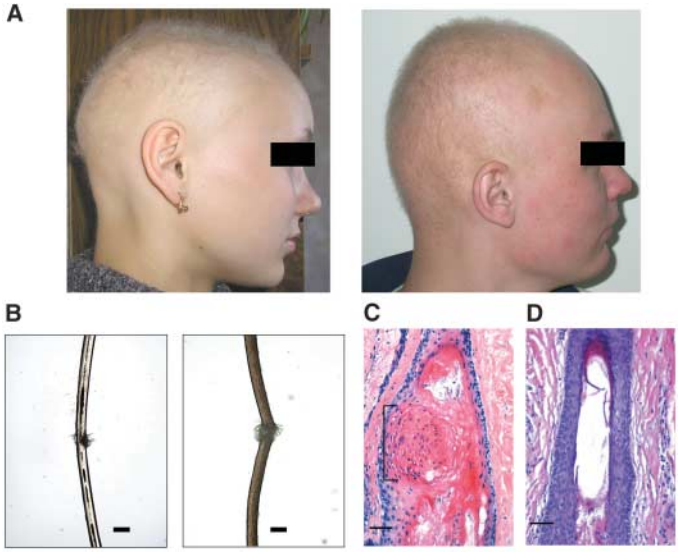

Fig. 1. Clinical presentation of hair growth defect and alopecia in Chuvash individuals. (**A**) Example of hypotrichosis and alopecia in a female adolescent (left) and a male adolescent (right). Note the sparse and short hairs on the scalp (shown with permission from the subjects). The phenotype is variable in males and females of different ages and can progresses to alopecia in adults. (**B**) Hair fibers from affected individuals showed common dystrophic structural alterations and signs of fracture and fragility. Scale bars, 100 μm. (**C** and **D**) Hair follicle histology in an affected individual (C) and in an unaffected control subject (D). Scale bars, 50 μm. In many follicles, the lower follicular infundibulum above the insertion of the sebaceous gland shows marked dilation with epithelial thinning and abnormal keratinization (brackets). There is a loss of the normal granular layer, with premature differentiation of the epithelium and a remarkable parakeratotic plug.

[1]Brudnick Neuropsychiatric Research Institute, Department of Psychiatry, University of Massachusetts Medical School, 303 Belmont Street, Worcester, MA 01604, USA. [2]Laboratory of Molecular Brain Genetics, Research Center of Mental Health, Russian Academy of Medical Sciences (RAMS), 113152, Moscow, Russian Federation (RF). [3]Lomonosov Moscow State University, Faculty of Bioengineering and Bioinformatics, 119992, Moscow, RF. [4]National Research Center for Medical Genetics, RAMS, RF. [5]GUZ President's Prenatal Center of Chuvash Republic, Cheboksary, Uritsky Street 43, RF. [6]Ministry of Health and Social Development of Chuvash Republic, Cheboksary, Uritsky Street 43, RF. [7]Department of Cancer Biology and Pathology, University of Massachusetts Medical School, Worcester, MA 01605, USA. [8]Vavilov Institute of General Genetics, Russian Academy of Sciences, Moscow, RF.

*To whom correspondence should be addressed. E-mail: Evgeny.Rogaev@umassmed.edu

selected arbitrarily or from loci implicated in hair defects of humans or rodents. This analysis revealed a potential linkage of the disorder to chromosome 3q26-27. Subsequent homozygous mapping in Mari families with known STR markers in this chromosomal region localized the mutant gene to a ~2.26-cM interval between D3S1617 and D3S3583 (Fig. 2A and figs. S2 to S4). The mapped interval contained 17 annotated genes, none of which had been previously implicated in hair growth, and some of the genes were excluded by direct mutation analysis of affected individuals. The discovery of shared common STR haplotypes on 3q27 in unrelated affected individuals indicated that the mutation in the two populations likely arose from a common founder. We speculated that an examination of high-density STR maps on mutant chromosomes of individuals that are separated by many generations might critically shorten the genomic interval. We isolated novel STRs and performed genotyping of 17 STR markers overlapping ~5 cM between D3S1571 and D3S1262. Maximum two-point logarithm of the odds ratio for linkage (lod) scores were found for two markers, (CA5) (Z_{max} = 11.98, θ = 0.00) and D3S1530 (Z_{max} = 9.09, θ = 0.00), located near each other. The analysis of shared and recombinant haplotypes in Mari families assigned the mutant gene to the 0.89-cM interval flanked by the D3S3592 and D3S1530 markers (Fig. 2 and fig. S4). By combining these data with the haplotypes in Chuvash families, we localized the gene to a

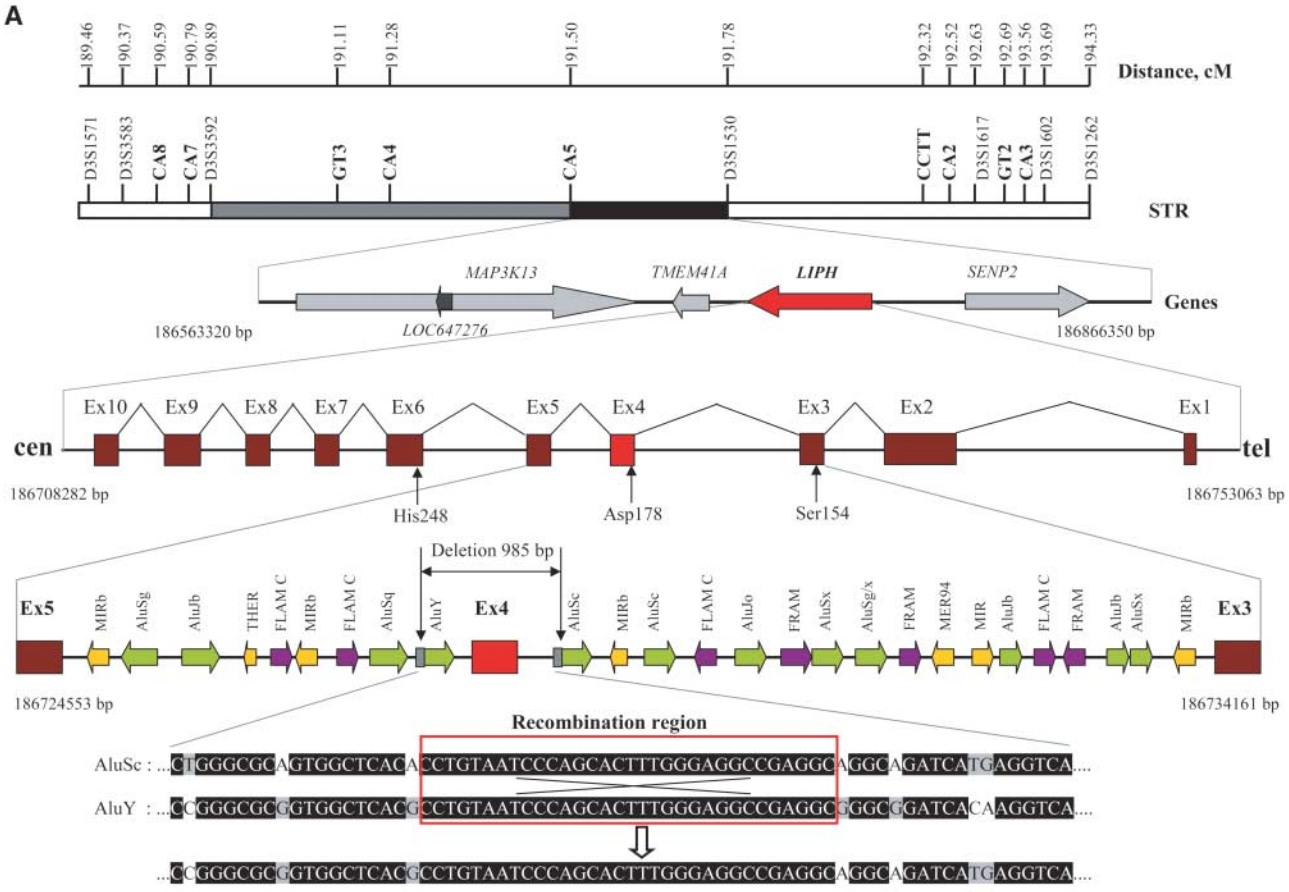

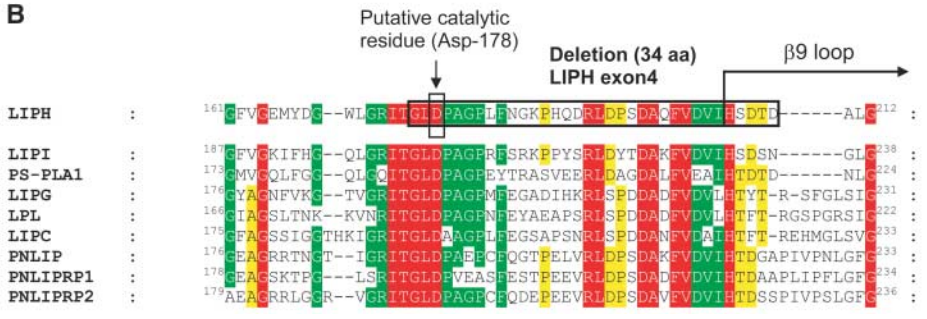

Fig. 2. Identification of a mutant gene for hypotrichosis by positional cloning. (**A**) The STR genotyping identified a linkage to the 3q27 region. The genetic map and genes located in the genomic region are shown. The markers in bold are STR markers newly identified in this study. The recombination events define (CA5) as centromeric and D3S1530 as telomeric boundaries of the minimal genetic interval. The gray and black bars span the haplotypes shared by Mari mutant carriers, and the black bar denotes the region for haplotypes shared by all affected individuals in the Mari and Chuvash populations. Four protein-coding genes and a transcribed sequence (*LOC647276*) were annotated in this region. Sequence analysis of the *LIPH* gene revealed that exon 4 and flanking intronic sequences were deleted in affected individuals. The locations of sites for putative catalytic amino acid residues in *LIPH* exons are shown by arrows. Introns 3 and 5 contain multiple copies of SINEs. Shown is an uneven recombination event between Alu repeat copies leading to the deletion. (**B**) Alignment of LIPH amino acid sequence with other members of the lipase family. Human paralogous genes are presented in the alignment. Exon 4 encodes a highly conserved domain containing evolutionarily invariant amino acid residues. The Asp[178] (exon 4), Ser[154] (exon 3), and His[248] (exon 6) of LIPH belong to a catalytic triad conserved in lipases (fig. S7). LIPH, NP_640341; LIPI, NP_945347; PS-PLA1, NP_056984; LIPG, NP_006024; LPL, NP_000228; LIPC, NP_000227; PNLIP, NP_000927; PNLIPRP1, NP_006220; PNLIPRP2, NP_005387.

~350-kb region encompassing four protein-coding genes (*MAP3K13*, *TMEM41A*, *LIPH*, and *SENP2*) (Fig. 2).

We sequenced the entire coding regions of the *MAP3K13*, *TMEM41A*, *SENP2*, and *LIPH* genes, including exon-intron junctions, in selected affected individuals and found no disease-associated mutations. We noted, however, that exon 4 of the *LIPH* gene was not amplified from DNA samples of affected individuals using flanking intronic polymerase chain reaction (PCR) primers. A PCR product derived from *LIPH* exon 4 was detected in the parents but not in any affected individuals, suggesting that the deletion of exon 4 existed in a heterozygous state in the parents and in a homozygous state in individuals with hypotrichosis.

To map the deletion breakpoints, we designed a series of primers in the genomic region between exon 3 and exon 5, generated PCR products of mutant alleles harboring the deletion, and performed direct sequencing. This mapping of breakpoints determined that a ~985-bp deletion eliminates exon 4 and flanking intronic sequences. We then examined all families and confirmed this deletion in the homozygous state in affected individuals and in the heterozygous state in their parents (Figs. 2 and 3). The genomic region between exon 3 and exon 5 is unusually densely saturated by SINE (short interspersed nuclear element) repeats dispersed in the human genome (*10*). Sequencing of PCR products from the deletion and from wild-type alleles predicts that the deletion is a result of unequal recombination between copies of Alu retrotransposons flanking exon 4. The recombination event presumably occurred between highly homologous 5′ regions of the two members of distant subfamilies of Alu elements (Fig. 2A).

To determine the frequency of the mutant allele, we tested 2292 chromosomes in population samples collected irrespective of the hypotrichosis phenotype from Volga-Ural and other regions of Russia. As anticipated, we found heterozygous individuals with the *LIPH* deletion in populations of Chuvash (the mutant allele frequency $P = 0.033$) and Mari ($P = 0.030$) origin. No mutant allele was found in other Finno-Ugric populations (Udmurths) or Russian populations from distant geographic regions. The data suggest that there are more than 98,000 heterozygous mutant carriers and 1,500 homozygous affected individuals in populations of Mari and Chuvash descent. The number of mutation carriers in this region may be higher because of the mutant gene flow to other ethnic groups (SOM Text).

Deletion of exon 4 does not alter the reading frame of the *LIPH* gene; however, the deletion eliminates an evolutionarily conserved domain in the predicted protein (Fig. 2 and figs. S6 and S7). The protein product, lipase H (alternatively called mPA-PLA$_1\alpha$), has a striking sequence similarity to phospholipases and members of the large triglyceride lipase family. Like all lipases, lipase H contains a putative catalytic amino acid triad: Ser^{154}, Asp^{178}, and His^{248} (*11*, *12*). Replacement of the amino acid triad residues by site-directed mutagenesis abolishes enzymatic activity of lipases (*12*–*15*). The *LIPH* mutation associated with hypotrichosis deletes the critical Asp^{178}, as well as several other evolutionarily conserved amino acid residues (Fig. 2B and fig. S7).

It has been postulated that phospholipases generate lysophosphatidic acids (LPA, 1- or 2-

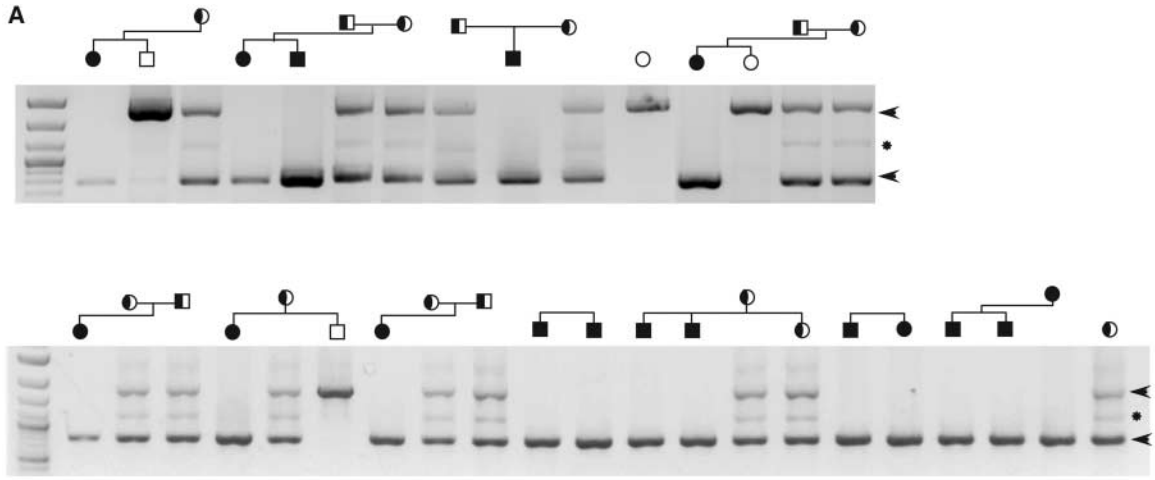

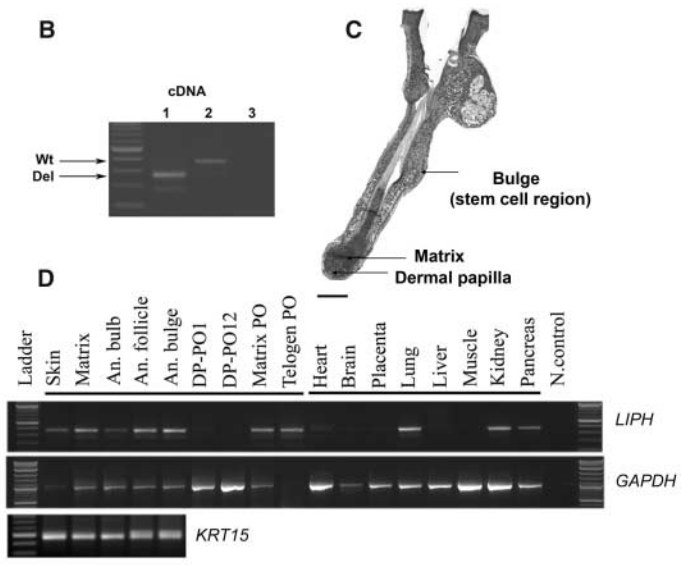

Fig. 3. (**A**) Examples of *LIPH* exon 4 deletion identified in affected individuals in Mari (upper panel) and Chuvash (lower panel) populations. PCR fragments in agarose gels are shown. Arrows indicate the upper band representing a normal allele and the lower band of the mutant deletion allele. *, heteroduplex PCR fragment observed in heterozygotes. All affected individuals are homozygous for exon 4 deletion. (**B**) Reverse transcription PCR (RT-PCR) analysis shows *LIPH* transcript missing exon 4 in cultured hair follicle bulge keratinocytes from an affected individual (lane 1), *LIPH* wild-type transcript (lane 2), and negative control (no template) (lane 3). (**C**) Microphotograph of hair follicle showing sections used for RNA preparation. Scale bar, 100 μm. (**D**) Semiquantitative RT-PCR analysis of *LIPH* mRNA in the hair follicles in comparison with other tissues. The *KRT15* (*keratin 15*) gene highly expressed in hair follicles and the *GAPDH* (*glyceraldehyde-3-phosphate dehydrogenase*) housekeeping gene were used as controls. Prominent expression of *LIPH* was observed in a hair follicle bulge in anagen (an. bulge), the active phase of hair growth, but not in dermal papilla (DP) (see also supporting online material and fig. S8).

acyl-lysophosphatidic acids) from phospholipids (*16*, *17*). LPA has been described as an extracellular mediator of many biological functions, such as proliferation, antiapoptotic activity, and cytoskeletal organization, and appears to signal through at least five members of a family of G protein–coupled receptors (*12*, *17*–*22*). Lipase H is highly homologous to lipase I (*LIPI*) and phosphatidylserine-specific phospholipase A1 (*PS-PLA1*). These three proteins also share common structures of short lid domains and partially deleted β9 loop domains that probably determine the specificity of their phospholipase activity in the production of LPA (*14*, *23*) (figs. S7 and S9).

To elucidate whether the *LIPH* gene is expressed in hair follicle development, we analyzed mRNA transcripts isolated from human hair follicles and other tissues. The expression of *LIPH,* but not *LIPI* and *PS-PLA1*, was prominent in hair follicles, including the stem cell–rich bulge region (Fig. 3 and fig. S8). These data further indicate the importance of *LIPH* in normal hair formation and growth.

The physiological function of LIPH has not yet been elucidated. We speculate that intragenic deletion of the *LIPH* (loss-of-function mutation) abolishes the enzymatic activity of lipase H and diminishes the production of LPA mediators in hair follicles. Such lipid mediators may affect the migration, differentiation, or proliferation of keratinocytes, culminating in arrest of hair growth (fig. S9). However, LPA-independent mechanisms and other activities, for example, intracellular functioning of LIPH, cannot be ruled out. Like age-related hair loss in the general population, the hypotrichosis and alopecia described here are not associated with other pathologies, and they progress with age. The identification of a genetic defect in *LIPH* suggests that this enzyme regulates hair growth and therefore may be a potential target for the development of a therapeutic agent for the control of hair loss or growth.

References and Notes

1. R. Paus, G. Cotsarelis, *N. Engl. J. Med.* **341**, 491 (1999).
2. G. Cotsarelis, T. T. Sun, R. M. Lavker, *Cell* **61**, 1329 (1990).
3. S. Lyle *et al.*, *J. Cell Sci.* **111**, 3179 (1998).
4. K. A. Moore, I. R. Lemischka, *Science* **311**, 1880 (2006).
5. W. Ahmad *et al.*, *Science* **279**, 720 (1998).
6. A. Kljuic *et al.*, *Cell* **113**, 249 (2003).
7. E. Levy-Nissenbaum *et al.*, *Nat. Genet.* **34**, 151 (2003).
8. E. I. Rogaev, R. A. Zinchenko, G. Dvoryachikov, T. Sherbatich, E. K. Ginter, *Lancet* **354**, 1097 (1999).
9. Online Mendelian Inheritance in Man, OMIM database 604379 (www.ncbi.nlm.nih.gov/entrez/dispomim.cgi?id=604379).
10. E. S. Lander *et al.*, *Nature* **409**, 860 (2001).
11. W. Jin, U. C. Broedl, H. Monajemi, J. M. Glick, D. J. Rader, *Genomics* **80**, 268 (2002).
12. H. Sonoda *et al.*, *J. Biol. Chem.* **277**, 34254 (2002).
13. M. Hiraoka, A. Abe, J. A. Shayman, *J. Lipid Res.* **46**, 2441 (2005).
14. T. Hiramatsu *et al.*, *J. Biol. Chem.* **278**, 49438 (2003).
15. R. J. Kubiak *et al.*, *Biochemistry* **40**, 5422 (2001).
16. J. Aoki *et al.*, *Biochim. Biophys. Acta* **1582**, 26 (2002).
17. J. Aoki, *Semin. Cell Dev. Biol.* **15**, 477 (2004).
18. K. Bandoh *et al.*, *J. Biol. Chem.* **274**, 27776 (1999).
19. F. N. van Leeuwen, B. Giepmans, L. van Meeteren, W. Moolenaar, *Biochem. Soc. Trans.* **31**, 1209 (2003).
20. G. A. Piazza, J. L. Ritter, C. A. Baracka, *Exp. Cell Res.* **216**, 51 (1995).
21. W. H. Moolenaar, L. A. van Meeteren, B. N. Giepmans, *Bioessays* **26**, 870 (2004).
22. S. Choi, M. Lee, A. L. Shiu, S. J. Yo, G. W. Aponte, *Am. J. Physiol. Gastrointest. Liver Physiol*., published online 24 August 2006, 10.1152/ajpgi.00295.2006.
23. F. Carriere *et al.*, *Biochim. Biophys. Acta* **1376**, 417 (1998).

24. We thank the study participants; colleagues who assisted in evaluation of the patients; V. Nikishina and O. Plotnikova for technical support; and S. Borinskaya, N. Yankovsky, and E. Khusnutdinova for providing some of the population DNA samples. The project was supported in part by a program of the Presidium of the Russian Academy of Sciences, "Biodiversity and Dynamics of Gene Pools" (to E.I.R.). S.L. was supported by NIH K08-AR02179 and the Ellison Medical Foundation. The collection of blood samples was approved by the Institutional Review Board (IRB) and Ethical Committee of the Center of Medical Genetics (Moscow), with informed consent obtained from all affected individuals and their relatives.

Supporting Online Material

www.sciencemag.org/cgi/content/full/314/5801/982/DC1
Materials and Methods
SOM Text
Figs. S1 to S10
Table S1
References

1 August 2006; accepted 6 October 2006
10.1126/science.1133276

Microtubule-Severing Activity of *Shigella* Is Pivotal for Intercellular Spreading

Sei Yoshida,[1,4] Yutaka Handa,[1,4] Toshihiko Suzuki,[1,4] Michinaga Ogawa,[1,4] Masato Suzuki,[1,4] Asuka Tamai,[5] Akio Abe,[5] Eisaku Katayama,[2] Chihiro Sasakawa[1,3,4]*

Some pathogenic bacteria actually invade the cytoplasm of their target host cells. Invasive bacteria acquire the propulsive force to move by recruiting actin and inducing its polymerization. Here we show that *Shigella* movement within the cytoplasm was severely hindered by microtubules and that the bacteria destroyed surrounding microtubules by secreting VirA by means of the type III secretion system. Degradation of microtubules by VirA was dependent on its α-tubulin–specific cysteine protease–like activity. *virA* mutants did not move within the host cytoplasm and failed to move into adjacent cells.

Cytoplasm-invading pathogens, including *Shigella* (*1*–*3*), *Listeria monocytogenes* (*4*–*6*), the spotted-fever group *Rickettsia* (*7*–*9*), *Mycobacterium marinum* (*10*), and *Burkholderia pseudomallei* (*11*, *12*), induce local actin polymerization at one pole of the bacterium, which gives them the propulsive force to move within the cytoplasm and into adjacent host cells, an important bacterial activity for establishing an infectious foothold and for renewing replicative niches. Although the bacterial proteins involved in mediating actin polymerization differ, they share the ability to recruit and activate actin-related proteins 2 and 3 in complex (Arp2/3) in the vicinity of the bacterial surface, which induces local actin polymerization (*13*–*15*). The actin-based motility of *Shigella* is mediated by the special interplay between an outer membrane protein, VirG (IcsA), and the neural Wiskott-Aldrich syndrome protein (N-WASP) (*16*, *17*). When VirG and Cdc42 bind to N-WASP, N-WASP becomes activated and, in turn, recruits the Arp2/3 complex (*17*, *18*).

The rate of motility and direction of movement of pathogens within the host cytoplasm, however, is highly variable and depends on the stage of bacterial multiplication and location in the host cell (*19*). The bacterial movement behavior of motile *Shigella* is heterogeneous: Some bacteria suddenly change direction, spin around, or stop moving within the cytoplasm, independent of bacterial division (fig. S1) (*20*), whereas bacterial movement at the perinuclear surface or along the periphery of the cytoplasm tends to proceed smoothly and rapidly, which suggests that some intracellular structure, such as a subcellular organelle or the cytoskeleton, influences the rate of motility. This notion is supported by studies on *L. monocytogenes*, whose movement in host cells is affected by a subcellular organelle and the cytoskeleton (*21*).

VirA is a *Shigella* effector, secreted by means of the type III secretion system (TTSS), that is

[1]Department of Microbiology and Immunology, [2]Department of Basic Medical Sciences, [3]Department of Infectious Control, International Research Center for Infectious Diseases, Institute of Medical Science, University of Tokyo, 4-6-1, Shirokanedai, Minato-ku, Tokyo 108-8639, Japan. [4]CREST, Japan Science and Technology Corporation (JST). 4-1-8, Honche, Kawaguchi-shi, Saitama 332-0012, Japan. [5]Laboratory of Bacterial Infection, Kitasato Institute for Life Science, Kitasato University, 5-9-1 Shirokane, Minato-ku, Tokyo 108-8641, Japan.

*To whom correspondence should be addressed. E-mail: sasakawa@ims.u-tokyo.ac.jp

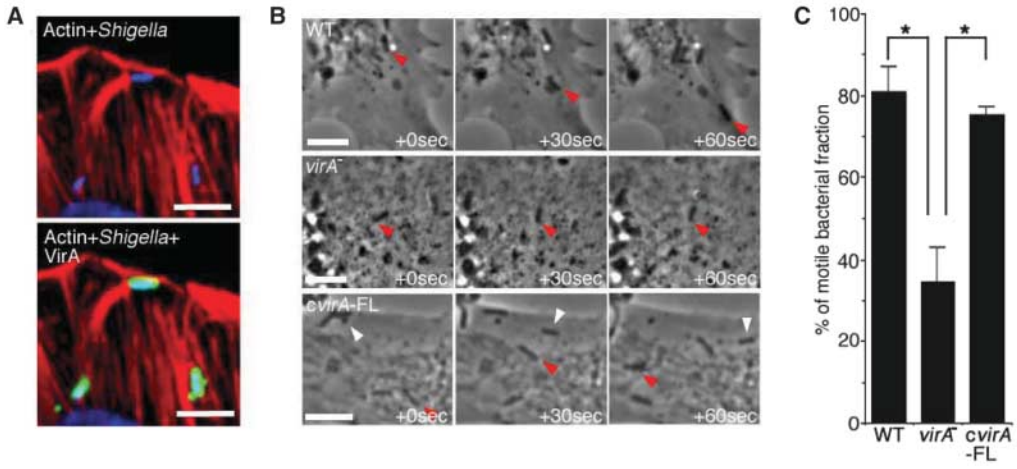

Fig. 1. VirA activity facilitates bacterial movement. (**A**) COS-7 cells were infected with *Shigella* and stained for DNA with TOPRO-3 to identify the bacteria (blue), with rhodamine-phalloidin for actin (red) and with a VirA-specific antibody for VirA (green). Scale bar, 5 μm. (**B**) COS-7 cells were infected with the WT (WT), the *virA* mutant (*virA*$^{-}$), or the full-length VirA complementation strain (c*virA*-FL), and the movement of each strain in the cells was observed. Arrowheads indicate bacteria. Scale bar, 5 μm. (**C**) The fraction of motile bacteria was investigated and its percentage was calculated. *$P < 0.05$.

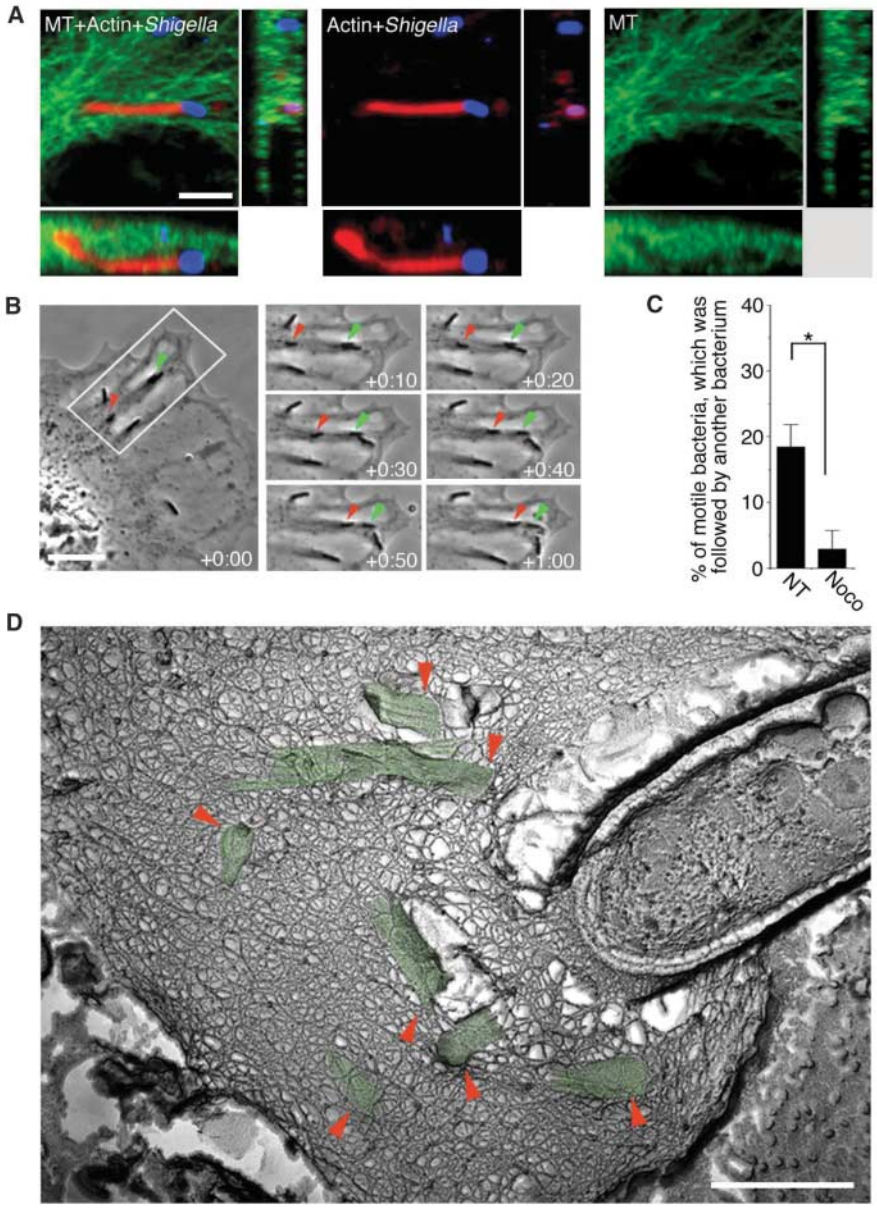

Fig. 2. *Shigella* destroys the host MT network during spreading. (**A**) COS-7 cells were infected with the WT and stained with rhodamine-phalloidin (actin, red), an antibody against *S. flexneri* lipopolysaccharide (*Shigella*, blue), and an antibody against α-tubulin (MT, green). Scale bar, 5 μm. (**B**) COS-7 cells were infected with WT, and the bacterial movement of each in the cells was observed. Arrowheads indicate bacteria. Scale bar, 5 μm. (**C**) Nocodazole-treated (Noco) and untreated (NT) cells were infected. The fraction of motile bacteria under each condition was investigated and its percentage was calculated. *$P < 0.05$. (**D**) FFEM image of the *Shigella*-induced F-actin network and destroyed MTs (red arrowheads, green) in COS-7 cells. Scale bar, 0.2 μm.

required for entry into epithelial cells and subsequent intra- and intercellular spreading (*22*). VirA can interact with the α,β-tubulin heterodimer and can induce microtubule (MT) destabilization in vitro and in vivo (*23*, *24*). VirA expression by *Shigella* is highly responsive to intracellular conditions (*22*, *25*), and *virA* mutants fail to disseminate into adjacent cells, which suggests that VirA plays a pivotal role in promoting the intra- and intercellular spreading of *Shigella* (*22*).

To clarify the role of VirA in the intracellular *Shigella* motility process, we localized VirA secreted by intracellular wild-type *Shigella* (WT) by immunofluorescence microscopy. Around 80 min after bacterial invasion of COS-7 cells, VirA signals were detected on the motile bacterial surface, which formed a long actin tail at one pole of the bacterium (Fig. 1A). We used time-lapse photography to investigate the intracellular behavior of the WT, c*virA*-FL (the *virA* gene was replaced with a cloned full-length *virA* gene), and the *virA* mutant (*virA*$^-$). Although both the WT and c*virA*-FL moved smoothly, *virA*$^-$ occasionally changed direction but did not move (Fig. 1B). Around 80 min after invasion, the *virA* mutant, like the WT, formed a long actin tail (fig. S2A), which suggested that the defect in the motility of *virA*$^-$ was not directly related to the VirG activity required for formation of the actin tail. At this stage of infection, about 80% of the WT and c*virA*-FL were motile, whereas only about 30% of the intracellular *virA* mutant were motile (Fig. 1, B and C). Thus, VirA activity is pivotal for promotion of bacterial motility.

To determine whether cytoplasmic MT structures act as a physical barrier to bacterial movement, COS-7 cells pretreated with the MT-destabilizing drug nocodazole were infected with the *virA* mutant. Although the motile WT population in COS-7 cells treated with or without nocodazole was ~60%, the motile *virA* mutant population in the cells treated with nocodazole was as high as ~60%, compared with ~20% in the untreated cells (fig. S2, B and C). The movement of the WT in the COS-7 cells occasionally followed a zigzag path. At some point the bacterial movement would stop, and the bacteria would change direction (+20 and 30 s) and continue to move within the cytoplasm (+40 s) (fig. S1A). The bacterial movement in cells pretreated with nocodazole, however, became smooth (fig. S1B). Bacterial movement in the cytoplasm of COS-7 treated with nocodazole tended to proceed smoothly by sliding, without stopping, in contrast to the movement in the cells not treated with nocodazole. The highest speed in the cells not treated with nocodazole was 0.68 μm/s, and the slowest speed was 0.08 μm/s (fig. S1C), whereas the highest speed in the cells treated with nocodazole was 0.48 μm/s, and the lowest speed was 0.13 μm/s (fig. S1D). Clearly, the speed with which *Shigella* moved in the cytoplasm exhibited greater variation in cells not treated with nocodazole. The standard deviation of the speed of the WT in the untreated cells was significantly greater than in the cells treated with nocodazole (fig. S1E). By contrast, when COS-7 cells were treated with taxol, an agent that freezes MT instability, the distribution of the standard deviation of the bacterial speed in COS-7 cells was not substantially different (fig. S1F).

To further characterize bacterial movement within the cytoplasm, we examined COS-7 cells infected with WT by immunofluorescence confocal microscopy, 80 min after invasion. In some areas of bacterial movement within the cytoplasm, MTs were lacking (Fig. 2A). The tunnel-like area created through the MT networks behind the bacteria corresponded to the area where the actin tail of the motile bacterium had formed (Fig. 2A and fig. S3). A tunnel-like area created behind motile *Shigella* was also observed in other cell lines (fig. S3). When we viewed motile bacteria by time-lapse photography, they occasionally followed the same course as created by the bacterium ahead of them (Fig. 2B). After 80 to 120 min after invasion, ~20% of motile bacteria were followed by another bacterium along the same course, whereas only 3% of motile bacteria in the cells pretreated with nocodazole were followed by another bacterium along the same course (Fig. 2C). Thus, the tunnel created by the first motile bacterium facilitates the movement of the second. We then performed freeze-fracture electron microscopy (FFEM) to further characterize the tunnel-like zone visualized by MT staining (*20*). Fragmented structures (Fig. 2D) were frequently detected within the actin tail created by motile *Shigella*, which resembled the characteristic MT structure (see also below); this observation strongly suggested that motile *Shigella* could break down surrounding MTs as it moves. Indeed, when motile *Shigella* were quadruple stained for F-actin, bacterium, MTs, and VirA and examined by confocal immunofluorescence microscopy, the VirA signal was detected on the bacterial surface, where the local MTs surrounding the bacterium had been destroyed (fig. S4).

The VirA-treated MTs underwent severe segmentation and appeared much rougher than the MTs incubated with buffer alone (Fig. 3, A and B). Both the VirA-treated MTs and the fragmented structures detected in the *Shigella* actin tail were composed of six strips, a characteristic of MTs (Fig. 3, B to D), which suggests that the VirA protein secreted by motile *Shigella* was involved in breaking down the surrounding MTs as the bacteria moved.

Because the distinctive two-dimensional structure resembled that of a group of cysteine peptidases known as the Clan CA family (Fig. 4A) (*26*, *27*), we investigated whether VirA acts

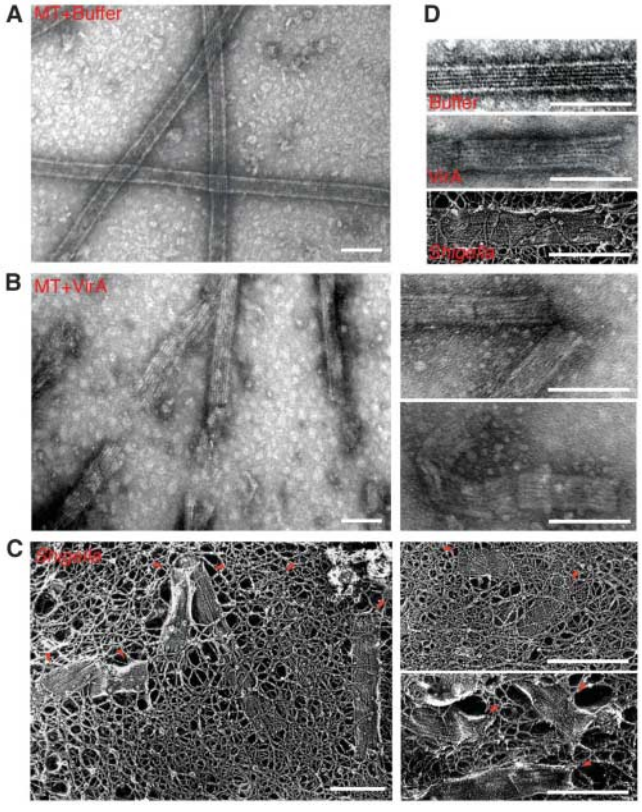

Fig. 3. VirA secreted from motile *Shigella* destroys surrounding MTs. (**A**) Electron microscopic (EM) image of the MTs in vitro. (**B**) EM images of the VirA-treated MTs in vitro. (**C**) FFEM images of the *Shigella*-induced F-actin network and destroyed MTs (red arrowheads) in COS-7 cells. (**D**) Comparison between the EM image of the VirA-treated MTs (middle) and FFEM image of *Shigella*-induced MT destruction (bottom). EM image of MTs treated with buffer alone (top) as a control. The twice-cycled MT proteins that contained MAPs (microtubule-associated proteins, known as MT-stabilizing factors) prepared from bovine brain lysates were used in (A) and (B). After inducing the polymerization, MTs were incubated with VirA proteins, which were purified from the glutathione *S*-transferase fusion protein GST-VirA, in PIPES-based buffer containing 1.3 M glycerol (*23*) at 37°C for 30 min, and analyzed by EM (*20*, *23*). Scale bar, 0.1 μm.

as a cysteine protease. β-Tubulin was reproducibly precipitated by VirA-specific antibody, but α-tubulin was not (Fig. 4B) (*23*). α-Tubulin was highly degraded, but β-tubulin was not degraded at all, when tubulin was incubated with VirA-FL (full-length VirA) in the protease buffer for 120 min (Fig. 4, C and D). To confirm the cysteine protease–like activity of VirA, cysteine 34 was replaced by serine (VirA-C34S), and VirA-C34S was tested for its ability to degrade α-tubulin by incubating tubulin heterodimer under the same conditions. The immunoprecipitation assay with VirA-specific antibody indicated that both α-tubulin and β-tubulin interacted with VirA-C34S but that α-tubulin was degraded less efficiently than VirA-FL (Fig. 4B). Indeed, when tubulin was incubated with VirA-FL or VirA-C34S in the protease buffer for 120 min, VirA-FL resulted in greater degradation of α-tubulin than VirA-C34S (Fig. 4E). When leupeptin, a serine and cysteine protease inhibitor, was added to the assay medium under the same conditions, VirA-FL activity was completely inhibited (Fig. 4F). Although less effective than leupeptin, another cysteine protease inhibitor, cystatin C, also inhibited the degradation of α-tubulin by VirA

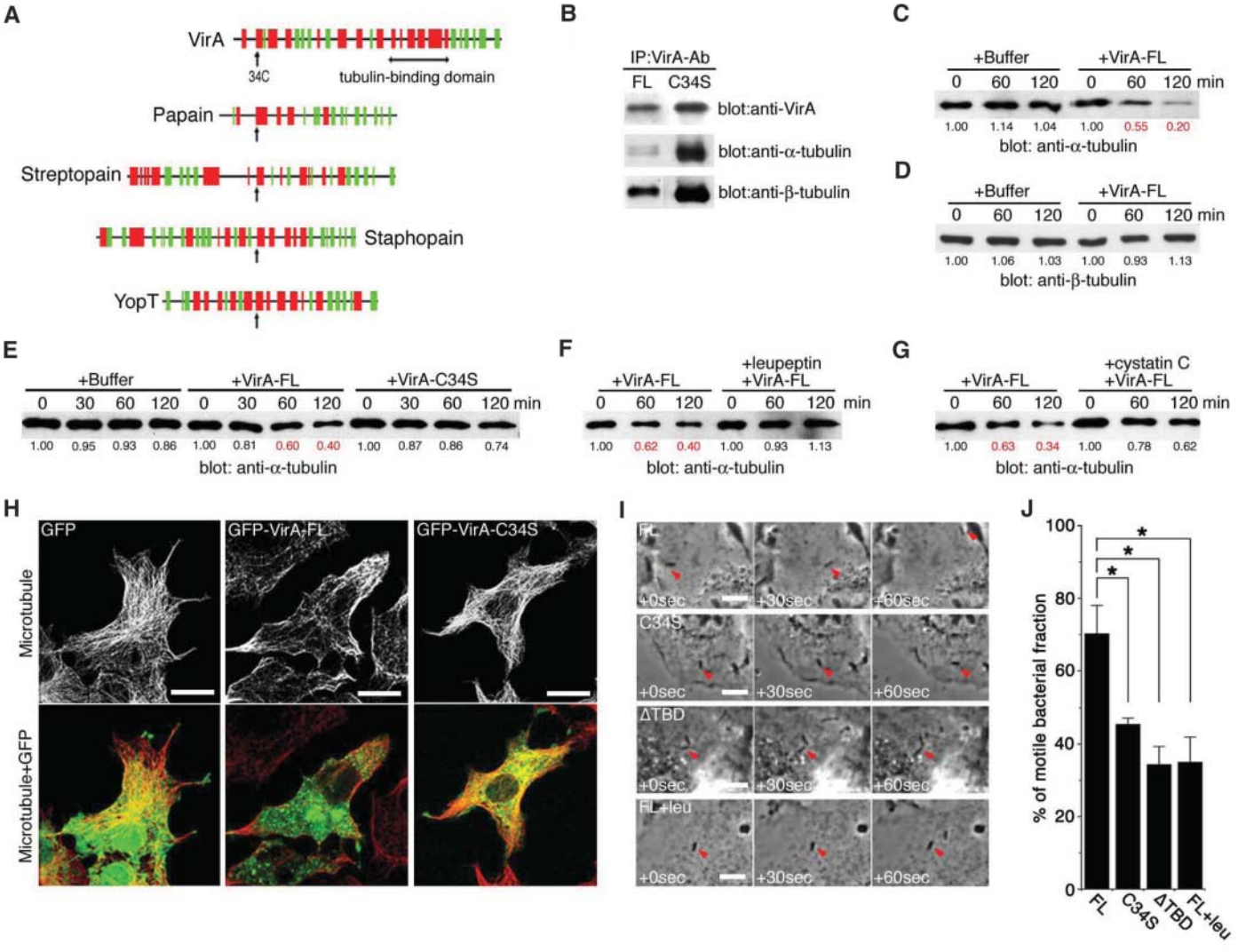

Fig. 4. VirA has cysteine protease–like activity and a critical cysteine residue. (**A**) Comparison of the secondary structure profile of VirA and of the CA clan of cysteine proteases, papain, streptopain, staphopain, and YopT, using the 3D-PSSM protein folding recognition server (*30*). The red box represents the α helix, and the green box represents the β sheet. "34C" indicates Cys^{34}, which is located at the start of a major α helix. (**B**) Purified human tubulin (0.5 μM) (HeLa cells) heterodimer (composed of α- and β-tubulin) was mixed with purified VirA-FL (1 μM) or VirA-C34S (1 μM) in a protease assay buffer [20 mM Hepes, pH 7.4, 10 mM DTT, 0.1% CHAPS, 10% sucrose, 1 mM 4-(2-aminoethyl) benzenesulfonyl fluoride hydrochloride (AEBSF)] on ice. After incubation at 37°C for 3 hours, the mixture was immunoprecipitated with VirA-specific antibody at 4°C overnight, and the immunoprecipitates were subjected to immunoblotting. (**C**) After mixing 1 μM tubulin and 1 μM VirA-FL, they were incubated at 37°C for 60 or 120 min, and samples were analyzed by immunoblotting with an antibody against α-tubulin. (**D**) Same as in (C), but an antibody against β-tubulin was used. The numbers below the images are the result of the NIH image analysis. (**E**) After mixing 1 μM tubulin with 1 μM VirA-FL or 1 μM VirA-C34S, the mixture was incubated at 37°C for 60 or 120 min, and analyzed by immunoblotting with an antibody against α-tubulin. The blots were quantified by measuring relative intensity with NIH-image software version 1.63, and the values are indicated below the images. (**F** and **G**) After mixing 1 μM tubulin, 1 μM VirA-FL, and leupeptin (100 μg/ml) (F) or cystatin C (1 μM) (G) in a plastic well, they were incubated at 37°C for 60 or 120 min and analyzed by immunoblotting with an antibody against α-tubulin. The numbers below the images are the results of NIH image analysis. (**H**) GFP–VirA-FL or GFP–VirA-C34S was expressed in COS-7 cells. After fixation, the cells were subjected to immunofluorescence staining. Scale bar, 10 μm. (**I**) COS-7 cells were infected with *cvirA*-FL (FL), *cvirA*-C34S (C34S), and *cvirA*-ΔTBD (ΔTBD); leupeptin-treated COS-7 cells were infected with *cvirA*-FL (FL+leu). Movement of each of the bacteria in the cells was observed. Arrowheads indicate bacteria. Scale bar, 5 μm. (**J**) The percentage of the motile bacterial fraction of (I) was calculated. *$P < 0.05$.

(Fig. 4G). To confirm the effect of the substitution of serine for cysteine 34 on VirA activity in vivo, we investigated the MT structure of COS-7 cells transfected with green fluorescent protein pGFP–VirA-FL or pGFP–VirA-C34S (*20*). The MT networks were severely disrupted in the COS-7 cells transiently expressing GFP–VirA-FL, but not in those expressing GFP–VirA-C34S (Fig. 4H). Indeed, when cell lysates containing GFP–VirA-FL or GFP–VirA-C34S were pulled down by GFP-specific antibody, more α-tubulin and β-tubulin were precipitated by GFP–VirA-C34S than by GFP–VirA-FL. Consistent with these results, time-lapse photography showed that the motility rate of *Shigella* expressing VirA-C34S (c*virA*-C34S, the VirA-C34S complementation strain) in COS-7 cells was less than that of c*virA*-FL (Fig. 4, I and J). Because the portion of VirA encompassing residues 224 through 315 [tubulin-binding domain (TBD)] (Fig. 4A) has been shown to be involved in interaction with tubulin in vitro (*23*), we created a VirA-ΔTBD complementation strain (c*virA*-ΔTBD) and investigated intracellular movement. The bacterial motility rate of c*virA*-ΔTBD was further decreased compared with that of c*virA*-C34S (Fig. 4, I and J). It was also decreased when the cells were treated with leupeptin (Fig. 4, I and J), which demonstrated that VirA-protease–like activity was important for promoting intracellular bacterial movement.

To establish the in vivo role of VirA in bacterial infection, C57BL/6 mice were intranasally infected with 5×10^7 CFU of the WT, the *virA*$^-$, c*virA*, c*virA*-C34S, or TTSS-deficient mutant (*20*). Each mouse was weighed after bacterial infection, and the survival rate was calculated (fig. S5). Although 100% of the mice were killed by the WT by day 9, none were killed by the *virA*$^-$ or TTSS-deficient mutant. Although 100% of the mice were killed by c*virA* under the same conditions, only 60% were killed by c*virA*-C34S. Thus, the VirA activity that degrades MT contributes to *Shigella*'s pathogenicity and that the cysteine 34 of VirA is a crucial residue for its activity.

It is noteworthy that *L. monocytogenes* can recruit Op18 (stathmin), an MT-sequestering host protein (*28*), in the vicinity of the bacterial surface in infected host cells (*29*). Perhaps the Op18 recruited by intracellular *L. monocytogenes* causes local destruction of MTs surrounding the bacterium, and that facilitates bacterial movement.

In conclusion, the ability of VirA to degrade MTs by means of cysteine protease–like activity is critical to the intra- and intercellular spreading by intracellular *Shigella* that leads to bacillary dysentery, even though host-cell MT structures obstruct bacterial movement (fig. S6).

References and Notes

1. S. Makino, C. Sasakawa, K. Kamata, M. Yoshikawa, *Cell* **46**, 551 (1986).
2. M. L. Bernardini, J. Mounier, H. D'Hauteville, P. J. Sansonetti, *Proc. Natl. Acad. Sci. U.S.A.* **86**, 3867 (1989).
3. M.-C. Lett *et al.*, *J. Bacteriol.* **171**, 353 (1989).
4. L. G. Tilney, D. A. Portonoy, *J. Cell Biol.* **109**, 1597 (1989).
5. E. Domann *et al.*, *EMBO J.* **11**, 1981 (1992).
6. C. Kocks *et al.*, *Cell* **68**, 521 (1992).
7. N. Teysseire, C. Chiche-Portiche, D. Raoult, *Res. Microbiol.* **143**, 821 (1992).
8. R. A. Heinzen, S. F. Hayes, M. G. Peacock, T. Hackstadt, *Infect. Immun.* **61**, 1926 (1993).
9. E. Gouin *et al.*, *Nature* **427**, 457 (2004).
10. L. M. Stamm *et al.*, *J. Exp. Med.* **198**, 1361 (2003).
11. W. Kespichayawattana, S. Rattanachetkul, T. Wanun, U. Utaisincharoen, S. Sirisnha, *Infect. Immun.* **68**, 5377 (2000).
12. K. Breitbach *et al.*, *Cell. Microbiol.* **5**, 385 (2003).
13. D. Pantaloni, C. L. Clainche, M.-F. Carlier, *Science* **292**, 1502 (2001).
14. F. Frischknecht, M. Way, *Trends Cell Biol.* **11**, 30 (2001).
15. E. Gouin, M. D. Welch, P. Cossart, *Curr. Opin. Microbiol.* **8**, 35 (2005).
16. T. Suzuki, H. Miki, T. Takenawa, C. Sasakawa, *EMBO J.* **17**, 2767 (1998).
17. C. Egile *et al.*, *J. Cell Biol.* **146**, 1319 (1999).
18. T. Suzuki *et al.*, *J. Exp. Med.* **191**, 1905 (2000).
19. H. Ogawa, A. Nakamura, R. Nakaya, *Jpn. J. Med. Sci. Biol.* **21**, 259 (1968).
20. Materials and methods are available as supporting material on *Science* Online.
21. P. A. Giardini, J. A. Theriot, *Biophys. J.* **81**, 3193 (2001).
22. K. Uchiya *et al.*, *Mol. Microbiol.* **17**, 241 (1995).
23. S. Yoshida *et al.*, *EMBO J.* **21**, 2923 (2002).
24. S. Yoshida, C. Sasakawa, *Trends Microbiol.* **11**, 139 (2003).
25. B. Demers, P. J. Sansonetti, C. Parsot, *EMBO J.* **17**, 2894 (1998).
26. A. J. Barrett, N. D. Rawlings, *Biol. Chem.* **382**, 727 (2001).
27. V. Turk, B. Turk, D. Turk, *EMBO J.* **20**, 4629 (2001).
28. L. Cassimeris, *Curr. Opin. Cell Biol.* **14**, 18 (2002).
29. T. Pfeuffer, W. Goebel, J. Laubinger, M. Bachmann, M. Kuhn, *Cell. Microbiol.* **2**, 101 (2000).
30. The 3D-PSSM protein folding recognition server (www.sbg.bio.ic.ac.uk/~3dpssm).

Supporting Online Material

www.sciencemag.org/cgi/content/full/314/5801/985/DC1
Materials and Methods
Figs. S1 to S6
References

28 July 2006; accepted 29 September 2006
10.1126/science.1133174

HTRA1 Promoter Polymorphism in Wet Age-Related Macular Degeneration

Andrew DeWan,[1] Mugen Liu,[2]* Stephen Hartman,[3]* Samuel Shao-Min Zhang,[2]* David T. L. Liu,[4] Connie Zhao,[5] Pancy O. S. Tam,[4] Wai Man Chan,[4] Dennis S. C. Lam,[4] Michael Snyder,[3] Colin Barnstable,[2] Chi Pui Pang,[4] Josephine Hoh[1,2]†

Age-related macular degeneration (AMD), the most common cause of irreversible vision loss in individuals aged older than 50 years, is classified as either wet (neovascular) or dry (nonneovascular). Inherited variation in the complement factor H gene is a major risk factor for drusen in dry AMD. Here we report that a single-nucleotide polymorphism in the promoter region of *HTRA1*, a serine protease gene on chromosome 10q26, is a major genetic risk factor for wet AMD. A whole-genome association mapping strategy was applied to a Chinese population, yielding a *P* value of $<10^{-11}$. Individuals with the risk-associated genotype were estimated to have a likelihood of developing wet AMD 10 times that of individuals with the wild-type genotype.

Age-related macular degeneration (AMD) is the leading cause of vision loss and blindness among older individuals in the United States and throughout the developed world. It has a complex etiology involving genetic and environmental factors. AMD is broadly classified as either dry (nonneovascular) or wet (neovascular). The dry form is more common and accounts for about 85 to 90% of patients with AMD; it does not typically result in blindness. The primary clinical sign of dry AMD is the presence of soft drusen with indistinct margins (extracellular protein deposits) between the retinal pigment epithelium (RPE) and Bruch's membrane. The large accumulation of these drusen is associated with central geographic atrophy (CGA) and results in blurred central vision. About 10% of AMD patients have the wet form, in which new blood vessels form and break beneath the retina [choroidal neovascularization (CNV)]. This leakage causes permanent damage to surrounding retinal tissue, distorting and destroying central vision. The factors that underlie why some individuals develop the more aggressive wet form of AMD, while others have the slowly progressing dry type, are not yet understood.

Complement factor H (CFH) has been suggested to mediate drusen formation (*1*). In our previous whole-genome association study, in which the presence of large drusen was the primary phenotype under investigation, the CFH Y402H variant, in which Tyr^{402} is replaced by His, was shown to be a major genetic risk factor (*2*). More recently, it has been reported that the highest odds ratio for CFH Y402H was seen for cases with AMD grade 4 (i.e., the presence of CGA) in comparison with AMD grade 1 controls (*3*). An association between AMD and CFH Y402H, as well as other intronic CFH variants, has been demonstrated for more than ten different Caucasian populations (*4*–*7*).

In this report, we present results of investigations aimed at identifying novel genetic variant(s) that predispose individuals to the wet, neovascular AMD phenotype. Unlike our previous studies which were conducted in a Caucasian cohort (*2*), this investigation focused on patients of Asian descent. There were several reasons for this decision. First, epidemiological observations indicate that neovascular AMD is more prevalent among Asians than Caucasians (*8–10*), and the soft indistinct drusen that are characteristic of dry AMD are rarely seen in Asian individuals (*11–13*). Consistent with these clinical observations, the CFH Y402H variant has been shown to occur less frequently in individuals of Japanese and Chinese ancestry (<5%) than in Caucasians (>35%) (*14–16*).

From a cohort of Southeast Asians in Hong Kong, we identified 96 patients previously diagnosed with wet AMD and 130 age-matched control individuals who were AMD-free (*17*, *18*). Retinal fundus photographs were examined from each of the 226 study participants. Indocyanine Green dye angiography was performed to exclude cases with polypoidal choroidal vasculopathy and to verify that CNV (AMD grade 5) was present in all cases (fig. S1). The AMD cases and controls had a mean age of 74 (*19*). Other characteristics of the study population are summarized in table S1.

We conducted a whole-genome association study on this Asian cohort to scan for single nucleotide polymorphisms (SNPs), using previously described genotyping and data-quality surveillance procedures (*2*). Of the 97,824 autosomal SNPs that were informative and passed our quality-control checks (*19*), rs10490924 was the only polymorphism that showed a significant association with AMD when we used the Bonferroni criteria (Table 1). The allele-frequency chi-square test yielded a P value of 4.1×10^{-12} (Fig. 1A and Table 1). The odds ratio was 11.1 (95% confidence interval [CI] 4.83 to 25.69) for those carrying two copies of the risk allele when compared with wild-type homozygotes, but was

[1]Department of Epidemiology and Public Health, Yale University, 60 College Street, New Haven, CT 06520, USA. [2]Department of Ophthalmology and Visual Science, Yale University, 330 Cedar Street, New Haven, CT 06520, USA. [3]Department of Molecular, Cellular, and Developmental Biology, Yale University, 219 Prospect Street, New Haven, CT 06520, USA. [4]Department of Ophthalmology and Visual Sciences, The Chinese University of Hong Kong, Hong Kong, China. [5]Genomics Resource Center, Rockefeller University, 1230 York Avenue, New York, NY 10021, USA.

*These authors contributed equally to this work.
†To whom correspondence should be addressed. E-mail: josephine.hoh@yale.edu

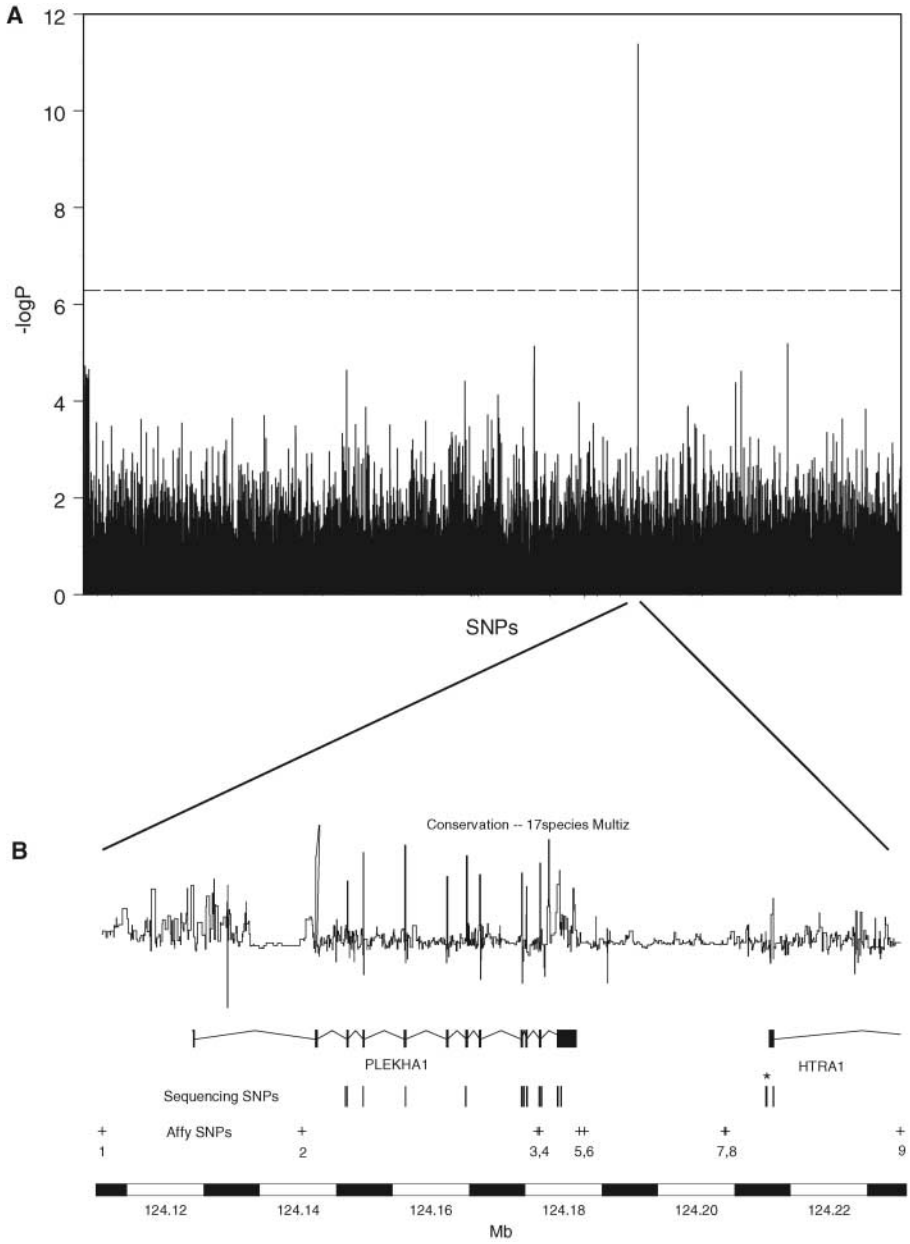

Fig. 1. Genome-wide distribution of P values and characteristics of the associated genomic region. (**A**) Distribution of P values for the SNPs in a whole-genome association study of AMD. P values are plotted as the $-\log_{10}(P)$ with the SNPs in chromosomal order along the x axis. The dashed horizontal line indicates the Bonferroni adjusted threshold for significant association at the 0.05 level. (**B**) A schematic of the genes in the 4-gamete (*19*) region on chromosome 10q26, as well as the location of SNPs genotyped by microarrays (+) and identified through sequencing (I). SNP rs10490924 is labeled "8," and rs11200638 is marked with an asterisk. Above are the gene conservation data obtained from the University of California Santa Cruz (UCSC) Golden Path database for the 4-gamete region. The data show the degree of evolutionary conservation among 17 species by using the multiz alignment; an increase in the height of the bar indicates an increase in the level of conservation.

indistinguishable from unity, 1.7 (95% CI 0.75 to 3.68), for those having a single risk allele. The risk homozygote accounted for 86% of the population attributable risk (PAR), although this number may be artificially inflated, because the risk allele was carried by more than half (~55%) of the AMD cohort (Table 1). When likelihood ratio tests were adjusted for gender and smoking status or when genomic control methods were applied to control for population stratification, there was little change in significance levels (*19*).

SNP rs10490924 resides between two genes on chromosome 10q26 (Fig. 1B): *PLEKHA1* encoding a pleckstrin homology domain–containing protein (GenBank ID 59338) and *HTRA1* encoding a heat shock serine protease also known as *PRSS11* (GenBank ID 5654). The low sequence homology across species in the intergenic region containing rs10490924 indicates that it is not evolutionarily conserved (Fig. 1B). Chromosome 10q26 has been linked to AMD in many independent family studies, and this linkage region was previously narrowed to SNP rs10490924 (*5*). SNP rs10490924 was originally thought to result in a protein coding change in the hypothetical locus LOC387715 (*20*, *21*). Because only a single cDNA sequence was found in placental tissue, LOC387715 was subsequently removed from the GenBank database. Thus, it is reasonable to hypothesize that SNP rs10490924 is a surrogate marker that is correlated, or is in linkage disequilibrium (LD), with the putative AMD disease–causing variant in the vicinity. Unfortunately, haplotype analyses using our genotype data or data from the International HapMap Project were unsuccessful in identifying where the functional site resides (*19*).

We therefore sequenced the entire local genomic region, including promoters, exons, and intron-exon junctions of both *PLEKHA1* and *HTRA1*, in search of the functional variant. We sequenced 50 cases that were homozygous for the risk allele and 38 controls that were homozygous for the wild-type allele on the basis of the genotypes of the marker SNP rs10490924. Of the 43 SNPs or insertion/deletion polymorphisms identified (Fig. 1B and table S6), one SNP (rs11200638), located 512 base pairs (bp) upstream of the *HTRA1* putative transcriptional start site and 6096 bp downstream of SNP rs10490924, exhibited a complete LD pattern with SNP rs10490924. Genotyping of the entire cohort revealed that SNP rs11200638 occurred at frequencies similar to those for SNP rs10490924 ($P = 8.2 \times 10^{-12}$ for the allele-association chi-square test), and the two SNPs were almost in complete LD ($D' > 0.99$) (Table 1).

Computational analysis (*19*) of the *HTRA1* promoter sequence predicted that SNP rs11200638 resides within putative binding sites for the transcription factors adaptor-related protein complex 2α (AP2α) and serum response factor (SRF). This DNA segment, containing the wild-type allele, is part of a CpG island and closely matches the consensus response sequences of these two transcription factors (fig. S5). The presence of the risk allele was predicted to alter the affinity of AP2α and SRF for the *HTRA1* promoter.

To verify that the predicted transcription factors bind to the *HTRA1* promoter in cultured human cells, we performed chromatin immunoprecipitation (ChIP) followed by quantitative real-time polymerase chain reaction (qPCR) analyses. Lysates were prepared from growing human cervical carcinoma cells (HeLaS3) heterozygous at rs11200638. ChIP was conducted with rabbit polyclonal antibodies against AP2α or SRF. qPCR tests of the ChIP DNA samples confirmed that both AP2α and SRF bind upstream of the *HTRA1* gene (Fig. 2 and fig. S5).

To investigate the influence of SNP rs11200638 on the *HTRA1* promoter, human ARPE19 (retinal pigment epithelium) and HeLaS3 cells were transiently transfected with a luciferase reporter plasmid driven by the *HTRA1* promoter, harboring either the wild-type (GG) or the risk homozygote (AA) genotype. Preliminary results showed a persistent trend of higher luciferase expressions with the AA compared with the GG genotype (fig. S7). Other factors such as epigenetic or environmental conditions also appeared to play a role for the different genotypes in response to different transcription factors. Further rigorous investigations to address this issue are warranted.

These results, together with the preliminary in vivo observations (*22*), suggest that the sequence change associated with SNP rs11200638 enhances the transcription of *HTRA1* in individuals homozygous for the risk allele.

The *HTRA1* gene encodes a heat shock serine protease that is activated by cellular stress (*23*). It is expressed in the mouse and human retina (*24*) (fig. S4), and its expression in human fibroblasts increases with advancing age (*25*). Drusen from the eyes of Caucasian patients with wet AMD stain positive for HTRA1 in immunohistochemistry experiments (*22*). This suggests that the two processes, neovascularization and drusen formation, may not be completely independent, rather, they may converge.

In summary, we have shown that the functional SNP rs11200638 in the promoter region of *HTRA1* is significantly associated with wet AMD in an Asian population. This association has been extended to a Caucasian population (*22*). To dissect genetic factors important to the complex phenotype of AMD, the power of trans racial gene mapping was exploited by using a population with a more precisely defined phenotype. On the basis of these and earlier genetic findings, a general model for the pathogenesis of AMD can be proposed. Geographic atrophy with large drusen and neovascularization jointly define AMD. Two major genes, *CFH* and *HTRA1*, in two different biological pathways, each affect the risk for a distinct component of

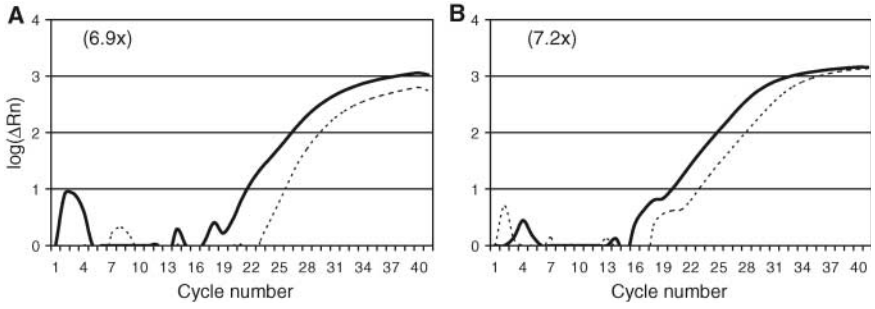

Fig. 2. Evaluation of transcription factor binding to the *HTRA1* promoter. (**A**) AP2α (solid line), (**B**) SRF (solid line), and (A and B) normal rabbit IgG (dashed line) ChIP DNA were prepared from HeLaS3 cells and analyzed by qPCR to assess the binding of AP2α and SRF to the putative binding sites upstream of *HTRA-1*. Positive and negative control promoters were also tested (*19*). The log (ΔRn) (fluorescence intensity over the background) is plotted against the PCR cycle number. The ΔΔCt values (fold increases of transcription calculated relative to reference PCR reactions) are shown in parentheses. Three replicate batches of the ChIP DNA samples were prepared, each of which was tested by qPCR at least twice.

Table 1. Association, odds ratios, and PAR for AMD in a Chinese population. Odds ratio and PAR compare the likelihood of AMD in individuals with the listed genotype of risk allele versus those homozygous for the wild-type allele.

SNP (alleles)	Risk allele	Allelic χ^2 nominal P	Heterozygous risk versus wild-type homozygotes		Homozygous risk versus wild-type homozygotes	
			Odds ratio (95% CI)	PAR (%) (95%CI)	Odds ratio (95%CI)	PAR (%) (95% CI)
rs10490924(G/T)	T	4.08×10^{-12}	1.66 (0.75–3.68)	29 (0–63)	11.14 (4.83–25.69)	86 (69–94)
rs11200638(G/A)	A	8.24×10^{-12}	1.60 (0.71–3.61)	27 (0–61)	10.00 (4.38–22.82)	84 (66–93)

the AMD phenotype: *CFH* influences the drusen that characterize dry AMD, whereas *HTRA1* influences CNV, the hallmark of the wet disease type. These two processes can be combined, which leads to the composite phenotypes that are seen in some cases of AMD.

References and Notes

1. G. S. Hageman *et al.*, *Proc. Natl. Acad. Sci. U.S.A.* **102**, 7227 (2005).
2. R. J. Klein *et al.*, *Science* **308**, 385 (2005).
3. E. A. Postel *et al.*, *Ophthalmology* **113**, 1504 (2006).
4. J. Maller *et al.*, *Nat. Genet.* **38**, 1055 (2006).
5. S. Haddad, C. A. Chen, S. L. Santangelo, J. M. Seddon, *Surv. Ophthalmol.* **51**, 316 (2006).
6. M. Li *et al.*, *Nat. Genet.* **38**, 1049 (2006).
7. A. Thakkinstian *et al.*, *Hum. Mol. Genet.* **15**, 2784 (2006).
8. A. C. Bird, *Eye* **17**, 457 (2003).
9. R. Klein *et al.*, *Ophthalmology* **113**, 373 (2006).
10. T. S. Chang, D. Hay, P. Courtright, *Can. J. Ophthalmol.* **34**, 266 (1999).
11. M. A. Sandberg, A. Weiner, S. Miller, A. R. Gaudio, *Ophthalmology* **105**, 441 (1998).
12. M. Uyama *et al.*, *Br. J. Ophthalmol.* **84**, 1018 (2000).
13. M. Yuzawa, K. Hagita, T. Egawa, H. Minato, M. Matsui, *Jpn. J. Ophthalmol.* **35**, 87 (1991).
14. N. Gotoh *et al.*, *Hum. Genet.* **120**, 139 (2006).
15. H. Okamoto *et al.*, *Mol. Vis.* **12**, 156 (2006).
16. M. A. Grassi *et al.*, *Hum. Mutat.* **27**, 921 (2006).
17. L. Baum *et al.*, *Ophthalmologica* **217**, 111 (2003).
18. C. P. Pang *et al.*, *Ophthalmologica* **214**, 289 (2000).
19. Materials and methods are available online as supporting material on *Science* Online.
20. A. Rivera *et al.*, *Hum. Mol. Genet.* **14**, 3227 (2005).
21. J. Jakobsdottir *et al.*, *Am. J. Hum. Genet.* **77**, 389 (2005).
22. Z. Yang *et al.*, *Science* **314**, 992 (2006).
23. T. Clausen, C. Southan, M. Ehrmann, *Mol. Cell* **10**, 443 (2002).
24. J. Tocharus *et al.*, *Dev. Growth Differ.* **46**, 257 (2004).
25. D. H. Ly, D. J. Lockhart, R. A. Lerner, P. G. Schultz, *Science* **287**, 2486 (2000).

26. We express our greatest appreciation to the patients, the control subjects, and their families for participating in this study; and we thank S. Chiang and B. Zhang for technical and logistic assistance. Supported in part by the Lim Por Yen Eye Foundation (D.L., C.P.), the David Woods Kemper Memorial Foundation (C.B.), Macular Vision Research Foundation (C.B., J.H.), the Ellison Medical Foundation (J.H.), an institutional award from the Howard Hughes Medical Institute to the Yale School of Medicine (J.H.), and grants from the Claude D. Pepper Older Americans Independence Center at Yale University School of Medicine (J.H.), the NIH (M.S., C.B., J.H.), and the Verto Institute (J.H.). *HTRA1* sequencing data are available on http://variation.yale.edu/dataDownload.html.

Supporting Online Material

www.sciencemag.org/cgi/content/full/1133807/DC1
Materials and Methods
Figs. S1 to S7
Tables S1 to S8
References and Notes

14 August 2006; accepted 5 October 2006
Published online 19 October 2006;
10.1126/science.1133807
Include this information when citing this paper.

A Variant of the *HTRA1* Gene Increases Susceptibility to Age-Related Macular Degeneration

Zhenglin Yang,[1,2,3]* Nicola J. Camp,[4]* Hui Sun,[5] Zongzhong Tong,[1,2] Daniel Gibbs,[1,2] D. Joshua Cameron,[1,2] Haoyu Chen,[1,2] Yu Zhao,[1,2] Erik Pearson,[1,2] Xi Li,[1,2] Jeremy Chien,[6] Andrew DeWan,[7] Jennifer Harmon,[1,2] Paul S. Bernstein,[1] Viji Shridhar,[6] Norman A. Zabriskie,[1] Josephine Hoh,[7] Kimberly Howes,[1] Kang Zhang[1,2]†

Age-related macular degeneration (AMD) is the most common cause of irreversible vision loss in the developed world and has a strong genetic predisposition. A locus at human chromosome 10q26 affects the risk of AMD, but the precise gene(s) have not been identified. We genotyped 581 AMD cases and 309 normal controls in a Caucasian cohort in Utah. We demonstrate that a single-nucleotide polymorphism, rs11200638, in the promoter region of *HTRA1* is the most likely causal variant for AMD at 10q26 and is estimated to confer a population attributable risk of 49.3%. The *HTRA1* gene encodes a secreted serine protease. Preliminary analysis of lymphocytes and retinal pigment epithelium from four AMD patients revealed that the risk allele was associated with elevated expression levels of *HTRA1* mRNA and protein. We also found that drusen in the eyes of AMD patients were strongly immunolabeled with HTRA1 antibody. Together, these findings support a key role for HTRA1 in AMD susceptibility and identify a potential new pathway for AMD pathogenesis.

Age-related macular degeneration (AMD) is the leading cause of irreversible blindness in developed countries, affecting 10 million people worldwide (*1*, *2*). Early AMD is characterized by the presence of soft drusen in the macula without vision loss. Advanced AMD is associated with vision loss due to either geographic atrophy of retinal pigment epithelium (RPE) and photoreceptors (GA or dry AMD) or neovascular choriocapillary invasion across Bruch's membrane into RPE and photoreceptor layers (wet AMD). The prevalence of AMD is rising as a result of increasing life expectancy, but the etiology remains poorly understood. Both genetic predisposition (*3*) and environmental factors such as smoking (*4*) play an important role in AMD pathogenesis.

Previous work has shown that allelic variants of genes encoding members of the alternative complement pathway, including complement factor H (CFH) (*5*–*9*) and factor B/C2, affect an individual's risk of developing AMD (*10*). In particular, variants of the *CFH* gene on chromosome 1q31 confer a major risk for AMD (*5*–*9*, *11*, *12*). Several independent association studies have implicated a second major locus for AMD at chromosome 10q26 (*12*–*16*). To identify the critical gene at this locus, we genotyped 442 AMD cases and 309 controls in a Caucasian cohort in Utah, using a panel of 15 single-nucleotide polymorphisms (SNPs) centered around the highest risk associated SNP, rs10490924. In agreement with previous reports, rs10490924 was found to have a significant association signal [$P = 8.1 \times 10^{-8}$ for an additive allele-dosage model, $OR_{het} = 1.35$ (0.99, 1.86), $OR_{hom} = 6.09$ (3.27, 11.34), T allele: 39.7% in cases versus 24.7% in controls]. However, of the 15 SNPs analyzed, rs11200638 was the most significantly associated variant [$P = 1 \times 10^{-9}$, $OR_{het} = 1.86$ (1.35, 2.56), $OR_{hom} = 6.56$ (3.23, 13.31), A allele: 40.3% in cases versus 25.2% in controls] (Fig. 1A and table S2). In terms of the significance of the association, the TA haplotype across rs10490924 and rs11200638 was superior to rs10490924 ($P = 2.2 \times 10^{-9}$), but inferior to rs11200638.

To investigate these associations further, we genotyped an additional 139 AMD patients for these two variants. The results for both SNPs increased in significance (rs10490924, $P = 1.2 \times 10^{-8}$; rs11200638, $P = 1.6 \times 10^{-11}$), with variant rs11200638 remaining the best single variant explaining the association [$OR_{het} = 1.90$ (1.40, 2.58), $OR_{hom} = 7.51$ (3.75, 15.04)]. We next considered association analyses based on genotypes at both rs11200638 and the CFH rs1061170 (Y402H) variant at chromosome 1q31. In a global two-locus analysis enumerating all nine two-locus genotype combinations, the association with AMD was significant ($\chi^2 = 56.56$, 8 df; $P = 2.2 \times 10^{-9}$). Table 1 shows the risk estimates for each two-locus genotype combination compared with the baseline of no risk genotypes (TT at CFHY402H and GG at

[1]Department of Ophthalmology and Visual Sciences, Moran Eye Center, University of Utah School of Medicine, Salt Lake City, UT 84132, USA. [2]Program in Human Molecular Biology and Genetics, Eccles Institute of Human Genetics, University of Utah School of Medicine, Salt Lake City, UT 84132, USA. [3]Sichuan Medical Science Academy and Sichuan Provincial People's Hospital, Sichuan 610071, China. [4]Division of Genetic Epidemiology, Department of Biomedical Informatics, University of Utah School of Medicine, Salt Lake City, UT 84108, USA. [5]Department of Physiology and Jules Stein Eye Institute, School of Medicine at UCLA, Los Angeles, CA 90095, USA. [6]Department of Laboratory Medicine and Experimental Pathology, Mayo Clinic College of Medicine, Rochester, MN 55905, USA. [7]Department of Epidemiology and Public Health, Yale University, New Haven, CT 06520, USA.

*These authors contributed equally to this work.
†To whom correspondence should be addressed. E-mail: kzhang@hmbg.utah.edu

rs11200638). The association of rs11200638 to AMD was significant when analyzed conditional on the presence of the CFH C risk allele ($P = 5.9 \times 10^{-8}$). In particular, this conditional analysis indicates an allele-dosage effect such that homozygotes for the A risk allele of rs11200638 are at an increased risk [$OR_{hom} = 7.29$ (3.18, 16.74)] over that of heterozygotes [$OR_{het} = 1.83$ (1.25, 2.68)] in all AMD cases, even when compared with a baseline that includes individuals who carry the risk genotypes at *CFH*. With an allele-dosage model, the estimated population attributable risk (PAR) for rs11200638 is 49.3%. Consistent with an additive effect, the estimated PAR from a joint model with CFH Y402H (that is, for a risk allele at either locus) is 71.4%.

The SNP rs11200638 is located 512 base pairs (bp) upstream of the transcription start site of the *HTRA1* gene (also known as *PRSS11, NM_002775*). Using MatInspector (Genomatix Software, GmbH, München, Germany), to scan putative transcription factor binding sites within this region, we identified a conserved AP2/SRF binding element that is altered by the A risk allele. To investigate the functional significance of the SNP, we used real-time reverse transcription polymerase chain reaction (RT-PCR) to study the expression levels of *HTRA1* mRNA in lymphocytes of four AMD patients carrying the risk allele AA and three normal controls carrying the normal allele GG (Fig. 1B and fig. S1A). The *HTRA1* mRNA levels in lymphocytes from AMD patients with the AA genotype were higher by a factor of ~2.7 than those in normal controls with the GG genotype (Fig. 1B). The mean HTRA1 protein level in RPE of four AMD donor eyes with a homozygous AA risk allele was higher by a factor of 1.7 than that of six normal controls with a homozygous GG allele (fig. S2). Unfortunately, our analysis of human eye tissue was limited because we were able to obtain only four AMD donor eyes with an AA genotype out of the 60 donors for this study; therefore, these data thus far show a trend toward higher expression with the risk AA allele. Immunohistochemistry experiments revealed that HTRA1 immunolabeling is present in the drusen of three AMD patients (Fig. 1C and fig. S1, B and C).

The *HTRA1* gene encodes a member of a family of serine proteases expressed in the mouse retina and RPE (*17*). HTRA1 appears to regulate the degradation of extracellular matrix proteoglycans. This activity is thought to facilitate access of other degradative matrix enzymes, such as collagenases and matrix metalloproteinases, to their substrates (*18*). Conceivably, overexpression of HTRA1 may alter the integrity of Bruch's membrane, favoring the invasion of choroid capillaries across the extracellular matrix, as occurs in wet AMD. HTRA1 also binds and inhibits transforming growth factor-β (TGF-β), an important regulator of extracellular matrix deposition and angiogenesis (*17*). DeWan *et al.* (*19*) report that the same *HTRA1* SNP is associated with a wet AMD phenotype in a Chinese population. Together, these findings support a key role for HTRA1 in AMD susceptibility and identify a potential new pathway for AMD pathogenesis.

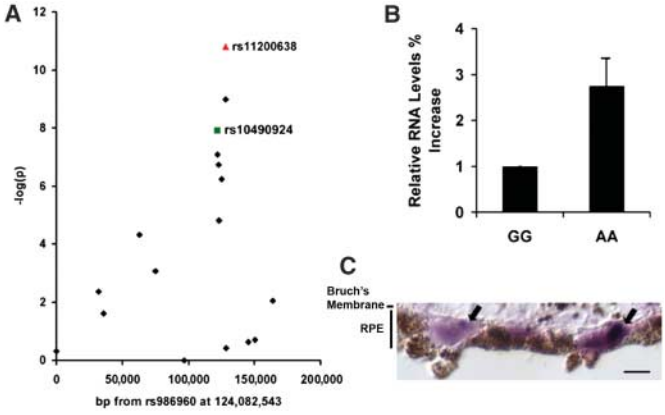

Fig. 1. Genetic association (**A**) and preliminary analysis of HTRA1 mRNA and protein expression in AMD (**B** and **C**). (A) Graphed log *P*-values (*y* axis) from association analyses for the 15 SNPs at the 10q AMD region using 442 AMD cases and 309 controls (see also table S2). For the rs10490924 (green square) and rs11200638 (red triangle) SNPs, associations were derived from a larger sample size (581 AMD cases). (B) Real-time RT-PCR semi-quantitative analysis of *HTRA1* RNA levels in blood lymphocytes from three AMD patients with the AA genotype and three normal controls with the GG genotype. The statistical significance of the differences in expression level was examined using an independent samples *t* test (SPSS version 13.0): AA:GG ($P = 0.02$). Each RT-PCR reaction was run twice, and the error bars indicate the 95.0% confidence interval of the mean. (C) Drusen is immunolabeled with HTRA1 antibody in an eye from a patient with wet AMD. The staining (arrows) occurs between RPE and Bruch's membrane. Similar results were obtained in another two AMD eyes (fig. S1, B and C). Scale bar = 20 μm.

Table 1. Two-locus odds ratios for *HTRA1* rs11200638 and *CFH* rs1061170. Odds ratios with 95% confidence intervals in parentheses were calculated to compare each genotypic combination to the baseline of homozygosity for the common allele at both loci (TT/GG).

SNP		*HTRA1* rs11200638		
		GG	AG	AA
CFH rs1061170 (Y402H)	TT	1.00	1.80 (0.93,3.49)	3.43 (0.62,19.00)
	CT	1.07 (0.59,1.94)	2.31 (1.28,4.17)	7.31 (2.68,19.93)
	CC	3.07 (1.50,6.27)	3.97 (1.93,8.15)	31.52 (4.01,247.96)

References and Notes

1. National Advisory Eye Council, *Report of the Retinal Diseases Panel: Vision Research: A National Plan, 1994–1998* (U.S. Department of Health and Human Services, Publication NIH 93-3186, Bethesda, MD, 1993).
2. K. Attebo, P. Mitchell, W. Smith, *Ophthalmology* **103**, 357 (1996).
3. C. C. Klaver *et al.*, *Arch. Ophthalmol.* **116**, 1646 (1998).
4. J. M. Seddon, W. C. Willett, F. E. Speizer, S. E. Hankinson, *JAMA* **276**, 1141 (1996).
5. R. J. Klein *et al.*, *Science* **308**, 385 (2005).
6. A. O. Edwards *et al.*, *Science* **308**, 421 (2005).
7. J. L. Haines *et al.*, *Science* **308**, 419 (2005).
8. G. S. Hageman *et al.*, *Proc. Natl. Acad. Sci. U.S.A.* **102**, 7227 (2005).
9. K. P. Magnusson *et al.*, *PLoS Med.* **3**, e5 (2006).
10. B. Gold *et al.*, *Nat. Genet.* **38**, 458 (2006).
11. M. Li *et al.*, *Nat. Genet.* **38**, 1049 (2006).
12. J. Maller *et al.*, *Nat. Genet.* **38**, 1055 (2006).
13. A. Rivera *et al.*, *Hum. Mol. Genet.* **14**, 3227 (2005).
14. J. Jakobsdottir *et al.*, *Am. J. Hum. Genet.* **77**, 389 (2005).
15. S. A. Fisher *et al.*, *Hum. Mol. Genet.* **14**, 2257 (2005).
16. S. Schmidt *et al.*, *Am. J. Hum. Genet.* **78**, 852 (2006).
17. C. Oka *et al.*, *Development* **131**, 1041 (2004).
18. S. Grau *et al.*, *J. Biol. Chem.* **281**, 6124 (2006).
19. A. DeWan *et al.*, *Science* **314**, 989. Published online 19 October 2006. 10.1126/science.1133807 (2006).

20. We thank the participating AMD patients and their families. We thank G. Brinton, J. Carver, A. Crandall, M. Teske, A. Jorgensen, E. Brinton, and R. MacArthur for assistance in obtaining blood samples; W. Baehr, R. Marc, and N. Perrimon for critical reading of the manuscript; D. Lim and E. Smith for editorial assistance; and the Utah Lions Eye Bank and P. Bhosale for assistance in obtaining eye donor tissues. We acknowledge the following grant support to K.Z.: NIH (R01EY14428, R01EY14448, P30EY014800, and GCRC M01-RR00064), Foundation Fighting Blindness, Ruth and Milton Steinbach Fund, Ronald McDonald House Charities, Macular Vision Research Foundation, Research to Prevent Blindness, Val and Edith Green Foundation, and the Simmons Foundation; to H.S.: Ruth and Milton Steinbach Fund; to Z.Y.: Knights Templar Eye Research Foundation; to N.C.: K07 (NCI CA98364); to J.H.: NIH (R01EY15771), Ellison Medical Foundation, Macular Vision Research Foundation, an institutional award from Howard Hughes Medical Institute to Yale School of Medicine, and grants from the Claude D. Pepper Older Americans Independence Center at Yale University School of Medicine, and the Verto Institute; to V.S.: Mayo Clinic and Foundation.

Supporting Online Material

www.sciencemag.org/cgi/content/full/1133811/DC1
Materials and Methods
Figs. S1 and S2
Tables S1 and S2
References

14 August 2006; accepted 6 October 2006
Published online 19 October 2006;
10.1126/science.1133811
Include this information when citing this paper.

5′-Triphosphate RNA Is the Ligand for RIG-I

Veit Hornung,[1] Jana Ellegast,[1] Sarah Kim,[1] Krzysztof Brzózka,[3] Andreas Jung,[2] Hiroki Kato,[2] Hendrik Poeck,[1] Shizuo Akira,[2] Karl-Klaus Conzelmann,[3] Martin Schlee,[4] Stefan Endres,[1] Gunther Hartmann[4]*

The structural basis for the distinction of viral RNA from abundant self RNA in the cytoplasm of virally infected cells is largely unknown. We demonstrated that the 5′-triphosphate end of RNA generated by viral polymerases is responsible for retinoic acid–inducible protein I (RIG-I)–mediated detection of RNA molecules. Detection of 5′-triphosphate RNA is abrogated by capping of the 5′-triphosphate end or by nucleoside modification of RNA, both occurring during posttranscriptional RNA processing in eukaryotes. Genomic RNA prepared from a negative-strand RNA virus and RNA prepared from virus-infected cells (but not from noninfected cells) triggered a potent interferon-α response in a phosphatase-sensitive manner. 5′-triphosphate RNA directly binds to RIG-I. Thus, uncapped 5′-triphosphate RNA (now termed 3pRNA) present in viruses known to be recognized by RIG-I, but absent in viruses known to be detected by MDA-5 such as the picornaviruses, serves as the molecular signature for the detection of viral infection by RIG-I.

Receptor-mediated detection of pathogen-derived nucleic acids assists in protecting the host genome from invading foreign genetic material. Retinoic acid–inducible protein I (RIG-I) recognizes a specific set of RNA viruses (Flaviviridae, Paramyxoviridae, Orthomyxoviridae, and Rhabdoviridae) (*1*–*3*), whereas a second member of this protein family, melanoma differentiation–associated gene 5 (MDA-5), is responsible for the antiviral defense against a reciprocal set of RNA viruses (Picornaviridae) (*3*). The four members of the Toll-like receptor (TLR) family (TLR3, TLR7, TLR8, and TLR9) involved in viral nucleic acid recognition are located in the endosomal membrane. TLRs are largely dispensable for effective antiviral defense, whereas the two cytosolic helicases MDA-5 and RIG-I (*1*) are essential for controlling viral infection.

The molecular characteristic of "double-strandedness" seems to allow for the distinction of self and nonself RNA. In the endosome, long double-stranded RNA (dsRNA) and its mimic polyinosinic-polycytidylic acid [poly(I:C)] but not single-stranded RNA (ssRNA) are recognized by TLR3 (*4*). In the cytosol, abundant self RNA complicates our understanding of recognition of nonself RNA. It is generally accepted that long dsRNA in the cytoplasm is detected as nonself and is thought to be recognized by MDA-5 and RIG-I (*1*, *5*). Recently, it was demonstrated that poly(I:C) is a ligand for MDA-5 but not RIG-I (*3*, *6*), whereas long dsRNA was found to activate RIG-I but not MDA-5 (*3*). One study suggests that synthetic short dsRNA with blunt ends is recognized by RIG-I and that two-nucleotide overhangs at the 3′ end block this recognition (*7*). Another group reported that short dsRNA (such as small interfering RNA), when generated by in vitro transcription, induced type I interferon (IFN) in cell lines (*8*). Together, these results suggest that there is more to cytoplasmic RNA recognition than long dsRNA.

We hypothesized that motif patterns or sequences in RNA may exist that are preferentially recognized. Long in vitro–transcribed RNA was transfected in monocytes and plasmacytoid dendritic cells (PDCs), and IFN-α production was assessed. We found that a 2500-nucleotide-long RNA molecule, but not the TLR9 ligand CpG-A (*9*) or the TLR7/8 ligand R848, stimulated a strong IFN-α response in primary human monocytes (fig. S1A). In vitro–transcribed RNA required a minimal length of 19 bases to efficiently induce IFN-α in monocytes (fig. S1B). Our results suggest that a molecular characteristic shared by all in vitro–transcribed RNA molecules, such as the 5′-triphosphate, rather than a specific sequence motif is responsible for IFN-α induction in monocytes.

To study the sequence-independent contribution of the 5′-triphosphate, we compared IFN-α induction of synthetic (5′-hydroxyl) and in vitro–transcribed (5′-triphosphate) versions of the immunostimulatory ssRNA oligonucleotide 9.2s (isRNA9.2s), which is composed of 19 nucleotides (*10*). We found that only the in vitro–transcribed version of isRNA9.2s, not the synthetic isRNA9.2s,

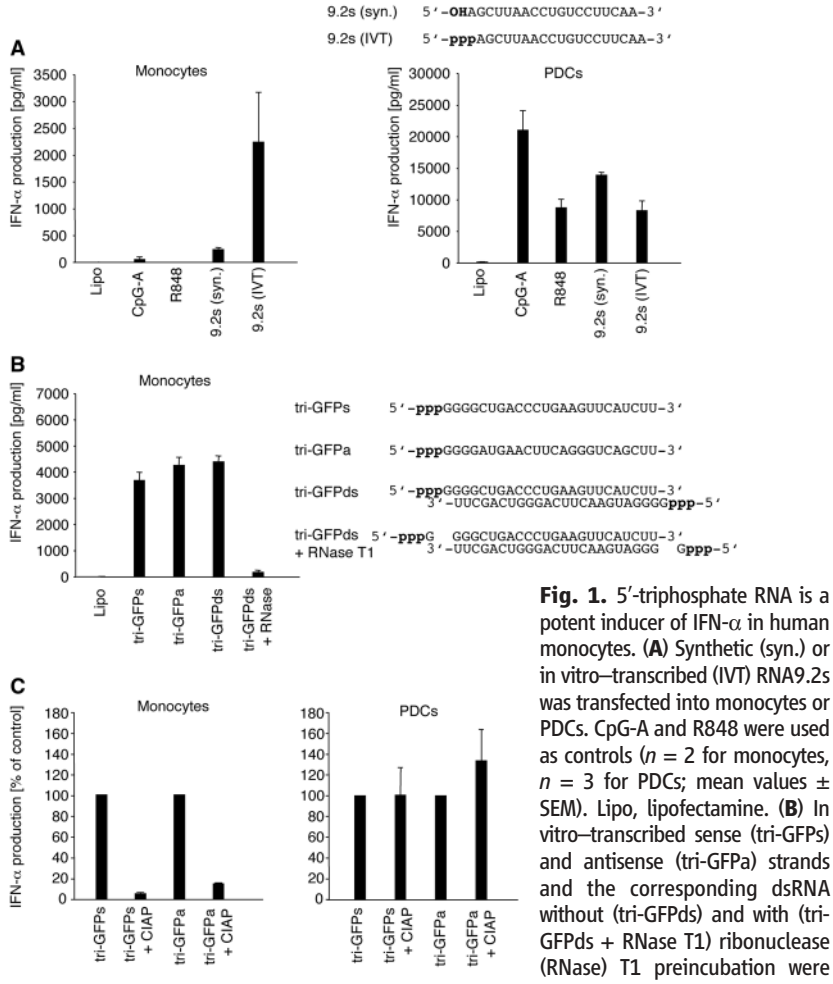

Fig. 1. 5′-triphosphate RNA is a potent inducer of IFN-α in human monocytes. (**A**) Synthetic (syn.) or in vitro–transcribed (IVT) RNA9.2s was transfected into monocytes or PDCs. CpG-A and R848 were used as controls (n = 2 for monocytes, n = 3 for PDCs; mean values ± SEM). Lipo, lipofectamine. (**B**) In vitro–transcribed sense (tri-GFPs) and antisense (tri-GFPa) strands and the corresponding dsRNA without (tri-GFPds) and with (tri-GFPds + RNase T1) ribonuclease (RNase) T1 preincubation were transfected into monocytes (n = 2; mean values ± SEM). (**C**) Tri-GFPs and tri-GFPa were dephosphorylated with calf intestine alkaline phosphatase (CIAP) and subsequently transfected into monocytes and PDCs (n = 2; mean values of normalized data ± SEM).

[1]Division of Clinical Pharmacology, Department of Internal Medicine, University of Munich, 80336 Munich, Germany. [2]Department of Host Defense, Research Institute for Microbial Diseases, Osaka University, Suita 565–0871, Osaka, Japan. [3]Department of Virology, Max von Pettenkofer Institute and Gene Center, University of Munich, 81377 Munich, Germany. [4]Division of Clinical Pharmacology, University Hospital, University of Bonn, 53105 Bonn, Germany.

*To whom correspondence should be addressed. E-mail: gunther.hartmann@ukb.uni-bonn.de

strongly induced IFN-α production in monocytes (Fig. 1A). PDCs, known to detect ssRNA oligonucleotides via TLR7, produced IFN-α in response to both in vitro–transcribed and synthetic isRNA9.2s (Fig. 1A). Next, we used in vitro transcription to generate a dsRNA oligonucleotide with an overhang of one nucleotide at the 5′ position. The two single-stranded oligonucleotides (tri-GFPs and tri-GFPa) and the double-stranded oligonucleotide (tri-GFPds) induced comparable levels of IFN-α in monocytes (Fig. 1B). Cleavage of the 5′ overhang (including the 5′-triphosphate) of the dsRNA (tri-GFPds) (Fig. 1B) or dephosphorylation of the 5′ end completely abrogated the IFN response (Fig. 1C). PDCs, however, showed no decrease in IFN production when oligonucleotides were dephosphorylated (Fig. 1C). Together, these data indicate that the 5′-triphosphate is at least one well-defined structural feature responsible for IFN-α–inducing activity of in vitro–transcribed RNA in monocytes and that a 5′-triphosphate confers IFN-α–inducing activity to both ssRNA and dsRNA.

We examined the influence of a 7-methyl-guanosine cap on the IFN-α–inducing activity of 5′-triphosphate RNA. We found that RNA transcribed in the presence of a synthetic cap analog (containing ~80% capped RNA) was much less active in inducing IFN-α in monocytes as compared to uncapped in vitro–transcribed RNA (Fig. 2A). A strong decrease in IFN-α production in both monocytes and PDCs could be seen when either pseudouridine or 2-thiouridine was substituted for uridine (Fig. 2B). Analogous results were obtained when 2′-O-methylated uridine 5′-triphosphate (UTP) was incorporated into the triphosphate RNA oligonucleotides instead of UTP (Fig. 2C). These results indicate that common eukaryotic posttranscriptional modifications suppress the immunostimulatory activity of triphosphate RNA.

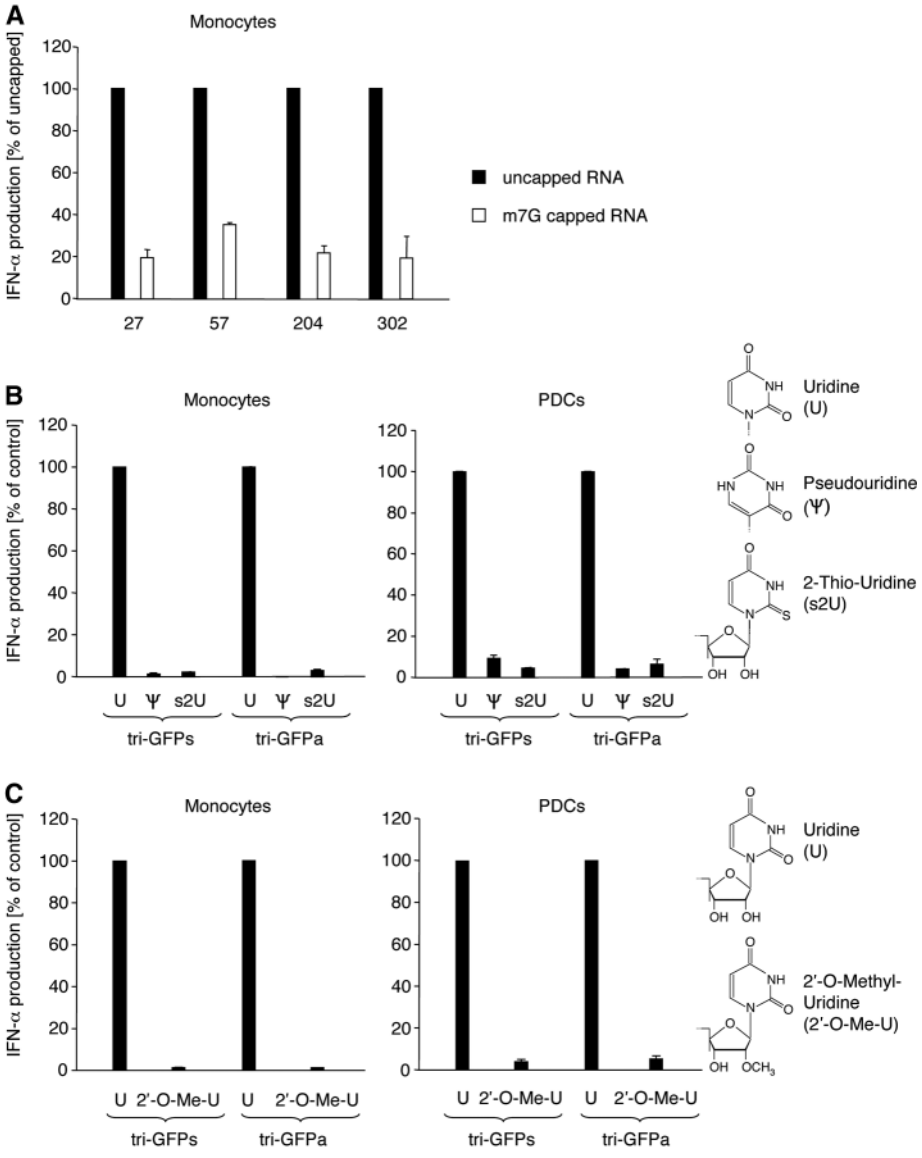

Fig. 2. 7-methyl-guanosine capping and base or sugar modifications abolish IFN-α induction by 5′-triphosphate RNA. (**A**) RNA molecules of various lengths (27, 57, 204, and 302 nucleotides) transcribed in the presence of the cap analog *N*-7-methyl-GpppG (m7G-capped RNA) or standard nucleoside triphosphates (uncapped RNA) were transfected into monocytes ($n = 2$; mean values of normalized data ± SEM). The absolute values for the respective RNA transcripts were 1401, 2351, 797, and 2590 pg/ml. (**B** and **C**) Tri-GFPs and tri-GFPa were transcribed in vitro in the presence of either UTP, pseudouridine 5′-triphosphate, or 2-thiouridine-5′-triphosphate (B), or 2′-*O*-methyluridine-5′-triphosphate (C) and subsequently transfected into monocytes or PDCs [$n = 2$ for (B), $n = 3$ for (C); mean values of normalized data ± SEM].

Triphosphate RNA–mediated IFN-α induction required neither endosomal maturation nor TLR7 (fig. S4). Human embryonic kidney (HEK) 293 cells, overexpressing full-length RIG-I, strongly responded to 5′-triphosphate RNA9.2s, whereas synthetic isRNA9.2s was inactive (fig. S5A). Consistent with these results, wild-type and MDA-5$^{-/-}$ mouse embryo fibroblasts (MEFs) produced large amounts of IFN-β in response to 5′-triphosphate RNA, whereas no response was detected in RIG-I$^{-/-}$ MEFs (Fig. 3A). Endogenous transcription of triphosphate RNA, by means of a cytosolically expressed T7 RNA polymerase (Pol), also induced a strong IFN response in a RIG-I–dependent fashion (fig. S5, B and C). Together, these data provide evidence that RIG-I but not MDA-5 is required for the recognition of 5′-triphosphate RNA and that recognition of 5′-triphosphate RNA is not confined to immune cells.

To assess the importance of 5′-triphosphate RNA in the recognition of virus infection by RIG-I, we used rabies virus (RV), which is a prototypical rhabdovirus. Wild-type RV (SAD L16) encodes a potent antagonist of IFN induction, the phosphoprotein P. In contrast, RV genetically engineered to express little P (SAD ΔPLP) efficiently induces IFN (*11*). SAD ΔPLP infection per se triggered a potent IFN response in African green monkey kidney (Vero) cells that could be further increased through overexpression of RIG-I and strongly suppressed by the dominant-negative mutant RIG-IC (Fig. 3B). These results indicate that RIG-I is required for the initiation of an IFN response upon RV infection, as has been observed for other negative-strand viruses (NSVs), such as vesicular stomatitis virus and influenza (*3*). In addition, RNA isolated from RV-infected BSR cells, but not from noninfected cells, induced a potent IFN response in HEK 293T cells. This IFN production was abrogated when the RNA isolates were dephosphorylated (Fig. 3C), indicating that the 5′-phosphorylation status was critical for recognition. RNA from NSVs and NSV-infected cells is not considered infectious and does not allow the initiation of a replicative cycle. Indeed, the fact that RNA from RV SAD L16–infected cells was equally potent in terms of IFN-β induction as RNA from RV SAD ΔPLP–infected cells indicated that little or no productive translation and replication was initiated through

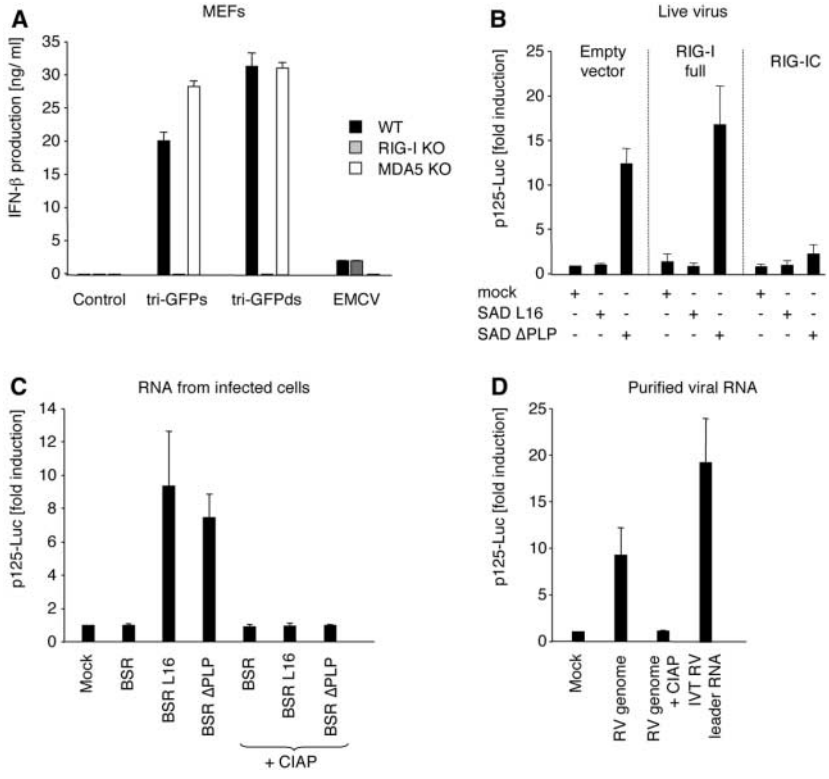

Fig. 3. 5′-triphosphate RNA and viral RNA induce a type I IFN response with RIG-I. (**A**) IFN-β production of MEFs from RIG-I– or MDA-5–deficient (KO) mice or wild-type (WT) mice transfected with tri-GFPs or tri-GFPds or infected with encephalomyocarditis virus (EMCV) at a multiplicity of infection (MOI) of 1 (mean values ± SEM of one representative experiment out of three). (**B**) Vero cells were transfected with the empty vector, RIG-I full, or RIG-IC and subsequently were either mock infected or infected with RV SAD L16 or RV SAD ΔPLP at an MOI of 3. p125-Luc, reporter plasmid encoding firefly luciferase downstream of the IFN-β gene promoter. (**C**) HEK 293T cells were transfected with 1 μg of total RNA isolated from noninfected BSR cells or from BSR cells infected with RV L16 (BSR L16) or RV ΔPLP (BSR ΔPLP). RNA was pretreated with CIAP as indicated [(B) and (C), mean values of normalized data (mock = 1) ± SEM of one representative experiment out of two]. (**D**) RNA from gradient-purified virions (RV L16) or CIAP-treated RNA from purified virions or in vitro–transcribed RNA corresponding to the 5′-terminal leader sequence of the RV SAD L16 complementary RNA were used to stimulate HEK 293T cells. Data from the experiment are shown as mean fold values (mock = 1) of triplicates ± SEM.

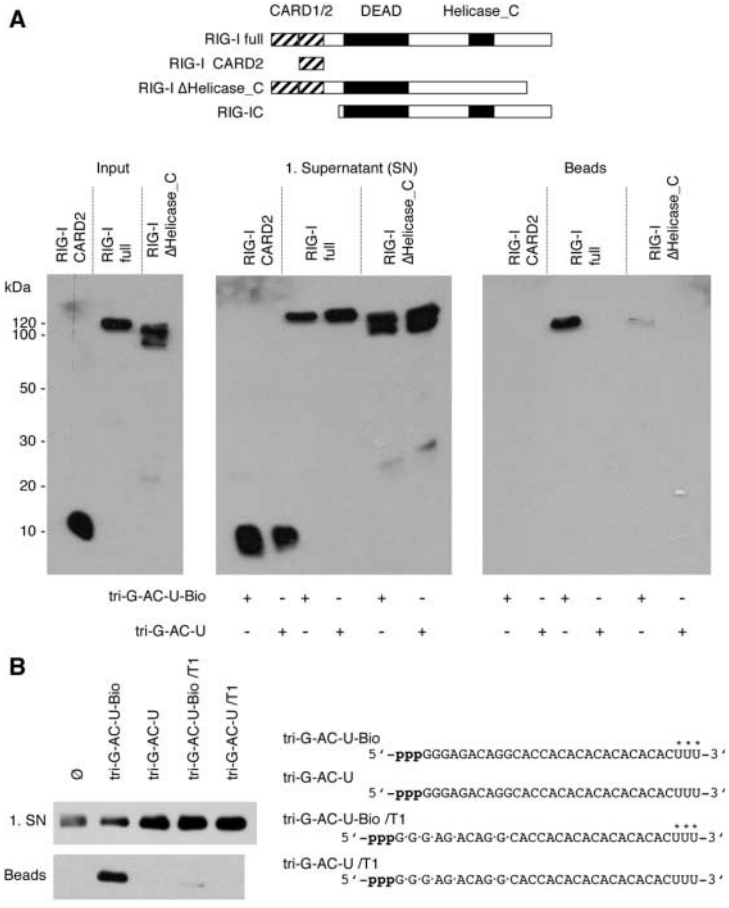

Fig. 4. 5′-triphosphate RNA directly binds to RIG-I. (**A**) HEK 293 cells were transfected with full-length RIG-I, RIG-I CARD2, or RIG-I ΔHelicase_C. Cell lysates were co-incubated with the indicated RNA oligonucleotides. For one representative experiment out of two, the input, the supernatants of the first wash (1. SN), and the bead-bound fraction (Beads) are depicted. (**B**) RNA with and without RNase T1 pretreatment (removal of the 5′ portion of the oligonucleotide containing the triphosphate group) was co-incubated with purified RIG-IC. The first supernatant and the bead-bound fraction of one representative pulldown experiment out of three are shown. Circled slash, control without oligonucleotide.

the transfection of the respective RNA isolates. To completely rule out the possibility that replication of RV was required to trigger an IFN response, we isolated full-length RNA from virions and assessed it for the induction of IFN expression. Transfection of purified RV RNA effectively stimulated IFN induction in HEK 293T cells, whereas dephosphorylation of the genomic RV RNA isolates completely abrogated the observed IFN response (Fig. 3D). Together, these results demonstrate that RIG-I directly recognizes genomic RNA from RV independently of replication.

We next performed in vitro binding assays, testing the ability of 5′-triphosphate RNA to pull down RIG-I. RNA oligonucleotides with 3′-terminal biotin tags were generated and coincubated with whole-cell lysate from HEK 293 cells overexpressing full-length RIG-I and truncated versions of RIG-I. Although the 5′-triphosphate biotin oligonucleotide (tri-G-AC-U-Bio) was able to immunoprecipitate full-length RIG-I, no or little pulldown was seen when truncated versions of RIG-I (RIG-I CARD2 and RIG-I ΔHelicase_C) were tested for binding of the triphosphate RNA (Fig. 4A, right panel). Purified RIG-IC was also efficiently pulled down by triphosphate RNA oligonucleotides (Fig. 4B, second lane), but not if the initial 5′-triphosphate group was enzymatically removed before coincubation (Fig. 4B, fourth lane). These results indicate that 5′-triphosphate RNA directly binds to full-length RIG-I, and therefore RIG-I is the direct receptor responsible for the recognition of 5′-triphosphate RNA.

Our results provide evidence that uncapped unmodified 5′-triphosphate RNA (now termed 3pRNA) is a well-defined molecular structure of viral nucleic acids that is detected by RIG-I in the cytosol of eukaryotic cells. Many of the RNA species in the cytosol of eukaryotes are known to lack a free 5′-triphosphate group, although all RNA transcripts generated in the nucleus of a eukaryotic cell initially contain a 5′-triphosphate. Matured Pol I–transcribed ribosomal RNAs (rRNAs) in the cytosol have a monophosphate group at the 5′ end (*12*). mRNAs and small nuclear RNAs transcribed by Pol II are capped with a 7-methyl-guanosine group that is attached to the 5′-triphosphate (*13*). All mature tRNAs (Pol III) have a 5′-monophosphate (*14*), as is likely to apply to 5S rRNA. U6 RNA receives a γ-monomethylphosphate cap structure after transcription (*15*). 7SL RNA (Pol III), however, has a triphosphate at the 5′ end and is present at high copy numbers in the cytosol. Therefore, the presence or absence of a 5′-triphosphate might not be the only structural feature of RNA responsible for the distinction of self and viral RNA. Eukaryotic RNA undergoes substantial posttranscriptional modifications. The host machinery that guides nucleoside modifications and 2′-O-methylation of the ribose backbone is located in the nucleus (*16*). Because most RNA viruses do not replicate in the nucleus, extensive modification of viral RNA seems unlikely.

The mRNAs of viruses infecting eukaryotic cells commonly contain 7-methyl-guanosine cap structures at their 5′ ends and polyadenylate tails at their 3′ ends. Nonetheless, in many viruses, RNA synthesis leads to transient cytosolic viral RNA intermediates with an uncapped 5′-triphosphate end. RNA transcripts of all positive-strand RNA viruses of the family Flaviviridae start with an uncapped 5′-triphosphate, and members of all of these virus genera were reported as being recognized by RIG-I (*2*, *3*, *17*). Segmented NSVs initiate genomic and the complementary antigenomic RNA replication by a primer-independent de novo mechanism resulting in a 5′-triphosphate–initiated transcript (*18*). NSVs with a nonsegmented genome, including the paramyxoviruses and rhabdoviruses, initiate both replication and transcription de novo leading to 5′-triphosphate RNA in the cytosol. Consequently, genomic RNA from NSVs per se is expected to trigger an IFN response without the need for replication and presumed dsRNA formation. All viruses in the picornavirus-like supergroup use an RNA-dependent RNA Pol that exclusively uses a protein as a primer for both positive- and negative-strand RNA production; as a consequence, during the life cycle of picornaviruses, uncapped triphosphorylated 5′ ends are absent (*19*). Thus, although RIG-I is expected to be involved in the detection of Flaviviridae and NSVs, it cannot detect picornaviruses.

References and Notes

1. M. Yoneyama *et al.*, *Nat. Immunol.* **5**, 730 (2004).
2. R. Sumpter Jr. *et al.*, *J. Virol.* **79**, 2689 (2005).
3. H. Kato *et al.*, *Nature* **441**, 101 (2006).
4. L. Alexopoulou, A. C. Holt, R. Medzhitov, R. A. Flavell, *Nature* **413**, 732 (2001).
5. S. Rothenfusser *et al.*, *J. Immunol.* **175**, 5260 (2005).
6. L. Gitlin *et al.*, *Proc. Natl. Acad. Sci. U.S.A.* **103**, 8459 (2006).
7. J. T. Marques *et al.*, *Nat. Biotechnol.* **24**, 559 (2006).
8. D. H. Kim *et al.*, *Nat. Biotechnol.* **22**, 321 (2004).
9. M. Kerkmann *et al.*, *J. Biol. Chem.* **280**, 8086 (2005).
10. V. Hornung *et al.*, *Nat. Med.* **11**, 263 (2005).
11. K. Brzozka, S. Finke, K. K. Conzelmann, *J. Virol.* **80**, 2675 (2006).
12. M. Fromont-Racine, B. Senger, C. Saveanu, F. Fasiolo, *Gene* **313**, 17 (2003).
13. A. J. Shatkin, J. L. Manley, *Nat. Struct. Biol.* **7**, 838 (2000).
14. S. Xiao, F. Scott, C. A. Fierke, D. R. Engelke, *Annu. Rev. Biochem.* **71**, 165 (2002).
15. R. Singh, R. Reddy, *Proc. Natl. Acad. Sci. U.S.A.* **86**, 8280 (1989).
16. W. A. Decatur, M. J. Fournier, *J. Biol. Chem.* **278**, 695 (2003).
17. T.-H. Chang, C.-L. Liao, Y.-L. Lin, *Microbes Infect.* **8**, 157 (2006).
18. G. Neumann, G. G. Brownlee, E. Fodor, Y. Kawaoka, *Curr. Top. Microbiol. Immunol.* **283**, 121 (2004).
19. Y. F. Lee, A. Nomoto, B. M. Detjen, E. Wimmer, *Proc. Natl. Acad. Sci. U.S.A.* **74**, 59 (1977).

20. This study was supported by grants from the Bundesministerium für Bildung und Forschung (Biofuture 0311896) and the Deutsche Forschungsgemeinschaft (HA 2780/4-1 and Sonderforschungsbereich 571) to G.H., a grant from the Sonderforschungsbereich 455 to K.C., two grants from the Förderprogramm für Forschung und Lehre (489 to V.H. and 2004/33 to S.K.), and by the Graduiertenkolleg 1202 of the Deutsche Forschungsgemeinschaft. This work is part of the thesis of J.E. and S.K. at the University of Munich. We thank S. Rothenfusser for critically reading the manuscript.

Supporting Online Material

www.sciencemag.org/cgi/content/full/1132505/DC1
Materials and Methods
SOM Text
Figs. S1 to S5
Table S1
References

14 July 2006; accepted 18 September 2006
Published online 12 October 2006;
10.1126/science.1132505
Include this information when citing this paper.

RIG-I–Mediated Antiviral Responses to Single-Stranded RNA Bearing 5′-Phosphates

Andreas Pichlmair,[1] Oliver Schulz,[1] Choon Ping Tan,[1] Tanja I. Näslund,[2] Peter Liljeström,[2] Friedemann Weber,[3] Caetano Reis e Sousa[1]*

Double-stranded RNA (dsRNA) produced during viral replication is believed to be the critical trigger for activation of antiviral immunity mediated by the RNA helicase enzymes retinoic acid–inducible gene I (RIG-I) and melanoma differentiation–associated gene 5 (MDA5). We showed that influenza A virus infection does not generate dsRNA and that RIG-I is activated by viral genomic single-stranded RNA (ssRNA) bearing 5′-phosphates. This is blocked by the influenza protein nonstructured protein 1 (NS1), which is found in a complex with RIG-I in infected cells. These results identify RIG-I as a ssRNA sensor and potential target of viral immune evasion and suggest that its ability to sense 5′-phosphorylated RNA evolved in the innate immune system as a means of discriminating between self and nonself.

The innate immune response to viral infection is characterized by the rapid production of a range of cytokines, most prominently type I interferons (IFN-α/β) (*1*). Specialized plasmacytoid dendritic cells (pDC) produce IFN-α/β when RNA or DNA viral

genomes in endosomes trigger toll-like receptors (TLRs) 7, 8, and 9 (*2*). Other cell types rely on cytoplasmic virus sensors such as the RNA helicases RIG-I and MDA5 (*3*–*7*), which are believed to be activated by dsRNA produced during viral replication or convergent transcription of viral genes (*8*). Viral recognition pathways can be targeted as a means of immune escape (*9*). For example, influenza A virus NS1 protein suppresses IFN-α/β production in animal models, cell lines, and primary cells (*10*), including conventional (nonplasmacytoid) dendritic cells (cDC), a critical cell type for the induction of adaptive immunity (*11*, *12*). NS1 possesses an RNA binding domain at the N terminus (*13*) and some evidence suggests that it exerts its suppressive effect by sequestering dsRNA (*10*).

[1]Immunobiology Laboratory, Cancer Research UK, London Research Institute, London WC2A 3PX, UK. [2]Department of Microbiology, Tumor and Cell Biology, Karolinska Institutet, Stockholm 17177, Sweden. [3]Department of Virology, University of Freiburg, Freiburg 79104, Germany.

*To whom correspondence should be addressed. E-mail: caetano@cancer.org.uk

To address whether this is the case, we first confirmed that influenza A virus (A/PR/8/34 strain) inhibits IFN-α/β production through the action of NS1. cDC derived from murine bone marrow progenitors (BM-DC) (*14*) infected with a mutant virus lacking the protein (ΔNS1) produced 100 times more IFN-α than did cells infected with the parental wild-type strain (Fig. 1A) (*11*, *12*). This was independent of the TLR7-TLR8-TLR9 adaptor MyD88 (Fig. 1A), suggesting that the effect occurred by means of the cytoplasmic pathway. We then assessed the extent to which dsRNA is generated during influenza replication. Consistent with recent data (*15*), no dsRNA was detected in BM-DC or in more permissive Vero cells (Fig. 1, B and C, and fig. S1) with either ΔNS1 or the wild-type virus, even though the cells were uniformly infected (fig. S2). In contrast, dsRNA was detectable upon transfection with poly inosinic:cytidylic acid (poly I:C), a synthetic dsRNA, or infection with encephalomyocarditis virus (EMCV), a picornavirus (Fig. 1, B and C, and fig. S1). We next examined the ability of NS1 to inhibit responses to Semliki Forest virus (SFV), which, similar to EMCV, generates high levels of dsRNA (*16*). Cells infected with a recombinant SFV encoding NS1 (SFV-NS1) expressed NS1 protein (fig. S3), but produced levels of IFN-α comparable to cells infected with a control recombinant virus or wild-type SFV (Fig. 1D). Similarly, transfection with NS1 had no effect on the induction of an IFN-β reporter in response to EMCV or SFV, although it potently inhibited the response to ΔNS1 influenza or Sendai virus (SeV) (Fig. 1E) (*13*). Notably, the latter two viruses generate minimal levels of dsRNA (Fig. 1, B and C) (*15*), but induce high levels of IFN-α (Fig. 1, A and E, and fig. S4), whereas EMCV and SFV induce high levels of dsRNA (Fig. 1, B and C, and fig. S3) (*16*), but lower levels of IFN-α (Fig. 1E and fig. S4). Collectively, these data indicate that neither IFN-α induction nor the inhibitory effect of NS1 correlates with the presence of dsRNA.

SeV and ΔNS1 influenza are recognized by RIG-I, whereas EMCV is recognized by MDA5 (*6*, *7*). Therefore, we investigated whether the virus-specific effects of NS1 reflected its ability to interact with RIG-I. Consistent with this possibility, RIG-I tagged with green fluorescent

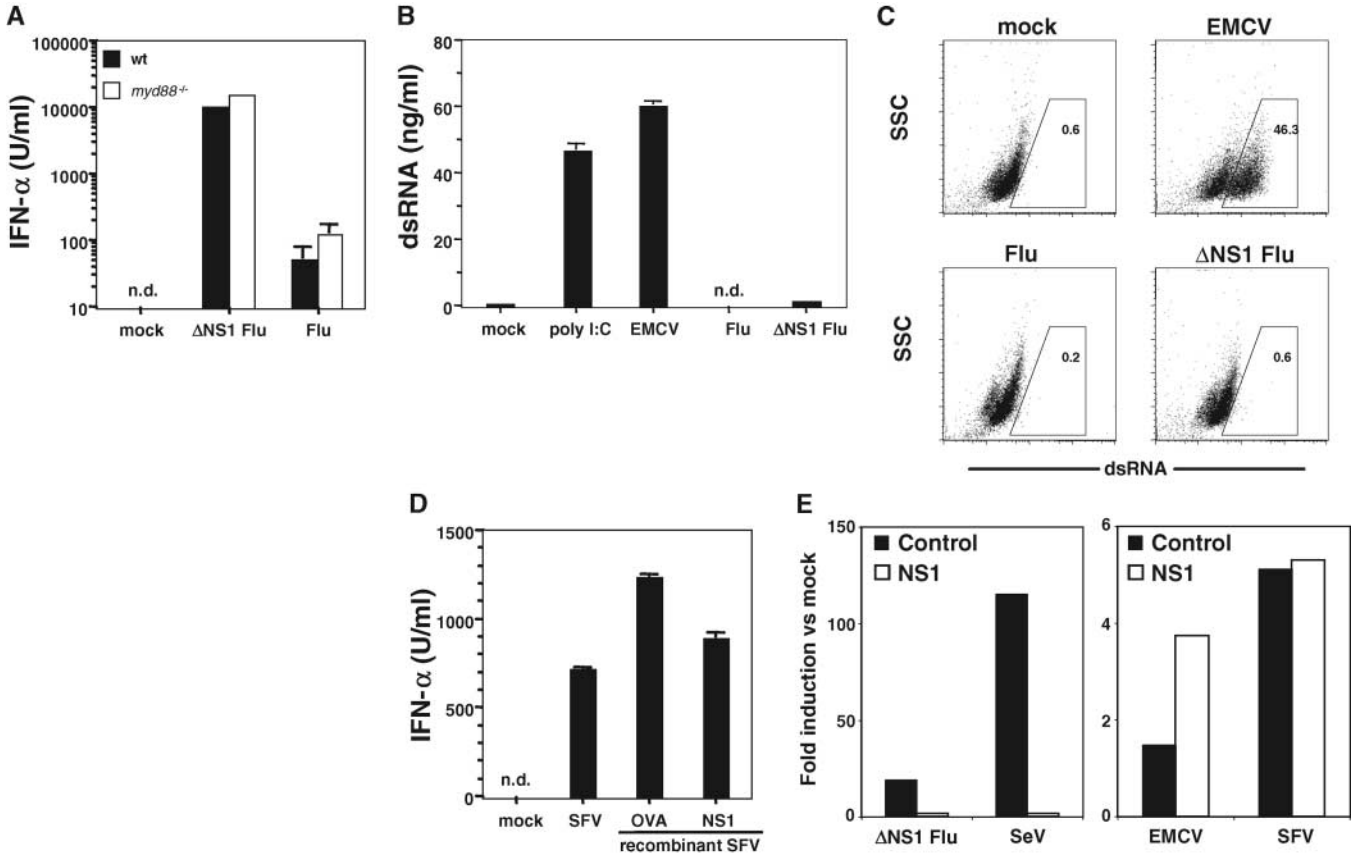

Fig. 1. Neither NS1 inhibition nor the induction of IFN-α/β correlates with viral dsRNA. (**A**) BM-DC from C57BL/6 (wt) or *myd88*$^{-/-}$ mice were cultured overnight in medium alone (mock) or with wild-type or ΔNS1 influenza virus. Data are average IFN-α levels of triplicate samples. (**B** and **C**) dsRNA in Vero cells 6 hours after infection with influenza virus or EMCV or after transfection with poly I:C measured by enzyme-linked immunosorbent assay (B) or flow cytometry (C). Numbers in (C) indicate the percentage of cells in gate. SSC, side scatter. (**D**) Same as (A), but cells were infected with wild-type SFV or recombinant SFV encoding NS1 or an irrelevant protein [ovalbumin (OVA)]. (**E**) Induction of luciferase activity in human embryonic kidney (HEK) 293 cells cotransfected with IFN-β reporter plasmids together with NS1-encoding plasmid or control empty vector and subsequently infected with the indicated viruses. Error bars in (A), (B), and (D) show means + SD. n.d., none detectable.

protein (GFP) or a hemagglutinin peptide (HA) coprecipitated with NS1 from postnuclear lysates of influenza-infected cells (Fig. 2, A and B). In addition, the cytoplasmic fraction of NS1 colocalized with GFP–RIG-I in infected cells (Fig. 2C). In contrast, MDA5 did not associate with NS1 in infected cells (Fig. 2B). These results suggest that NS1 selectively targets RIG-I rather than dsRNA during influenza virus infection.

Given the lack of dsRNA in infected cells, we addressed whether RIG-I might be activated directly by the influenza ssRNA genome. Transfection with genomic RNA extracted from influenza virions (flu vRNA) induced potent activation of the IFN-β reporter (Fig. 3A) and production of IFN-α and interleukin (IL)–6 by BM-DC at levels comparable or superior to those obtained by transfection with poly I:C (Fig. 3C). This was not due to the generation of progeny virus because flu vRNA transfection did not result in viral replication (Fig. 3B), consistent with the evidence that vRNA from negative strand viruses is not infectious (*17*). The response to flu vRNA was RIG-I dependent, given that it was inhibited by dominant negative RIG-I or by small interfering RNA (siRNA)–mediated knockdown of RIG-I in either mouse or human cells (Fig. 3D and fig. S5). RIG-I blocked responses to SeV but not EMCV (Fig. 3D), as expected (*6*), confirming the specificity of RIG-I reduction. NS1 suppressed the response to flu vRNA, and this was partly relieved by two point mutations previously reported to attenuate NS1 binding to RNA (*18*) (mutNS1, Fig. 3A). Finally, the addition of purified RIG-I to flu vRNA led to the formation of complexes with high molecular weight (Fig. 3E), demonstrating that RIG-I directly binds the influenza genome. Thus, RIG-I recognizes influenza ssRNA genomes and signals for cytokine production unless suppressed by NS1.

Mouse mRNA, total mammalian RNA [consisting of ~70% ribosomal RNA (rRNA)], and mammalian or bacterial tRNA did not elicit IFN responses (fig. S6), suggesting that RIG-I recognition is specific for viral RNA. Influenza vRNA is uncapped (*17*), and phosphorylated 5′

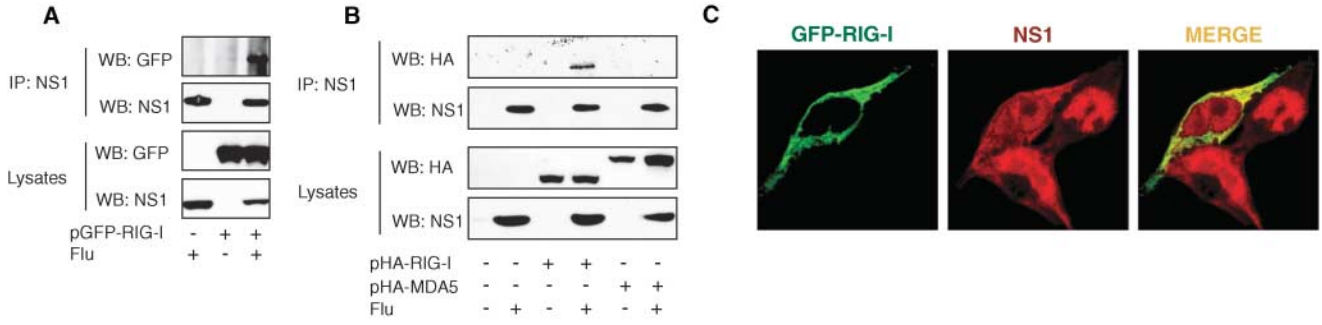

Fig. 2. The NS1 protein of influenza A virus interacts with RIG-I but not MDA5. (**A** and **B**) 293T cells were transfected with pGFP–RIG-I (A) or with pHA–RIG-I or pHA-MDA5 (B), and 12 hours later they were infected or not infected with influenza virus, as indicated. At 24 hours, cells were lysed and analyzed by Western blot (WB) for the presence of NS1 and GFP (A) or NS1 and HA (B) in total cell lysates (lower panels) or after immunoprecipitation (IP) with an antibody to NS1 (upper panels). (**C**) 293T cells were transfected with GFP–RIG-I, infected with influenza virus at 16 hours, and stained for NS1 at 24 hours. Shown are GFP–RIG-I, NS1, and the merged image.

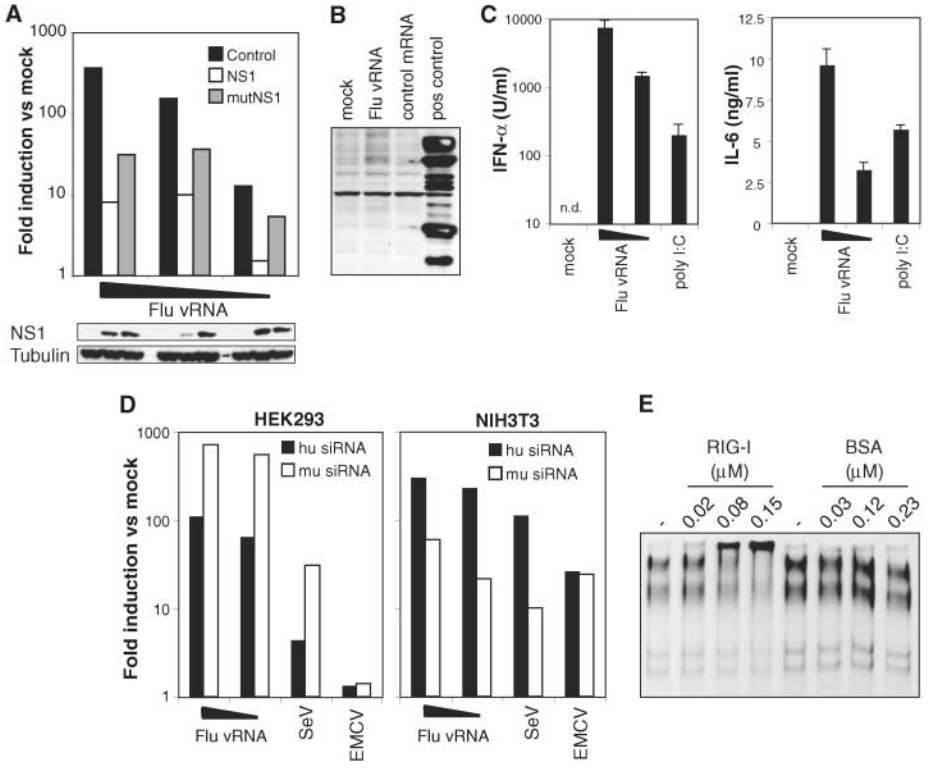

Fig. 3. Influenza vRNA triggers innate responses in a RIG-I–dependent manner. (**A**) HEK293 cells were cotransfected with IFN-β reporter plasmids and NS1 expression plasmid (NS1 or mutNS1) or empty vector (control). After 24 hours, cells were transfected with flu vRNA (0.2, 0.04, or 0.008 μg) and luciferase activity was measured at 38 hours. Western blots show the presence of NS1 or tubulin. (**B**) Lysates from cells transfected with flu vRNA or control mouse mRNA were probed with polyclonal antibody against influenza proteins. Influenza-infected cells served as positive (pos) control. (**C**) IFN-α and IL-6 accumulation in overnight culture supernatants from BM-DC that were mock treated or transfected with flu vRNA (1 and 0.2 μg) or poly I:C (0.5 μg). n.d., none detectable. Error bars show means + SD. (**D**) Inhibition of responses to flu vRNA by RIG-I reduction. Human HEK293 cells and mouse NIH 3T3 cells were cotransfected with IFN-β reporter plasmids and siRNAs specific for mouse or human RIG-I. After 72 hours, cells were transfected with flu vRNA (0.2 or 0.04 μg) or were infected with SeV or EMCV. Luciferase activity was measured at 86 hours. (**E**) Cold electrophoretic mobility shift assay analysis of RIG-I and flu vRNA interaction. Flu vRNA (1.08 nM) was incubated with the indicated concentrations of purified FLAG–RIG-I or bovine serum albumin (BSA) and resolved by electrophoresis. RNA was visualized by SYBR Green staining.

termini present in siRNA and ssRNAs generated by in vitro transcription have been reported to induce IFN-α/β when transfected into cells (*19*). We confirmed the latter observation (fig. S7) and tested whether flu vRNA recognition similarly depends on the presence of 5′-phosphates. Treatment with calf intestinal phosphatase (CIP) completely abrogated the stimulatory properties of flu vRNA (Fig. 4, A and B). This was due to phosphatase activity rather than nonspecific effects of CIP, given that it could be blocked by inorganic phosphate or EDTA (fig. S8). Furthermore, CIP did not affect the ability of vRNA to stimulate TLR7-dependent IFN-α production from pDC-containing cell populations (fig. S8). Vesicular stomatitis virus (VSV) also has an uncapped genome (*17*) and is recognized by RIG-I (*6*). Similar to influenza, transfection with VSV vRNA induced an IFN response, which was completely abrogated by previous CIP treatment (Fig. 4, C and D). Consistent with the evidence that EMCV is not recognized by RIG-I (*6*, *7*), EMCV vRNA failed to induce a response when transfected into cells at amounts comparable to flu or VSV vRNA (Fig. 4C). These data suggest that cells use RIG-I to respond to the phosphorylated 5′ termini of uncapped ssRNA viral genomes.

Finally, we assessed whether 5′ phosphorylation contributes to RIG-I binding. In vitro transcribed RNA formed a complex with RIG-I in cell lysates, which was less resistant to salt extraction when the RNA was pretreated with CIP (Fig. 4E). In vitro binding assays that used purified RIG-I confirmed that complexes with CIP-treated RNA were less stable (fig. S9). Notably, the addition of control but not CIP-treated RNA to cell lysates promoted the formation of a complex containing NS1 and RIG-I (Fig. 4F), mimicking the association seen in infected cells (Fig. 2). RIG-I associated only weakly with the NS1 mutant (mutNS1, Fig. 4F), which binds ssRNA poorly when compared with wild-type protein (fig. S10). Thus, RIG-I preferentially forms stable complexes with RNA that contains phosphorylated 5′ ends and NS1 is recruited to such complexes at least in part through its RNA binding domain.

The ability to sense viral presence is critical for initiating innate and adaptive immunity to viral infection. We found that virus recognition can be accomplished by RIG-I–mediated sensing of ssRNA viral genomes bearing 5′-phosphates. This can be blocked by viral antagonists such as the NS1 protein of influenza A virus, which is found in a complex with RIG-I (supporting online material text). Our results demonstrate that the repertoire of antiviral defense strategies includes the detection of cytoplasmic ssRNA, explaining how some viruses that produce little or no dsRNA (*15*) can be efficiently recognized, even before viral replication (*20*). Consistent with the evidence that RIG-I can bind to dsRNA in vitro (*4*, *5*), our data do not exclude the possibility that the complex of RIG-I and ssRNA is stabilized by the presence of intramolecular double-stranded regions, such as the panhandle structures that are found at the ends of the influenza genome (*17*). However, this is not sufficient to induce RIG-I activation unless the ssRNAs also contain phosphorylated 5′ termini. Notably, many RNA viruses have uncapped RNAs bearing 5′-triphosphates. In picornaviruses, a notable exception, the vRNA is covalently linked to a small protein, VPg (*17*), perhaps explaining why EMCV cannot be recognized by RIG-I (*6*, *7*). The 5′-phosphates are also absent from self-mRNA as a result of the addition of a 7-methyl-guanosine cap and may be largely inaccessible in rRNA and tRNA, through association with ribosomal proteins or formation of cloverleaf structures containing 3′ overhangs. Thus, the cytoplasmic presence of RNA containing accessible 5′-phosphates allows discrimination between self and viral RNA, indicating that, similar to dsRNA, 5′ phosphate–bearing ssRNA constitutes a viral "pathogen-associated molecular pattern" (*21*). This finding, added to the recent discovery of innate sensing of cytoplasmic DNA (*22*–*24*), suggests a parallel

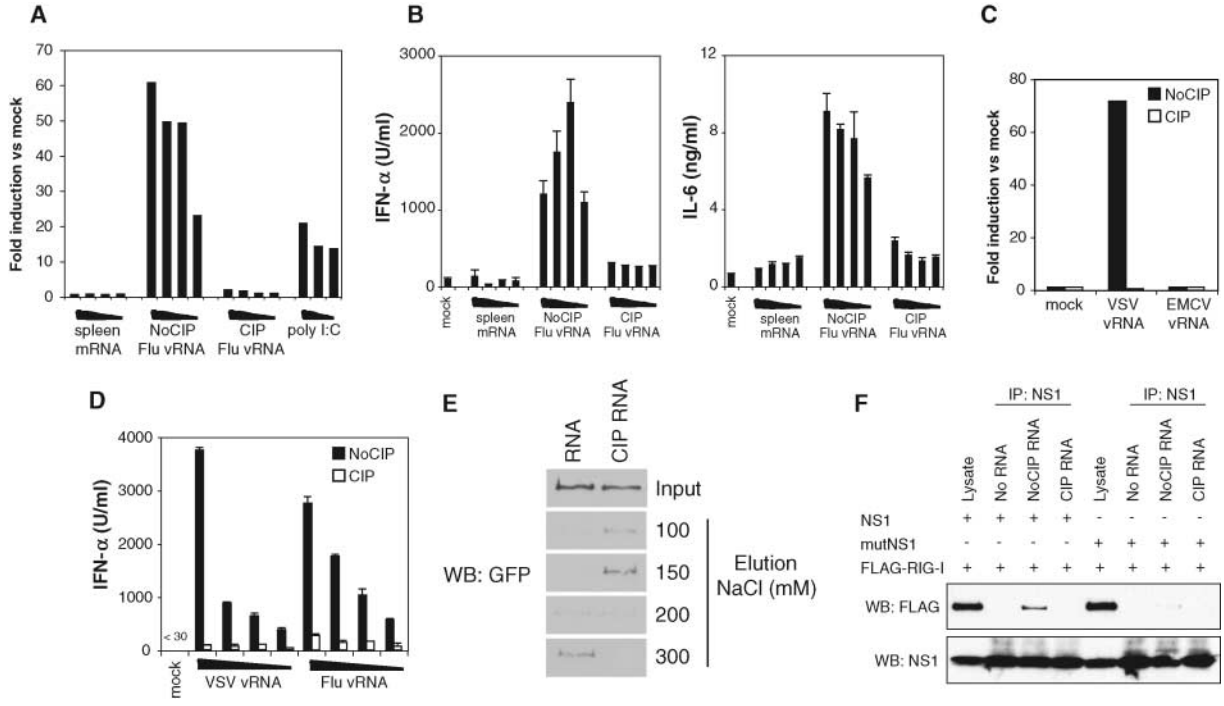

Fig. 4. ssRNAs containing phosphorylated 5′ ends bind RIG-I and activate antiviral responses. HEK293 cells transfected with IFN-β reporter and Renilla luciferase control plasmids (**A** and **C**) or BM-DC (**B** and **D**) were transfected with different amounts (0.6, 0.2, 0.06, or 0.02 μg) of mouse spleen mRNA or flu vRNAs, or with vRNA from 8×10^7 plaque-forming units VSV (C) or fivefold serial dilutions thereof (D). RNAs were pretreated with CIP or not (NoCIP). Luciferase activity [(A) and (C)] or IFN-α and IL-6 [(B) and (D)] were measured after overnight culture. (**E**) In vitro transcribed biotinylated RNA was treated with or without CIP, bound to streptavidin beads, and incubated with lysates from 293T cells transfected with GFP–RIG-I. Data show protein eluted from the beads by washing with buffer containing the specified NaCl concentrations. (**F**) Lysates of 293T cells cotransfected with pFLAG–RIG-I and pCAAGS-NS1 or pCAAGS-mutNS1 were incubated with or without 7SK-as RNA that had been either mock or CIP treated. After immunoprecipitation (IP) with the antibody to NS1, the presence of RIG-I and NS1 was analyzed by Western blot (WB).

between cytosolic and endosomal viral recognition, with MDA5, RIG-I, and the cytosolic DNA receptor constituting functional homologs of TLR3, TLR7, TLR8, and TLR9. Similar to virologists, the innate immune system may therefore have learned to classify viruses by their genomes.

References and Notes

1. A. N. Theofilopoulos, R. Baccala, B. Beutler, D. H. Kono, *Annu. Rev. Immunol.* **23**, 307 (2005).
2. T. Kawai, S. Akira, *Nat. Immunol.* **7**, 131 (2006).
3. M. Yoneyama *et al.*, *Nat. Immunol.* **5**, 730 (2004).
4. M. Yoneyama *et al.*, *J. Immunol.* **175**, 2851 (2005).
5. S. Rothenfusser *et al.*, *J. Immunol.* **175**, 5260 (2005).
6. H. Kato *et al.*, *Nature* **441**, 101 (2006).
7. L. Gitlin *et al.*, *Proc. Natl. Acad. Sci. U.S.A.* **103**, 8459 (2006).
8. B. L. Jacobs, J. O. Langland, *Virology* **219**, 339 (1996).
9. A. Garcia-Sastre, C. A. Biron, *Science* **312**, 879 (2006).
10. A. Garcia-Sastre, *Virology* **279**, 375 (2001).
11. S. S. Diebold *et al.*, *Nature* **424**, 324 (2003).
12. A. Fernandez-Sesma *et al.*, *J. Virol.* **80**, 6295 (2006).
13. X. Wang *et al.*, *J. Virol.* **74**, 11566 (2000).
14. Materials and methods are available as supporting material on *Science* Online.
15. F. Weber, V. Wagner, S. B. Rasmussen, R. Hartmann, S. R. Paludan, *J. Virol.* **80**, 5059 (2006).
16. O. Schulz *et al.*, *Nature* **433**, 887 (2005).
17. D. Knipe, P. M. Howley, Eds., *Fields Virology* (Lippincott Williams & Wilkins, Philadelphia, PA, ed. 4, 2001).
18. W. Wang *et al.*, *RNA* **5**, 195 (1999).
19. D. H. Kim *et al.*, *Nat. Biotechnol.* **22**, 321 (2004).
20. S. E. Collins, R. S. Noyce, K. L. Mossman, *J. Virol.* **78**, 1706 (2004).
21. C. A. Janeway Jr., *Cold Spring Harb. Symp. Quant. Biol.* **54**, 1 (1989).
22. Y. Okabe, K. Kawane, S. Akira, T. Taniguchi, S. Nagata, *J. Exp. Med.* **202**, 1333 (2005).
23. K. J. Ishii *et al.*, *Nat. Immunol.* **7**, 40 (2006).
24. D. B. Stetson, R. Medzhitov, *Immunity* **24**, 93 (2006).

25. This work was funded by Cancer Research UK. We thank I. Kerr for SFV and EMCV, T. Muster for ΔNS1, J. Skehel for purified influenza, S. Diebold for flu vRNA isolation and GFP RNA synthesis, A. Bergthaler for VSV vRNA, J. Yewdell for the antibody to NS1, C. Basler for FLAG–RIG-I, and A. Garcia-Sastre for NS1 constructs. We are grateful to members of the Immunobiology Laboratory for support.

Supporting Online Material

www.sciencemag.org/cgi/content/full/1132998/DC1
Materials and Methods
SOM Text
Figs S1 to S10
References

25 July 2006; accepted 2 October 2006
Published online 12 October 2006;
10.1126/science.1132998
Include this information when citing this paper.

Direct Measurement of the Full, Sequence-Dependent Folding Landscape of a Nucleic Acid

Michael T. Woodside,[1,2] Peter C. Anthony,[3] William M. Behnke-Parks,[2] Kevan Larizadeh,[2] Daniel Herschlag,[4] Steven M. Block[2,5]*

Nucleic acid hairpins provide a powerful model system for understanding macromolecular folding, with free-energy landscapes that can be readily manipulated by changing the hairpin sequence. The full shapes of energy landscapes for the reversible folding of DNA hairpins under controlled loads exerted by an optical force clamp were obtained by deconvolution from high-resolution, single-molecule trajectories. The locations and heights of the energy barriers for hairpin folding could be tuned by adjusting the number and location of G:C base pairs, and the presence and position of folding intermediates were controlled by introducing single-nucleotide mismatches.

Elucidating the mechanisms by which proteins and nucleic acids fold into three-dimensional structures is key to developing insights into biomolecular function (*1*), improving predictive models (*2*, *3*), and understanding the basis of diseases linked to misfolding (*4*). For more than two decades, free-energy landscape formalisms have provided the fundamental conceptual framework for describing folding (*5*). Numerous experimental and theoretical studies have probed specific features of folding landscapes, including the properties of transition states (*6*), intermediate states (*7*), and the ruggedness of the energy surface (*8*). Experiments, however, have characterized only limited aspects of the folding landscape, such as the locations and heights of energy barriers and how these barriers change when perturbed by solvent substitutions, temperature jumps, substrate changes, or mutations (*9*). Direct measurements of the shape of an energy landscape at all points along the reaction coordinate have not been feasible. Here, we show how the full energy landscape for the formation of a nucleic acid hairpin can be derived from sufficiently high-resolution trajectories of single-molecule folding.

Single nucleic-acid hairpins subjected to mechanical loads provide a powerful model system for investigating energy landscapes and understanding the effects of primary and secondary structure on folding (*10*–*13*). The molecular end-to-end extension is recorded during the folding transition and supplies a natural reaction coordinate that can be related directly to the number of bases paired in the hairpin stem. Previous work has characterized specific aspects of the folding landscape. In particular, short hairpins tend to fold as simple, two-state systems (*10*, *13*), indicative of a single-transition energy barrier. Conventional analysis of single-molecule records supplies the free-energy difference between the folded and unfolded states, as well as the height and location of the barrier (*10*). For hairpins with random (unpatterned) stem sequences, the barrier is typically located close to the unfolded state, with a height controlled largely by the size of the loop (*13*). However, finer details of the folding landscape have been heretofore inaccessible, due to limited spatial and temporal resolution, as well as instrumental baseline drift. Using a high-bandwidth, passive force clamp with an ultra-stable dumbbell assay (*14*), we have now been able to reconstruct the shape of the landscape.

Sets of DNA hairpins were synthesized in which the heights and locations of energy barriers were systematically varied, as well as the numbers and locations of any folding intermediates. Sequences were designed based on a model of the sequence-dependent energy landscape derived from the thermodynamic and mechanical properties of nucleic acids (*13*, *15*). Both ends of the hairpins were attached to long handles of double-stranded DNA (dsDNA) (*13*) bound specifically to polystyrene beads held in a dumbbell configuration by two independently controlled optical traps (Fig. 1A). A constant force, F, was applied with a force clamp (*14*), and high-resolution trajectories of the end-to-end extension (~0.1 nm/√Hz) were recorded for a range of forces. The extensions of folded, unfolded, and any intermediate states were measured directly from these records. The locations and heights of energy barriers between these states were computed from the force-dependence of the state lifetimes (*10*, *13*). These measurements of specific points on the landscape were then taken as benchmarks for an experimental determination of the free energy at every point along the reaction coordinate, deconvolving the measured probability distribution of hairpin extension to correct for blurring effects arising from thermal motions associated with the beads and the DNA tether.

A typical record of extension under load (Fig. 1B) shows two-state folding behavior: Two nearly Gaussian peaks in the extension histogram correspond to the folded and unfolded states. Here, $F \approx F_{1/2}$, the load at which the hairpin spends equal time in each state. The lifetimes of the folded (τ_f) and unfolded (τ_u) states depend exponentially on F according to $\tau_f(F) \propto$

[1]National Institute for Nanotechnology, National Research Council of Canada, Edmonton AB, Canada, T6G 2M9. [2]Department of Biological Sciences, [3]Biophysics Program, [4]Department of Biochemistry, [5]Department of Applied Physics, Stanford University, Stanford, CA 94305, USA.

*To whom correspondence should be addressed. E-mail: sblock@stanford.edu

$\exp(-F\Delta x_f^{\ddagger}/k_BT)$, where $\Delta x_f^{\ddagger}$ is the distance to the barrier from the folded state and k_BT is the thermal energy (*16*); an analogous expression holds for $\tau_u(F)$. Previously, the transition state (TS) for folding a hairpin with an unpatterned stem sequence was found to involve the formation of 1 or 2 base pairs adjacent to the loop (*13*), resulting in an energy barrier near the unfolded state. In contrast, the barrier for the hairpin in Fig. 1B lies much closer to the folded ($\Delta x_f^{\ddagger} = 5.4 \pm 0.5$ nm) than to the unfolded state ($\Delta x_u^{\ddagger} = 13 \pm 1$ nm), which implies that the TS requires the formation of ~15 base pairs. This difference in behavior is due to the particular sequence selected for the hairpin: A contiguous block of strong G:C base pairs placed near the base of an A:T-rich stem moves the barrier nearer to the folded state (Fig. 1B, inset).

We created a family of hairpins in which the TS position was systematically manipulated by moving the block of G:C base pairs to various locations within the stem (table S1). Determining the barrier location for each hairpin, we found that the TS moved in concert with the G:C block, always located at the edge of the block nearest the loop (Fig. 1C and table S2). The sum of $\Delta x_f^{\ddagger}$ and $\Delta x_u^{\ddagger}$ agreed well with the distance between folded and unfolded states (Δx), as expected for a pure two-state system. Measurements were in excellent agreement with landscape model predictions (Fig. 1C).

We also created a family of hairpins where the barrier position was fixed at the center of the stem using a G:C block, but the barrier height was altered by changing the overall stem G:C content (table S1). State lifetimes measured at $F_{1/2}$ for each hairpin (*17*) varied by a factor of ~600 over the entire family (Fig. 1D and table S2). Assuming Arrhenius behavior for the lifetimes, $\tau_{1/2} = \tau_0 \exp(\Delta G^{\ddagger}_{1/2}/k_BT)$, where $\Delta G^{\ddagger}_{1/2}$ is the barrier height at $F_{1/2}$ and τ_0^{-1} is the attempt rate at zero force, these results show that the barrier height changed by $6.4 \pm 0.7\ k_BT$, matching the variation predicted by the model, $6.9 \pm 0.2\ k_BT$. Altogether, the results of Fig. 1 confirm the remarkable level of control afforded by this system over the folding landscape: The TS can be placed at will along the reaction coordinate and its energy adjusted over a wide range simply by manipulating the hairpin sequence.

Extension records such as those in Fig. 1B and (*10*, *12*, *13*) have traditionally been interpreted in terms of two-state folding over a single energy barrier. However, not all hairpin sequences exhibit strict, two-state folding behavior. For example, it was recently reported that the nominal "folded state" may, in fact, consist of an ensemble of states comprised of the folded state plus a series of frayed states with one or more base pairs unzipped (*13*). Moreover, short-lived intermediate states may be present that are unobservable at the available temporal resolution (*18*). Simple two-state analysis ignores details of the trajectory between folded and unfolded states because the motion is taken to be instantaneous, and properties of the energy landscape are inferred only from characteristics of the two states. To induce the hairpin to spend more time between folded and unfolded states, and to observe intermediate properties during folding more clearly, we manipulated the sequence to produce a local potential well between the folded and unfolded states by inserting a single T:T mismatch at various positions along the hairpin stem.

When the mismatch was placed at the seventh base pair from the base of the stem, extension records at $F \approx F_{1/2}$ revealed a shoulder on the histogram peak at low extension (nominally, the folded state), indicative of a third peak represent-

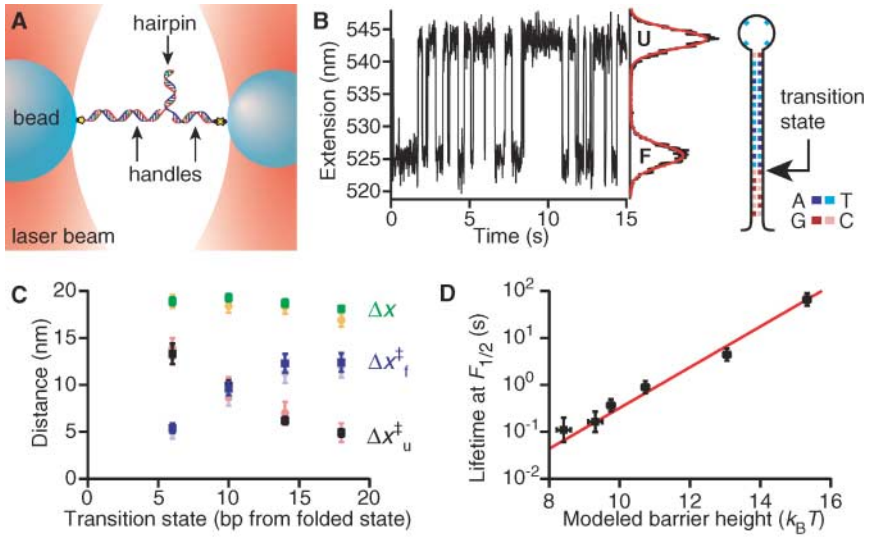

Fig. 1. (**A**) Cartoon of the experimental geometry, showing a DNA hairpin attached at each end to dsDNA handles bound to two optically trapped beads (not to scale). (**B**) Extension record of a hairpin designed with an energy barrier 6 bp from the base of the stem (sequence at right) displays two states, folded (F) and unfolded (U). (**C**) Unfolding distance Δx (green) and distance to barrier from unfolded state $\Delta x^{\ddagger}_u$ (black) and folded state $\Delta x^{\ddagger}_f$ (blue), as a function of the expected transition state location. Data (±SEM) agree well with model predictions for Δx (yellow), $\Delta x^{\ddagger}_u$ (red), and $\Delta x^{\ddagger}_f$ (purple). (**D**) Lifetime of folded/unfolded states at $F_{1/2}$ as a function of the expected barrier height. The lifetime rises exponentially with the modeled barrier height, with slope $(k_BT)^{-1}$ (red line).

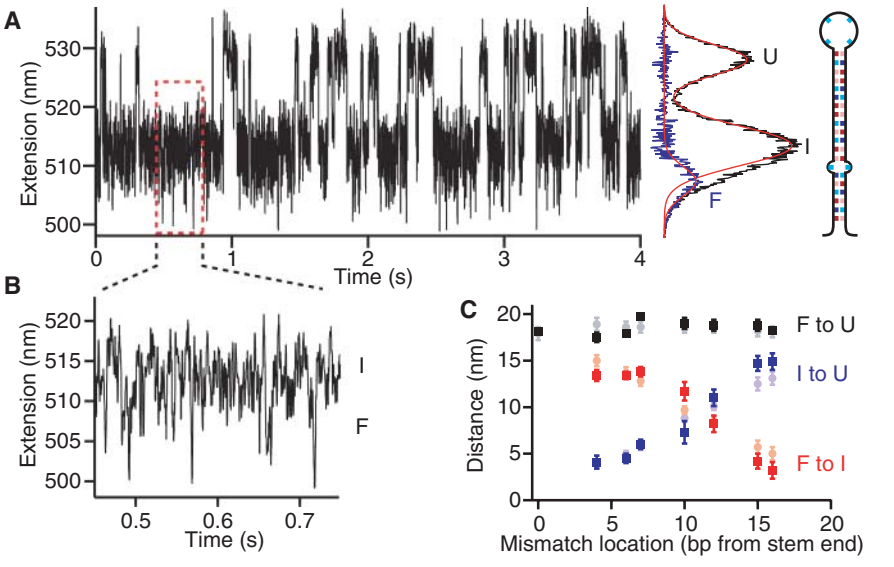

Fig. 2. (**A**) Extension record of hairpin with a T:T mismatch 7 bp from the base of the stem (sequence at right). Fit of extension histogram to two Gaussian peaks reveals a third Gaussian residual (fits in red, residual in blue), indicating three states: unfolded (U), intermediate (I), and folded (F). (**B**) Blow-up of the extension record shows rapid, ~5-nm fluctuations between F and I states. (**C**) Distance from F to U (black), F to I (red), and I to U (blue) plotted versus the mismatch location. The intermediate state location moves in concert with the mismatch, in good agreement with model predictions (light-colored solid circles in gray, orange, purple), which indicates that the intermediate state consists of a hairpin folded up to the mismatch.

ing an intermediate state (Fig. 2A). Such a shoulder was observed systematically in all records, but associated only with the low-extension peak. The existence of an intermediate state may also be inferred from the rapid fluctuation of ~5-nm amplitude recorded at low extensions (Fig. 2B). Similar results were obtained by introducing an A:A or a G:T mismatch, rather than T:T. Repeating these measurements for an entire family of hairpins with mismatches located 4 to 16 base pairs (bp) from the base of the stem (table S1), we consistently observed the signature of an intermediate state, whose distance from the folded and unfolded states depended on the location of the mismatch (Fig. 2C; table S2). When we interpret the hairpin extension in terms of the number of base pairs formed, the intermediate states correspond to hairpins partially folded up to the point of mismatch.

These results demonstrate the precision with which certain features of the folding landscape can be determined, but they define only a few key points on the energy landscape. Notably, they don't address more general features of the landscape, such as the widths and curvatures of the potential wells or barriers, which are known to affect folding (*19*). By further analyzing the folding trajectories, however, the entire landscape along the reaction coordinate can be reconstituted. The free energy at a given extension, $\Delta G(x)$, is related to the probability density, $P(x)$, through $\Delta G(x) = -k_B T \ln[P(x)]$ (*20*). Although conceptually straightforward, this method of determining $\Delta G(x)$ requires accurate measurements of $P(x)$ in the region between the states, where the hairpin spends little time (~100 to 300 μs, here). Hundreds to thousands of transitions must therefore be sampled at high bandwidth, necessitating exceptional instrumental stability. A second complication is that the measured extension represents that of a hairpin attached to dsDNA handles and beads, rather than an isolated hairpin. The thermal and mechanical properties of the trapped dumbbell smooth and dampen the apparent motions of the hairpin (*13*). The underlying energy landscape may be recovered from $P(x)$, however, by a deconvolution process.

To reconstruct the full energy landscape, we measured the folding trajectory of single hairpins at $F \approx F_{1/2}$ at high bandwidth (50 kHz) for 5 to 15 min and created a histogram of the extension, $P(x)$. Instrumental drift was typically ≤1 nm. The point spread function (PSF) for the deconvolution, $S(x)$, was estimated from extension histograms of the folded state for a hairpin with 100% stem G:C content and found to be a Gaussian curve (fig. S2), whose width is governed by the stiffness of the trapped dumbbell (*14*). The energy landscape was then determined by a constrained nonlinear iterative deconvolution (*21*) of the extension histogram. An initial guess for the potential, $\Delta G^{(0)}(x)$, was constructed by assuming parabolic potential wells located at the histogram maxima, separated by a parabolic barrier whose height and position were determined from the measured, force-dependent rates (as in Fig. 1). The associated extension probability $p^{(0)}(x)$ was then convolved with the PSF and compared with $P(x)$. The difference was subtracted from $p^{(0)}(x)$, constraining the probability to be between 0 and 1, and the process was iterated (*15*). The solutions, $p^{(n)}(x)$, and associated landscapes, $\Delta G^{(n)}(x)$, are shown in Fig. 3, along with the measured $P(x)$, $\Delta G(x)$, and residuals $R(x) = P(x) - S(x) \otimes p^{(n)}(x)$, for four different hairpin sequences designed to explore a range of barrier positions, heights, and possible intermediate states. Shown in Fig. 3 are a 20-bp stem with a TS located 18 bp from the base of the stem (Fig. 3A), a 20-bp stem with TS located 6 bp from the base of the stem (Fig. 3B), a 20-bp stem with T:T mismatch located 7 bp from the end of the stem (Fig. 3C), and an unpatterned stem sequence of length 30 bp (Fig. 3D). In all four cases, the deconvolution algorithm generated a stable solution with acceptably small residuals.

The subtle differences seen in $P(x)$ and $\Delta G(x)$ were sharpened by the deconvolution procedure into recognizably different landscapes that reflected the underlying sequence and recapitulated the results in Figs. 1 and 2. In Fig. 3A, the barrier is located near the unfolded state, whereas in Fig. 3B it is nearer the folded state. The hairpin in Fig. 3C, which contains a mismatch, shows a clearly-resolved intermediate state, corresponding to partial folding up to the point of mismatch. These measurements go beyond the previous results, however, by revealing details of the well and barrier shapes. For example, the en-

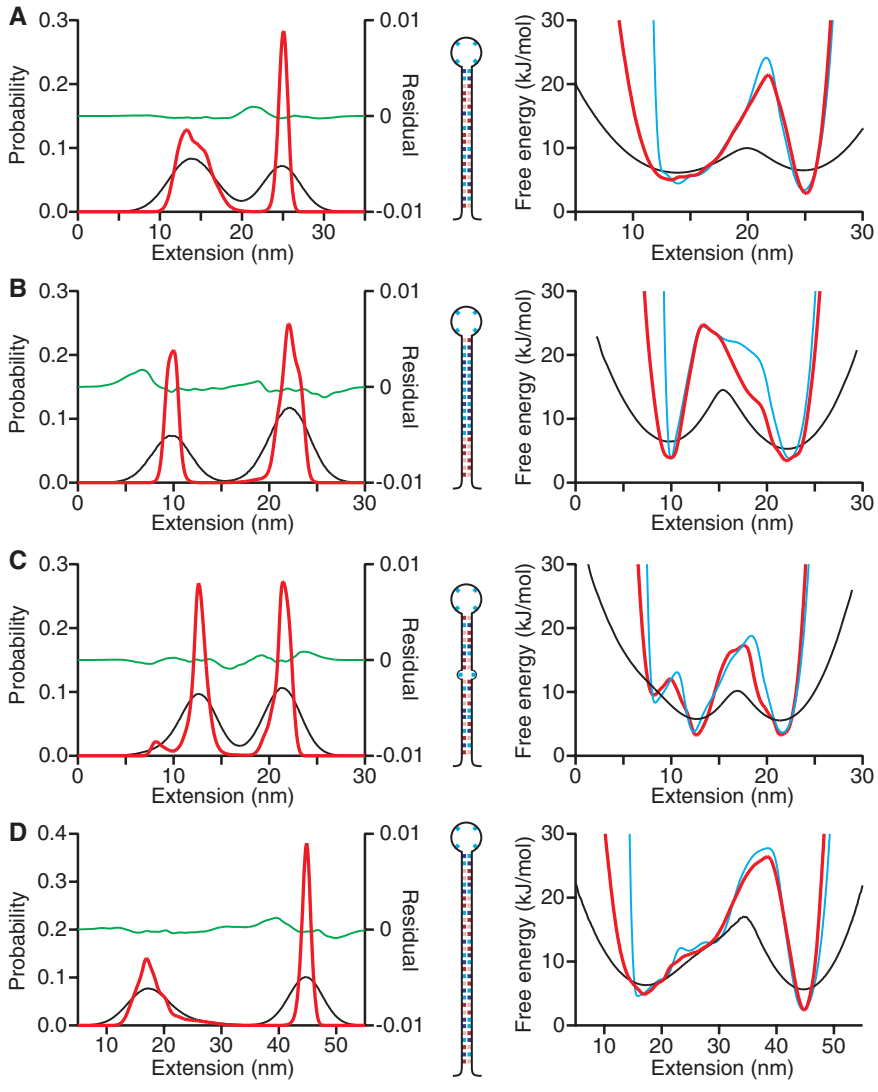

Fig. 3. Potential landscapes determined by deconvolution of the extension histograms based on thousands of folding transitions. Experimental probability distributions and associated free-energy landscapes (black) were deconvolved to remove the effects of blurring caused by thermal motions of beads attached to the hairpin via elastic handles. Probability distributions (left column) and landscapes (right column) recovered by Gaussian deconvolution (red) have small residual errors (green) and agree well with energy landscapes predicted by the model (blue). (**A**) Hairpin with a transition state 18 bp from the base of the stem. (**B**) Hairpin with a transition state 6 bp from the base of the stem. (**C**) Hairpin with a T:T mismatch 7 bp from the base of the stem. (**D**) Hairpin with an unpatterned, 30-bp stem sequence.

ergy minimum for the folded state in Fig. 3A is significantly broader than that in Fig. 3B: The width of this well supplies direct evidence that the nominally folded state for this hairpin actually consists of an ensemble of states with up to ~4 bp unzipped. A similar situation is seen in Fig. 3D, although the slightly steeper well suggests that the fully folded state plays a more dominant role in this mixed ensemble than it does in Fig. 3A. The energy barriers in Figs. 3A and D are clearly different: The barrier in Fig. 3D is wider than in Fig. 3A, indicating a TS that is less well-defined and therefore more susceptible to experimental perturbation, e.g., by mutagenesis or solvent condition changes.

To explore the validity of these measurements, we compared the experimental landscapes with predictions of the model (Fig. 3). We found excellent agreement across the entire landscape for all hairpins studied (within $<1\ k_BT$), with two exceptions. At the lowest extensions, corresponding to regions deconvolved from physical compressions of the double helix (which can arise from thermal fluctuations), as well as elongations, the experimental potential is systematically less stiff than the model. This discrepancy may be attributable to an inaccurate description of the confining potential, somewhat arbitrarily taken to be a Morse potential (*22*). In addition, the barrier for exiting the unfolded state in Fig. 3B rises to the TS more slowly than predicted, lagging by up to $3\ k_BT$ at the point of greatest discrepancy. We speculate that this deviation may result from the large number of base pairs that must be formed to reach the TS from the unfolded state, which allows more opportunities for abortive refolding attempts involving misfolded base pairs. In principle, the sequence for this particular hairpin allows for a number of misfolded states containing short, 2- to 3-bp helices. Any such misfolding, neglected in the model, would tend to increase the probability of extensions near the unfolded state, exactly as observed.

The deconvolution approach described here has known limitations. To obtain adequate statistics, folding must occur sufficiently frequently that large numbers of transitions can be recorded. In the present case, this places a practical limit on the folding rate of $\sim 0.1\ s^{-1}$, which is faster than some slow folding transitions found in proteins or ribozymes. The numerical stability of any deconvolution process depends on the quality of the input data (both for the record being analyzed and the PSF used). In practice, only a limited range of frequency information can be recovered by deconvolution, which restricts the resolution of the reconstructed landscape, particularly at the shortest length scales (*23*). Moreover, experimental noise may become amplified by deconvolution, which produces artifactual features that further complicate determinations of short-scale behavior (*21*) The challenges posed by deconvolution, however, may be mitigated by increasing the stiffness of the experimental system, which reduces the smoothing of trajectories (*24*). Improvements may be achieved by increasing the stiffness of the handles (e.g., by making them shorter or from materials other than dsDNA). Application of the approach described here to peptides or more complex nucleic acid sequences may supply further insights into how energy landscapes guide the folding process.

References and Notes

1. A. Fersht, *Structure and Mechanism in Protein Science* (Freeman, New York, 1999).
2. D. Petrey, B. Honig, *Mol. Cell* **20**, 811 (2005).
3. P. Bradley, K. M. S. Misura, D. Baker, *Science* **309**, 1868 (2005).
4. C. M. Dobson, *Nature* **426**, 884 (2003).
5. J. N. Onuchic, P. G. Wolynes, *Curr. Opin. Struct. Biol.* **14**, 70 (2004).
6. V. Daggett, A. R. Fersht, *Trends Biochem. Sci.* **28**, 18 (2003).
7. P. S. Kim, R. L. Baldwin, *Annu. Rev. Biochem.* **59**, 631 (1990).
8. C. Hyeon, D. Thirumalai, *Proc. Natl. Acad. Sci. U.S.A.* **100**, 10249 (2003).
9. J. Buchner, T. Kiefhaber, Eds., *Protein Folding Handbook* (Wiley-VCH, Weinheim, Germany, 2005).
10. J. Liphardt, B. Onoa, S. B. Smith, I. Tinoco Jr., C. Bustamante, *Science* **292**, 733 (2001).
11. B. Onoa *et al.*, *Science* **299**, 1892 (2003).
12. P. T. X. Li, D. Collin, S. B. Smith, C. Bustamante, I. Tinoco Jr., *Biophys. J.* **90**, 250 (2006).
13. M. T. Woodside *et al.*, *Proc. Natl. Acad. Sci. U.S.A.* **103**, 6190 (2006).
14. W. J. Greenleaf, M. T. Woodside, E. A. Abbondanzieri, S. M. Block, *Phys. Rev. Lett.* **95**, 208102 (2005).
15. Materials and methods are available as supporting material on *Science* Online.
16. G. I. Bell, *Science* **200**, 618 (1978).
17. Because all lifetimes were measured at $F_{1/2}$, the folded and unfolded states were nearly isoenergetic for every hairpin, and Hammond behavior was neither expected nor observed.
18. J. M. Fernandez, S. Chu, A. F. Oberhauser, *Science* **292**, 653 (2001).
19. H. A. Kramers, *Physics* **7**, 284 (1940).
20. Experimentally determined probability densities have been used to measure the energy landscape for a micron-scale bead hopping between adjacent optical traps (*25*), to probe the elasticity of kinesin molecules (*26*), and to support the existence of otherwise hidden intermediate states based on thermal fluctuations (*27*), but not to measure the energy landscape for a molecular transition.
21. P. A. Jansson, Ed., *Deconvolution of Images and Spectra* (Academic Press, New York, ed. 2, 1997).
22. A likely explanation for the weak confining potential observed experimentally is that the hairpin can rotate, effectively producing extensions lower than the folded state as the handles move past one another, driven by thermal fluctuations.
23. In practice, we found a resolution limit of ~2 nm, which includes the effects of instrumental drift.
24. We measured the probabilities and free energy in an unclamped configuration (data in Fig. 3, A to C) because passive force-clamping reduces the system stiffness (*14*).
25. L. I. McCann, M. Dykman, B. Golding, *Nature* **402**, 785 (1999).
26. S. Jeney, E. H. K. Stelzer, H Grubmüller, E.-F. Florin, *Chem Phys Chem* **5**, 1150 (2005).
27. K. A. Walther, J. Brujić, H. Li, J. M. Fernandez, *Biophys. J.* **90**, 3806 (2006).

28. We thank members of the Block lab and the Ribozyme Folding Project for helpful discussions and manuscript comments. Supported by NIH PO1-GM066275.

Supporting Online Material

www.sciencemag.org/cgi/content/full/314/5801/1001/DC1
Materials and Methods
Figs. S1 and S2
Tables S1 and S2
References

8 August 2006; accepted 29 September 2006
10.1126/science.1133601

Ion Selectivity in a Semisynthetic K^+ Channel Locked in the Conductive Conformation

Francis I. Valiyaveetil,* Manuel Leonetti, Tom W. Muir,† Roderick MacKinnon†

Potassium channels are K^+-selective protein pores in cell membrane. The selectivity filter is the functional unit that allows K^+ channels to distinguish potassium (K^+) and sodium (Na^+) ions. The filter's structure depends on whether K^+ or Na^+ ions are bound inside it. We synthesized a K^+ channel containing the D-enantiomer of alanine in place of a conserved glycine and found by x-ray crystallography that its filter maintains the K^+ (conductive) structure in the presence of Na^+ and very low concentrations of K^+. This channel conducts Na^+ in the absence of K^+ but not in the presence of K^+. These findings demonstrate that the ability of the channel to adapt its structure differently to K^+ and Na^+ is a fundamental aspect of ion selectivity, as is the ability of multiple K^+ ions to compete effectively with Na^+ for the conductive filter.

Potassium channels are exquisitely selective for K^+ over Na^+, even though Na^+ (Pauling ionic radius 0.95 Å) is smaller than K^+ (Pauling ionic radius 1.33 Å) (*1*). The selection of K^+ and rejection of Na^+ occurs in a segment of the ion conduction pathway called the K^+ selectivity filter (*2*). The filter binds two fully dehydrated K^+ ions by providing protein oxygen atoms that offset the energy cost of ion dehydration (*3*, *4*). Conduction occurs when a third K^+ ion enters and a resident K^+ ion exits in a concerted manner. The Na^+ ion is virtually excluded from conducting through the selectivity filter (*5*, *6*).

The K^+ selectivity filter adopts a fundamentally different atomic structure depending on whether K^+ or Na^+ is present in the solution in

ERRATUM

Post date 9 February 2007

Reports: "Direct measurement of the full, sequence-dependent folding landscape of a nucleic acid" by M. T. Woodside *et al.* (10 Nov. 2006, p. 1001). On page 1002, the key in Fig. 2C is incorrect: In the legend for Fig. 2C, the descriptions of the color blocks should read "Distance from F to U (black), F to I (blue), and I to U (red) plotted versus the mismatch location." The hairpin sequence shown in Fig. 3C is also incorrect. The corrected Fig. 3C is shown here.

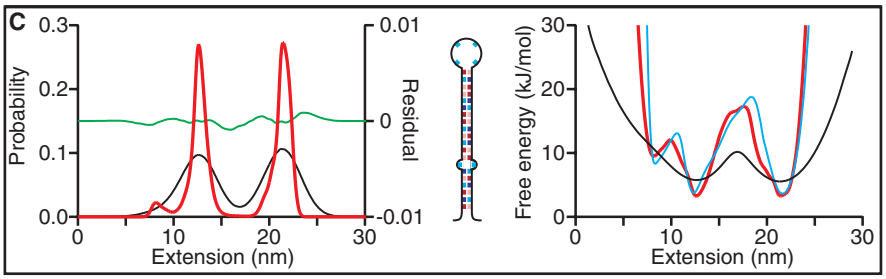

Fig. 3C

which the channel is crystallized (*3*, *4*). In solutions containing K^+ (≥20 mM), the KcsA K^+ channel selectivity filter exhibits four K^+ binding sites designated sites 1 through 4 (Fig. 1A), whereas in solutions containing Na^+ (3 mM K^+, 150 mM Na^+) the filter adopts a "collapsed" conformation that no longer contains native binding sites at sites 2 and 3 (Fig. 1B). The K^+ structure is referred to as "conductive" because the queue of K^+ ions within the filter connects the intracellular and extracellular solutions. The Na^+ structure is referred to as "nonconductive" because the filter is pinched shut in the middle. The conformational changes that occur in going from the nonconductive to the conductive structure involve protein atoms that directly coordinate K^+ ions as well as atoms buried within the protein core up to a distance of 15 Å away from the ion pathway (Fig. 1, C and D) (*4*).

The binding of K^+ ions to the filter drives the conformational change from nonconductive to conductive: In crystal structures, the transition occurs between 3 mM and 20 mM K^+ (while maintaining ionic strength constant with Na^+) (*3*). This means that Na^+ (or the absence of K^+) favors the nonconductive conformation and K^+ stabilizes the conductive conformation. At an intuitive level, this is clearly a beneficial property of a molecular device whose function is to conduct K^+ and prevent Na^+ conduction. At a more detailed analytic level, the differential response of the filter's structure to K^+ and Na^+ implies two important features of K^+ selectivity. First, ion selectivity is a property of the protein structure not just locally (at the ion-binding sites) but also globally, because the conformational changes associated with the binding of K^+ ions extend far from the binding sites. Second, ion selectivity may be inextricably linked to the multi-ion nature of the K^+ selectivity filter, because the filter must contain two K^+ ions to achieve its conductive conformation.

One way to investigate the importance of the K^+-induced conformational change is to interfere with it and see how selectivity is affected. The conformational change from conductive to nonconductive involves a rotation of the main chain at Gly^{77} that brings about occlusion of ion site 2 by the α-CH_2 of the glycine (Fig. 1, A and B). The role of Gly^{77} as a surrogate D–amino acid has been demonstrated through synthesis of a functional KcsA K^+ channel with a D-alanine at position 77 ($KcsA^{D\text{-}Ala77}$) (*7*). We have now determined the crystal structure of this channel

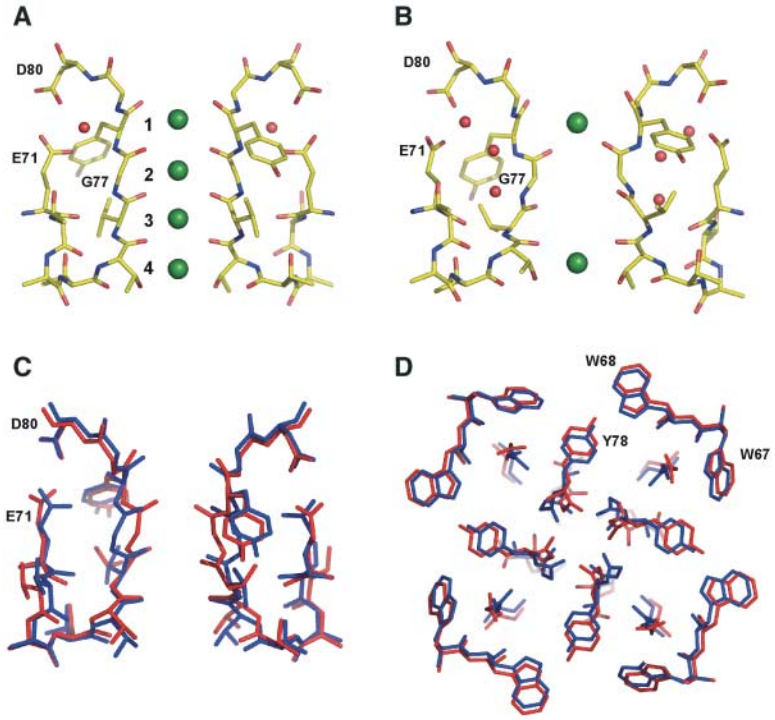

Fig. 1. Dependence of the conformation of the selectivity filter of K^+ channels on K^+ concentration. (**A**) Close-up view of the selectivity filter of wild-type KcsA channel in the presence of high K^+ concentrations [K^+]. Two of the diagonally opposite subunits are shown in stick representation. K^+ ions are depicted as green spheres and water molecules as red spheres. The K^+ binding sites in the selectivity filter are labeled. (**B**) The structure of the selectivity filter in low [K^+], represented as in (A). (**C** and **D**) Superposition of the selectivity filter of wild-type KcsA in the presence of high [K^+] (blue) and low [K^+] (red). (C) shows a side view; (D) depicts a top view extending ~15 Å out from the center of the filter. Aromatic residues that undergo conformation changes are indicated.

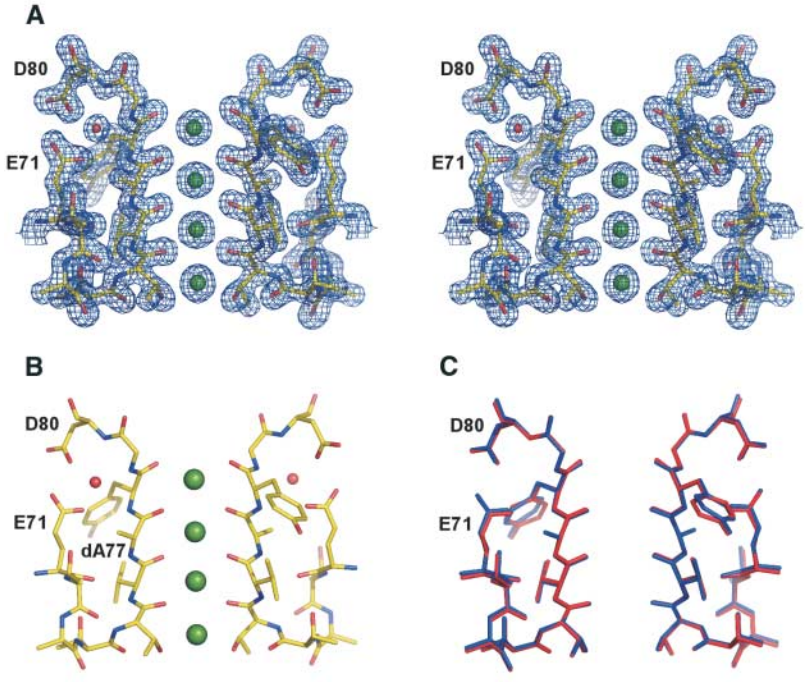

Fig. 2. Structure of the selectivity filter of $KcsA^{D\text{-}Ala77}$ in the presence of high [K^+]. (**A**) Stereo view of the electron density of the selectivity filter of $KcsA^{D\text{-}Ala77}$. The $2F_{obs} - F_{calc}$ electron density map contoured at 2.0σ for the diagonally opposite subunits is shown. (**B**) Structure of the selectivity filter of $KcsA^{D\text{-}Ala77}$ in high [K^+] represented as in Fig. 1. (**C**) Superposition of the selectivity filter of $KcsA^{D\text{-}Ala77}$ (blue) and the wild-type KcsA channel (red) in the presence of high [K^+].

Laboratories of Molecular Neurobiology and Biophysics and Synthetic Protein Chemistry, Rockefeller University and Howard Hughes Medical Institute, 1230 York Avenue, New York, NY 10021, USA, and Department of Biology, Ecole Normale Superieure, 46 rue d'Ulm, 75005 Paris, France.

*Present address: Department of Physiology and Pharmacology, Oregon Health Sciences University, 3181 SW Sam Jackson Park Road, Mail Code L334, Portland, OR 97239, USA.

†To whom correspondence should be addressed. E-mail: mackinn@rockefeller.edu (R.M.), muirt@rockefeller.edu (T.W.M.)

with data to 1.7 Å Bragg spacings in a solution containing 150 mM K^+ (Fig. 2A). Aside from the additional methyl group from D-alanine, the structure of $KcsA^{D\text{-}Ala77}$ is essentially identical to the wild-type conductive structure (Fig. 2, B and C), with a root-mean-square deviation of 0.16 Å for all non-hydrogen atoms from positions Glu^{71} to Asp^{80}.

The important aspect of $KcsA^{D\text{-}Ala77}$ for the present study is depicted in Fig. 3, A and B. Shown is the predicted structure of $KcsA^{D\text{-}Ala77}$ if it were to adopt the nonconductive conformation similar to the wild-type KcsA channel (Fig. 3B). The four methyl groups of the D-alanine (one from each subunit) should prevent this conformation because they clash with each other. Thus, in principle, $KcsA^{D\text{-}Ala77}$ should be forced to remain in the conductive conformation through destabilization of the nonconductive conformation. To test whether this is indeed the case, we determined the structure of $KcsA^{D\text{-}Ala77}$ in the presence of 149 mM Na^+ + 1 mM K^+ with data to 2.4 Å Bragg spacings. At this low K^+ ion concentration, the wild-type channel adopts the nonconductive conformation but $KcsA^{D\text{-}Ala77}$ clearly adopts the conductive conformation (Fig. 3, C and D). Electron density for ions in the filter suggests reduced occupancy. If we assume that the ions are K^+, then the sum of occupancies for all four sites is ~1.1 compared to 1.8 for $KcsA^{D\text{-}Ala77}$ in 150 mM K^+ and 2.1 for wild-type KcsA in 150 mM K^+ (*3*). An alternative explanation for the reduced electron density in $KcsA^{D\text{-}Ala77}$ at 149 mM Na^+ + 1 mM K^+ is that Na^+ may begin to replace K^+. The most important point, however, is that the protein structure of $KcsA^{D\text{-}Ala77}$ is essentially the same in 1 mM and 150 mM K^+ (Fig. 3E), and both of these structures are similar to the conductive structure of the wild-type channel (Fig. 2C). Therefore, the $KcsA^{D\text{-}Ala77}$ channel appears to be captured in the conductive conformation at low concentrations of K^+.

To test the effect of this phenomenon on ion selectivity, we reconstituted the $KcsA^{D\text{-}Ala77}$ channel into planar lipid membranes and studied its properties in various mixtures of K^+ and Na^+ (Fig. 4). With 150 mM K^+ in the internal solution and 20 mM K^+ + 130 mM Na^+ in the external solution, the current reverses very near the calculated Nernst potential for the K^+ gradient (–52 mV), which means that the channel selects K^+ under these conditions (Fig. 4A). With 150 mM Na^+ in the internal solution and 150 mM K^+ in the external solution, inward current is observed at all voltages (Fig. 4B). Alternatively, when the K^+ solution is placed on the inner side of the membrane and Na^+ on the external side, only outward current (or zero current) is observed at all voltages (Fig. 4C). These results indicate that the $KcsA^{D\text{-}Ala77}$ channel conducts only K^+ in mixtures of Na^+ and K^+.

Wild-type–like selectivity in the presence of high K^+ concentrations is not surprising because the structure of the $KcsA^{D\text{-}Ala77}$ channel is essentially identical to that of the wild-type channel at high K^+ concentrations. Structural differences between these channels only occur in solutions with low K^+ concentrations, in which the wild-type channel adopts the nonconductive conformation and the $KcsA^{D\text{-}Ala77}$ channel remains in the conductive conformation. In the absence of K^+ and presence of 150 mM Na^+ on both sides of the membrane, the $KcsA^{D\text{-}Ala77}$ channel conducts Na^+ (Fig. 4D). The Na^+ current is definitely mediated by the K^+ channel because it is completely blocked by the specific K^+ channel inhibitor agitoxin2 ($AgTx_2$) (*8*). The wild-type KcsA K^+ channel does not conduct Na^+ in the absence of K^+ (Fig. 4E). In this experiment the presence of channels in the membrane is first documented by having K^+ on one side of the membrane, and then K^+ is replaced with Na^+ with the use of a perfusion apparatus.

To summarize the data, the wild-type KcsA K^+ channel prevents Na^+ from conducting through its filter, whether or not K^+ is present in solution. The $KcsA^{D\text{-}Ala77}$ channel prevents Na^+ conduction as long as K^+ is present but conducts Na^+ if K^+ is absent. These channels differ in that $KcsA^{D\text{-}Ala77}$ fails to enter the nonconductive conformation when the K^+ concentration is lowered. This result implies that a conductive filter structure in the absence of K^+ will allow Na^+ to conduct. From this we infer that K^+ channels normally prevent Na^+ conduction in solutions with very low K^+ not because Na^+ is unable to diffuse across the conductive filter, but because Na^+ (or the absence of K^+) favors the nonconductive conformation.

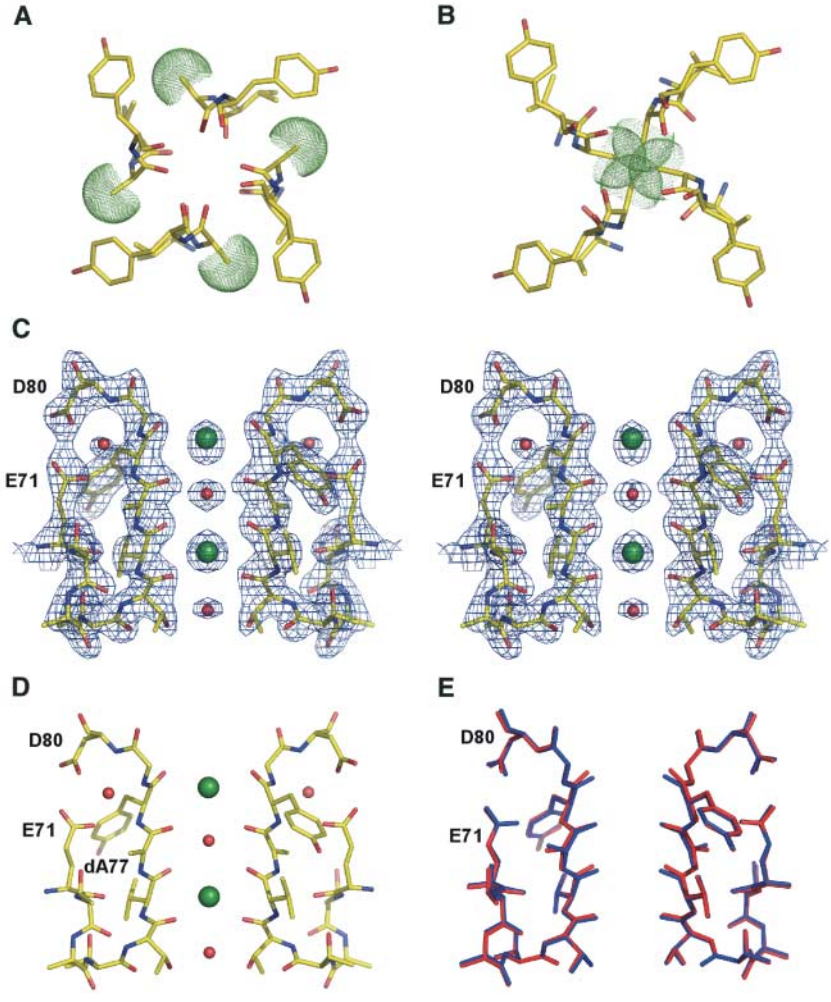

Fig. 3. Structure of the selectivity filter of $KcsA^{D\text{-}Ala77}$ in the presence of low [K^+]. (**A**) Top view of the structure of the selectivity filter of $KcsA^{D\text{-}Ala77}$ in high [K^+]. The methyl side chain of the D-Ala residue in each of the four subunits is shown in van der Waals (VDW) sphere representation. (**B**) A hypothetical structure of $KcsA^{D\text{-}Ala77}$ in the low [K^+] collapsed state. The methyl side chain of the D-Ala residue is again shown in VDW sphere representation. (**C**) Stereo view of the electron density of the selectivity filter of $KcsA^{D\text{-}Ala77}$ in the presence of low [K^+]. The $2F_{obs} - F_{calc}$ electron density map contoured at 2.0σ for the diagonally opposite subunits is shown. (**D**) The structure of the selectivity filter of $KcsA^{D\text{-}Ala77}$ in low [K^+] represented as in Fig. 1. (**E**) Superposition of the selectivity filter of the $KcsA^{D\text{-}Ala77}$ in high [K^+] (blue) and low [K^+] (red).

The adaptive nature of the filter conformation is not the sole basis of ion selectivity. An additional layer of ion selectivity is revealed by the KcsA$^{D\text{-}Ala77}$ channel, which selectively conducts K^+ in the presence of Na^+ even though its selectivity filter is locked in the conductive conformation. Selectivity in this case can be understood if K^+ successfully competes for the binding sites in the conductive form of the filter. In other words, the two K^+ ions residing in the conductive filter block Na^+ conduction. Because the presence of two K^+ ions is a prerequisite for the formation of the conductive conformation in the wild-type channel, Na^+ ions will be unable to permeate. This explanation is not inconsistent with the conduction of Na^+ through the conductive filter in the absence of K^+ (which is only observable in the KcsA$^{D\text{-}Ala77}$ channel). When Na^+ enters the filter in the absence of competing K^+ ions, we do not know whether Na^+ is partially hydrated or how it interacts with the binding sites.

The above discussion underscores two essential ideas: first, that the ability of the selectivity filter to adapt structurally in an ion-specific manner to K^+ and Na^+ is a fundamental aspect of ion selectivity, and second, that the prevention of Na^+ conduction in solutions containing both K^+ and Na^+ is connected directly to the selective nature of the binding sites in the conductive filter, which binds multiple K^+ preferentially over Na^+ when these two ions compete for the binding sites.

Selective conduction of K^+ over Na^+ ultimately stems from the filter's ability to adopt different structures in response to K^+ and Na^+ as well as from the selective nature of multiple binding sites in the conductive filter, which enable K^+ to compete against Na^+. The ability to adopt a conductive conformation in response to K^+, in which the binding sites are size-matched to K^+, is a property of the protein structure. We predict that attempts to synthesize novel K^+ selectivity filters will be successful only if the structures can capture the correct responsiveness to K^+ versus Na^+ (*9*). Attempts to understand K^+ selectivity through computation must take into account the entire selectivity filter occupied by two K^+ ions, because the experiments here show that an "empty" filter conducts Na^+.

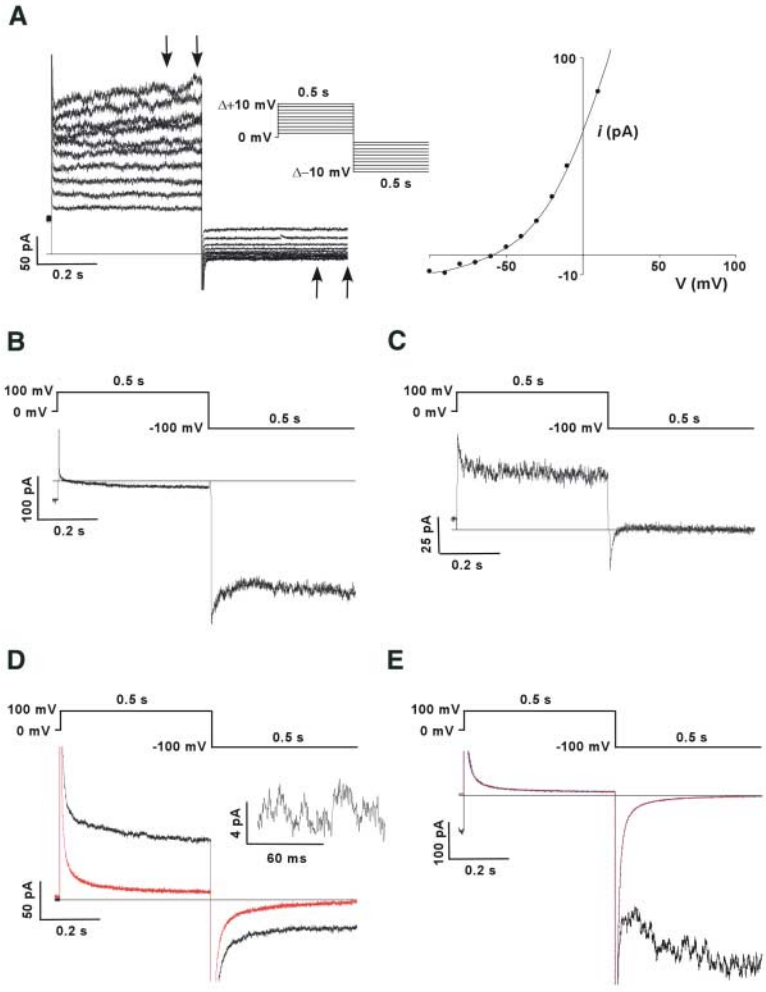

Fig. 4. Electrophysiological characterization of KcsA$^{D\text{-}Ala77}$. (**A**) Determination of ionic selectivity. Macroscopic currents were recorded using 10 mM succinate and 150 mM KCl (pH 4.0) as the internal solution, and 10 mM Hepes, 20 mM KCl, and 130 mM NaCl (pH 7.0) as the external solution. Current values between the time points indicated by arrows were averaged and plotted against the voltage applied for determining the reversal potential (Nernst potential = −52.3 mV). (**B**) Currents for KcsA$^{D\text{-}Ala77}$ were recorded using 10 mM succinate and 150 mM NaCl (pH 4.0) as the internal solution, and 10 mM Hepes and 150 mM KCl (pH 7.0) as the external solution. (**C**) Currents for KcsA$^{D\text{-}Ala77}$ were recorded using 10 mM succinate and 150 mM KCl (pH 4.0) as the internal solution, and 10 mM Hepes and 150 mM NaCl (pH 7.0) as the external solution. For (A) to (C), leak currents were determined by blocking channel currents using 5 μM $AgTx_2$ and were subtracted. (**D**) Currents for KcsA$^{D\text{-}Ala77}$ were recorded using 10 mM succinate and 150 mM NaCl (pH 4.0) as the internal solution, and 10 mM Hepes and 150 mM NaCl (pH 7.0) as the external solution. The amount of leak current was determined by the addition of 5 μM $AgTx_2$ (red trace). Inset is a magnified view of the current traces showing KcsA$^{D\text{-}Ala77}$ channel activity in the presence of Na^+. (**E**) Currents for wild-type KcsA were recorded using 10 mM succinate and 150 mM NaCl (pH 4.0) as the internal solution, and 10 mM Hepes and 150 mM KCl (pH 7.0) as the external solution (black trace). Also shown is the current after replacement of the external solution with 10 mM Hepes and 150 mM NaCl (pH 7.0) by perfusion (blue trace). The amount of leak current was determined by the addition of 5 μM $AgTx_2$ (broken red trace).

References and Notes

1. B. Hille, *Ionic Channels of Excitable Membranes* (Sinauer Associates, Sunderland, MA, ed. 3, 2001).
2. D. A. Doyle *et al.*, *Science* **280**, 69 (1998).
3. Y. Zhou, R. MacKinnon, *J. Mol. Biol.* **333**, 965 (2003).
4. Y. Zhou, J. H. Morais-Cabral, A. Kaufman, R. MacKinnon, *Nature* **414**, 43 (2001).
5. J. H. Morais-Cabral, Y. Zhou, R. MacKinnon, *Nature* **414**, 37 (2001).
6. M. LeMasurier, L. Heginbotham, C. Miller, *J. Gen. Physiol.* **118**, 303 (2001).
7. F. I. Valiyaveetil, M. Sekedat, R. MacKinnon, T. W. Muir, *Proc. Natl. Acad. Sci. U.S.A.* **101**, 17045 (2004).
8. R. MacKinnon, S. L. Cohen, A. Kuo, A. Lee, B. T. Chait, *Science* **280**, 106 (1998).
9. J. C. Mareque Rivas, H. Schwalbe, S. J. Lippard, *Proc. Natl. Acad. Sci. U.S.A.* **98**, 9478 (2001).

10. We thank S.-Y. Lee for assistance with crystallographic data collection and analysis, and E. Gouaux for providing computer access to F.I.V. Supported by NIH grants EB001991 and GM55843 (T.W.M.) and GM43949 (R.M.). R.M. is an Investigator of the Howard Hughes Medical Institute. The high- and low-K^+ KcsA$^{D\text{-}Ala77}$ structure coordinates and reflection files are deposited in the Protein Data Bank under accession numbers 2IH3 and 2IH1, respectively.

Supporting Online Material

www.sciencemag.org/cgi/content/full/314/5801/1004/DC1
Materials and Methods
Table S1
References

3 August 2006; accepted 10 October 2006
10.1126/science.1133415

RNA helicases—specifically retinoic acid inducible gene I (RIG-I) and melanoma differentiation–associated gene 5 (MDA5)—play critical roles in sensing viral double-stranded RNA (dsRNA) and controlling infection (*4*, *5*). It is thought that upon binding to dsRNA, they become activated and trigger a chain of signaling events that result in an immune response (see the figure). Helicase activity [unwinding dsRNA into single-stranded RNA (ssRNA)] may not be required to trigger signaling because the amino-terminal portion of RIG-I, which lacks the entire helicase domain by artificial deletion, is constitutively active and can trigger cytokine production without viral infection. Instead, the helicase domain of RIG-I may act as a switch, triggered by a conformational change induced by its helicase-like activity.

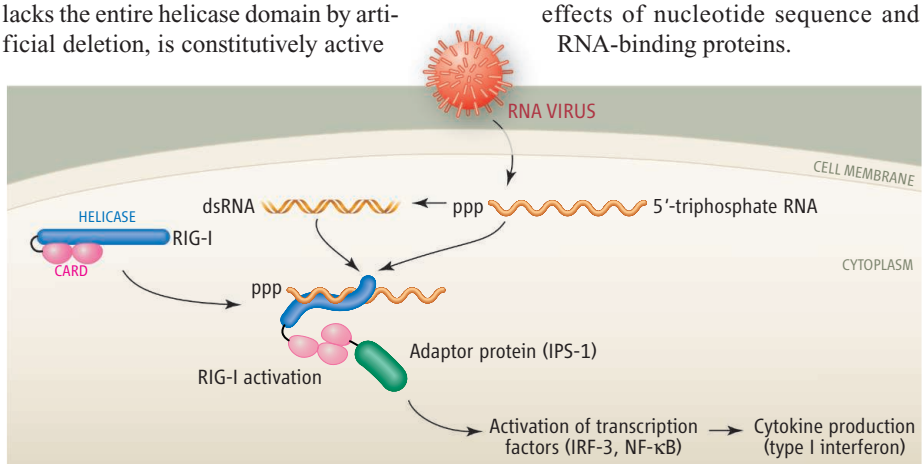

Viral sensing. In the cytoplasm, viral dsRNA or ssRNA containing 5′-triphosphate (ppp) is specifically recognized by RIG-I, initiating interferon production. In some cells, free viral nucleic acids, including those released from infected and killed cells, can be internalized by endocytosis and detected by Toll-like receptors in endosomes, also leading to interferon production. These mechanisms may cooperate to detect invading viruses and thence to initiate immune responses.

dsRNA is virtually absent in mammalian cells, and its molecular structure is considerably different from that of cellular genomic dsDNA. Some RNA viruses, such as encephalomyocarditis virus, generate dsRNA in cells as a by-product of viral replication, but not every virus accumulates such dsRNA. Hornung *et al.* show that ssRNA synthesized in vitro—and thus, that have acquired a 5′-triphosphate—induce interferon production when injected into cultured human cells. Moreover, artificial capping and base modification of 5′-triphosphate ssRNA abrogated detection by RIG-I in injected cells. RIG-I also associated with 5′-triphosphate ssRNA in vitro, suggesting that RIG-I could be a direct viral RNA receptor. But the authors acknowledge that this structure of RNA may only be part of a recognition signal. Cellular primary transcripts contain 5′-triphosphate. However, many self-RNAs undergo various processing steps that remove or mask the 5′-triphosphate moiety: Messenger RNA acquires a 7-methyl-guanosine cap structure at its 5′ end; transfer RNA undergoes 5′ cleavage and a series of nucleotide base modifications; ribosomal RNA readily complexes with ribosomal proteins. But there are also abundant self-RNAs in the cytoplasm that contain 5′-triphosphate, such as 7SL RNA, which is not recognized by RIG-I, indicating that there is more to the molecular signature than 5′-triphosphate. It is necessary to take into account the possible effects of nucleotide sequence and RNA-binding proteins.

This ability to discriminate between self and nonself resembles prokaryotic restriction. In bacteria harboring restriction enzymes that cleave at specific nucleic acid sequences, bacterial genomic DNA is protected from digestion. For example, some recognition sequences are methylated and are thus resistant to cleavage, whereas unmodified invading nuclei acids, such as that of a bacteriophage, are selectively destroyed by restriction enzymes. The common principle underlying these systems is that self-molecules are appropriately modified to avoid being detected.

Pichlmair *et al.* observed that some viruses, including influenza A virus, do not produce appreciable amounts of dsRNA, yet can activate RIG-I (*3*). They also found that ssRNA, such as that of genomic influenza virus, which is uncapped and contains phosphate at the 5′ end, associates with and activates RIG-I. NS1 protein encoded by influenza A virus has been known to affect host immune responses. However, the ability of NS1 to inhibit interferon synthesis in infected cells has been controversial. NS1 contains an RNA-binding domain that is thought to bind to dsRNA and prevent interferon production (*6*). But other work suggests that the RNA-binding activity of NS1 has nothing to do with interferon production (*7*). Pichlmair *et al.* explored a possible connection between a role of NS1 in interferon inhibition and RIG-I function. They found that NS1 forms a complex with RIG-I and propose that this interaction prevents the RIG-I signaling cascade in response to viral infection.

The findings of Hornung *et al.* and Pichlmair *et al.* highlight a new strategy to discriminate viral RNA from the numerous self-RNA species in the host cell cytoplasm. A tight discrimination is crucial because the viruses are replicating inside the cells. On the other hand, endosomal detection is a mechanism to sense a danger signal derived from an infected cell. Apparently, these distinct systems cooperate to maximally respond to the invaders. Some viruses escape 5′-triphosphate detection. The VPg protein of picornavirus covalently attaches to the 5′ end of viral RNA, thus masking it. However, this virus is known to accumulate dsRNA during the course of replication, and this molecular pattern may be detected by another sensor, MDA5 (*5*). The NS3/NS4A protein of hepatitis C virus (*8*) indirectly blocks RIG-I function by destroying its downstream signaling molecule. And influenza A virus may use NS1 protein to thwart host cell detection. Because these immune response blockers are virus encoded, a subtle balance between them and the antiviral activity of host cells will determine the outcome of infection. In this regard, antiviral therapy with either interferon or an interferon inducer could potentially reverse the effect of virus-encoded immune response blockers. The present reports also suggest that designing RNA molecules as a harmless mimicry of a virus could be used as antiviral and immunomodulatory therapies.

References

1. V. Hornung *et al.*, *Science* **314**, 994 (2006); published online 12 October 2006 (10.1126/science.1132505).
2. A. Pichlmair *et al.*, *Science* **314**, 997 (2006); published online 12 October 2006 (10.1126/science.1132998).
3. E. M. Creagh, L. A. J. O'Neil, *Trends Immunol.* **27**, 352 (2006).
4. M. Yoneyama *et al.*, *Nat. Immunol.* **5**, 730 (2004).
5. H. Kato *et al.*, *Nature* **441**, 101 (2006).
6. J. Talon *et al.*, *Proc. Natl. Acad. Sci. U.S.A.* **97**, 4309 (2000).
7. J. Y. Min, R. M. Krug, *Proc. Natl. Acad. Sci. U.S.A.* **103**, 7100 (2006).
8. E. Meylan *et al.*, *Nature* **437**, 1167 (2005).

10.1126/science.1135756

Potentiometric Titrator

The Potentiometric Titrator (COM-1600) is flexible, compact, and easy-to-use. It can process large numbers of samples when configured with the automation option. A large color graphics liquid crystal display displays real-time titration curves and differential curves to show reaction tendencies, etc. Measurement with half the sample volume is possible by using sample vessels and electrode holders designed for small amounts of samples. Useful functions for maintenance such as electrode information display and reagent remaining volume indication are also provided. The titration results and titration conditions, including titration/differential curve data, can be downloaded easily to a computer for recalculation, storage, and reprocessing.
JM Science For information 800-495-1678 www.jmscience.com

Protein Extraction from Insect Cells

Focus Insect Proteome kit makes use of a strong chaotropic buffer to release and solubilize virtually all insect cell proteins, including difficult-to-solubilize membrane proteins, from a large array of insect cell types. The resulting extracted samples require no further clean-up and can be loaded directly on IPG-Strips for two-dimensional gels or used for other applications.
G-Biosciences/Genotech For information 800-628-7730 www.GBiosciences.com

Angiogenesis Array

The ProteoPlex Human Angiogenesis Array measures eight angiogenesis-associated cytokines. Cytokine antibodies are spotted in quadruplicate, allowing statistical data analysis. The complete microarray kit includes complimentary slide scanning and analysis service in many sales regions, opening microarray technology to researchers who do not have ready access to scanning equipment.
EMD Biosciences For information 800-628-8470 www.novagen.com/proteoplex

Detector Integration

The Coulochem III high-performance liquid chromatography detectors (HPLC) can now be interfaced directly to the Agilent Chemstation through a standard USB interface. This interface allows for control and direct digital data acquisition of ESA's most popular HPLC detectors in the ChemStation environment.
ESA Biosciences For information +44 1844-239381

Cell Culture System

The Nunc Opticell Cell Culture system provides a sealed, sterile environment for growing and transporting cell cultures. The device reduces the time and labor required for experimental steps such as imaging, cell separation, antibody production, transfection, cloning, shipping of live cells, and short-term cryopreservation. Less than 6 mm thick, OptiCell is a standard microtiter plate-sized chamber that provides a growth surface of 100 cm^2. It takes up a fraction of the space and half the media volume of 75 cm^2 flasks. The cells grow on clear, nonfluorescent polystyrene membrane surfaces, enabling observation of live and fixed cryostaining in situ with any optical device or microscope. Both adherent and non-adherent cells can be cultured in OptiCell, and the system is suitable for production of cell by-products such as monoclonal antibodies and cytokines.
Nalge Nunc International For information 800-446-2543 www.nuncbrand.com

Cryostat with Disinfection

The CM1850 UV Cryostat is the first designed with AgProtect, Leica's new, patented antimicrobial ion coating. The instrument provides protection to laboratory users by reducing exposure to airborne and surface pathogens while also providing high-quality sections. When sectioning fresh tissue specimens in a cryostat, operators can be exposed to infectious pathogens. To provide protection in addition to personal protective equipment, the CM1850 UV features ultraviolet (UV) light to disinfect surfaces and the air within the chamber without generating condensation, toxic fumes, residues, or contaminated liquid waste. The cryochamber can be rapidly disinfected with UV light at any time without warming or defrosting. The AgProtect antimicrobial silver ion coating covers the outside surfaces and provides protection by penetrating the membranes of microbes and preventing replication.
Leica For information 800-248-0123 www.leica-microsystems.com

Literature

Constant Temperature Equipment: Circulators is a 32-page guide that includes complete performance specifications, application information, and technical tips on more than 30 heating/refrigerating circulating baths and immersion circulators. The circulators are designed to provide economical and reliable temperature control in a wide variety of industrial, pharmaceutical, laser, electronics, environmental, chemical, and laboratory applications. They can be used for stand-alone operation as well as cooling/heating of external devices. They are available with operating temperature ranges as broad as -40° C to +200° C.
PolyScience For information 800-229-7569 www.polyscience.com

Newly offered instrumentation, apparatus, and laboratory materials of interest to researchers in all disciplines in academic, industrial, and government organizations are featured in this space. Emphasis is given to purpose, chief characteristics, and availability of products and materials. Endorsement by *Science* or AAAS of any products or materials mentioned is not implied. Additional information may be obtained from the manufacturer or supplier by visiting www.science.labvelocity.com on the Web, where you can request that the information be sent to you by e-mail, fax, mail, or telephone.